
Atmospheric Liquid Water and Water Vapour under All-Sky Conditions

DISSERTATION
ZUR ERLANGUNG DES DOKTORGRADES
DER MATHEMATISCH-NATURWISSENSCHAFTLICHEN FAKULTÄT
DER CHRISTIAN-ALBRECHTS-UNIVERSITÄT
ZU KIEL

VORGELEGT VON

Heike Hauschildt



Kiel, Dezember 2006

Referent:	Prof. Dr. Andreas Macke
Korreferent:	Prof. Dr. Ralf Ludwig
Tag der mündlichen Prüfung:	31.01.2007
Zum Druck genehmigt:	Kiel, 31.01.2007

Der Dekan

Contents

Abstract	v
Zusammenfassung	vii
List of figures	xiii
List of tables	xvi
1 Introduction	1
2 Water vapour, clouds, and climate	5
3 Compilation of retrieval techniques	11
3.1 Overview of retrieval techniques and instruments	11
3.1.1 Ground based instruments and techniques	12
3.1.2 Satellite instruments and techniques	16
3.1.3 Conclusions	26
3.2 AMSU and AVHRR techniques	27
3.2.1 AMSU	28
3.2.2 Microwave retrieval of LWP and TPW	30
3.2.3 AVHRR	32
3.2.4 AVHRR retrieval of cloud properties	33
3.2.5 Data quality	35
3.2.6 Additional data	36

4	A microwave retrieval based on neural network	37
4.1	Neural Network	38
5	Comparison of microwave retrieval algorithms	43
5.1	Comparison of the NN algorithm to the AVHRR retrieval	43
5.2	Dependency on sub-FOV cloud cover	47
5.3	Comparison of the NN algorithm to the Grody algorithm	49
6	Ground-based retrieval of TPW in all-sky atmospheres	53
6.1	Cloud to clear TPW differences	53
6.1.1	TPW under all-sky and clear-sky conditions	62
6.1.2	TPW statistics for Lindenberg	63
6.2	The excess water vapour	73
6.2.1	Distinction of clear and cloudy cases from radiosoundings	73
6.2.2	All-sky vs clear-sky TPW	80
6.2.3	Sensitivity study	85
6.2.4	Excess water vapour for Europe	89
6.3	The vertical distribution of excess water vapour	92
6.4	Layered excess water vapour	97
6.5	Concluding remarks	100
6.6	NAO	100
7	Satellite-based retrieval of TPW in all-sky atmosphere	105
7.1	Global TPW distributions	106
7.2	Excess water vapour over the North Atlantic	111
7.3	Concluding remarks	116
8	Final summary and conclusions	123
	Appendix	126
A	Abbreviations and Acronyms	127

B Cloud Cover	131
C Frequency distributions	135
D Cloud — clear statistics from radiosonde measurements	137
E Spatial TPW as measured from Satellite	147
E.1 South Atlantic	147
E.2 Pacific	152
E.3 Indic	157
E.4 Antarctic circumpolar ocean	162
Bibliography	167

Abstract

Water vapour is an inhomogeneous quantity on all temporal and spatial scales. Its natural variability plays a crucial role in the climate system. Through positive feedback water vapour takes an important part in anthropogenically induced changes in climate resulting from increases in carbon dioxide and other greenhouse gases. Hence, determining its spatial and temporal variability is a challenging task. The development of a complete and accurate global water vapour data set is critical to an adequate understanding of the Earth's climate system. These data is essential for studies concerning the energy and water cycle including poleward energy transports, radiation budget studies, general circulation model verification and global change research. The demands on the water vapour climatology are increasing in terms of temporal and spatial resolution.

The first climatologies were based on radiosonde measurement. Radiosonde measurements take place primary over land at distant points and do not show small scale spatial water vapour variations. The use of satellite instruments enables global measurements. Different methods based on the different spectral channels are in use. Infrared and visible techniques offer measurements with a sufficient spatial resolution but they only work in the absence of significant cloud cover. Over the oceans additional informations are determined by microwave instruments. Here clouds are translucent.

Microwave instruments have large observing geometries. The measured signal is the integral over this area. The question arises wether the retrieved liquid water path or total precipitable water depends on the sub pixel inhomogeneity. To answer this question liquid water paths retrieved from measured scattered solar radiation have been compared to results from microwave retrievals. No influence on the sub-pixel cloud cover was found.

The SEVIRI instrument on METEOSAT-8 enables the retrieval of total precipitable water with a high spatial and temporal resolution for clear-sky scenes only. Therefore, an improvement of climatologies for the SEVIRI covered regions is possible. A water vapour climatology based on clear-sky measurements will lead to an underestimation in total precipitable water when the cloudy-skies contain more water vapour than clear-skies. This effect is called *clear-sky bias*. Microwave techniques can monitor water vapour in clear and cloudy atmospheres but are limited to homogeneous emitting surfaces like ocean areas. The difference in water vapour in clear and cloudy scenes is retrieved using microwave and radiosonde data.

The concept of excess water vapour as measure of the total precipitable water ratio of all-sky to clear-sky atmospheres is introduced. The excess water vapour is investigated on different time scales. The excess water vapour is depending on the clear sky total precipitable water. Due to the coupling of temperature and water vapour in the clear sky atmosphere the excess water vapour is depending on the temperature.

For low mean clear-sky total precipitable water the excess water vapour is about 1.3 and decreases with increasing clear-sky total precipitable water. The resulting underestimation of water vapour due to neglecting the cloud-covered scenes is about 1-2 kg/m². This underestimation was found using satellite and ground-based data. For radiosonde ascents the whole profile and the relation of water vapour to the height is investigated. The vertical distribution of total precipitable water the excess water vapour function for each layer resembles the one for the whole vertical integral. For investigations of the energy and radiation balance corrections of the total precipitable water climatology used as input data can be made with the results shown in this study.

Zusammenfassung

Wasser ist die wichtigste Komponente im Klimasystem. Betrachtet man die Atmosphäre, so beeinflusst das enthaltene Wasser über Absorption und Streuung die Energiebilanz unseres Planeten. Wasserdampf ist auf zeitlichen und räumlichen Skalen inhomogen verteilt. Seine natürliche Variabilität spielt eine entscheidende Rolle im Klimasystem. Durch positive Rückkopplungen unterstützt der Wasserdampf anthropogene Klimaänderungen. Daher ist es wichtig seine räumliche und zeitliche Variabilität zu erfassen. Die Entwicklung eines vollständigen und genauen globalen Wasserdampfdatensatzes ist wichtig für das vollständige Verständnis des Klimasystems. Diese Daten sind für die Studien des Energie- und Wasserzyklus, der Strahlungsbilanz, der allgemeinen Zirkulation und Klimamodelle wesentlich. Die Qualitätsansprüche, die an Wasserdampfklimatologien heutzutage gestellt werden, erhöhen sich hinsichtlich der zeitlichen und räumlichen Auflösung.

Die ersten Klimatologien basierten auf Radiosonden. Radiosondenaufstiege finden primär über Land statt. Satelliteninstrumente ermöglichen die globale Fernerkundung von Wasserdampf und Wolkenwasser. Es sind unterschiedliche Methoden, die auf Messungen in verschiedenen spektralen Bereichen beruhen, gebräuchlich. Techniken im infraroten und sichtbaren Spektralbereich messen mit einer ausreichenden räumlichen Auflösung. In diesem Spektralbereich sind Wolken opak und verhindern dadurch die Fernerkundung der gesamten Atmosphäre. Über den Ozeanen können zusätzliche Informationen aus der Messung der Emissionen im Mikrowellenbereich des Spektrums gewonnen werden. In diesem Bereich sind Wolken durchlässig.

Mikrowelleninstrumente haben große Beobachtungsgeometrien. Das gemessene Signal ist das Integral über diesen Bereich. Es stellt sich die Frage, ob das abgeleitete Flüssigwasser bzw. Gesamtwasser von der Inhomogenität innerhalb der Beobachtungsgeometrie abhängig ist. Mittels eines Vergleichs des mittleren Flüssigwassers aus Messungen der rückgestreuten solaren Strahlung und aus Mikrowellenmessungen wurde kein Einfluss des Bedeckungsgrads innerhalb der Beobachtungsgeometrie auf den mittleren Flüssigwasserpfad gefunden.

Das SEVIRI-Instrument auf METEOSAT-8 ermöglicht die Ableitung des atmosphärischen Gesamtwassers mit einer hohen zeitlichen und räumlichen Auflösung, allerdings nur im wolkenfreien Fall. Wasserdampfklimatologien basierend auf wolkenfreien Situationen führen zu einer systematischen Unterschätzung des Gesamtwassers, wenn man annimmt, dass in der bewölkten Atmosphäre mehr Wasser enthalten ist als in der unbewölkten. Aus dem Vergleich von Mikrowellen Messungen Mikrowellenmessungen in bewölkten und unbewölkten Fällen wird daher die Unterschätzung im unbewölkten Fall abgeleitet. Hierfür wurden sowohl Messungen im Mikrowellenbereich als auch Radiosondenmessungen verwandt.

Das Konzept des überschüssigen Wasserdampfs (EWV) als Maß des Verhältnisses des Wasserdampfs unter bewölkten Szenen zu dem unter wolkenfreien Szenen wird hier einge-

führt. Der EWW ist abhängig vom mittleren Gesamtwasser im unbewölkten Fall sowie von der Temperatur. Für mittlere Gesamtwasserpfade der unbewölkten Szenen ergibt sich im Vergleich zu allen Szenen ein Faktor von 1.3. Dieser nimmt mit Zunahme des Wasserdampfs im unbewölkten Fall ab. Die Unterschätzung des Gesamtwassers beläuft sich daher auf 1-2 kg/m². Diese Ergebnisse wurden aus den beiden Datensätzen, globalen Satellitendaten sowie Radiosondendaten abgeleitet. Mittels der Radiosondendaten wurde weiterhin die vertikale Verteilung des Wasserdampfs untersucht. Die abgeleiteten Faktoren für die gesamte Atmosphäre sind vergleichbar mit denen für einzelne Schichten. Untersuchungen der Energie- und Strahlungsbilanz, bei denen als Eingangsdaten Klimatologien des Gesamtwassers eingehen, können daher anhand der hier gezeigten Ergebnisse korrigiert werden.

List of Figures

2.1	Monthly mean clear-sky TPW	6
2.2	Water vapour feedback	7
3.1	Weighting functions for zenith looking passive microwave radiometer	14
3.2	Attenuation depending on the wavelength	17
3.3	Weighting functions for the IR channels of SEVIRI	20
3.4	Scheme of the relation of the observed wavelength to the originating height	21
3.5	AMSU-A weighting functions	22
3.6	AMSU-A asymmetry	29
3.7	Composition of the MW-signal	30
3.8	Transmittance as function of the MW-frequency	31
3.9	Sketch of AVHRR channel 1 reflectances depending on surface	33
3.10	Observed reflectivity depending on optical depth	34
4.1	Distribution of the used radiosonde ascents	38
4.2	Relation brightness temperature to LWP and TPW	39
4.3	Basic structure of neural network	40
4.4	Root mean square error depending on NN set up	41
4.5	Correlation of the test data set to the NN retrieval	42
5.1	LWP fields derived with AVHRR and AMSU, 14th April 2001	44
5.2	LWP AVHRR versus LWP AMSU	45
5.3	LWP AVHRR versus LWP AMSU, dependency on scan angle	46
5.4	Influence of cloud cover on a $2.5^\circ \times 2.5^\circ$ grid	48

5.5	LWP field from 9.9.2001 at 14:35	50
5.6	TPW field from 9.9.2001 at 14:35	50
5.7	Correlation between NN-retrieved and NOAA-NESDIS atmospheric prop- erties	51
6.1	TPW per cloud class for Lindenberg	54
6.2	Bias estimator after Gaffen and Elliot (1993) for Lindenberg	55
6.3	Correlation of between the stations	63
6.4	10-years time series of radiosonde ascents at Lindenberg	64
6.5	Annual cycle derived from the 10-years time series	65
6.6	Anomalies of the 10-years timeseries	66
6.7	Surface pressure depending on season	67
6.8	2-m temperature dependong on season	68
6.9	Relative humidity depending on season	69
6.10	TPW depending on season	70
6.11	Seasonal minimum dewpoint difference of radiosonde ascents	75
6.12	Seasonal minimum dewpoint difference of radiosonde ascents	76
6.13	Monthly mean clear-sky (left) and cloudy-sky (right) TPW depending on the distinction criteria	77
6.14	Monthly mean clear-sky (left) and cloudy-sky (right) TPW depending on the distinction criteria	78
6.15	Monthly mean TPW depending on cloud cover	79
6.16	Monthly and yearly mean TPW (clear) versus TPW (cloud)	80
6.17	Time series of radiosonde parameter for Lindenberg in May 1997	81
6.18	Monthly mean clear-sky versus all-sky TPW	82
6.19	Seasonal mean clear-sky versus all-sky TPW	83
6.20	Underestimation in TPW retrieved from German radiosonde stations	84
6.21	Variability introduced by number of data points	85
6.22	Dependency of amount of data	86
6.23	Regression based on 60% of the data	87
6.24	Dependency of the clear-sky TPW towards the clear-sky definition in ra- diosonde ascents	87

6.25	Geographical distribution of European stations	88
6.26	Relation of monthly mean TPW in all-sky depending on clear-sky TPW	89
6.27	Relation of monthly mean TPW in all-sky depending on clear-sky TPW depending on the pressure system	90
6.28	Relation of monthly mean TPW in all-sky depending on clear-sky TPW depending on the pressure system and the season	90
6.29	Relation of monthly mean TPW in all-sky depending on clear-sky TPW depending on the pressure system and the season	91
6.30	Mean vertical profiles for January	92
6.31	Mean vertical profiles for April	93
6.32	Mean vertical profiles for July	94
6.33	Mean vertical profiles for October	95
6.34	Frequency distribution of surface pressure and 500 hPa level height related to TPW	96
6.35	Layered TPW all-sky to clear-sky relation for the layer 1000 hPa to 850 hPa	97
6.36	Layered TPW all-sky to clear-sky relation for the layer 850 hPa to 700 hPa and 700 hPa to 500 hPa	98
6.37	Layered TPW all-sky to clear-sky relation for the layer 500 hPa to 300 hPa and 300 hPa to 200 hPa	99
6.38	The time series of the winter mean NAO index after Hurrell	100
6.39	Comparison of the TPW all-sky and TPW anomaly to the NAO	101
6.40	Comparison of the TPW clear and excess water vapour to the NAO	102
7.1	Monthly mean all-sky TPW derived from AMSU	106
7.2	Monthly mean clear-sky TPW derived from AMSU	107
7.3	Monthly mean LWP derived from AMSU	108
7.4	Monthly mean ratio (all-sky TPW divided by clear-sky TPW) derived from AMSU	109
7.5	Monthly mean difference all-sky TPW minus clear-sky TPW derived from AMSU	110
7.6	Monthly mean all-sky TPW derived from AMSU over the North Atlantic	111
7.7	Monthly mean clear-sky TPW derived from AMSU over the North Atlantic	112
7.8	Monthly mean excess water vapour derived from AMSU over the North Atlantic	113

7.9	Relation of clear-sky TPW to the all-sky TPW	114
7.10	Relation of clear-sky TPW to the all-sky TPW	115
7.11	Excess water vapour depending on the clear-sky TPW for the year 2004 . .	116
7.12	Excess water vapour depending on the clear-sky TPW for four years	117
7.13	Zonal distribution of the ratio (all-sky TPW by clear-sky TPW)	117
7.14	Frequency distribution of the excess water vapour of each month for the North Atlantic for four years	118
7.15	Global frequency distribution of the excess water vapour of each month for four years	119
7.16	Frequency distribution of the excess water vapour for the North Atlantic and global for four years	120
B.1	Influence of cloud cover on a $4^\circ \times 4^\circ$ grid.	132
B.2	Influence of cloud cover on a $1.0^\circ \times 1.0^\circ$ grid.	133
C.1	TPW and LWP frequency distributions on a 1.0 grid	136
D.1	10 years of data from Schleswig sorted by the observed cloud cover.	139
D.2	The bias estimators and the probability according to Gaffen and Elliot (1993) for Schleswig.	140
D.3	10 years of data from Stuttgart sorted by the observed cloud cover.	141
D.4	The bias estimators and the probability according to Gaffen and Elliot (1993) for Stuttgart.	142
D.5	10 years of data from Essen sorted by the observed cloud cover.	143
D.6	The bias estimators and the probability according to Gaffen and Elliot (1993) for Essen.	144
E.1	South Atlantic: Relation of clear-sky TPW to the all-sky TPW.	147
E.2	South Atlantic: Relation of clear-sky TPW to the all-sky TPW.	148
E.3	South Atlantic: Excess water vapour depending on the clear-sky TPW. . .	148
E.4	South Atlantic: Excess water vapour and underestimation depending on the clear-sky TPW.	149
E.5	South Atlantic: Zonal distribution of the excess water vapour.	149
E.6	Frequency distribution of the excess water vapour of each month for the South Atlantic.	150

E.7	Frequency distribution of the excess water vapour for the South Atlantic.	151
E.8	Pacific: Relation of clear-sky TPW to the all-sky TPW.	152
E.9	Relation of clear-sky TPW to the all-sky TPW.	153
E.10	Excess water vapour depending on the clear-sky TPW.	153
E.11	Excess water vapour depending on the clear-sky TPW.	154
E.12	Pacific: Zonal distribution of the excess water vapour.	154
E.13	Frequency distribution of the excess water vapour of each month for the Pacific.	155
E.14	Frequency distribution of the excess water vapour for the Pacific.	156
E.15	Indic: Relation of clear-sky TPW to the all-sky TPW.	157
E.16	Indic: Relation of clear-sky TPW to the all-sky TPW.	158
E.17	Excess water vapour depending on the clear-sky TPW for the Indic.	158
E.18	Excess water vapour depending on the clear-sky TPW for the Indic.	159
E.19	Indic: Zonal distribution of the excess water vapour.	159
E.20	Frequency distribution of the excess water vapour of each month for the Indic.	160
E.21	Frequency distribution of the excess water vapour of each month for the Indic.	161
E.22	Antarctic circumpolar ocean: Relation of clear-sky TPW to the all-sky TPW.	162
E.23	Antarctic circumpolar ocean: Relation of clear-sky TPW to the all-sky TPW.	163
E.24	Excess water vapour depending on the clear-sky TPW for the Antarctic circumpolar ocean.	163
E.25	Excess water vapour depending on the clear-sky TPW for the Antarctic circumpolar ocean.	164
E.26	Antarctic circumpolar ocean: Zonal distribution of the excess water vapour.	164
E.27	Frequency distribution of the excess water vapour of each month for the Antarctic circumpolar ocean.	165
E.28	Frequency distribution of the excess water vapour for the Antarctic circumpolar ocean.	166

List of Tables

3.1	Compilation of ground-based and air-borne techniques	17
3.2	Overview satellite instruments	18
3.3	Compendium retrieval techniques	26
3.4	Instrument characteristics	27
3.5	AMSU instrument characteristics	28
3.6	AVHRR channel informations	32
3.7	Satellite status informations	36
6.1	Monthly mean TPW in the cloud classes for Lindenberg	58
6.2	Monthly mean TPW in the cloud classes for Schleswig and Essen	59
6.3	Monthly mean TPW in the cloud classes for Stuttgart	60
6.4	Monthly ratios of the mean TPW in the cloud classes for all stations	61
6.5	Correlation coefficients of the stations	62
6.6	Statistical parameters of of the season relation shown in Figures: 6.7, 6.8, and 6.10	71
6.7	Statistical parameters of of the season relation shown in Figures: 6.9	72
6.8	Parameter of the fitting function for different stations	84
6.9	Correlation of the TPW all-sky to clear-sky relation on the pressure system and the season	88
6.10	Correlation of the winter mean NAO index after Hurrell with TPW	104
7.1	The parameters of the function expressing the ratio vs clear-sky TPW using all years	120
7.2	Statistical parameters discribing the frequency distributions of the excess water vapour.	121

D.1	Seasonal and annual mean TPW in kg/m^2 in the cloud classes.	138
D.2	Seasonal ratios of the mean TPW in a cloud class.	145
E.1	South Atlantic: The parameters of the function expressing the excess water vapour vs clear-sky TPW.	151
E.2	Pacific: The parameters of the function expressing the excess water vapour vs clear-sky TPW.	156
E.3	Indic: The parameters of the function expressing the excess water vapour vs clear-sky TPW.	161
E.4	Antarctic circumpolar ocean: The parameters of the function expressing the excess water vapour vs clear-sky TPW.	166

Chapter 1

Introduction

Water is the most important quantity in the Earth climate system. Focusing on the atmosphere, water exists in gaseous, liquid and solid form. Due to absorption, emission and scattering effects the radiation budget and therefore the energy budget of the Earth and the atmosphere. This work regards ways of determining a water vapour climatology under all-sky atmospheric conditions. Remote sensing methods to derive water vapour and cloud liquid water are discussed here.

The spatial and temporal pattern of atmospheric water vapour describes the current state of our climate system. Water vapour is an inhomogeneous quantity on all temporal and spatial scales. Its natural variability plays a crucial role in the climate system. Water vapour affects the tropospheric temperature due to greenhouse warming stronger than other atmospheric gases. It is the mandatory condition for clouds and the hydrological cycle. The changes in cloud cover control the net warming/cooling processes. The range in estimated climate sensitivity of 1.5 to 4.5° C for a CO₂ doubling is largely dictated by the interaction of model water vapour feedbacks with the variations in cloud behavior among existing models (IPCC Working Group I (2001)). Hence, determining its spatial and temporal variability is a challenging task.

In literature several quantities concerning the atmospheric water are discussed. The total precipitable water (TPW) is the vertically integrated absolute humidity, whereas the upper tropospheric humidity (UTH) is the relative humidity of the upper troposphere. Unlike the TPW the relative humidity depends on the atmospheric temperature. For models and weather forecasting relative humidities are used. With early satellite instruments, single channel based humidity retrievals have been performed at 6.3 μm introducing broad weighting functions that give the mean UTH. However, TPW is a more complete quantity observing changes in the atmospheric water vapour and will be used henceforth.

The vertical integrated water vapour denoted as total precipitable water (TPW) is derived using various techniques. Hauschildt and Macke (2004) summarises previous work on the

retrieval of TPW from ground and satellite based measurements. A common problem in remote sensing from satellite of water vapour path is the limitation to clear-sky observations for infrared and solar retrieval techniques. Microwave techniques for the retrieval of TPW are only applicable over ocean areas. Other techniques are not mature.

The question, therefore, arises whether there is a significant difference in mean values between TPW in cloudy- and clear-sky observations? It is important to know at which time scales this bias is most apparent and how it can be corrected. It seems obvious that the atmospheric water vapour in cloudy skies exceeds the TPW in clear-skies. Warm front clouds are associated with advection of warm humid air. Furthermore, convective clouds transport moisture from the boundary layer into the free atmosphere. Gaffen and Elliot (1993) found that the climatological column water vapour content of clear-sky atmospheres derived from north hemispheric radiosoundings is significantly lower than for cloudy-skies. The magnitude of the bias is lower in tropical regions than at midlatitudes where the largest values are found in winter. The variability cannot be explained by variations in surface temperature or by instrument biases. However, quantitative estimates of the variation of TPW with cloud cover are lacking. Crewell et al. (2002) estimate the difference between mean TPW in cloudy to clear-skies from ground based microwave radiometer measurements. For the European area they retrieve a mean ratio (TPW (cloud) / TPW (clear)) of 1.2 to 1.3, showing a slight dependency on latitude. However, these values were derived from two months of measurements, only.

Inside clouds the relative humidity usually remains close to 100 % although considerable departures from this value have been observed. In cumulus clouds the relative humidity ranges from 80 % at the cloud boundary to supersaturation in the centre of the cloud exceeding 107 %. The median of the supersaturation is given with 0.1 %. Outside the cloud the relative humidity drops to values near 70 % due to turbulent mixing. Flights through clouds over Montana show supersaturation ranging from - 0.5 % to + 0.5 %, but averaged to 0 % (see Pruppacher and Klett (1997), Chapter 2).

Marsden and Valero (2004) showed that water vapour in clear-sky situations is lower compared to convective situations. The increase in the resulting greenhouse effect from the clear to the cloudy case cannot be explained by the increase in vertical integrated water vapour and larger sea surface temperatures. An explanation is found in the humidity profile: an increase of upper tropospheric water vapour is observed. The absolute amount of water vapour decreases with height by three orders of magnitude from the boundary layer to the upper-troposphere. The contribution of the specific water vapour layer to the effective greenhouse effect increases with height. Hence, it is important to monitor the water vapour profile as well. In this study the focus is set on the difference in integrated water vapour clear and cloudy atmosphere. Observations from satellites for both situations are only available from microwave instruments in frequencies where clouds do not block the satellite view. A common method here is a two frequency scheme which leads to vertical integrated water vapour.

To constitute a TPW climatology from ground based measurements (using the advantage of high temporal resolution, measurements under all-sky situations, long time series) would lead to several problems. These observations are limited to land surfaces and the distribution of these stations is inhomogeneous over the continents. A global coverage is only available from satellite measurements. Here the temporal resolution depends on number of overpasses per surface point, satellite type (orbiting or geostationary) and number of satellites used. The majority of TPW satellite based estimates over land is derived using thermal measurements. This limits the observations to clear-sky situations. Over oceans TPW can be retrieved using microwave frequencies; here all-sky observations are possible. For IR-techniques a bias is introduced by systematically omitting cloudy atmospheres with their larger TPW. Climatologies based on orbiting satellites run into a sampling problem. For global coverage IR techniques are used, therefore only clear-sky scenes are observed. For one surface point TPW observations are only available when no clouds are in the footprint. This reduces the amount of useful data. Therefore only by chance a moist scene near clouds maybe observed. This leads to an overestimation of clear-sky cases in the climatologies and consequently to a dry bias.

The focus of this study is the estimation of the TPW in all-sky situations based on satellite data. The examination of the difference in TPW for clear and cloudy situations will lead to a quantification of the climatological excess water vapour (EWV). This in turn may be used to correct TPW climatologies based on clear-sky measurements.

In chapter 2 a short summary of the previous work is given. The physical basis and available retrieval techniques are described in chapter 3. Based on neural network technique an algorithm for the retrieval of LWP and TPW from microwave measurements is developed (chapter 4). A comparison of the neural network retrieval scheme with other methods is given in chapter 5. Further, the influence of clouds on the water vapour path retrieval is investigated. Returning to the main interest in the difference in clear-sky to all-sky TPW, radiosonde ascents are used to define the difference in TPW in clear- and all-sky situations. A closer view on the time series of TPW and standard meteorological quantities like surface pressure, temperature, humidity, the height of the 500 hPa level, and the cloud cover given in the synoptical observations is performed for one station exemplarily (chapter 6).

The concept of climatologies requires large scale coverage. For this purpose satellite microwave observations over the oceans are used. The monthly mean TPW fields derived from Advanced Microwave Sounding Unit (AMSU) measurements of TPW are shown in chapter 7. Final conclusions and an outlook are given in chapter 8.

Chapter 2

Water vapour, clouds, and climate

Several measurement campaigns, retrieval techniques, and model sensitivity studies concerning water vapour and its impact on the climate system are resumed in Hauschildt and Macke (2004). An overview is given here.

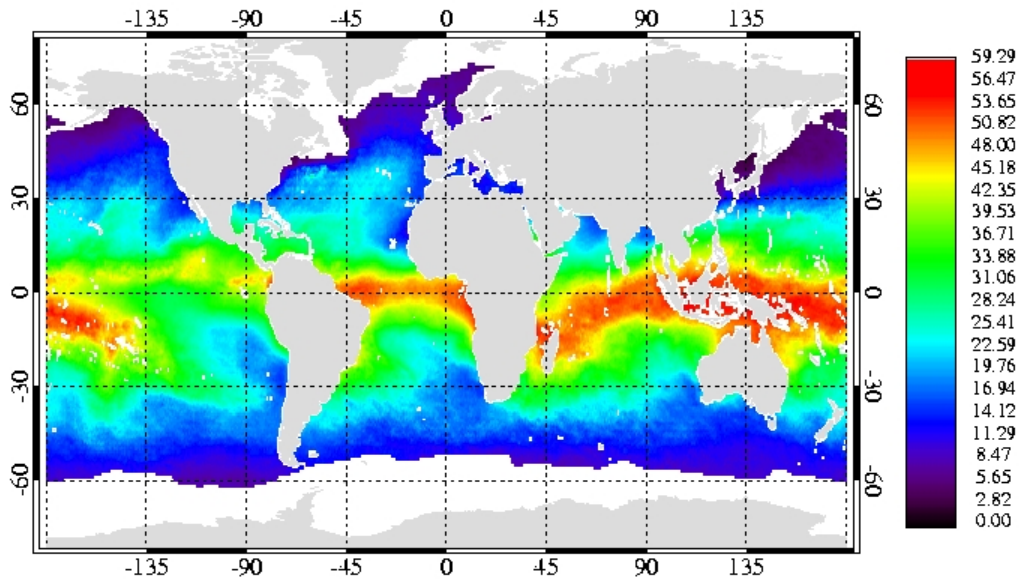
The global mean water vapour path as evaluated by Trenberth et al. (1987) is 26 kg/m^2 . The geographical distribution varies from $\sim 5 \text{ kg/m}^2$ in the polar region to $\sim 60 \text{ kg/m}^2$ in the tropics. These values were derived using global analysis from the European Centre of Medium Range Weather Forecasts (ECMWF). Monthly mean total precipitable water (TPW) fields derived from AMSU measurements over the oceans are shown in figure 2.1. The humid atmospheres in the inner tropical convergence zone (ITCZ) are clearly visible. From January to July the ITCZ moves north in the Atlantic. In the Indic ocean the monsoon area is pronounced by large TPW values. In the western Pacific the warm pool area appears as a region with large water vapour amount. The TPW varies with latitude and season. Hence, determining its variability is a challenging task.

Atmospheric water vapour absorbs mainly the thermal emittance of the surface. This increases the atmospheric temperature. Thus, the atmosphere can contain more water vapour. This positive natural feedback mechanism characterises the strong water vapour greenhouse effect and is shown in figure 2.2. Furthermore the anthropogenic greenhouse forcing induced by CO_2 which is also a strong thermal absorber couples to the water vapour feedback. The absorption by CO_2 increases the atmospheric temperature which will lead to more water vapour. A warmer atmosphere has a larger vertical extend. The irradiation at the surface is lower because of the increasing optical depth of the atmosphere. The ability of the atmospheric column to absorb thermal energy is higher. Thus, the energy loss to space is lower and the atmospheric temperature increases.

Because of its strong greenhouse effect, the importance of a detailed knowledge of the water vapour distribution is prominent in the climate warming discussions. By means of a radiative transfer sensitivity study Bühler et al. (2004) examine the influence of water

vapour in clear sky atmosphere on outgoing longwave radiation (OLR). A water vapour

A: January



B: July

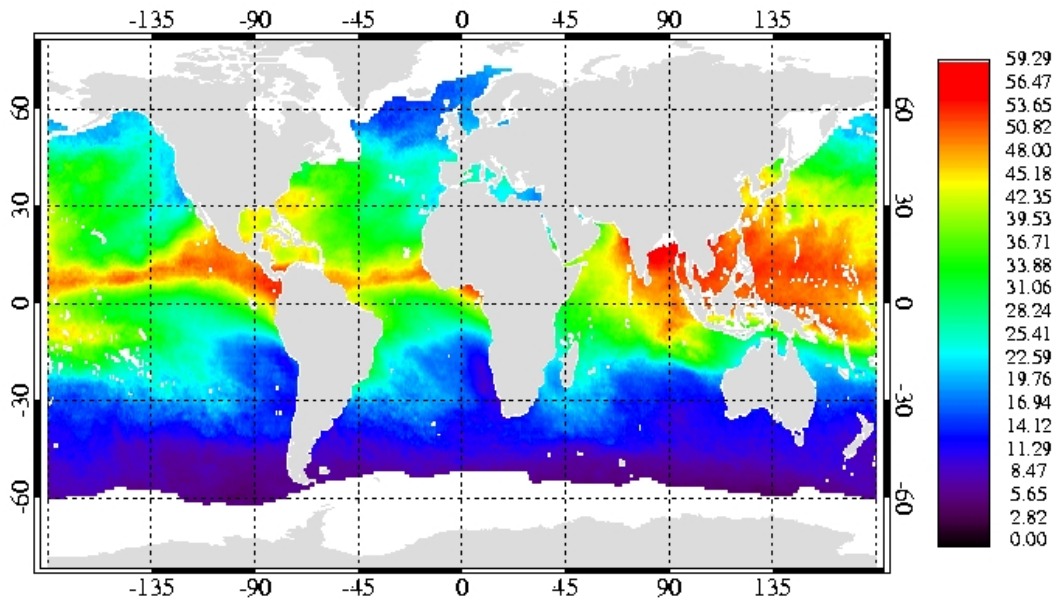


Figure 2.1: Monthly mean clear-sky TPW [kg/m^2] for (A) January and (B) July 2004. Clear-sky TPW is derived from AMSU measurements. The grid size is 0.5° . Clear-sky is defined as a LWP of $0 \text{ kg}/\text{m}^2$ is observed.

increase of 20% in the tropics has the same reducing impact on the outgoing longwave radiation as a CO₂ doubling. Whereas a decrease of 20% shows the same impact on the OLR as a mean atmospheric temperature increase of 1K. The major parts of the OLR variability can be explained by changes in the mean atmospheric temperature, humidity and the CO₂.

Stephens and Tjemkes (1993) considered a linear relationship between the greenhouse effect G and the total precipitable water. The greenhouse effect is defined as the relation of the surface temperature T_s to the planetary temperature T_e . The temperatures can be expressed by the radiative effective optical depth using a grey body model. For the Earth's atmosphere this optical depth is expressed by the integrated total precipitable water, w .

$$G = \frac{T_s^4}{T_e^4} = a + bw \quad (2.1)$$

The authors demonstrated that the slope factor b is largely governed by the variation of temperature with height in the atmosphere and that the intercept a is determined by a variety of factors including the assumed profile of water vapour as well as the concentrations of other greenhouse gases. Thus, the clear sky greenhouse effect is assessable from satellite by measurements of temperature and TPW. The correlation between the greenhouse

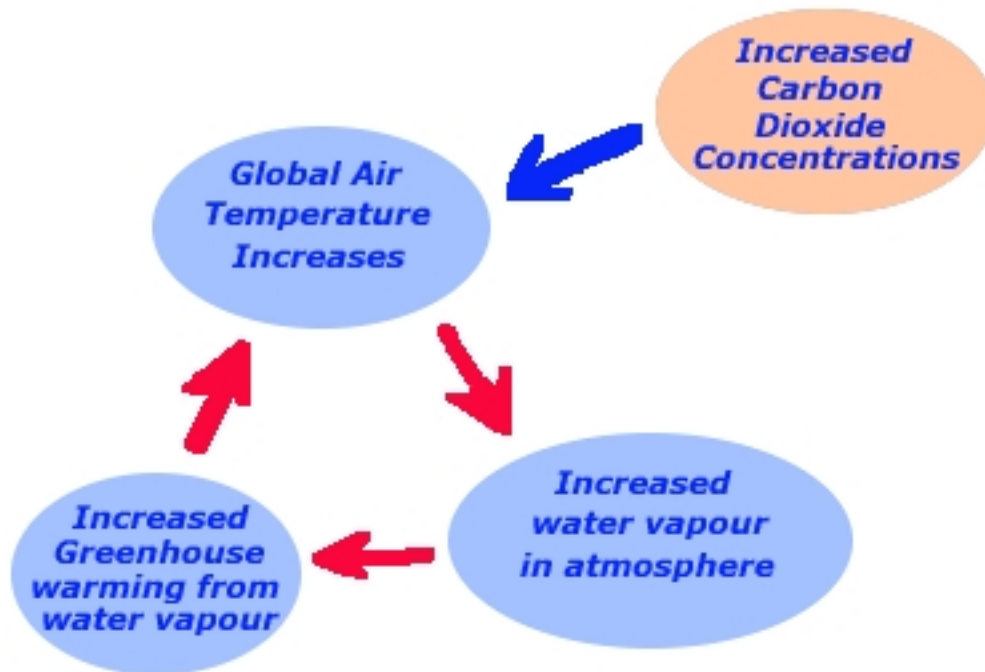


Figure 2.2: Water vapour feedback characterises the greenhouse radiative forcing Peixoto and Oort (1992).

effect, derived from Earth radiation budget and sea surface temperature observations, and using coincident Special Sensor Microwave/Imager (SSM/I) microwave observations of TPW for clear sky observations is 0.8. The retrieved greenhouse effect is not a direct measure of the water vapour feedback, which is not observed, because the true greenhouse effect is a consequence of numerous linked processes and feedbacks.

During the Cirrus Regional Study of Tropical Anvils and Cirrus Layers – Florida Area Cirrus Experiment (CRYSTAL–FACE) in July 2002 aircraft measurements in the infrared region were performed to estimate the greenhouse effect as a measure of the evaporative feedback of ocean and atmosphere. Marsden and Valero (2004) investigate the differences in the greenhouse effect due to water vapour absorption in cloudy compared to clear sky scenes. They conclude that convection and upper tropospheric moisture are the most important elements for the greenhouse efficiency.

Microwave retrieval techniques are based on the strong emission of the atmospheric water against the radiatively cold oceanic background. To investigate the TPW for cloud and clear scenes it is important to identify cloudy scenes. One advantage of microwave retrieval is the simultaneously retrieval of TPW and liquid water path (LWP). For these measurements ground based instruments are used as the truth. While TPW retrievals can be validated with colocated measurements from ground based sensors such as radiosondes, Global Positioning System (GPS) receiver, and Raman Lidar, retrieval validation of liquid water path is more complicated. In the European project CLIWA–NET, Cloud Liquid Water Network, different methods in remote sensing of cloud properties, TPW, and LWP were compared and the benefits of a surface based network of microwave instruments were investigated. During the last CLIWA–NET campaign (BBC) a ground based microwave intercomparison was performed to compare both instruments and the LWP retrieval algorithms. These algorithms are based on statistical correlations between brightness temperatures and LWP and TPW respectively. Resulting differences between the various used algorithms are caused by different cloud models and absorption schemes (see Löhnert and Crewell (2003)). The authors show, that for statistical LWP retrievals, RMS errors can be reduced by using an increasing number of frequencies. But the influence of the cloud model statistics becomes more significant as more channels are used. Different cloud models represent different possible states of the atmosphere. To best describe the universal state of the atmosphere, the cloud statistics used for algorithm development should contain a mixture of different statistics from different cloud models. Another source of uncertainty in the LWP and TPW retrieval are the different established absorption models used in the radiative transfer model calculations. Crewell and Löhnert (2003) show that the mean differences between the absorption schemes defined by Liebe (1989) and Liebe et al. (1993) are in the range of 1–2 K for lower frequencies, whereas a larger bias for higher frequencies (50, 89 GHz) occurs. The Rosenkranz (1998) absorption scheme gives similar results as Liebe (1989). Using two channel (23, 31GHz) radiometer retrieval for the LWP an error in the brightness temperature of 1 K can lead to LWP errors of more than 30 g/m² whereas the use of additional information from a 90 GHz channel improves the accuracy by 50 %. Some attempts to reduce the uncertainties in the

absorption schemes at 90 GHz are made, see Cruz Pol et al. (1998).

From radiosonde measurements the global vertical structure can be derived with a limited temporal and spatial resolution. Only ground based microwave radiometers with a profiling ability offer possibilities to derive the vertical structure in much higher temporal resolution. The vertically integrated water vapour is retrieved with time resolutions ranging from seconds to minutes depending on the radiometer sampling technique. Since ground based measurements represent point measurements, a regional TPW distribution can be maintained with a limited fidelity due to the limited distribution of contribution radiometers. Satellite based instruments offer better spatial coverage. Various techniques have been developed that are using different spectral bands to derive informations of the atmospheric water vapour, see Hauschildt and Macke (2004).

On board polar orbiting satellites infrared sensors like the High-resolution Infrared Radiation Sounder (HIRS) allow to derive the water vapour content in clear sky atmospheres only, because clouds are opaque in this spectral range. In the microwave spectrum non-precipitating clouds are translucent, so that sensors like the Special Sensor Microwave/Imager (SSM/I), the Spectral Sensor Microwave/Temperature (SSM/T-2) and the Advanced Microwave Sounding Unit (AMSU) offer the possibility to derive the TPW. These techniques are limited to ocean surfaces because the emission from the surface needs to be small and homogeneous within the radiometer field of view (FOV). These radiometers yield TPW products with a spatial resolution of about 60 km which is sufficient for resolving the TPW variability on a daily scale. Due to the polar orbits and limited swath the temporal variability of the water vapour fields related to synoptical processes cannot be resolved.

Radiosondes offer humidity data for more than 50 years. The changes in equipment of one station during the years and the various radiosonde types introduce an artificial temporal and spatial variability in the derived TPW fields. This uncertainty is investigated by Soden and Lanzante (1996) by comparing radiosonde upper-tropospheric humidity (UTH) with UTH derived from TIROS Operational Vertical Sounder (TOVS) measurements at $6.7 \mu\text{m}$ wavelength. The advantage of satellite measurements is that the basic technique is consistent over the globe. An error in the retrieval will lead to a systematic bias effecting the absolute numbers but the spatial variability is correct. Nevertheless, the retrieval of TPW or upper-tropospheric humidity with TOVS is limited to clear-sky scenes. The higher humidities in clouds and their vicinity are neglected, which leads to an underestimation of climatological water vapour. The dry bias in the upper-tropospheric humidity in TOVS estimates as shown by Soden and Lanzante (1996) are assumed to be about 4%. This estimation is derived by comparing all radiosondes and those in clear-sky cases.

Lanzante and Gahrs (2000) introduced the temporal sampling bias (TSB) in UTH climatologies based on satellite data. They investigated the difference between continuously observing radiosondes (6 times per day) and satellite based measurements which are maxi-

mum twice per day over an individual radiosonde station. A satellite UTH is available only when the atmosphere is cloud free. Thus, the satellite misses potentially moist cases and with two measurements per day, it cannot resolve diurnal cycle, which is found to be small, see Gldner and Spnkuch (1999). The temporal sampling bias ranges from -1 to 21 % relative humidity in the 500 hPa level for the different stations. The authors show further a latitudinal dependency of the clear-sky bias in the upper-troposphere. In the Tropics high convective towers hamper the satellite retrieval of humidity, the satellite misses the moistest cases. Considering radiosonde ascents at 63 stations during 1987-1991 the climatological mean values showed an underestimation in terms of UTH of 5 to 10%. Higher biases in upper tropospheric humidity occur in the Tropics. Trends in upper tropospheric humidity may be underestimated due to global warming; with increasing temperature the absolute humidity will increase but the relative humidity may be unchanged.

Chapter 3

Compilation of retrieval techniques

In section 3.1 numerous techniques to derive atmospheric water are reviewed. In the section 3.2 two common techniques to derive cloud liquid water and the satellite instruments are described more deeply. One retrieval technique is based on the relation of measured microwave radiation measured with AMSU towards the water content of the atmosphere. The algorithm described here is the standard NOAA NESDIS algorithm for water vapour and cloud liquid water derived from AMSU measurements. The other described technique is based on measurements of the reflectivity of solar radiation measured with AVHRR. The reflectivity is linked to the atmosphere beneath the scattering layer. This method is an indirect technique to derive optical properties of clouds.

3.1 Overview of retrieval techniques and instruments

There are numerous techniques to determine the atmospheric water vapour and cloud liquid water from ground based, air borne and space borne sensors. By far the most in-situ measurements of atmospheric water are taken from radiosonde humidity sensors. Laser-based measurements of water vapour absorption (Lyman- α) onboard research aircrafts provide continuous measurements during specific field campaigns, only. Most other methods are based on the relation of measured radiances to the water vapour concentrations. This relation is often derived by using numerous radiosonde profiles characterising the variability of the atmospheric state. In the following different retrieval techniques are shown and several intercomparison studies are summarised. A focus is set on the influence of clouds on the retrievals, the uncertainties of the methods and the attempts to quantify the water vapour inside the clouds. Most of the techniques find their limitations in the presence of clouds. In the infrared spectra clouds are opaque, so the retrieval of the total precipitable water is not possible. Some attempts are made to retrieve the water vapour above the clouds from infrared radiation measurements for cloud covered areas. The best

opportunity to derive TPW in cloudy areas is given by microwave instruments. The methods are working for non-precipitating liquid water clouds, scattering of microwaves at large ice particles and raindrops weakens the relation between water content and radiances; from satellite the retrieval is limited to ocean areas.

3.1.1 Ground based instruments and techniques

Radiosonde

Radiosonde measurements are an important database for weather and climate forecast models. They are often used as ground truth for validating humidity measurements based on other techniques and for the deduction of retrieval algorithms. From a variety of radiosonde types differing by the transmission techniques and humidity sensors, the Vaisala radiosonde is the most common type. The humidity is measured by the so called Humicap sensor which measures the relative humidity in the range 0–100 %. The Humicap makes use of a thin polymer film which either absorbs or releases water vapour. The dielectric properties of the polymer film are depending on the amount of water contained. The changes in electric capacity of the sensor induced by the amount of water are converted into relative humidities. This technique is insensitive to dust, particle dirt and most chemicals. The accuracy is about 2 %. Other measuring techniques are based on humidity dependent expansion of materials. However, during the ARM program's water vapour intensive observation periods Revercomb et al. (2003) found discrepancies in humidity measurements for the entire vertical profile due to calibration differences. Humidity profiles measured with two sondes mounted on the same balloon agree within the range of 8-12 %; the variability within a calibration batch is larger than between different calibration batches¹. This difference is altitude independent. In the study they use the microwave radiometer humidity profiles to scale the radiosonde profiles to reduce the instrument variability. Miller et al. (1999) mentioned chemical contamination in the humidity sensor field depending of the type of packaging desiccant. The latter problem is solved in August 1998 by changing the packaging desiccant. It is not known if discontinuities appear in the humidity records.

Radiosonde ascents performed from 1994 and 2001 were compared to ground based microwave radiometer (MWR) retrieved humidity profiles with the assumption that microwave remote sensing provides more reliable humidity measurements, particular in the upper troposphere. The radiosondes show a 5 % dry bias. Turner et al. (2003) provide an empirical method for correcting the radiosonde humidity profiles based on a constant scaling factor. This factor does not take different calibrations into account.

¹Calibration batch: During the production process the radiosondes are calibrated in a specific environment which is exposed to small changes. After a while the calibration target is renewed and set to the standard values.

Bates and Jackson (2001) report an underestimation for upper tropospheric humidity, because the humidity sensor cannot resolve the small variations in cold and dry atmospheres. Differences occur between different radiosonde types as reported in Westwater (1997). The Vaisala Humicap humidity sensor retrieve humidities below 20 % more accurate compared to other sensors. But there is a bias between the humidity sensors used for american sondes and the Humicap for the whole humidity range. Algorithms e.g. for LWP based on one type of radiosonde data reflect these biases as shown in Ferrare et al. (1995).

Nevertheless, humidity and temperature profiles from radiosondes are commonly used in climate research. Many stations provide long timeseries of radiosonde data with several ascents per day. The more advanced microwave and lidar techniques are very limited in the covered region. Meanwhile, radiosondes are displaced by satellite and GPS retrieved humidities in the assimilation schemes of the weather prediction models.

To assess differences between water vapour in clear- and cloudy-skies it is necessary to detect the cloud occurrences from temperature and humidity profiles. Auxilliary informations like cloud cover are important as the sonde does not necessary pass a cloud during the ascent. In many studies the cloud detection is based on a thresholding schemes. Chernykh and Eskridge (1996) relate the second derivative of the temperature and the humidity profile to the height in order to identify a cloudy level. In addition the cloud cover is estimated from the dewpoint depression depending on the temperature in four categories (0- 20, 20- 60, 60- 80, 80- 100 %) after Arabey (1975). Compared to synoptical observations the results for the cloud level detection agree well in 87 % of the investigated cases during day time and the cloud amount in 69 % of the cases. Using this estimation to retrieve cloud boundaries and comparing the results with lidar/ceilometer data for the ARM Southern Great Plains site, Naud et al. (2003) show good agreement within 125 m for the cloud base height when both instruments detect a cloud. Stronger differences occur comparing cloud heights from radar and radiosonde. Most differences can be explained by broken cloudiness, when it is not clear whether the active instrument sees the same cloud as the ascending radiosonde.

Wang and Rossow (1995) described a scheme to derive cloud base and cloud top heights from radiosonde measurements. In a first step a moist level is detected when the relative humidity exceeds 84 %. A set of moist level on top of each other is viewed as a cloud when the humidity increases by at least 3 % from the previous (lower) level and the maximum humidity of the moist level exceeds 87 %. The cloud top is reached when the humidity decreases with rates greater than 3 % to the following (upper) level. When cloud base and cloud top heights are below 500 m no cloud is detected. Here rain, drizzle or fog are responsible for the moisture. This method works quite well as comparisons with synoptical data show. For a study on stratocumulus clouds only (Wang et al., 1999) the thresholds were shifted to higher values (90 % for moisture and 95 % for cloud levels) to retrieve cloud levels in better consensus to synoptical observer estimates.

Karstens et al. (1994) use a threshold of 95 % to define a cloud layer. For these layers the adiabatic liquid water content (LWC) is derived depending on the air density, specific heat, latent heat of evaporation and the adiabatic lapse rates for dry and moist air. This gives the upper limit of LWC because entrainment processes are reducing the amount of condensed water. In this study the authors propose a modification of the LWC with respect to the entrainment induced reduction.

Ground based remote sensing

Radiosondes measurements are still the most important input for weather forecast models, despite their many disadvantages, for instance low temporal resolution, erroneous measurements especially of humidity, the inability to measure hydrometeors distribution, and their extremely high manpower costs. Strong efforts have been undertaken to develop alternative, ground based instruments for continuously monitoring the vertical structure of the atmosphere. Different types of active and passive sensors measure in different parts of the electromagnetic spectrum. Since the interaction of atmospheric components with atmospheric radiation changes with wavelength, spectrally diverse measurements contain different informations about the atmospheric composition.

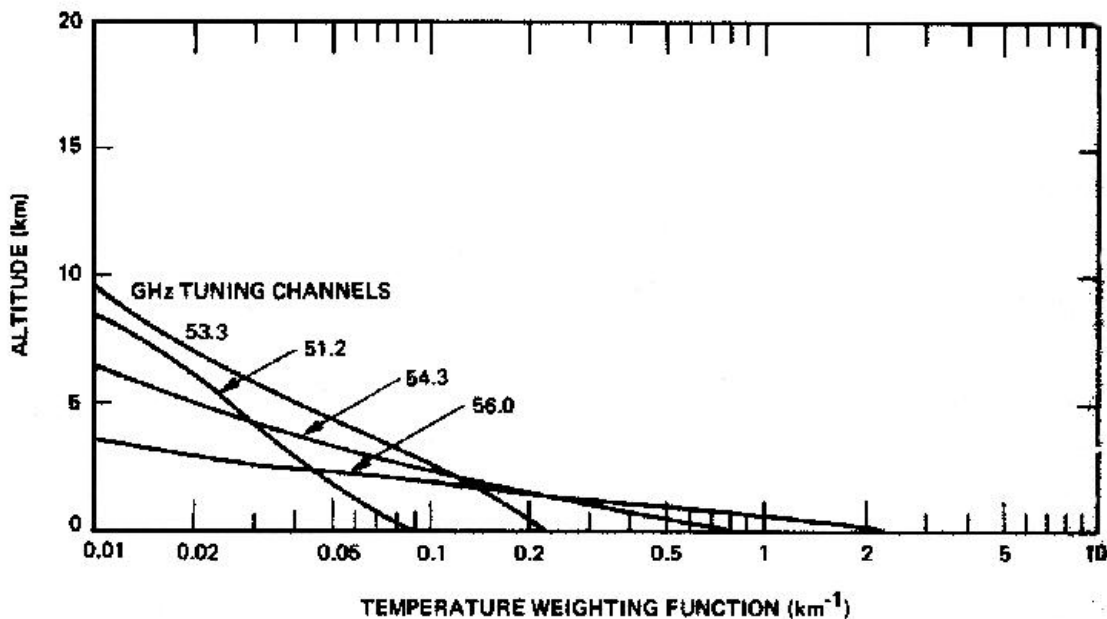


Figure 3.1: Unnormalised weighting functions for temperature as a function of height above the surface for observations from the surface looking at the zenith. The curves correspond to the emission by oxygen near the 60 GHz region (Elachi, 1987).

Passive microwave radiometer measure the radiation emitted by water vapour in the atmospheric column in viewing direction of the instrument. The principle is comparable to satellite microwave remote sensing retrievals described in section 3.1.2. At least measurements at two frequencies are needed to retrieve the TPW. Measuring the radiation at more frequencies enable the retrieval of a humidity profile. Figure 3.1 shows the uplooking weighting functions of oxygen emission near the 60 GHz band. The lower layers provide the strongest emission, which is also the least attenuated, while the higher layers provide low emission, which is additionally highly attenuated by the lower layers before it reaches the sensor (see Elachi (1987)).

Today, ground based microwave radiometers observe water vapour and cloud liquid water with a high temporal resolution on an operational basis. At meteorological observatories and during intensive field campaigns microwave radiometers are in use. Güldner and Spänkuch (1999) examine the diurnal cycle of integrated water vapour and liquid water path using two years of continuous data for the Lindenberg observatory (MOL). They found only small diurnal variations in the water vapour path of about 8 % in summer and 5 % in winter. The increase in TPW is strongest in the morning in summer, whereas in winter it is shifted to the afternoon. The authors conclude that the monthly mean TPW calculated from low resolution instruments like SSM/I is not effected by the diurnal cycle. Another finding is that the TPW increases by about 5 % within the two hours before rain.

To retrieve water vapour, temperature, and liquid water content profiles with ground based microwave radiometer, Peter (1994) propose an iterative algorithm based on a first guess profile from radiosonde and microwave brightness temperatures at five frequencies (23.87, 31.65, 22.235, 52.85 and 54.95 GHz). The advantage of this algorithm is the independency of a training data set. The latter limits the validity of the algorithm to the range of atmospheric conditions covered by the training data.

Beside the passive microwave techniques (described in section 3.1.2) active methods like the Raman lidar or the Differential absorption lidar (DIAL) are in use as well. Here the intensity and wavelength of the returning signal compared to the emitted beam contain informations of the atmospheric temperature and humidity profiles; see Whiteman and Ferrare (1992) and Whiteman et al. (2001) for the Raman lidar; Wulfmeyer and Bösenberg (1998) for the DIAL. These techniques are working in clear-sky conditions only.

Different types of active and passive sensors offer measurements in different parts of the electromagnetic spectrum containing information of the atmospheric water vapour. Therefore, a combination of instruments will improve the retrieved humidity profiles compared to single instrument methods. Westwater (1997) reports that auxilliary informations like standard meteorological parameters at surface level in addition to remote instruments improve the retrieval significantly. Löhnert et al. (2004) deploy a method to retrieve humidity, temperature, and cloud liquid water profiles. The approach combines a multichannel microwave radiometer, a cloud radar, a lidar-ceilometer, the nearest operational radiosonde

measurement, and ground-level measurements of standard meteorological properties with statistics derived from results of a microphysical cloud model. The algorithm is based on an optimal estimation method using the radiosonde ascent as a priori information. The resulting profiles are physically consistent in all parameters. A bias error is induced using different gas absorption models in the retrieval scheme. The best performance is retrieved using the Rosenkranz 1998 gas absorption model. This method offers the opportunity to retrieve temperature, humidity and cloud liquid water profiles on a continuous basis with high temporal resolution. This approach is limited to non-precipitating liquid water clouds.

Elgered and Jarlemark (1998) compared TPW time series derived from radiosonde and microwave radiometer data for 1981–1995 located at the Swedish west coast. Both time series show trends in observed TPW, but the sign is opposite. The uniformly in time sampled radiosonde data show an increase in TPW of 0.03 mm/yr with a standard deviation of 0.01 mm/yr. The microwave data, which are not at all uniformly sampled in time, show an decrease of 0.02 ± 0.01 mm/yr. Reducing the two data sets on the same data points they are in good agreement and the microwave measurements show the same trend as the radiosonde. Differences between the two techniques can be explained by drifts in the calibration or changes in the algorithms. They advise to additionally measure the atmospheric temperature to identify possible error sources.

At the Atmospheric Radiation Measurement (ARM) program's Southern Great Plains (SGP) Clouds and Radiation Testbed (CART) site several instruments including an automated Raman lidar and an automated Atmospheric Emitted Radiance Interferometer (AERI) are measuring the tropospheric water vapour profiles operationally. Turner et al. (2000) shows result of these techniques and comparisons to conventional methods like radiosonde retrievals. For non cloudy scenes both instruments perform very well and provide additional informations like aerosol profiles (lidar) and temperature profiles (AERI). The uncertainties are about 5 % during night and 10 % during daytime.

Beside the continuously measuring instruments placed on the surface, most of the instruments can be mounted on airplanes during specific measurement flights. Here measurements along the flight lags are available. Purposes are the derivation of in-situ measurements and generating of synthetic satellite measurements for validation purposes. Absorption measurements with the Lyman- α instrument offer direct measurements of the absorption in the water vapour band. A compilation of the different ground-based techniques including the Lyman- α is given in table 3.1.

3.1.2 Satellite instruments and techniques

Satellite remote sensing is based on radiation measurements modulated due to absorption, emission and scattering by the atmospheric constituents. The modulation depends on the

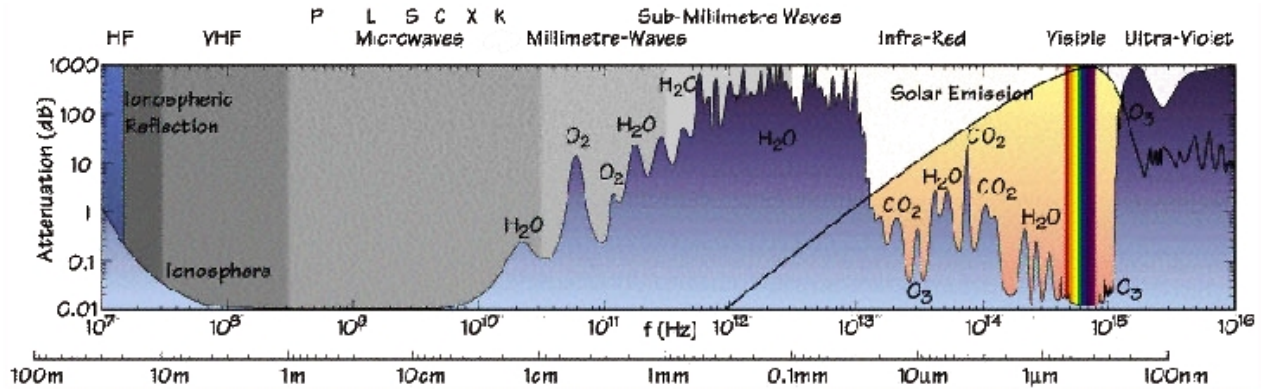


Figure 3.2: The attenuation depending on the wavelength for the electromagnetic spectrum. The atmospheric absorption bands are labeled by the main absorbing gases.

part of the radiation spectrum under consideration. Figure 3.2 shows atmospheric attenuation in the range from ultraviolet to radiowaves. In the far infrared the atmosphere is opaque whereas in the microwave region it is transparent except of two water vapour absorption lines (22.2 and 183 GHz) and two oxygen absorption bands (60 and 118 GHz). There are minor absorption bands related to ozone and other trace gases. Strong absorption in the infrared mostly due to H_2O and CO_2 is found. In the atmospheric water vapour window (8–12 μm) a strong ozone absorption line is disposed. For microwave radiation the atmosphere appears to be transparent beside a H_2O line at 22.235 GHz and 180 GHz and two O_2 lines at 53 GHz and 120 GHz. Remote sensing techniques for the retrieval of water vapour make use of spectral changes in molecular absorption. An overview of available satellite instruments is given in table 3.2.

Instrument	Retrieval	Quantity	Limitations and Advantages
Radiosonde	Profile	Humidity, Temperature, Wind	too low humidities at low temperatures limited spatial and temporal resolution
Microwave radiometer	Profile (multi channel), Integral (2 channel)	Temperature, Humidity	limited to non-precipitating, liquid water clouds continuous measurements
Lidar (Raman, DIAL)	Profile	Humidity	clear-sky
Lyman- α		Humidity	limited temporal and spatial resolution only during campaigns including flights

Table 3.1: Compilation of ground-based and air-borne techniques and their limitations.

Instrument	Satellite/Mission	Spectral Range	Frequency/Wavelength	Specifications	Resolution (FOV)
JPL-GPS	CHAMP	GPS		Limb	vertical 0.5-1.5 km
GOME	ERS-2	UV, VIS	240-790 nm	Nadir 5 channel	~ 40-320 km
MODIS	TERRA/AQUA	VIS, NIR	405-2155 nm, 1.360-14.389 μm	cross-track 36 channel	~ 1 km
MERIS	ENVISAT	VIS, NIR	400-1015 nm	cross-track 15 channel	0.3 km and 1.2 km
SCIAMACHY	ENVISAT	UV, VIS, NIR	240nm - 2380 nm	Nadir, occultation, limb 8 channel	30 km, 30 km, 250 km
SSM/I	DMSP	MW	19.0-85.0 GHz	conical at 54° 4 channel	13.0 km \times 15 km
SSM/T2	DMSP	MW	50.0-59.4 GHz, 91.0-183.0 GHz	Nadir, limb 7 channel	~ 48 km (Nadir)
HIRS	NOAA polar	VIS, NIR, IR	0.690-14.95 μm	cross-track 20 channel	~ 20 km (Nadir)
AMSU	NOAA polar	MW	23.8-183 GHz	cross-track 20 channel	~ 60 km (Nadir)
SEVIRI	MSG	VIS, NIR, IR	0.635-13.4 μm	scanning 12 channel	~ 4 km
IASI	METOP	NIR, IR	3.6-15.5 μm		

Table 3.2: Overview satellite instruments, their wavelength and the field of view (FOV).

Solar

The remote sensing of TPW is mainly conducted using microwave, far infrared, infrared and near infrared spectral features. The visible water vapor bands have not been used due to the incomplete state of the spectral data, which causes difficulties in the common absorption spectroscopy techniques. Maurellis et al. (2000) propose a new technique, named Optical Absorption Coefficient Spectroscopy technique (OACS) to use spectral data measured in the weak water vapor absorption band between 585 nm and 600 nm with data derived from the Global Ozone Monitoring Experiment (GOME). The retrieval is based on the HITRAN96 data base and accounting for the dependency of the line shape on the altitude and the spectral structure at instrument resolution. Former methods were not suitable for this absorption band due to the highly structured spectral appearance. The technique is applied on a transmittance spectra consisting on 69 measurements resembling the detector pixels spectral region of interest. The GOME retrieved TPW are compared with data from the ECMWF forecasts for different orbits and show good agreement.

Another technique to use spectral data in the visible water vapour absorption band around 590 nm is given by Lang et al. (2003). A spectral sampling technique for measurements of atmospheric transmission called the Spectral Structure Parametrisation (SSP) in order to retrieve the total water vapour columns from reflectivity spectra measured by the Global Ozone Monitoring Experiment (GOME). The SSP reduces the opacity functions and their weights to one structure parameter. This parameter characterises the spectral structure of the absorber within a specific wavelength range and a specific altitude. This method is suitable for relatively small sampling regions containing only a small number of absorption lines, e.g. for data from the GOME and SCIAMACHY instruments. The results compare well to independent values given by the data assimilation model of ECMWF and to retrievals with the OACS method.

These techniques can retrieve the TPW for clear-skies only. In cloudy atmospheres the measurements are related to the water vapour on top of the clouds. Using climatologies of humidity and temperature profiles and estimating the cloud top height the TPW is estimated for cloud affected measurements. Various correction schemes are under development; the quality of the cloud-corrected TPW is very sensitive to the estimated cloud top height.

From backscattered sunlight measured with MERIS Albert et al. (2001) suggest a method to derive water vapour above clouds. The retrieval scheme is based on measurements in the water vapour absorption band and window channel measurements. A regression type algorithm is derived from radiative transfer calculations using radiosonde ascents and taking the channel weighting functions into account. Bennartz and Fischer (2001b) propose a technique to retrieve the TPW from MERIS near infrared channels over land surfaces. The retrieved water vapour paths compare well to other measurements despite a significant bias. An explanation of the bias might be the neglect of the continuum

absorption of water vapour, which would lead to systematically lower transmissions in the radiative transfer simulations.

Gao and Kaufman (2003) propose a water vapour retrieval using MODIS based on ratios of radiances measured in three absorbing infrared channels (0.905, 0.936 and 0.904 μm) and the atmospheric window channels (0.865 and 1.24 μm). The algorithm is suitable over reflecting surfaces like land areas, ocean areas with sun glint and clouds. By using ratios of the radiance in two channels the effects of variations in the surface reflections can be removed. Typical errors in the derived water vapour are about 5–10%. The retrieved TPW are in good agreement with ground based microwave observations at ARM stations.

Infrared

The infrared satellite retrieval methods are based on the split-window technique in which the difference in absorption between two nearby infrared channels is used to estimate the TPW. The greater the difference between the brightness temperatures, the more water vapor found above the pixel whose brightness temperatures are being measured (Kidder and Vonder Haar (1995, Chapter 6)). Typical wavelengths used for water vapour retrieval

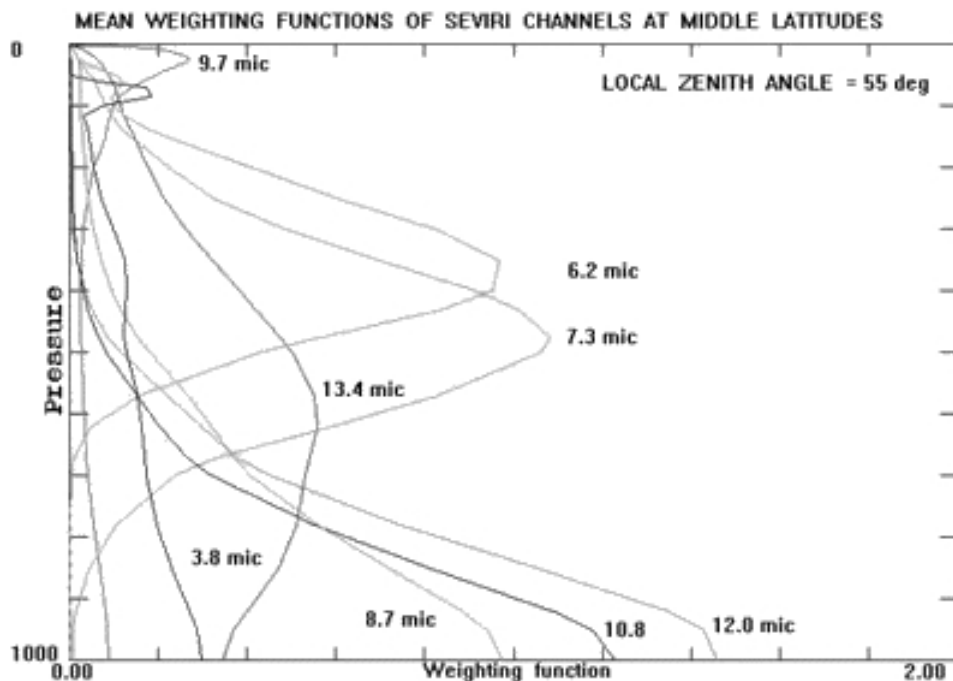


Figure 3.3: *Weighting functions for the thermal IR channels of SEVIRI on MSG-1 corresponding to a midlatitude atmosphere. For informations on SEVIRI see <http://www.eumetsat.int>.*

are $8.90 - 9.20 \mu\text{m}$, $9.31 - 9.41 \mu\text{m}$ or $9.15 - 9.65 \mu\text{m}$.

With more channels close to one absorption line it is possible to retrieve additional informations about the vertical distribution of water vapour. Depending on the used wavelengths the signal is mostly emitted from a specific height. Using more frequencies with different weighting functions (see figure 3.3), which describe the extinction profiles of the atmosphere, water vapour profiles can be retrieved. Each atmospheric layer is characterised by the peak in the weighting function. Figure 3.4 illustrates the relation of the located wavelength to the centre of the absorption line and the penetration depth.

There are various sensors based on infrared channels like HIRS, the Medium Resolution Imaging Spectrometer (MERIS) on ENVISAT, the Moderate Resolution Imaging Spectroradiometer (MODIS) on TERRA/AQUA and the proposed Infrared Atmospheric Sounding Interferometer (IASI) on future METOP satellites. All these instruments are carried on polar orbiting satellites only. On geostationary satellites IR channel instruments like the Spinning Enhanced visible and infrared Imager (SEVIRI) on MSG are used. For the IASI instrument Schlüssel and Goldberg (2002) show that the temperature and water vapour retrieval is not effected by sub-pixel cloud cover lower then 5 % when the occurrence of clouds is accounted for in the retrieval scheme based on model results. Infrared and solar retrieval techniques are limited to cloud free situations. All TPW retrievals are in good agreement with radiosonde data.

For the upper troposphere the retrieval accuracy of humidity profiles from infrared sensors is low (Bühler and Couroux (2003), Bühler and John (2005) and Bühler et al. (2004e)). The measured radiances mostly originate from lower levels as shown by their weighting functions. Soden et al. (2004) compared HIRS and radiosonde retrieved water vapour

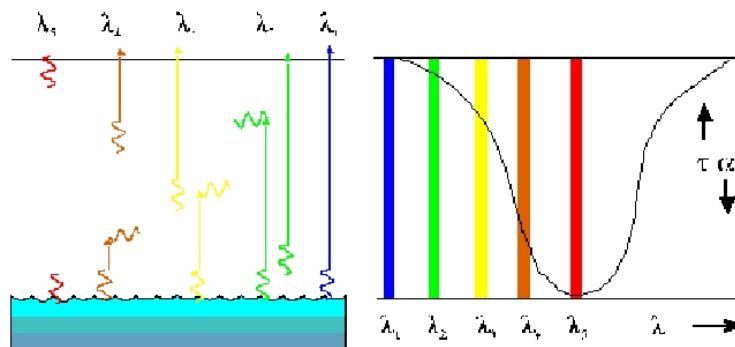


Figure 3.4: Scheme of the relation of the observed wavelength to the height where the radiation originates. On the right the wavelength position relative to an absorption line is shown. On the left the signal seen from a space borne or ground based instrument is shown.

and found differences in upper tropospheric humidity of about 40 %. This corresponds to a difference in clear-sky outgoing longwave radiation of 3.8 %. Weinstock et al. (1995) investigate the retrieval of water vapour in the upper troposphere and lower stratosphere using a Lyman- α hygrometer mounted on the NASA-ER2 airplane during the Central Equatorial Pacific Experiment (CEPEX). The aim of the campaign was to retrieve water vapour and to understand the mechanisms that transport the water vapour from the upper troposphere into the stratosphere. The retrieved water vapour contents of the upper troposphere and lower stratosphere compare well with previous retrievals. An annual averaged mixing ratio of water in air entering the tropical stratosphere is about 4.45 ppmv.

Microwave

Microwave radiometers offer the possibility to retrieve the TPW in clear and cloudy atmospheres. Passive microwave techniques measure the emission from the surface and the atmosphere. For the retrieval of atmospheric constituents it is compellent to know the background emission from the surface. Ocean surfaces appear cold and homogeneous in the microwave region and their variability in emittance depends on the sea surface temperature, the roughness, and the salinity. With ocean surface models the microwave emission can be assessed. Land surface emission is much stronger and depends on many variables which are inhomogeneous on small spatial scales. The retrieval of atmospheric properties is possible over ocean only. In the microwave region water vapour path and liquid water

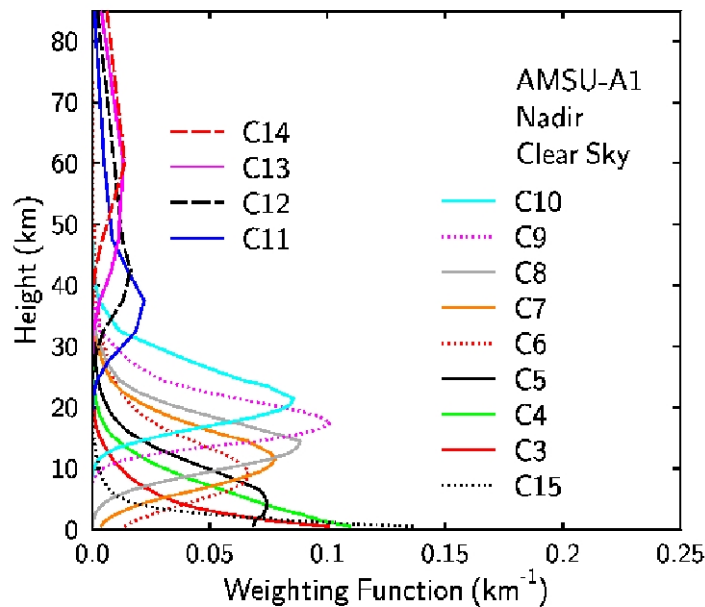


Figure 3.5: AMSU-A weighting functions. Each line/colour resembles one channel. E.g. Channel 7 (C7 – 54.94 GHz) has a maximum amplitude at 12km height.

path is retrieved simultaneously using at least two frequencies; one close to the water vapour absorption line and one in the window where the radiation is related to the condensed water. An algorithm using AMSU channels is described in Grody et al. (2001), a summary is given in section 3.2.2. As for ground based microwave techniques described in section 3.1.1 scattering at large raindrops and ice particles weakens the efficiency of the algorithm and limits its application to non-precipitating water clouds.

Humidity profiles can be obtained from measuring radiances at only the flanks of an appropriate absorption peak. Like for IR-measurements the measured radiance is related to an altitude by a corresponding weighting function. In figure 3.5 the weighting functions for the AMSU-channels are shown.

Basically a two frequency scheme is used where one frequency is near the water vapour absorption line and another in the window channel. Numerous algorithms based on the frequencies available from SSM/I, SSM/T2, MSU and AMSU can be found in literature, a selection is described in the study of Wahl et al. (2003). Comparing the retrieved water vapour path to radiosonde and ground based microwave measurements shows a reasonable agreement. Ruprecht (1996) shows a bias for SSM/I TPW compared to radiosonde in a way that the satellite retrieval overestimates for low TPW and underestimates for high TPW retrieved with radiosondes.

English (1999) suggests a method for humidity and temperature profiling over land and bright surfaces with AMSU. The atmospheric humidity and temperature profiles can be derived within an acceptable error range. The influence of surface emission is stronger in the LWP retrieval than for the humidity retrieval. However, the humidity retrieval is sensitive to the LWP as well.

With limb scanning instruments the profile of humidity and temperature for the tangent point can be retrieved. The sensor aperture angle results in an altitude error also called pointing error. For the pointing and temperature a possible retrieval algorithm for millimeter and sub-millimeter wavelength range is proposed by Verdes et al. (2002).

Combined Microwave and Infrared Techniques

The TIROS Operational Vertical Sounder (TOVS) equipped aboard NOAA's TIROS series of polar orbiting satellites consists of three instruments: the High Resolution Infrared Radiation Sounder (HIRS), the Microwave Sounding Unit (MSU) and the Stratospheric Sounding Unit (SSU). The MSU and SSU have been replaced with improved instruments, the AMSU-A and AMSU-B, on the newer satellites also mentioned as ATOVS.

A five level clear-sky water vapour profile algorithm using TOVS data is described in Chaboureaud et al. (1998). A neural network scheme is used for the solution of the ra-

diative transfer problem. The results compare well with SSM/I and radiosonde data. Uncertainties in the algorithm are larger in the upper atmosphere where radiosonde data and TOVS retrieval results differ most.

Engelen and Stephens (1999) compare TOVS/HIRS and SSM/T-2 retrieval techniques and the retrieved water vapour profiles. For the upper- and mid-troposphere the TPW retrieval using HIRS data is more reliable. The measured radiances in the HIRS channels originate from higher levels in the atmosphere, as described by the weighting functions. The lower atmosphere and the surface are contributing to the signal for dry atmospheres only. The SSM/T-2 informations are dominated by the lower levels. Due to the limitation in the infrared technique only cloud free situations are compared. In general the methods are sensitive to the quality of the input parameters, e.g. the sensor characteristics like signal to noise ratio. The authors assume a 3 % error in radiance for all, HIRS and SSM/T-2 channels, this translates in a brightness temperature error of ~ 7 K for SSM/T-2 which is larger than the noise values.

GPS

Global Positioning System (GPS) receivers can also be used for remote sensing of the water vapour path. The time varying zenith wet delay observed at each GPS receiver in a network can be transformed into an estimate of TPW overlying that receiver (Bevis et al., 1994). This transformation is achieved by multiplying the zenith wet delay by a factor whose magnitude is a function of certain constants related to the refraction of moist air and of the weighted mean temperature of the atmosphere. The mean temperature varies in space and time and must be estimated a priori e.g. by using numerical weather models, in order to transform an observed wet delay into TPW. Li et al. (2003) compared GPS and MODIS retrieved TPW with radiosonde humidities. TPW retrieved with GPS is in good agreement with radiosonde integrated water vapour. The variance is about 4 % and the correlation coefficient is 0.98. A significant day-night difference was found for Vaisala RS90 radiosonde comparing to GPS TPW, with a larger wet delay vs TPW proportionality during night time. The MODIS TPW retrieval is limited to day time, and the differences relative to GPS TPW or radiosonde TPW are larger than those between GPS TPW and radiosonde TPW. MODIS seems to overestimate the TPW compared to the other methods. Another comparison of GPS retrieved TPW with radiosonde data, water vapour radiometer (WVR), and Very Long Baseline Interferometry (VLBI) show relatively small differences of 3 % in TPW (Niell et al., 2001). While infrared measurements are only available for clear-sky cases and microwave measurement are limited to the oceans and to non-precipitating clouds, GPS retrievals are valid for all day and all sky situations.

Since mid 2001 the German geoscience satellite CHAMP (Challenging Minisatellite Payload) is continuously measuring atmospheric profiles using the GPS radio occultation technique. CHAMP measures the phase and amplitude variations of the GPS signal during an occultation event. Together with high-precision orbit information the atmo-

spheric path delay and the bending angle profile can be determined. These parameters are directly linked by the refraction to the vertical temperature and humidity vertical distribution. Schmidt et al. (2004) compare the retrieved temperature and humidity profiles to ECMWF reanalysis data and radiosondes. The results are promising. For the temperature profiles small biases occur which are related to assumptions made for the humidity profile in the retrieval algorithm. The humidity is retrieved by splitting the refractivity in a dry and a wet part which requires additional information of the level temperature. The Schmidt et al. (2004) algorithm uses ECMWF temperature. During the first 510 days CHAMP recorded 105,000 occultations. This shows the great opportunity given by the GPS systems for meteorological remote sensing. GPS radio occultation is independent on the present weather situation. The retrieval of water vapour and temperature is possible in cloudy-skies and during precipitation.

Compendium

Comparison of satellite retrieved water vapour path and liquid water path from microwave and infrared measurements show reasonable agreements under clear-sky conditions. Greenwald et al. (1997) compare GOES-NIR and SSM/I retrieved LWP and investigate the beamfilling error due to broken cloudiness in a microwave field of view. The beamfilling error is about 22% for broken cloudiness and the correlation between GOES-NIR and SSM/I LWP is depending on cloud cover. For overcast cases the relation is 0.93, whereas in broken cloudiness the correlation is 0.73. For the overcast case the retrieval using GOES-NIR shows higher LWP compared to SSM/I, while the SSM/I LWP retrieved in broken cloudiness is larger than the GOES-NIR. A comparison of different water vapour retrievals is given by Tjemkes and Visser (1994). It is shown that TOVS/HIRS and SSM/I TPW agree well for clear-sky cases. The authors assess the underestimation of all sky TPW due to the limitation to clear-sky cases for TOVS/HIRS retrieval in terms of OLR radiation by $2\text{-}3\text{W/m}^2$ compared to SSM/I.

On ERS-2, a microwave radiometer (MWR) and the Along Track Scanning Radiometer (ATSR) are used for the retrieval of TPW over oceans. ATSR views the Earth's surface at two different viewing angles and in three infrared bands. Comparison of microwave and ATSR TPW show good agreement (Barton, 2004) for clear-sky cases.

Bokoye et al. (2003) compare a 940 nm solar absorption band radiometer, GPS, and radiosonde analysis from a numerical weather prediction model over Canada and Alaska to investigate the strong seasonal variability in water vapour at high latitudes. The inter-comparisons show root mean square errors between 1.8 and 2.2 kgm^{-2} for the different instruments. The GPS shows best results, but for the retrieval it is necessary to be aware of the differences between arctic air masses and the generally used mid-latitude temperature profiles for the derivation of weighting coefficients for the retrieval.

In summary, table 3.3 shows the compilation the discribed techniques. The solar retrieval is limited to day light whereas the microwave retrieval is suitable over homogeneous emitting surfaces like the oceans. But for retrieving an all sky TPW microwave measurements are very important.

3.1.3 Conclusions

To derive a long, global TPW data set with a suitable temporal and spatial resolution only a combination of IR-sensors on geostationary and polar-orbiting satellites can be used. Due to the limitation in the observational technique the data set is limited to clear-sky TPW. As the global cloud cover exceeds 60% and previous work shows larger humidities in clouds an underestimation of global TPW is induced.

As the literature study shows the influence of neglecting cloud scenes in deriving the global TPW climatology is not examined. The water vapour feedback mechanism shows how sensitive the climate system reacts on changes in the atmospheric water. Therefore it is important to investigate the influence of clouds on the water vapour budget. A first step towards a more advanced global all-sky TPW is given in this work. Here the underestimation in TPW, the so-called clear-sky bias is investigated. Out of the combination of various TPW retrieval methods the water vapour difference in clear to cloudy cases is examined. The concept of the excess water vapour (EWV) is introduced in section 6.2. The EWV relates the difference in all-sky to clear-sky TPW to the clear-sky TPW and enables to name the underestimation in clear-sky TPW climatologies introduced by neglecting clouds. Anyway, due to the limitation in the microwave remote sensing retrieval algorithms to non-precipitating clouds, the excess water vapour climatology is limited to non-precipitating clouds as well.

Technique	Land	Ocean	Day	Night	Resolution	Restrictions
Solar	+	+	+	-	high spatial resolution	clear-sky
Infrared	+	+	+	+	high spatial resolution, on geostationary satellites high temporal resolution	clear-sky
GPS	+	+	+	+	low spatial resolution	
Microwave	-	+	+	+	low spatial resolution	no rain, no ice

Table 3.3: *Compendium of the retrieval techniques*

	AMSU-A	AMSU-B	AVHRR
scanning direction	cross-track	cross-track	cross-track
viewing angle	3.3°	1.1°	0.0745°
field of view	30	90	2048 LAC 408 GAC
resolution: nadir	50 km	16.3 km	1.1 km LAC 4.km GAC

Table 3.4: AMSU and AVHRR instrument characteristics.

3.2 AMSU and AVHRR techniques

The NOAA-KLM satellite generation is equipped with various instruments to retrieve the state of the atmosphere and the surface. This polar-orbiting satellites are on a sun-synchronous orbit performing a full circle in 102 minutes. The altitude is about 800 km. The big advantage of using instruments on the same satellite is that the co-location in time and space is limited to the scanning properties and not depending on problems due to different orbits. In this study two instruments are used. The Advanced Microwave Sounding Unit (AMSU), a successor of the MSU, which measures the microwave emission in 20 channels. The 20 channels are located in two instrument units, named A and B. The channel characteristics are different for the units. In this study only AMSU-A data is used. The main purpose of the instrument is to deliver brightness temperatures for assimilated into numerical weather prediction models. At the same time it is possible to retrieve cloud properties, humidity profiles, and surface properties like surface humidity and sea ice cover for both clear and cloudy skies.

Another instrument onboard the same satellite is the Advanced Very High Resolution Radiometer (AVHRR). AVHRR measures the radiances in the visible and near infrared spectral range. The new feature of this instrument is a $1.6\mu\text{m}$ channel. This channel operates during day time and is switched to $3.7\mu\text{m}$ channel for measurements during night time. The measured reflectance in the $1.6\mu\text{m}$ channel is related to the effective radius of cloud droplets in the upper cloud layer.

Both instruments are cross track scanning radiometer. This implies changing field of view sizes. The minimum field of view is at nadir position, with increasing sizes towards the extremes of the swath. The characteristics of both instruments are summarised in table 3.4

3.2.1 AMSU

The Advanced Microwave Sounding Unit (AMSU) is a 20 channel microwave cross track scanning instrument. The instrument consists of three modules. In table 3.5 the frequencies are listed, in table 3.4 the technical characteristics are shown. For more informations see the NOAA-KLM Users Guide (1998). AMSU measures the brightness temperatures for 30 field-of-views. The instrument is flying on the NOAA-KLM series.

Looking at the calibrated brightness temperatures at AMSU frequencies 23.8, 31.4, 50.3, and 89.0 GHz in relation to the scan angle a asymmetry is observed. Mainly the measurements at 31.4 GHz are affected. In figure 3.6 the observed asymmetry is shown. This asymmetry is forced by the position of the radiometer on board of the satellite. In Mo (1999) the correction for this asymmetry is described. However, the extreme scan positions are noisy, due to the large field of view. For the climatological TPW analysis in chapter 7, only the 20 inner most FOV are used.

Module	channel	frequency [GHz]	bandwidth [MHz]	error Ne Δ T [K]
AMSU-A2	1	23.80	251.02	0.211
	2	31.40	161.20	0.265
AMSU-A1	3	50.30	161.14	0.219
	4	52.80	380.52	0.143
	5	53.59 \pm 0.115	168.20	0.148
	6	54.40	380.54	0.154
	7	54.94	380.56	0.132
	8	55.50	310.34	0.141
	9	57.29	310.42	0.236
	10	57.29 \pm 0.217	76.58	0.250
	11	57.29 \pm 0.322 \pm 0.048	35.11	0.280
	12	57.29 \pm 0.322 \pm 0.022	15.29	0.399
	13	57.29 \pm 0.322 \pm 0.010	7.39	0.539
	14	57.29 \pm 0.322 \pm 0.004	2.94	0.914
	15	89.00	1998.98	0.165
AMSU-B	16	89.00	1000.00	0.37
	17	150.00	1000.00	0.84
	18	183.00 \pm 7.0	500.00	1.06
	19	183.00 \pm 3.0	1000.00	0.70
	20	183.00 \pm 1.0	2000.00	0.60

Table 3.5: AMSU instrument characteristics

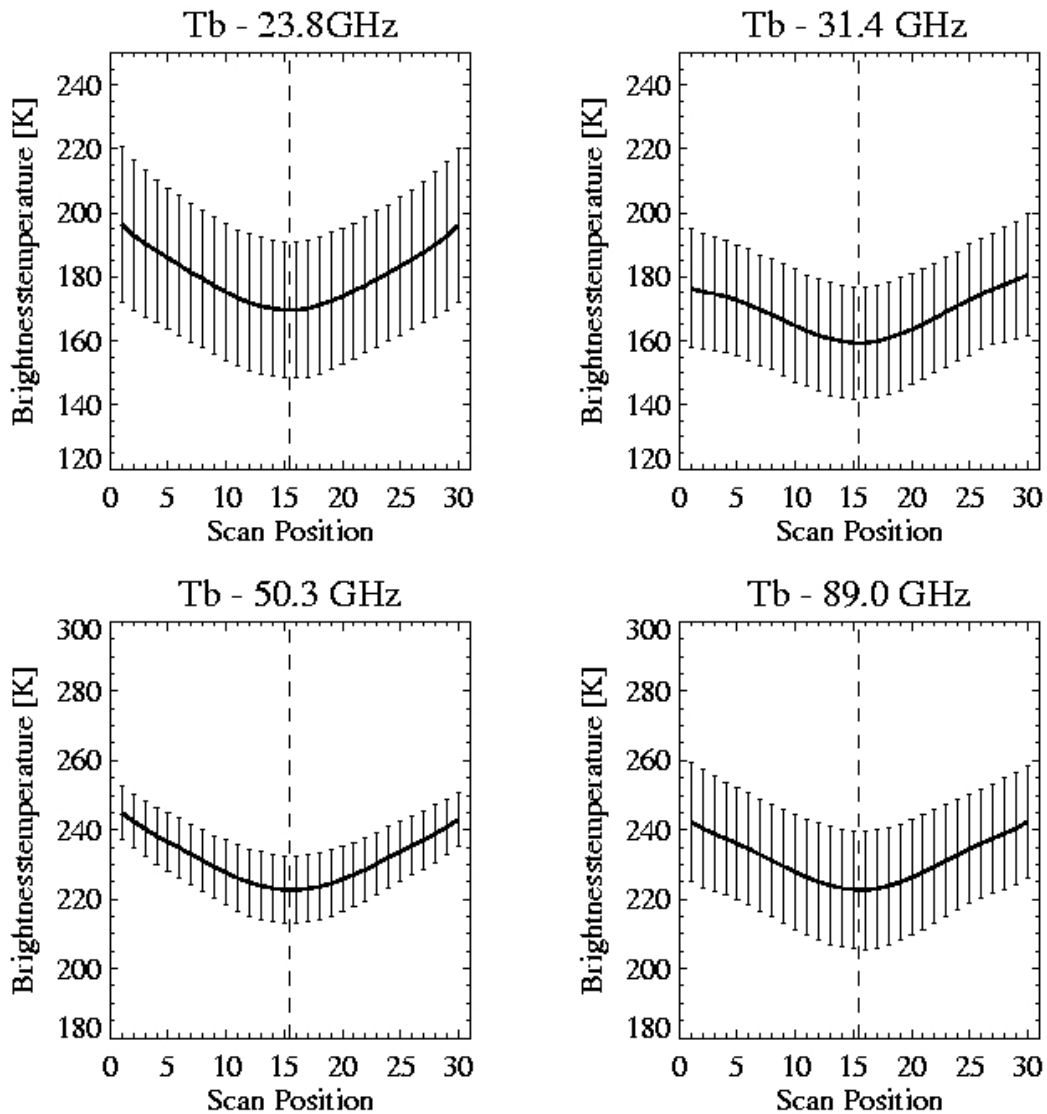
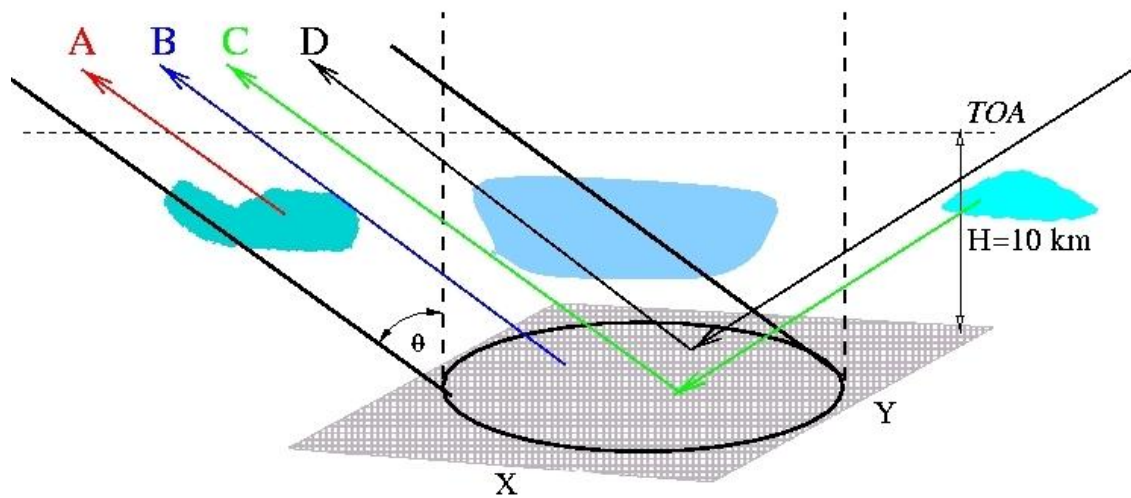


Figure 3.6: AMSU-A observed asymmetry in measured brightness temperatures. T_b denotes the brightness temperature at 28.4 GHz, 31.4 GHz, 50.3 GHz, and 89. GHz depending on scan angle. Mean and standard deviation of all 2001 AMSU poleward overpasses over the North Atlantic. Scan position is given west to east.

3.2.2 Microwave retrieval of LWP and TPW

The radiation measured in the microwave narrow frequency bands is the sum of the emissions from atmospheric gases, the surface and the atmospheric water, see figure 3.7. The surface emission (B) is well known over the oceans. Here it depends mainly on the sea surface temperature and the surface wind speed. The ocean gives a cold homogeneous background for the atmospheric emission. Over land the surface emission is highly variable. Thus, retrieval of atmospheric parameter using microwave radiances is only suitable, when the background information is homogeneous and well known, like over ocean areas. The variance is in the range of the emission from the atmosphere. The background emission from space (D) is well known. The remaining part is the emission from the atmosphere (A).

In figure 3.8 the transmission as a function of the frequency in the microwave spectra is



$$\begin{aligned}
 T_B &= T_A(1 - \exp(-\delta_A)) \\
 &+ (1 - \Gamma_r) T_S \exp(-\delta_A) \\
 &+ \Gamma_r \exp(-\delta_A) T_A(1 - \exp(-\delta_A)) \\
 &+ \Gamma_r T_{sp} \exp(-2\delta_A)
 \end{aligned}$$

$$\delta_A = \delta + \delta_{\text{gas}}$$

$$\delta_A \sim \text{LWP}$$

Figure 3.7: Composition of the microwave signal as measured with a satellite instrument, from von Bremen et al. (2002). (A) denotes the atmospheric emission, (B) the surface emission, (C) the reflected atmospheric emission and (D) the reflected background emission. The optical depth of the atmosphere is given by δ_A .

shown. For the LWP and TPW standard retrieval algorithm two frequencies are used. One near the water vapour absorption line (22.235 GHz), for AMSU it is the 23.4 GHz channel. The second frequency is chosen in the water vapour window, here the 31.4 GHz channel. The first radiance is stronger related to the water vapour in the atmospheric column, the second to the integrated liquid water, see figure 4. The signal in both channels is not exclusively related to the water vapour/LWP there is still some influence on the other compound. Therefore, the retrieval of one quantity is not independent of the other retrieval.

The NOAA–NESDIS algorithm Grody et al. (2001) is given as:

$$TPW = \cos \theta [c_0 + c_1 \ln(T_s - T_B(23.8)) + c_2 \ln(T_s - T_B(31.4))] \quad (3.1)$$

$$LWP = \cos \theta [d_0 + d_1 \ln(T_s - T_B(23.8)) + d_2 \ln(T_s - T_B(31.4))] \quad (3.2)$$

The coefficients c_0 and d_0 are functions of the viewing zenith angle θ and have been derived from radiative transfer calculations. The algorithm has been validated against SSM/I and radiosonde measurements. The coefficients (c and d) also depend on the wind speed and the used satellite platform (see <http://orbit-net.nesdis.noaa.gov>). The surface temperature, T_S , defines the radiative background.

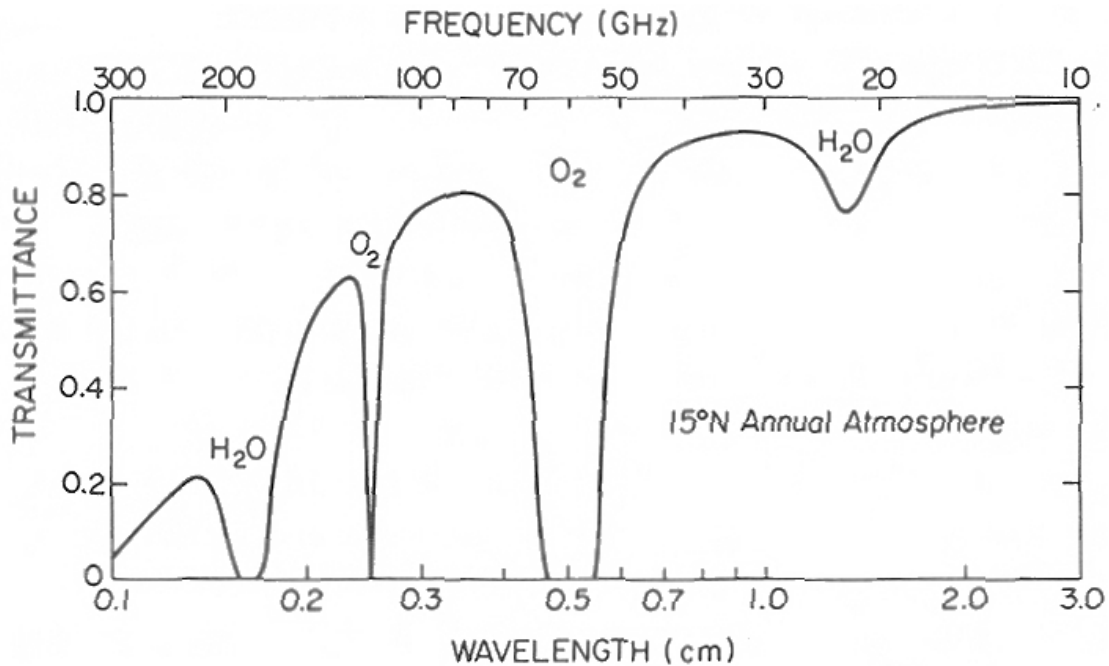


Figure 3.8: Transmittance as function of the microwave frequency, from Ulaby et al. (1981).

Channel	1	2	3a	3b	4	5
wavelength [μm]	0.58 - 0.68	0.725- 1.1	1.580- 1.64	3.55 - 3.93	10.3 - 11.3	11.5 - 12.5

Table 3.6: AVHRR channel informations.

If TPW larger than 70 kg/m^2 occur in a pixel, the retrieval assumes wrong TPW and reduces the TPW on behalf of increasing LWP.

3.2.3 AVHRR

The advanced very high resolution radiometer, AVHRR, is mainly used to study the spatial distribution of clouds. As AMSU, the AVHRR is an instrument on board NASA polar orbiting satellites. Since 1981 instruments with comparable configurations to the actual AVHRR series are operating. With the launch of NOAA-15, the first satellite of the NOAA-KLM series, the new AVHRR generation called AVHRR/3 is operating. Data from this AVHRR generation is used in this study.

AVHRR/3 has six channels centred at 0.6, 0.8, 1.6, 3.7, 10.8 and 11.9 μm . The AVHRR channels are summarised in table 3.6. The 1.6 and 3.7 μm are not operating at the same time. During day time the 1.6 μm and during night time the 3.7 μm is operating. The channels are optimised to measure cloud and surface characteristics with minimal contamination from other atmospheric constituents. The instrument calibration for the visible channels is done only pre-launch. There are no onboard calibration units. The post-launch calibration is done by comparing measured reflections with reflections from surface based targets. On the NOAA/NESDIS web site (<http://www2.ncdc.nasa.gov>) new calibration coefficients on a monthly basis are provided.

The 0.6 μm channel is mainly used to identify clouds. At this wavelength land and sea surfaces are dark and clouds appear bright. 0.8 μm in addition to 0.6 μm is mainly used to estimate the amount of vegetation. Sunlight at 0.6 μm is absorbed by vegetation but 0.8 μm radiation not. The 1.6 μm is used to enhance the cloud property retrivals. The measured radiance is depending on droplet size therefore effective radius retrieval are possible. The 3.7 μm measures signals from reflected sunlight and from thermal emission. In cloud free condition snow detection is possible. Isolating the solar contribution, the relation of the 3.7 μm signal to the 0.6 μm and 0.8 μm radiance can be related to droplet size of water clouds, see Nakajima and King (1990). During night time the difference in 3,7 μm and 10.8 μm is used to identify fog. The 10.8 μm is used to estimate temperature of clouds. Atmospheric absorption is low but not negilible at the channel. The difference in 11.9 μm and 10.8 μm is used to estimate the absorption at 10.8 μm . This is used to calculate the sea surface temperature. Overland this method is not valid, because the difference in these channels depend on the vegetation as well.

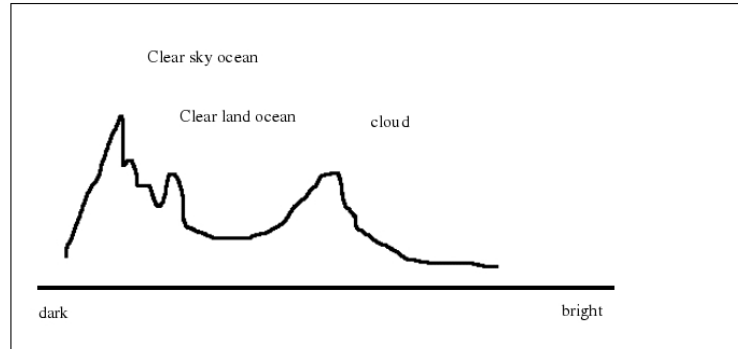


Figure 3.9: Sketch of a frequency distribution of channel 1 reflectances.

3.2.4 AVHRR retrieval of cloud properties

The retrieval of cloud properties from AVHRR measurements are based on look-up tables mainly. Here data sets consisting of sun-satellite geometry, cloud optical thickness, droplet sizes, surface reflectance, and radiances are built by radiative transfer modelling. In this study a cloud property retrieval scheme called KLAROS is used. KLAROS stands for KNMI local implementation of APOLLO retrievals in an operational system. A detailed description of KLAROS is given in Dlhopsky (1998). KLAROS is a two step approach. The first step is the identification of cloud filled pixel. This thresholding test is adopted from the AVHRR processing over land cloud and ocean (APOLLO), which was developed in the 1980's, see Saunders (1986) and Saunders and Kriebel (1988). In KLAROS the cloud detection is done automatically. The scheme is based on three test during day time and two during night time. Each test compares the measured radiance in the visible channel or the measured temperature in the near infrared with a threshold. The thresholds are set empirically. The tests are:

Temperature test:

$$T_{10.8 \mu m} < T_{10.8 \mu m}(\text{cloud} - \text{free}) - \text{threshold} \quad (3.3)$$

Reflectivity test:

$$R_{0.6 \mu m} > R_{0.6 \mu m}(\text{cloud} - \text{free}) + \text{threshold} \quad (3.4)$$

Semi-transparency test:

$$T_{10.8 \mu m} - T_{11.9 \mu m} > (T_{10.8 \mu m}(\text{cloud} - \text{free}) - T_{11.9 \mu m}(\text{clear} - \text{free})) + \text{threshold} \quad (3.5)$$

The T_λ define the equivalent black body temperature in the spectral channel denoted by λ . The R_λ denotes the reflectivity in the spectral channel. The measured values on

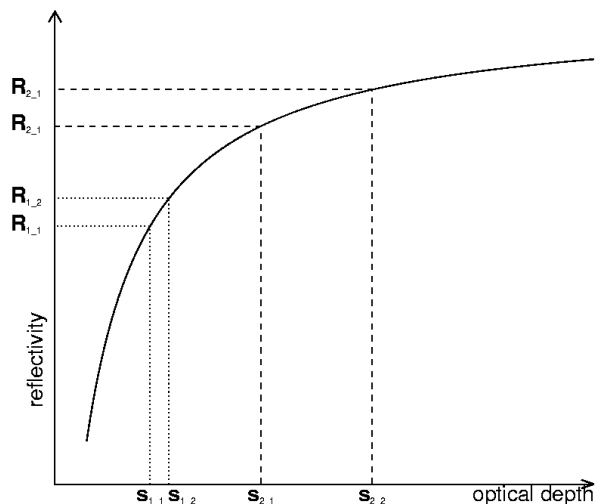


Figure 3.10: The relation of the measured reflectivity (R) of solar radiation to the optical depth (s) of a cloud.

the left hand side are compared to modelled cloud-free values. The cloud-free values are calculated by radiative transfer model. The surface temperature are derived from numerical weather prediction model used at the KNMI.

These thresholding techniques are used by many studies to identify clouds (e.g. Kastner and Kriebel (2000), Feijt and Jonker (1999)). The second step in KLAROS to derive cloud properties is performed for cloudy pixels only. For opaque clouds which are selected by the semi-transparency test cloud properties are derived by using look-up tables. The data set of the look-up table is derived from radiative transfer calculations. The radiative transfer is modelled by using for example the doubling adding techniques for short wave radiation. In this study the look-up tables for short wave radiation are derived from DAK (Doubling Adding KNMI) simulations. For the longwave radiation MODTRAN (moderate resolution transmittance) is used. The radiances according to a certain number of sun-satellite geometries, surface reflectivities, cloud parameters are calculated and stored in a data base. In KLAROS the effective radius, r_e was set to $10 \mu\text{m}$.

The measured radiances at $0.6 \mu\text{m}$ depending on the sun-satellite geometry are compared to the modelled radiances for an interpolated geometry and surface reflectivity. The cloud optical depth, τ for this pixel is retrieved. The liquid water path, LWP, is calculated with:

$$LWP = \frac{4}{3} \tau r_e \rho \frac{1}{D}. \quad (3.6)$$

The effective radius r_e is set to $10 \mu\text{m}$, the drop size distribution D in water clouds is set to 2.14 in the DAK calculations. According to Stephens (1984) the drop size distribution is 2. This technique is later in this study referenced as KLAROS scheme. A detailed description of the relation is given e.g. in Han et al. (1994).

In section 5.2 a fast cloud identification is performed. First cloudy pixels have to be identified. A common technique is based on two channels. A first thresholding test is done by using the temperature in the $10.4 \mu\text{m}$ channel. If the pixel has a temperature lower than 273, clouds are assumed. The second test makes use of the reflectance in the $0.6 \mu\text{m}$ channel. Here the pixel must be brighter than a dynamical threshold derived from the whole satellite scene. The distribution of channel 1 reflectances for a scene including clouds over land and sea as well as clear sky land and sea is shown in figure 3.9. Cloud free areas are represented by peaks in the dark end of the distribution, where ocean has a lower albedo as the land. A third peak is in the brighter edge of the distribution which is related to clouds. The dynamical threshold is fixed by the minimum in-between these peaking areas.

Using the solar reflectivity to retrieve the LWP leads to problems for clouds with large optical depth. In figure 3.10 the relation of the observed reflectivity depending on the optical depth is shown. This non-linear relation ship leads to clear relations for low optical depth. The function converges for large optical depth. Here small variations in the measured reflectivity will lead to large uncertainties in the optical depth retrieval.

During the CLIWA-NET project LWP and other cloud properties derived from AVHRR measurements were compared to ground-based measurements. Beside the problems in co-location of the instruments another problem occurs. AVHRR measures the spatial distribution with a resolution of about 1 km, but with a low temporal resolution. A ground-based instrument measures the properties for the zenith direction but with a high temporal resolution. To compare these measurements a suitable sampling in time and space has to be found. However, the KLAROS scheme give reasonable results for the optical properties.

The KLAROS scheme is a supervised tool to derive cloud properties from AVHRR radiances. Additional numerical weather prediction model data are needed. The scheme was developed for the Netherlands area. A transfer to larger regions was not straight forward. Within the CM-SAF project a european software for cloud property retrieval based on visible and near infrared radiances is developed, but it is still not operational. In this study the KLAROS is used for AVHRR LWP retrieval for the North sea to compare with AMSU measurements. A regional extend was not feasible.

3.2.5 Data quality

AVHRR and AMSU are onboard the NOAA-15, NOAA-16 and NOAA-17 satellites. The status of these satellites and the data quality differs, see table 3.2.5. It turned out that only data from NOAA-16 are appropriate for an analysis using both instruments. In section 5.2 the influence of the relation LWP – WVP on cloud cover derived from AVHRR measurements inside the AMSU FOV is investigated using near noon overpasses for the periode May to September 2001. For the study of the excess water vapour from global AMSU measurements data from February 2001 to October 2005 are used. The complete

Satellite	Start date	Status
NOAA-15	25.10.1998	Problems starting in summer 2000. AVHRR and AMSU channel instabilities and failures.
NOAA-16	24.01.2001	No problems reported.
NOAA-17	28.06.2003	Failure in different AMSU frequencies used in this study.

Table 3.7: *Satellite status informations.* Source: <http://www.saa.noaa.gov>. For informations on the instruments related to the overpasses see: <http://www.noaa.nesdis.gov/poesstatus/index.asp>.

year 2002 is excluded due to calibration problems.

3.2.6 Additional data

The Grody et al. (2001) algorithm needs surface informations. The surface informations used in this study are taken from the NCEP/NCAR reanalysis data (Kalnay and Coauthors (1996)). For the sea surface temperature (SST) the weekly Reynolds SSTs on a $1.0^{\circ} \times 1.0^{\circ}$ grid are used here. For the wind speed the six hourly reanalysis data on a $2.5^{\circ} \times 2.5^{\circ}$ grid are used.

Chapter 4

A microwave retrieval based on neural network

The LWP and TPW retrieval based on microwave measurements described in the previous chapter is based on the reduction of the radiative transfer equation disregarding scattering at large particles. A more reliable approach is a neural network based algorithm using detailed microwave radiative transfer calculations of the atmospheric conditions using radiosonde ascents.

For modelling the microwave radiative transfer, MWMOD (Microwave radiative transfer Model) developed by Simmer (1994) is used. Calculations are performed assuming non-precipitating clouds. Scattering at rain drops is excluded. Observed atmospheric profiles are used to calculate the microwave radiative transfer through the atmosphere. The profiles are derived from 8000 radiosonde ascents over the Atlantic ocean and from coastal stations. In figure 4.1 the positions of the radiosonde ascents are shown. Mainly profilings from the research vessel 'Polarstern' are used (for the Polarstern profiles see König-Langlo and Marx (1997)). All profiles used in this study exceed the 300 hPa level and ground synoptical observations exist. The adiabatic LWP is calculated from the humidity profiles using the scheme of Hargens (1992).

With MWMOD the LWP, TPW and the brightness temperature at 23.8, 31.4, 50.3 and 89.0 GHz are modelled for each radiosonde. Figure 4.2 shows the correlation between the LWP or WWP and the brightness temperatures. The brightness temperature at 23.8 GHz strongly depends on the total precipitable water. At 31.4 GHz the brightness temperature is depending on the liquid water. The distribution of the calculated brightness temperatures towards the TPW or LWP is dominated by a large variability. The non-linearity in the relation shown in figure 4.2 can be described with neural network techniques by making use of the large number of radiosonde humidity and temperature profiles to calculate the satellite measured brightness temperature with MWMOD.

4.1 Neural Network

The algorithm deduction using neural network techniques to derive geophysical parameter is a common used method, see for example Atkinson and Tatnell (1997). Details of the historical development of neural networks, their theory and efficiency are described in Rojas (1993). A comparison of neural networks and other statistical methods in remote sensing is given in Krasnopolsky et al. (1995).

Neural networks are a statistical tool to describe multi-dimensional non-linear relations,

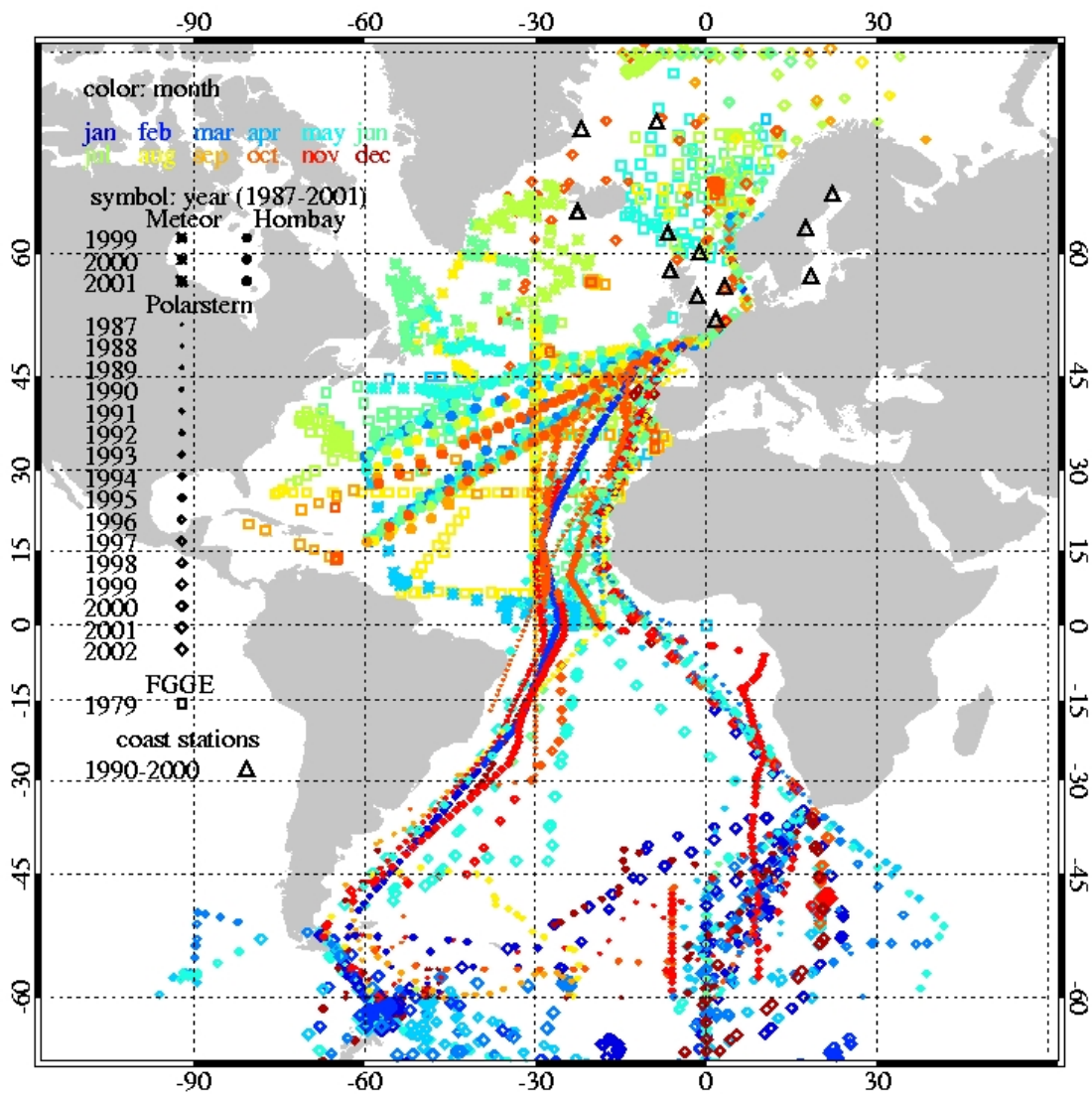


Figure 4.1: *Distribution of the used radiosonde ascents.*

like LWP or TPW with respect to the brightness temperatures at different microwave frequencies. The neural network used in this study is developed by F. Wagner at the Institute of theoretical physics at the University in Kiel. A detailed description is given in Wagner (1996). The minimisation algorithm is published by Lovelace and Wagner (1995). Retrievals of geophysical quantities based on neural network techniques provide better results as algorithms based on linear regression techniques.

Crucial in using neural networks to derive a retrieval algorithm are the definition of the optimal architecture of the net, the optimal parameter, and a representative data set. In figure 4.3 a sketch of the basic architecture of neural networks is given. A typical network consists of different layers. Each layer is build of neurons which produce the relations between the input parameters and the output parameters. Each relation is defined by its weight, which characterises the value on information for linking the input values to the output parameter. With initialising the net the starting weights are set assuming a linear approximation. During the iteration scheme the weights are varied. The network is trained by multiple presentation of input data and the resulting output parameter. The assignment of valuable input data to the resulting output parameter are found by iterations with minimizing a cost function. A seperated part of the input data is then used to validate the retrieved function to avoid memorising. In this study the input parameter are

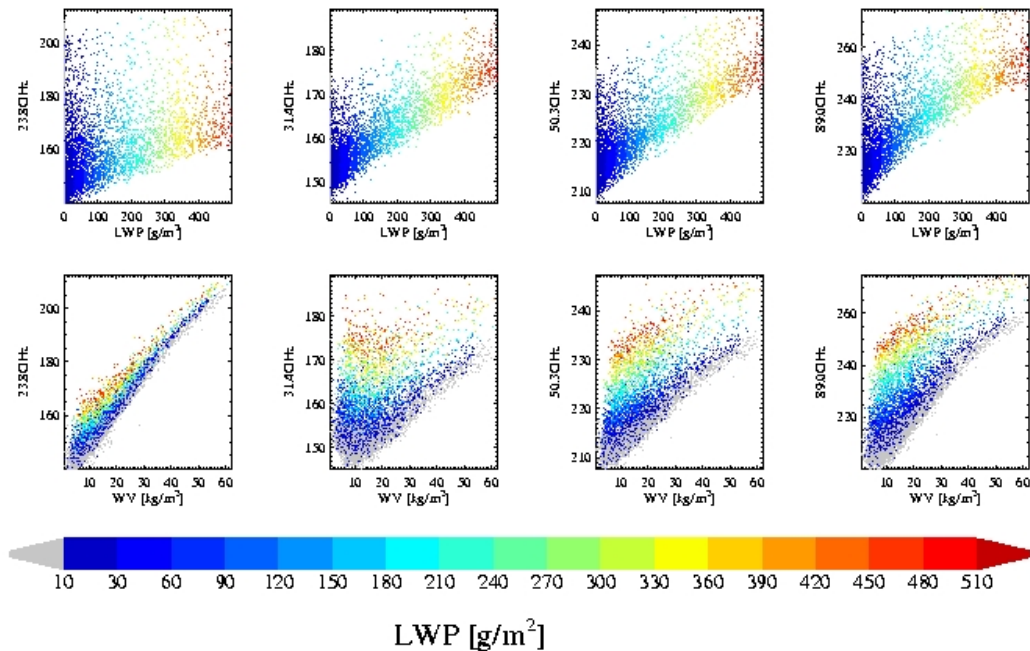
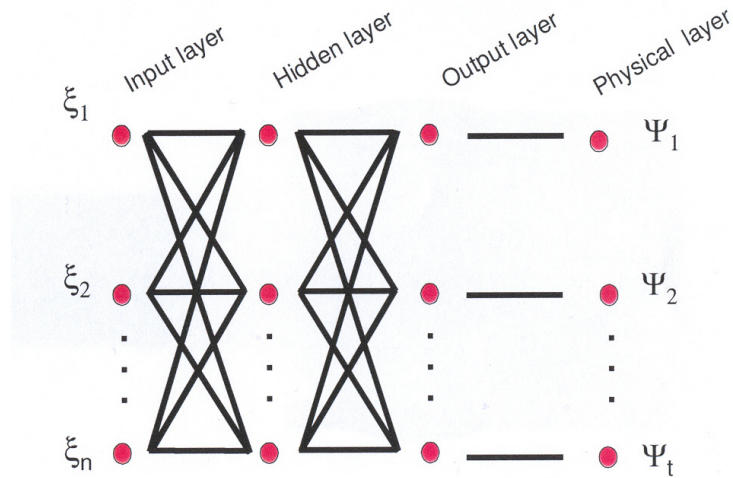


Figure 4.2: Calculated brightness temperatures in [K] at the AMSU channels for a sufficiently large number of atmospheric conditions as a function of LWP (upper panel) and TPW (lower panel, denoted as WV).

Figure 4.3: *Basic structure of neural network.*

the modelled brightness temperature at four AMSU frequencies (23.8, 31.4, 50.4, and 89.0 GHz). The output parameters are LWP and TPW. As AMSU is a cross track scanning instrument, the observations are at 30 scan positions. The scan angles are symmetrical to the nadir position.

From the humidity and temperature profiles of the radiosonde data described above the brightness temperatures at the AMSU frequencies are modelled with the microwave radiative transfer model MWMOD. The LWP and TPW is calculated with MWMOD as well.

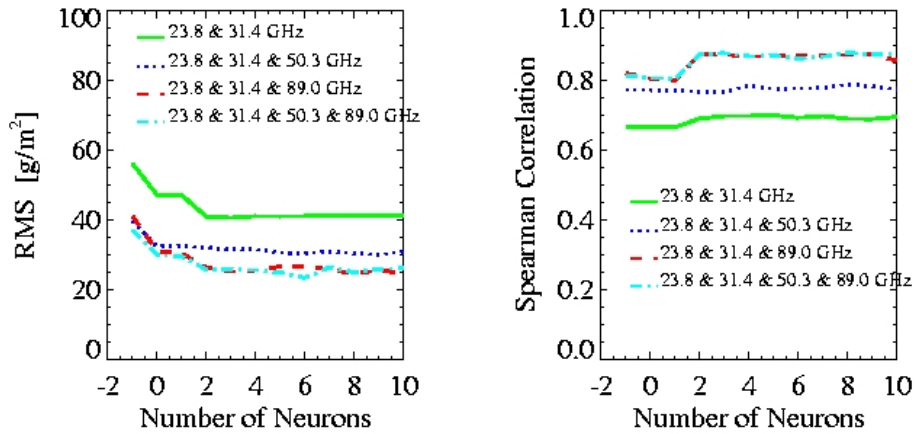
With these data the neural network is trained. The data set is splitted randomly into three parts, two for the training and one for the validation. During the training the neural network cross checks the retrieved algorithm against the results performed with the second data set. The aim is to minimize the cost function but to avoid over training, when the algorithm is not able to retrieve e.g. LWP in an suitable error marge from a new data set. When training and first step validation is done, the third data set is presented to the algorithm. The statistical error, the rms, is now taken as a quality measure for the derived algorithm.

For each architecture of the network, the neural network is started 100 times with slight variations of the starting points of the iterations. This reduces the probability that incidently a local minimum of the cost function is found. For training the network was build up with one hidden layer. The number of neurons on this layer was varied in the first process. In figure 4.4 the influence of the number of neurons on the hidden layer on the root mean square (RMS) error is shown for different input parameters. The linear regres-

sion is included in the figure with '1' neurons. A decrease in RMS is found for increasing number of hidden neurons. However, two neurons on the hidden layer are sufficient. A strong improvement is found when using more than the typical microwave frequencies, 23.8 and 31.4 GHz. The enhancement by using all four frequencies is small. But the informations kept in the signal at 50.3 and 89.0 GHz is different. Therefore, the input of more informations is only positive.

The correlation of the LWP derived from the neural network (denoted as NN) and the LWP of the input data is given in figure 4.5. The ranked correlation between the modeled TPW and the NN retrieved TPW is 0.99. For the LWP the correlation is 0.97. The neural

A: LWP



B: TPW

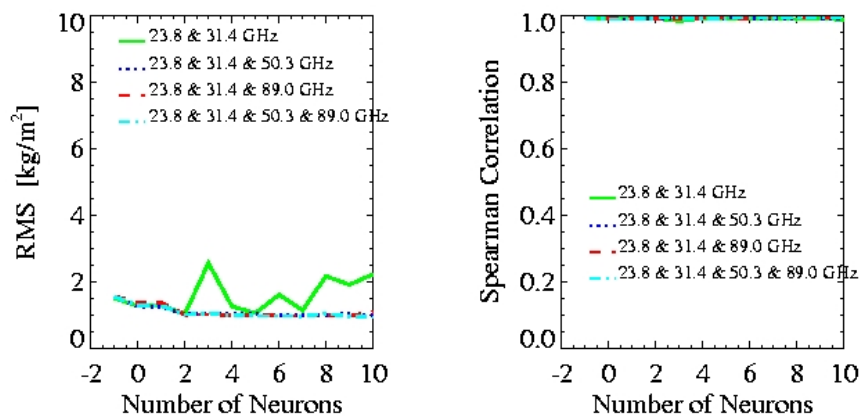
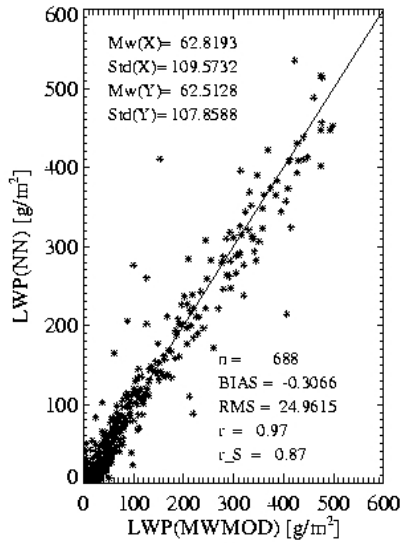


Figure 4.4: Dependency of the root mean square error of the NN set up. Number of hidden neurons and quality of the network. A: LWP, B:TPW

A: LWP



B: TPW

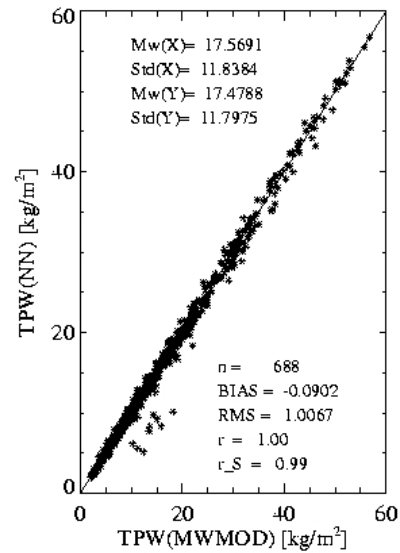


Figure 4.5: Correlation of the test data set to the NN retrieval. A: LWP, B:TPW

network is only able to interpolate in the limits defined by the training data set. It is not able to extrapolate. The validation data set is from the brightness temperatures in the limits given by the training data set, but still it is possible, that specific synoptical situations are not included. In figure 4.5 for the TPW a cluster of eight values seem to be not well represented by the neural network, an underestimation occurs. These data points may present such a situation not included in the training data set. This shows the limitations of the neural network technique. Therefore, it is ineluctable to use a comprehensive data set including a wide range of synoptical situations. Further research shows that the knowledge of surface parameters considerably increases the retrieved accuracy e.g. using the surface temperature as in the NESDIS algorithm.

Chapter 5

Comparison of microwave retrieval algorithms

In this chapter the neural network (NN) algorithm described in the previous section is applied to AMSU noon overpasses. In section 5.1 the NN is compared to AVHRR LWP retrieval. The region investigated is the North sea area. In section 5.2 the influence of the inhomogeneity of clouds inside the AMSU FOVs is investigated. Here the higher resolution of the AVHRR instrument is used to quantify the sub scale inhomogeneity. The NN algorithm is compared to the NOAA/NESDIS AMSU algorithm described in section 3.2.2. The results are given in section 5.3.

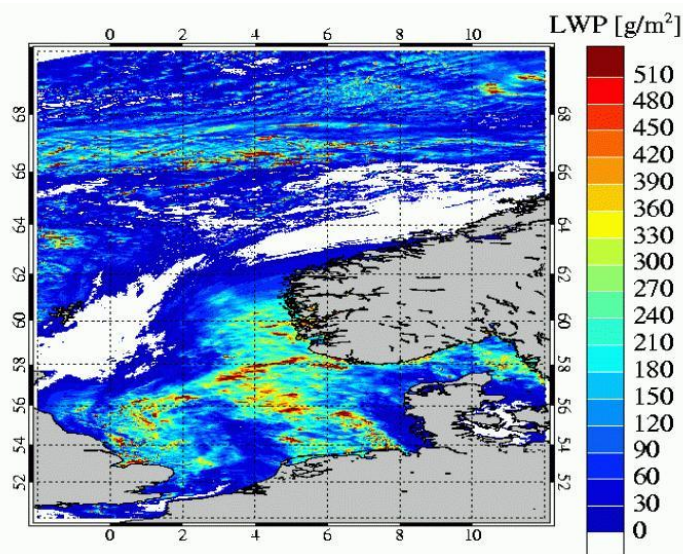
5.1 Comparison of the NN algorithm to the AVHRR retrieval

In section 3.2.4 the retrieval of LWP using solar reflection measured with AVHRR called KLAROS is described. In figure 5.1 the retrieved LWP for the 11 UTC overpass in pole ward direction on 14th April 2001 with both the AMSU NN and the AVHRR is shown. The high resolution AVHRR image clearly shows the small scale structure of the cloud. Averaging the small AVHRR field of views on the AMSU grid reduces the structure information. The averaging was performed for the LWP. The position of the particular AVHRR pixel inside the AMSU FOV was weighted in the averaging process with the AMSU antenna function. Looking at the AMSU retrieval higher values in LWP occur compared to the averaged AVHRR pixel. The near coastal AMSU FOV show larger values, which is due to the influence of surface emission. This can only be excluded if the measured brightness temperature when detailed information on the surface emission is available.

A common problem in microwave remote sensing is the large instrument's field of view. The measured signal corresponds to the integrated emission of the area covered. The results are smooth fields. Inhomogeneities inside a field of view cannot be detected. But do they

influence the retrieval? Comparing the two retrieval techniques depending on the cloud cover inside the AMSU-FOV in figure 5.2 shows reasonable agreement. Large scattering is due to the different scan angle. Figure 5.3 shows the correlation of the AMSU-LWP to the mean AVHRR-LWP for each scan angle assuming symmetry around Nadir position.

A: AVHRR



B: AVHRR on AMSU grid

C: AMSU

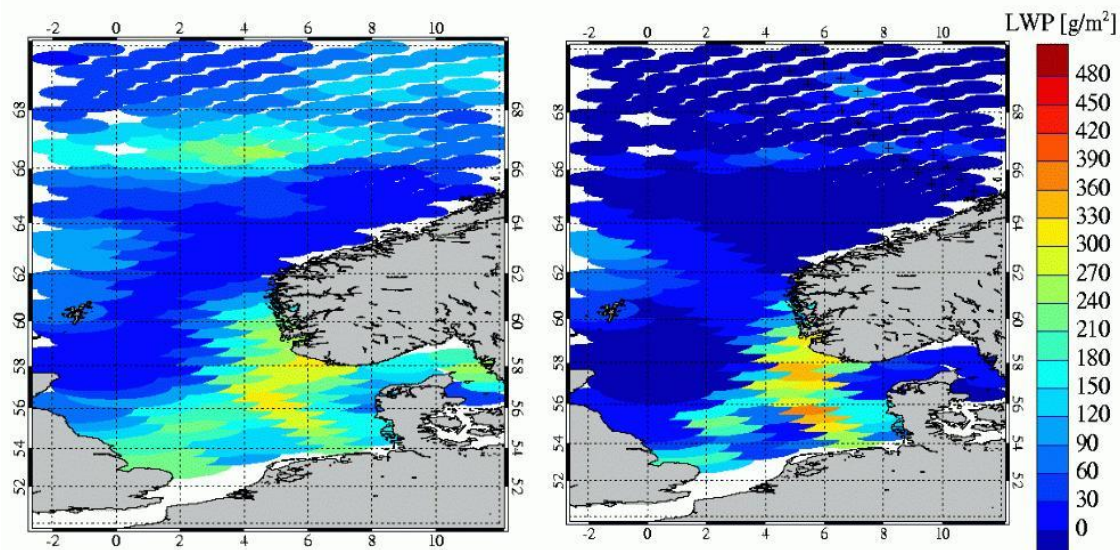


Figure 5.1: LWP field derived for the 14th April 2001 11UTC from AVHRR retrieval described in section 3.2.4. A: AVHRR resolution, B: AVHRR sampled on AMSU grid. C: AMSU LWP field using the NN.

The mean LWP derived from AVHRR is overestimating the LWP compared to the AMSU retrieval. The function describing the relation of the visible reflectance to the optical depth of the cloud saturates for large optical depth as shown in figure 3.10. Small variations in measured reflectance can lead to large variations in the retrieved optical depth and further in the LWP. Larger scattering at the cloud tops can occur due to the presence of ice particles. In the microwave regime ice does emit less radiation as liquid droplets, and reduces the emission of lower levels due to scattering. Less LWP is retrieved. Both effects can explain the correlation of the both techniques.

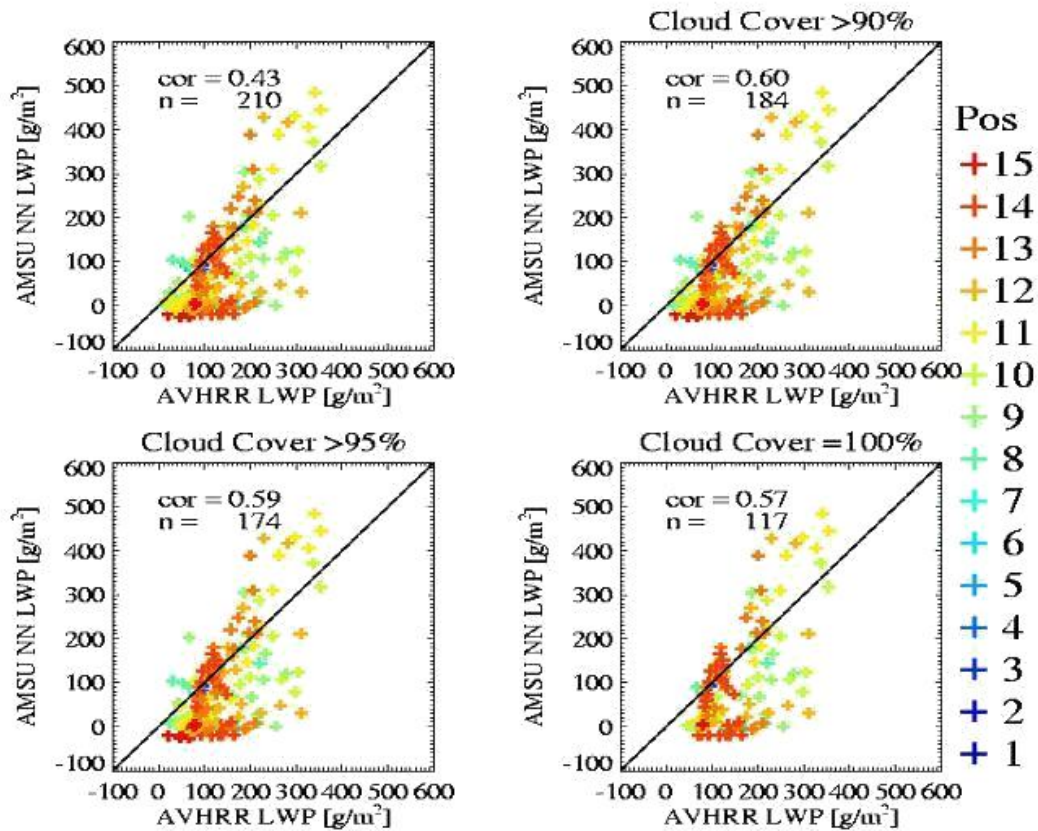


Figure 5.2: Comparison of LWP retrieved with AMSU (NN) and AVHRR for the 14th April 2001. Colours give the AMSU scan angle, 1 far field of view to 15 near nadir. The scan positions are symmetrical to the nadir position. Upper row: left: all cases, right: cloud cover of the AMSU FOV larger than 95%, lower row: left cloud clover of the AMSU FOV larger 95% and on the right total covered AMSU FOV.

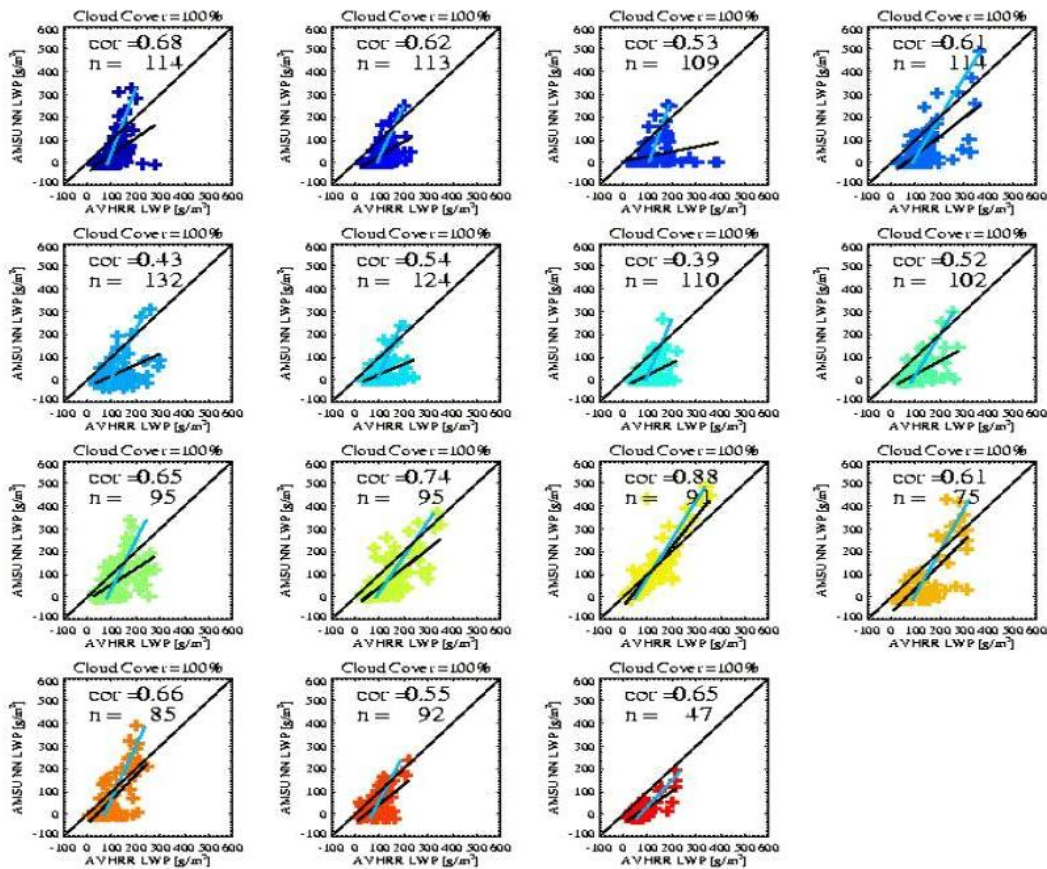


Figure 5.3: Comparison of LWP retrieved with AMSU (NN) and AVHRR for several overpasses over the North Atlantic during April 2001. Colours give the AMSU scan angle see figure 5.2, blue far field of view to red near nadir. The scan positions are symmetrical to the nadir position.

5.2 TPW and LWP retrieval from AMSU: dependency on FOV cloud cover

The main purpose of this study is to obtain a link between water vapour in clear and cloudy areas. This information shall be used in future corrections of the nice weather bias. As a first step, the dependency of climatological LWP/TPW relationships will be calculated as a function of cloud cover.

AVHRR data for daytime overpasses have been looked at to obtain cloud cover inside an AMSU FOV's. This was done for the North Atlantic region from May 2001 to September 2001. To handle the huge amount of data, only one overpass per day enters the averaging process. The data have been averaged into grid sizes of $1^\circ \times 1^\circ$, $2.5^\circ \times 2.5^\circ$ and $4^\circ \times 4^\circ$ degrees in order to estimate the dependency of the LWP-TPW relations on averaging scale. Temporal averaging has been performed for the entire time period. Figure 5.4 shows scatterplots of LWP and TPW for the $2.5^\circ \times 2.5^\circ$ degree grid box sizes. Results for the other grid box sizes are given in appendix B. Not surprisingly, LWP and TPW are positively correlated. No significant changes in the type and degree of the correlation with cloud cover can be inferred. The same is true for the results shown in the appendix.

Obviously, cloud cover alone does not sufficiently distinguish between cases of warm and humid or cold and dry cloudy atmospheres. Further studies are necessary which include improved cloud masks and - more importantly - cloud classification schemes. In the frame work of the CM-SAF cloud properties like cloud cover, cloud phase and cloud type as well as cloud physical properties like optical depth, effective radius and LWP are provided. These products can help to investigate the dependency of the relation LWP-TPW on the cloud properties.

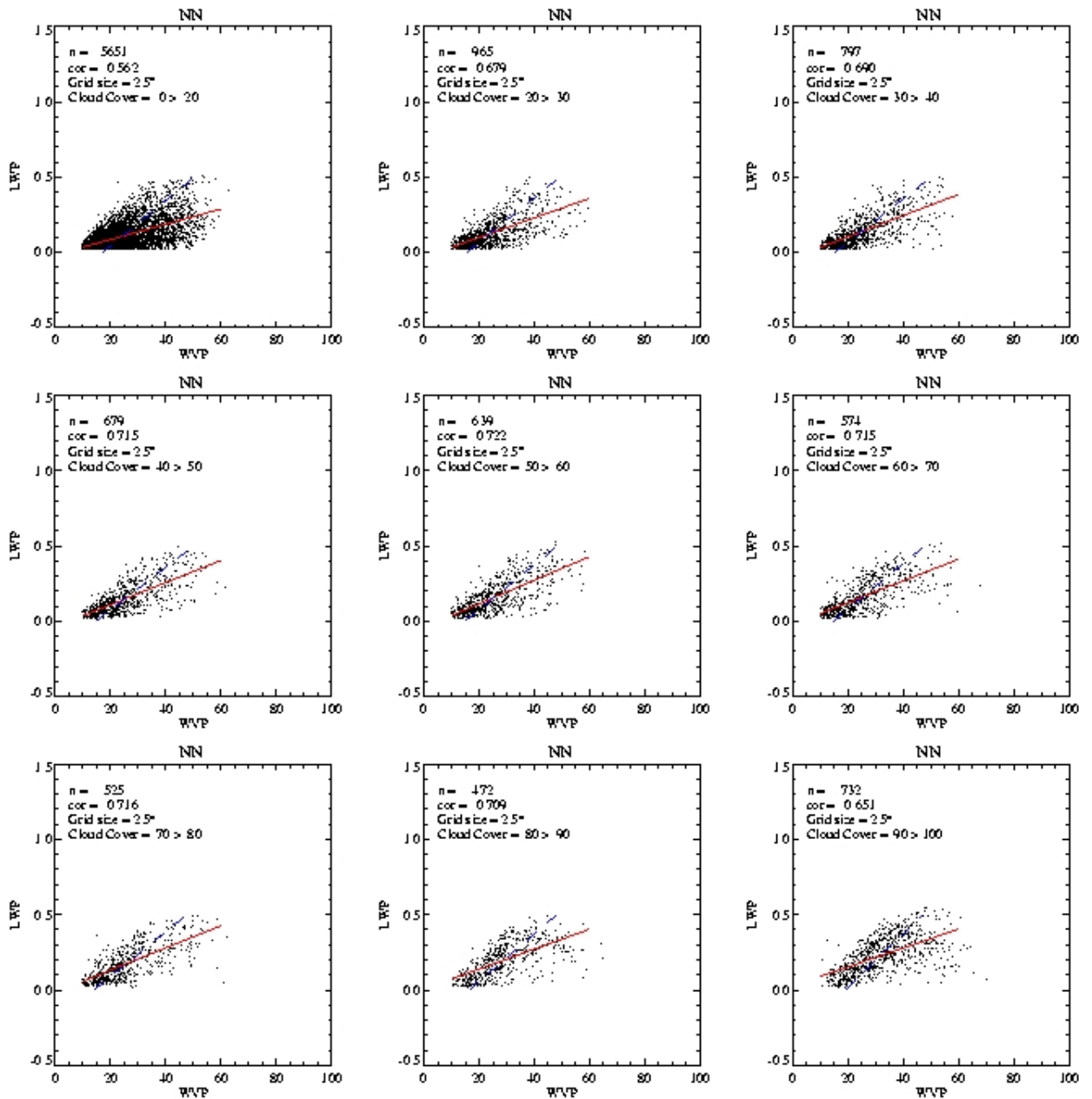


Figure 5.4: Influence of cloud cover on the relation LWP to TPW. LWP is given in kg/m^2 and the TPW in kg/m^2 . The retrieved values are sampled on a $2.5^\circ \times 2.5^\circ$ grid. In red the x-y correlation and in blue the y-x correlation is given.

5.3 Comparison of the NN algorithm to the Grody algorithm

In order to get an impression about the differences between the results from the statistical neural network scheme and the physically motivated NOAA-NESDIS algorithm, one specific satellite scene is analysed with both methods. Figures 5.5 and 5.6 show the retrieved LWP and TPW field for the NOAA-16 overpass over the North Atlantic from 9. 9. 2001, 14:35 UTC. While the results for the water vapor agree fairly well, large differences occur for the LWP results with a higher variability in the neural network derived fields. These differences are most likely caused by the use of surface informations in the NOAA-NESDIS algorithm. This may stabilize the retrieved atmospheric properties whereas the small-scale atmospheric noise introduces errors in the coupled neural network LWP/TPW retrieval. For the particular scene under consideration the neural network based LWP is larger than the NOAA-NESDIS by a factor of 1.5. This may be caused by the fact that the neural network scheme is trained for LWP smaller than 0.8 kg/m^2 while the NOAA-NESDIS scheme goes up to 2 kg/m^2 and that neural network regressions give unreliable results outside the training area.

Crewell and Löhnert (2003) show that small differences in retrieved LWP and TPW are a result of variations between various absorption models. The mean differences between Liebe (1989) and Liebe et al. (1993) are in the range of 1- 2 K for the lower frequencies, whereas a larger bias for higher frequencies (50, 89 GHz) occurs. The Rosenkranz (1998) model gives similar results as Liebe (1989). Some attempts to reduce these uncertainties are made, see Cruz Pol et al. (1998). In the present study the Liebe et al. (1993) scheme is used by MWMOD, whereas NOAA/NESDIS uses the Rosenkranz (1998) data. Nevertheless, the major differences between the neural network and the NOAA-NESDIS algorithms can not be explained by the different absorption schemes.

The neural network based TPW is slightly larger (factor of 6%) compared to the NOAA-NESDIS results (figure 5.7). Although the water vapor retrieval is less sensitive to surface conditions, the same reasons for the differences as described in the discussion of the LWP are suggested.

The brightness temperatures in the 23.8 GHz and 31.4 GHz channel are most sensitive to LWP and TPW. In both algorithm these dependencies are not completely separated. However, it depends on the algorithm whether it tends to derive more LWP or TPW on the expense of the other quantity, respectively. The neural network and the NOAA NESDIS algorithm have different tendencies in this aspect. The neural network tends to produce larger TPW instead of larger LWP in regions with thick clouds whereas the NOAA NESDIS algorithm obtains higher LWP values over these regions (see figure 5.5 and 5.6, respectively).

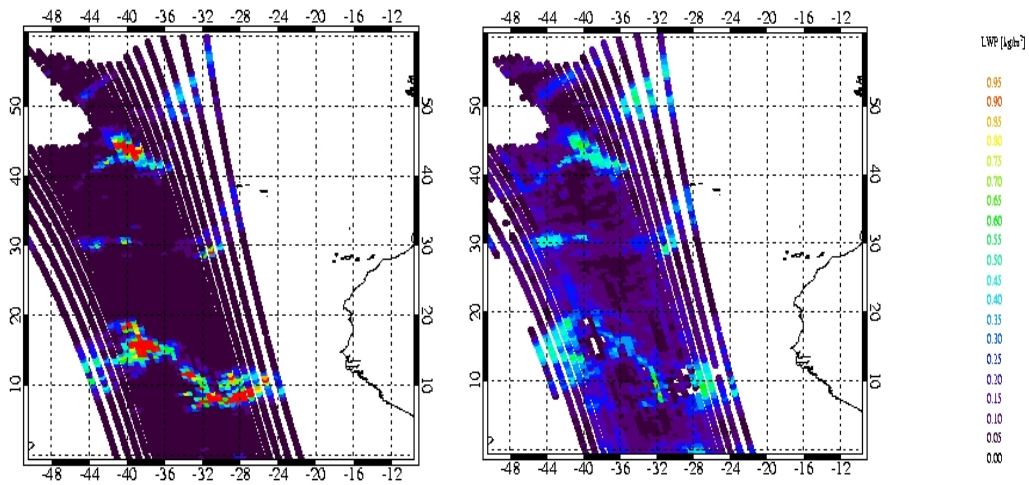


Figure 5.5: LWP field from 9.9.2001 at 14:35. Left: NOAA-NESDIS, right: neural network. The LWP is given in kg/m^2 .

Because of the most litaly incompleteness of the NN training data set and the resulting difficulties with the extrapolation we conclude to go ahead with the NOAA-NESDIS retrieval scheme within this study. The NOAA-NESDIS retrieval is used as the standard processing retrieval for AMSU in operational use. The TPW climatologies stay comparable towards other AMSU studies.

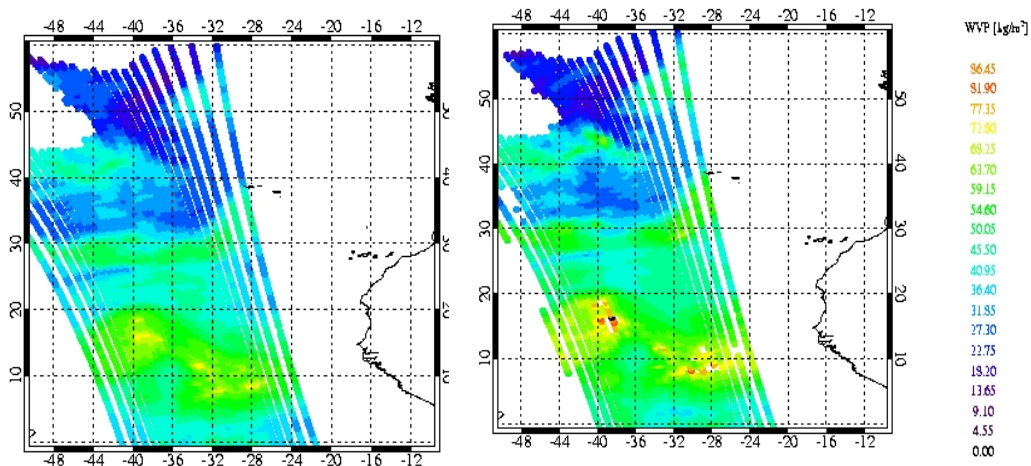


Figure 5.6: TPW field from 9.9.2001 at 14:35. Left: NOAA-NESDIS, right: neural network. The TPW is given in kg/m^2 .

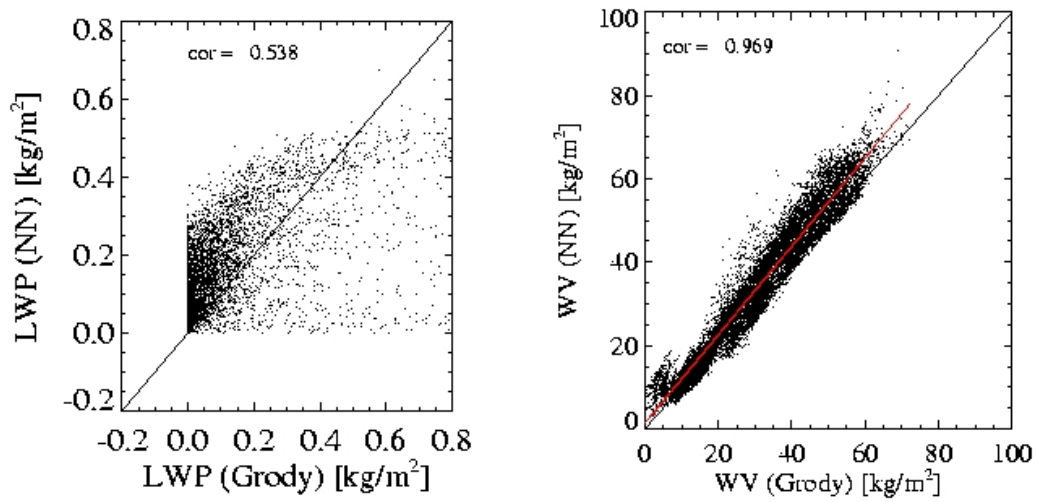


Figure 5.7: Correlation between NN-retrieved and NOAA-NESDIS atmospheric properties. Left: liquid water path, right: water vapour path. For the water vapour path the regression is given in red.

Chapter 6

Ground-based retrieval of TPW in all-sky atmospheres

Radiosondes provide a suitable ground truth for humidity profiling of the atmosphere. The total precipitable water (TPW) is defined as the vertical integrated absolute humidity (from surface to 300 hPa). In this section ten years of radiosonde ascents with corresponding cloud cover observations at the German stations Lindenberg, Schleswig, Essen, and Stuttgart are studied. The radiosonde ascents are used to check whether the TPW in cloudy skies is significantly different compared to clear-sky situations, see section 6.1. The general behaviour of TPW in the mid-latitudes is investigated in section 6.1.1. Results are shown exemplarily for the station Lindenberg. A focus is set on the difference in TPW for different atmospheric layers (see section 6.3). Furthermore, the relation of all-sky to clear-sky TPW for all stations and uncertainties and possible sources for them are estimated.

6.1 Cloud to clear TPW differences

The first question to be answered is whether there is more total precipitable water in cloudy-skies compared to clear-sky atmospheres. In the study of Gaffen and Elliot (1993) three years (1988-1990) of day time radiosoundings at 15 North hemispheric stations are used. The TPW is calculated from surface to 400 hPa. The data are categorised according to sky cloud cover from simultaneous surface visual cloud observations. The authors show significantly lower climatological TPW in clear-skies then in cloudy-skies. The variation in TPW with cloud cover is not only explainable by variations in air temperature, since an increase in cloud cover generally leads to a decrease in day time temperature.

To proof the climatological TPW difference between clear-skies and cloudy-skies Gaffen and Elliot (1993) categorise the TPW values by the observed cloud cover based on the

WMO-category of cloud amount where 0 oktas is clear (CLR), 1 to 4 oktas is scattered (SCT), 5 to 7 is broken (BKN), and 8 oktas is overcast (OVC). Reports of sky obscured and fog were discarded in this analysis. The data were separated into classes according to cloud cover and season. For each class the mean TPW has been calculated. The authors define the mean all-sky total precipitable water (\overline{TPW}_{ALL}) as:

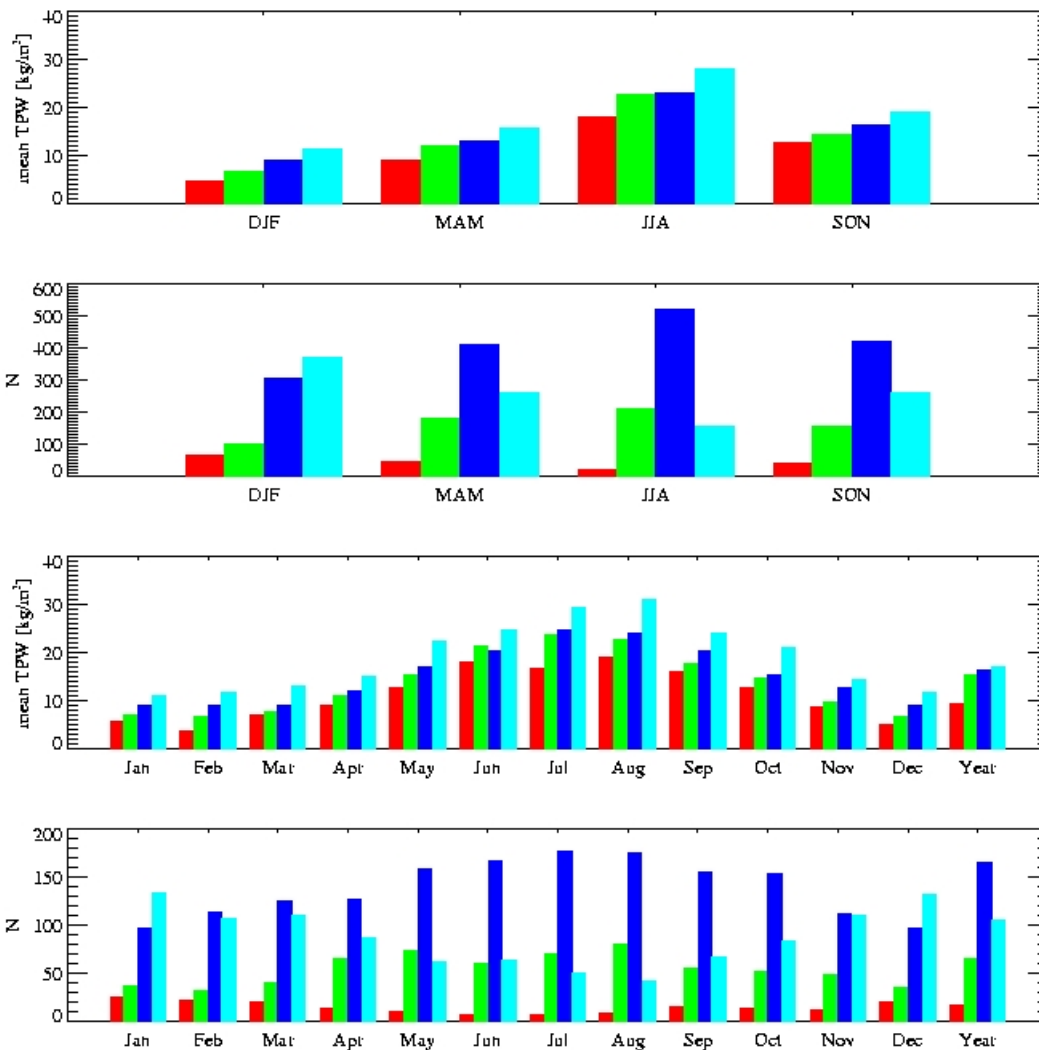


Figure 6.1: 10 years of data from Lindenberg sorted by the observed cloud cover: clear-sky in red, scattered cloudiness (1-4 oktas) in green, broken cloudiness (5-7 oktas) in blue, and overcast in cyan. From Top to bottom: Seasonal mean TPW in the cloud classes, number of cases per cloud class per season, monthly mean TPW per cloud classes and the number of cases per class. The last block in the monthly dispartment gives the yearly mean (the number of cases is given by the ordinate number times 10).

$$\overline{TPW}_{ALL} = \frac{N_{CLR}\overline{TPW}_{CLR} + N_{SCT}\overline{TPW}_{SCT} + N_{BKN}\overline{TPW}_{BKN} + N_{OVC}\overline{TPW}_{OVC}}{N_{CLR} + N_{SCT} + N_{BKN} + N_{OVC}} \quad (6.1)$$

were the subscripts refer to the cloud classes and N is the number of samples used to

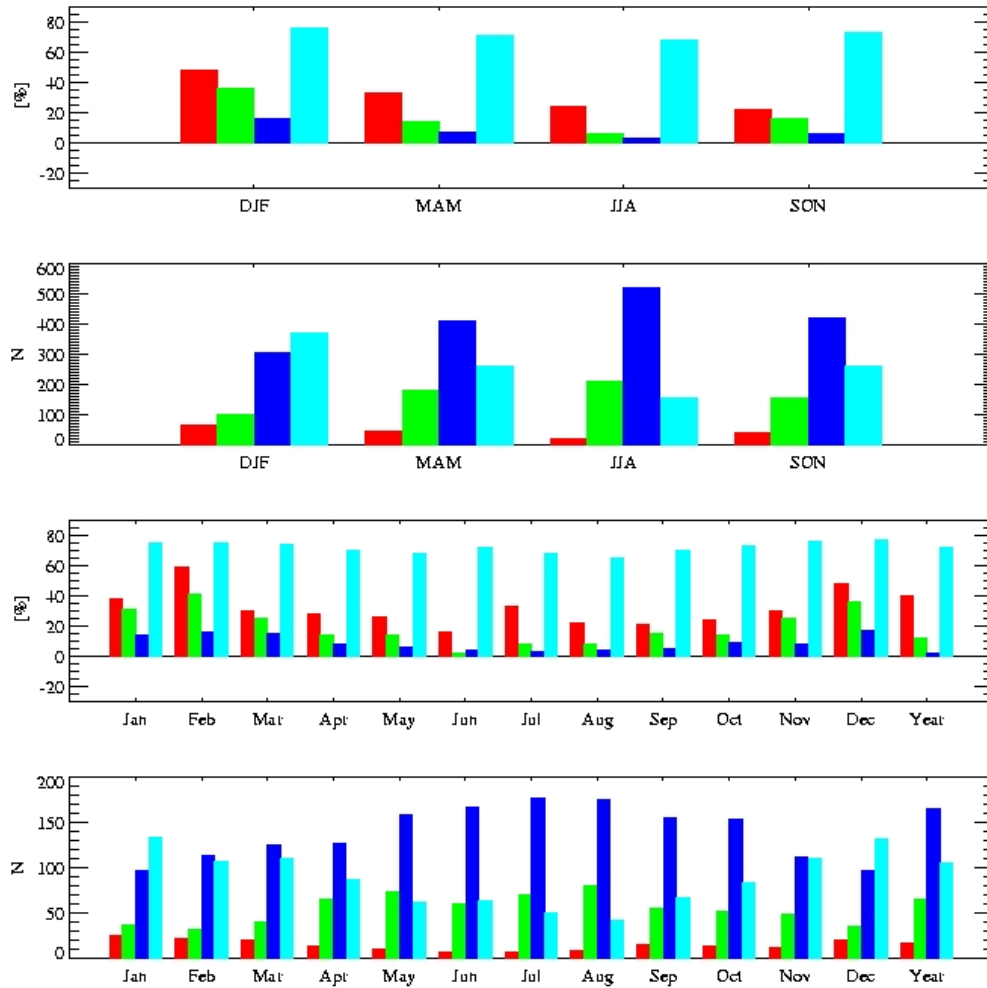


Figure 6.2: The bias estimators and the probability according to Gaffen and Elliot (1993): the b_0 in red, b_4 in green, b_7 in blue, and the probability in cyan. From Top to bottom: Seasonal bias estimators, number of cases per cloud class (see figure 6.1) per season, monthly bias estimators and the number of cases per class. The last block in the monthly dispartment gives the yearly mean (the number of cases is given by the ordinate number times 10).

calculate the mean. Three additional parameters are defined to quantify the bias in climatological (\overline{TPW}) values.

$$B_0 = 1 - \frac{\overline{TPW}_{CLR}}{\overline{TPW}_{ALL}}, \quad (6.2)$$

$$B_4 = 1 - \frac{N_{CLR} \overline{TPW}_{CLR} + N_{SCT} \overline{TPW}_{SCT}}{N_{CLR} + N_{SCT} \overline{TPW}_{ALL}}, \quad (6.3)$$

$$B_7 = 1 - \frac{N_{CLR} \overline{TPW}_{CLR} + N_{SCT} \overline{TPW}_{SCT} + N_{BKN} \overline{TPW}_{BKN}}{N_{CLR} + N_{SCT} + N_{BKN} \overline{TPW}_{ALL}}. \quad (6.4)$$

The subscripts (0, 4, 7) in equation 6.2 to 6.4 denote the maximum cloud cover included. For example B_0 expressed as a percentage gives the percent by which \overline{TPW}_{ALL} is underestimated when only clear-sky observations are included. B_0 and B_7 therefore define the extreme cases. The probability P of a radiosonde passing through a cloud is estimated by the product of the the probability of encountering a cloud for a given cloud cover category and the probability of occurrence of that category, summed over all categories,

$$P = \sum_{k=0}^8 \frac{k}{8} \frac{n_k}{N}. \quad (6.5)$$

Here the index k is the cloud-cover in oktas, n_k is the number of observations per category and N is the total number of observations.

Gaffen and Elliot (1993) analysed 3 years of radiosoundings. The radiosoundings were globally distributed. The amount of data per cloud category was low. Our data set includes only four German stations but 10 years of radiosoundings will lead to more robust statistics and enables the estimation of monthly means. In figure 6.1 the mean TPW per cloud class and the number of cases included are shown both for seasonal and monthly mean. An annual cycle of TPW related to the air temperature is observed (for one station the annual temperature cycle is shown in figure 6.4). Each month shows an increase in TPW with increasing cloudiness. Broken cloudiness is the most frequently observed cloud class for the German area. The number of clear-sky observations is low. An annual cycle in clear-sky observations is found for Lindenberg with significantly more clear cases in winter. In summer the number of overcast observations is lower than for the rest of the year.

The bias indices defined in equation 6.2 - 6.4 are shown in figure 6.2. B_0 is always larger than B_7 which is expected because the extreme situations are used. For B_0 only clear-sky

values are used to define the relation whereas for B_7 moist atmospheres with up to seven oktas observed cloud cover are used. Similar to Gaffen and Elliot (1993) the general behaviour of the bias indices is: $B_0 > B_4 > B_7$. The probability of a radiosonde to pass a cloud is shown in figure 6.2 as well. For Lindenberg the probability is larger than 70 % and decreases slightly towards summer. In appendix D results for Schleswig, Stuttgart, and Essen are shown.

Results for all stations are summarised in the following tables. In table 6.1, 6.2, and 6.3 the monthly mean TPW and the number of cases comprising the mean for the four stations. The results for the seasonal means are given in table D.1 in the appendix D. The bias indices and the probability of the radiosonde to pass a cloud are given in table 6.4 on a monthly basis and in table D.2 (see appendix D) on a seasonal basis. In summer the number of clear-cases are rare. For all stations the probability for the radiosonde to pass a cloud is larger than 50 %. For the station Schleswig the number of clear-sky observations in summer is very low. Schleswig is close to both North and Baltic sea. In summer a land-sea-circulation occurs due to the stronger warming over land than over the seas and convective clouds are formed. The observation time, 12 UTC is located around the main convective time.

For the station Stuttgart the number of clear-sky observations is small as well. Here local circulations and radiative heating of the surface with increases the unstability of the atmosphere are responsible for frequently occurring convective clouds at noon time.

The German stations are all located in the mid-latitudes. Thus, we do not expect strong latitudinal differences in TPW like Gaffen and Elliot (1993) report on their northern hemisphere stations. The all-sky annual mean TPW is about 16 kg/m^2 , the regional variability is less than 1 kg/m^2 . The annual cycle of the all-sky mean is defined by the minimum value in February of about 9.5 kg/m^2 and the maximum value in July of 25 kg/m^2 . The increase of TPW due to the presence of clouds is observed for all stations. Overcast scenes contain nearly three times the clear-sky TPW.

	Jan		Feb		Mar		Apr		May		Jun	
	TPW	N	TPW	N	TPW	N	TPW	N	TPW	N	TPW	N
Lindenberg												
CLR	5.90	25	3.80	22	7.18	21	9.04	14	12.97*	10	18.08*	8
SCT	7.09	37	6.70	32	7.87	40	11.31	66	15.48	74	21.49	60
BKN	9.24	97	9.06	114	9.14	126	12.12	128	17.28	159	20.52	167
OVC	11.18	134	11.90	107	13.00	111	15.14	88	22.33	62	24.81	64
ALL	9.57	293	9.47	275	10.27	298	12.69	296	17.73	305	21.57	299
	Jul		Aug		Sep		Oct		Nov		Dec	
CLR	16.87*	7	19.06*	9	16.12	16	12.77	14	8.91	12	5.03	20
SCT	23.77	71	22.86	81	17.83	56	14.82	52	9.77	49	6.85	35
BKN	24.88	178	24.18	175	20.31	156	15.52	154	12.93	112	9.17	97
OVC	29.61	50	31.16	42	24.27	68	21.15	84	14.51	110	11.72	132
ALL	25.21	306	24.64	307	20.53	296	16.83	304	12.83	283	9.78	284

Table 6.1: Monthly mean TPW in kg/m^2 in the cloud classes (*CLR* = clear, *SCT* = scattered (1-4 octas), *BKN* = broken (5-7 octas), *OVC* = overcast) and without regards to cloudiness (*ALL*) for Lindenberg. *N* gives the number of observations comprising the mean. Mean values based on less than 10 values are marked (*).

	Jan		Feb		Mar		Apr		May		Jun	
	TPW	N	TPW	N	TPW	N	TPW	N	TPW	N	TPW	N
Schleswig												
CLR	5.09*	3	4.07*	10	6.32	12	8.37*	10	17.85*	10	—*	0
SCT	6.49	49	5.10	35	7.20	56	9.33	59	12.83	77	18.32	60
BKN	8.85	119	8.57	130	8.70	132	11.64	153	15.56	169	18.91	185
OVC	12.32	107	13.29	91	13.21	97	16.32	67	22.68	47	23.60	52
ALL	9.73	278	9.56	266	9.80	297	12.14	289	16.04	303	19.61	297
	Jul		Aug		Sep		Oct		Nov		Dec	
CLR	28.58*	3	22.33*	5	22.36*	3	14.59*	3	6.37*	4	4.77*	6
SCT	20.84	74	20.99	88	16.79	62	11.28	59	8.90	48	6.20	55
BKN	22.58	193	22.87	183	18.65	169	15.42	176	11.23	132	9.44	107
OVC	27.43	37	29.63	30	25.98	65	21.17	65	15.89	96	13.53	107
ALL	22.81	307	22.99	306	19.90	299	15.84	303	12.36	280	10.28	275
	Jan		Feb		Mar		Apr		May		Jun	
	TPW	N	TPW	N	TPW	N	TPW	N	TPW	N	TPW	N
Essen												
CLR	5.16	12	4.70	17	6.04	18	8.91*	9	14.37*	5	27.38*	2
SCT	7.32	47	7.25	45	8.33	50	9.60	67	14.84	63	18.41	70
BKN	10.01	118	9.51	95	10.46	132	11.98	153	16.17	141	19.90	158
OVC	13.25	93	13.32	81	15.73	74	17.44	61	20.66	66	25.78	38
ALL	10.44	270	10.04	238	11.20	274	12.48	290	16.91	275	20.40	268
	Jul		Aug		Sep		Oct		Nov		Dec	
CLR	20.78*	9	22.79	12	15.31*	5	11.68*	10	8.85*	6	4.28	16
SCT	23.18	91	21.76	91	17.25	59	12.50	52	9.90	48	7.22	38
BKN	23.88	137	23.54	125	19.57	139	16.53	128	12.71	101	10.59	99
OVC	27.68	43	30.10	42	24.52	62	20.73	75	16.38	106	14.12	116
ALL	24.13	280	23.93	270	20.13	265	16.75	265	13.59	261	11.26	269

Table 6.2: Monthly mean TPW in kg/m^2 in the cloud classes (CLR = clear, SCT = scattered (1-4 octas), BKN = broken (5-7 octas), OVC = overcast) and without regards to cloudiness (ALL) for Schleswig and Essen. N gives the number of observations comprising the mean. Mean values based on less than 10 values are marked (*).

	Jan		Feb		Mar		Apr		May		Jun	
	TPW	N	TPW	N	TPW	N	TPW	N	TPW	N	TPW	N
Stuttgart												
CLR	5.12	16	4.97*	8	7.68	11	4.41*	1	16.03*	1	17.09*	2
SCT	7.61	37	7.46	37	7.73	41	10.47	44	15.07	56	20.63	64
BKN	9.88	86	9.41	94	10.85	77	12.79	98	16.85	99	20.98	97
OVC	10.80	98	11.77	69	13.43	77	14.51	47	21.75	58	23.92	37
ALL	9.58	237	9.68	208	11.02	206	12.64	190	17.71	214	21.37	200
	Jul		Aug		Sep		Oct		Nov		Dec	
CLR	18.71*	2	17.13*	2	16.77*	3	10.45*	6	8.33*	6	6.31*	4
SCT	22.15	85	22.61	78	16.01	52	12.79	46	9.56	24	8.17	27
BKN	26.04	91	24.10	92	19.55	97	16.13	108	12.57	87	10.83	96
OVC	27.89	36	29.70	25	25.01	49	20.42	59	14.75	93	12.41	86
ALL	24.74	214	24.15	197	19.93	201	16.43	219	13.07	210	11.04	213

Table 6.3: Monthly mean TPW in kg/m^2 in the cloud classes (*CLR* = clear, *SCT* = scattered (1-4 octas), *BKN* = broken (5-7 octas), *OVC* = overcast) and without regards to cloudiness (*ALL*) for Stuttgart. *N* gives the number of observations comprising the mean. Mean values based on less than 10 values are marked (*).

	Jan	Feb	Mar	Apr	May	Jun	Jul	Aug	Sep	Oct	Nov	Dec
Lindenberg												
CLR/OVC	0.53	0.32	0.55	0.60	0.58	0.73*	0.57*	0.61*	0.66	0.60	0.61	0.43
SCT/OVC	0.63	0.56	0.61	0.75	0.69	0.87	0.80	0.73	0.73	0.70	0.67	0.58
BKN/OVC	0.83	0.76	0.70	0.80	0.77	0.83	0.84	0.78	0.84	0.73	0.89	0.78
B0	0.38	0.60	0.30	0.29	0.27	0.16	0.33*	0.23*	0.21*	0.24	0.31	0.49
B4	0.31	0.42	0.26	0.14	0.14	0.02	0.08	0.09	0.15	0.15	0.25	0.37
B7	0.14	0.16	0.16	0.08	0.07	0.04	0.03	0.04	0.05	0.10	0.08	0.17
P	0.75	0.76	0.74	0.70	0.68	0.72	0.68	0.65	0.70	0.73	0.76	0.77
Schleswig												
CLR/OVC	0.41*	0.31	0.48	0.51	0.79	–	1.04*	0.75*	0.86*	0.69*	0.40*	0.35*
SCT/OVC	0.53	0.38	0.55	0.57	0.57	0.78	0.76	0.71	0.65	0.53	0.56	0.46
BKN/OVC	0.72	0.65	0.66	0.71	0.69	0.80	0.82	0.77	0.72	0.73	0.71	0.70
B0	0.48*	0.57	0.36	0.31	-0.11	–	-0.25*	0.03*	-0.12*	0.08*	0.48*	0.54*
B4	0.34	0.49	0.28	0.24	0.16	0.07	0.07	0.08	0.14	0.28	0.30	0.41
B7	0.17	0.20	0.17	0.10	0.08	0.04	0.03	0.03	0.08	0.09	0.15	0.20
P	0.79	0.77	0.73	0.72	0.68	0.73	0.69	0.66	0.74	0.76	0.78	0.76
Essen												
CLR/OVC	0.39	0.35	0.38	0.51*	0.70*	1.06*	0.75*	0.76	0.62*	0.56	0.54*	0.30
SCT/OVC	0.55	0.54	0.53	0.55	0.72	0.71	0.84	0.72	0.70	0.60	0.60	0.51
BKN/OVC	0.76	0.71	0.67	0.69	0.78	0.77	0.86	0.78	0.80	0.80	0.78	0.75
B0	0.51	0.53	0.46	0.29*	0.15*	-0.34*	0.14*	0.05	0.24*	0.30	0.35*	0.62
B4	0.34	0.35	0.31	0.24	0.12	0.09	0.05	0.09	0.15	0.26	0.28	0.44
B7	0.14	0.17	0.15	0.11	0.07	0.04	0.03	0.05	0.07	0.09	0.14	0.19
P	0.75	0.72	0.72	0.71	0.72	0.69	0.65	0.64	0.72	0.72	0.78	0.78
Stuttgart												
CLR/OVC	0.47	0.42*	0.57	0.30*	0.74*	0.71*	0.67*	0.58*	0.67*	0.51*	0.56*	0.51*
SCT/OVC	0.70	0.63	0.58	0.72	0.69	0.86	0.79	0.76	0.64	0.63	0.65	0.66
BKN/OVC	0.91	0.80	0.81	0.88	0.77	0.88	0.93	0.81	0.78	0.79	0.85	0.87
B0	0.47	0.49*	0.30	0.65*	0.09*	0.20*	0.24*	0.29*	0.16*	0.36*	0.36*	0.43*
B4	0.28	0.27	0.30	0.18	0.15	0.04	0.11	0.07	0.19	0.24	0.29	0.28
B7	0.09	0.11	0.13	0.05	0.08	0.03	0.03	0.03	0.08	0.09	0.10	0.08
P	0.76	0.75	0.73	0.73	0.72	0.67	0.63	0.62	0.70	0.72	0.81	0.81

Table 6.4: Monthly ratios of the mean TPW in a cloud class (CLR = clear, SCT = scattered (1-4 octas), BKN = broken (5-7 octas)) towards the overcast mean TPW (OVC) for each station. The bias indices (dimensionless) and the probability of a sounding passing through a cloud as defined in the equations 6.2 to 6.5 are given. A dash is given when no clear-sky observations are done, ratios and indices based on less than 10 observations are marked (*).

6.1.1 TPW under all-sky and clear-sky conditions

In this section the difference in mean TPW for clear- and all-sky atmospheres for different temporal scales is investigated. The final task is to obtain a conversion scheme to relate the clear-sky TPW climatologies derived from satellite measurements to the all-sky TPW. It is decisive to assess the variability at different time scales. For this purpose the radiosondes and synoptical data at four German weather stations are used. Observations are deployed for the years 1994 to 2003. Geographically, the stations are close to each other. Observations are not independent neither on temporal nor on spatial scale. Thus, the degree of dependence is examined.

The degree of dependence is examined using the correlation of the various time series. In Figure 6.3 station-to-station correlations are shown relative to Lindenberg for the stations Schleswig, Stuttgart, and Essen. The largest correlation is found for the surface temperature, surface pressure and the height of the 500 hPa level. The TPW shows lower correlations ranging from 0.65 to 0.76. In table 6.5 the correlation coefficients for the combinations of two stations are given. For geographically close stations the correlations are larger, as we are looking at nearly the same airmass. Since Stuttgart is located at a higher surface level, a bias in the near surface parameters is observed. In the following the station Lindenberg because it shows the highest occurrence of clear-sky observations at noon time, compared to the other stations.

	Lindenberg				Essen				Stuttgart			
	SLP	H500	Temp	TPW	SLP	H500	Temp	TPW	SLP	H500	Temp	TPW
Schleswig	0.94	0.92	0.94	0.76	0.89	0.90	0.89	0.75	0.75	0.84	0.89	0.65
	Schleswig				Essen				Stuttgart			
	SLP	H500	Temp	TPW	SLP	H500	Temp	TPW	SLP	H500	Temp	TPW
Lindenberg	0.94	0.92	0.94	0.76	0.88	0.89	0.89	0.71	0.82	0.91	0.91	0.73
	Schleswig				Lindenberg				Stuttgart			
	SLP	H500	Temp	TPW	SLP	H500	Temp	TPW	SLP	H500	Temp	TPW
Essen	0.89	0.90	0.89	0.75	0.88	0.89	0.89	0.71	0.93	0.93	0.91	0.79
	Schleswig				Lindenberg				Essen			
	SLP	H500	Temp	TPW	SLP	H500	Temp	TPW	SLP	H500	Temp	TPW
Stuttgart	0.75	0.84	0.89	0.65	0.82	0.91	0.92	0.73	0.93	0.93	0.91	0.79

Table 6.5: Correlation coefficients of the DWD stations Schleswig, Lindenberg, Essen, and Stuttgart for the TPW given, the surface temperature, the surface pressure and the height of the 500 hPa level.

6.1.2 TPW statistics for Lindenberg

Because of the similarity of the German stations here the behaviour of the TPW in all-sky situations 10-years of radiosonde profiles derived at the DWD station Lindenberg has been investigated. Time series of surface pressure, surface temperature, the height of the 500 hPa level, cloud cover and the TPW are shown in figure 6.4. The annual cycle in

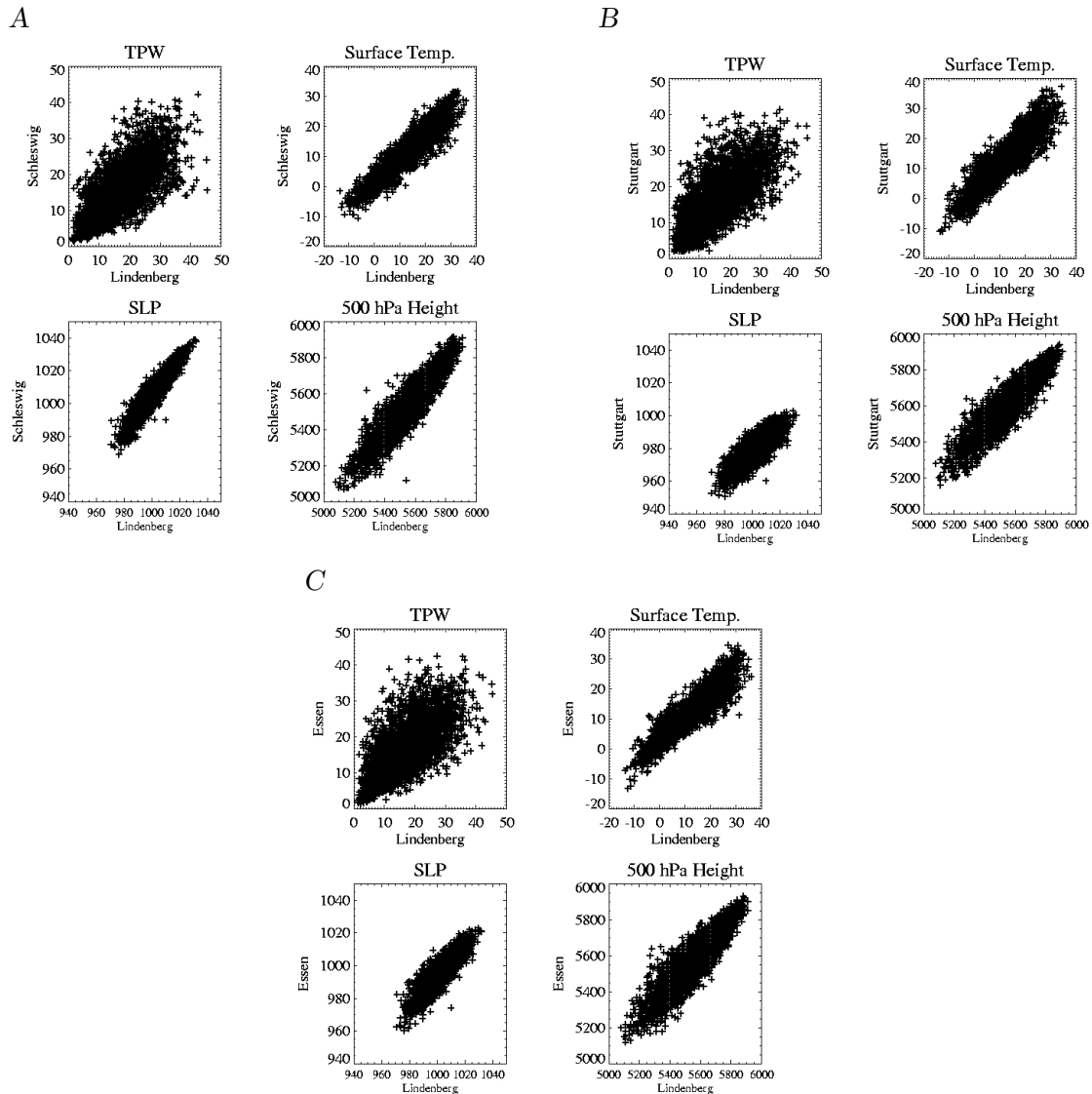


Figure 6.3: Correlation of TPW given in kg m^{-2} (upper left), the surface temperature in $^{\circ}\text{C}$ (upper right), the surface pressure in hPa (lower left) and the height of the 500 hPa level in m for the DWD stations Schleswig (y-axis) (A), Stuttgart (B), and Essen (C) and Lindenberg (x-axis). The correlation coefficients are given in table 6.5

the TPW is clearly visible as it follows strongly the temperature. From the ten years the mean annual cycle is calculated for all quantities (see figure 6.5). The variability of surface pressure and the height of the 500 hPa level is larger in winter than in summer. The weather is dominated by the passage of low pressure systems with their frontal systems related to different airmasses coinciding with higher (lower) 500-hPa level in warm (cold)

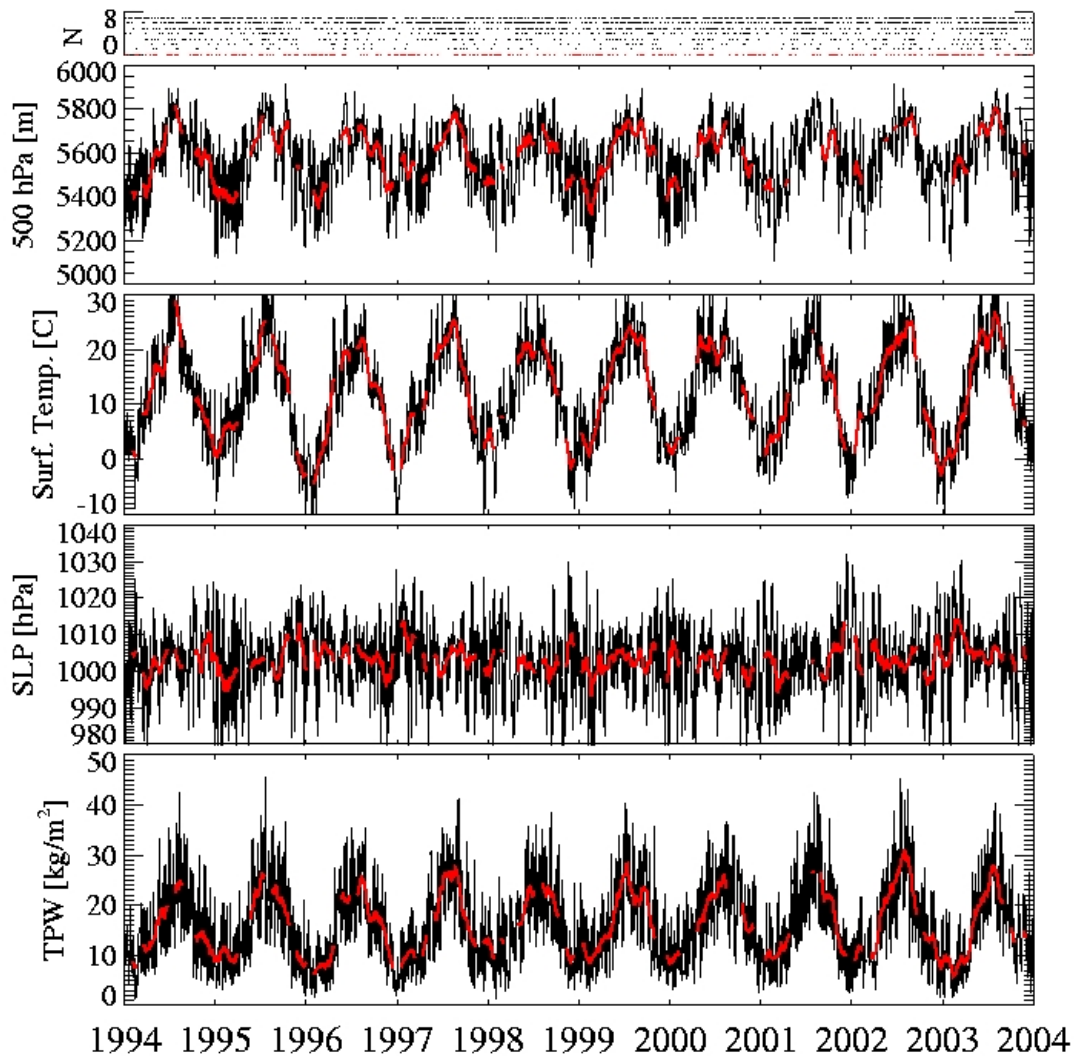


Figure 6.4: 10-years time series of the noon radiosonde ascents performed at the DWD station Lindenberg. The various panels top to bottom show: the cloud cover in octas (red accentuate the clear-sky), the height of the 500 hPa level, the temperature at the surface, surface pressure and the total precipitable water derived from the humidity profile. The red line denotes the 30-days running mean.

air. In contrast the variability in the TPW is larger in summer due to the strong coupling to temperature, since warm air can contain more humidity than cold air. The daily anomalies are shown in figure 6.6. The anomalies of the sea level pressure and 500 hPa level have the same direction, e.g. a positive sea level pressure anomalies corresponds to higher temperatures and to a positive 500 hPa level height anomalies. The variability in the TPW follows this structure, but the deviation from the mean is small compared to the temperature anomalies.

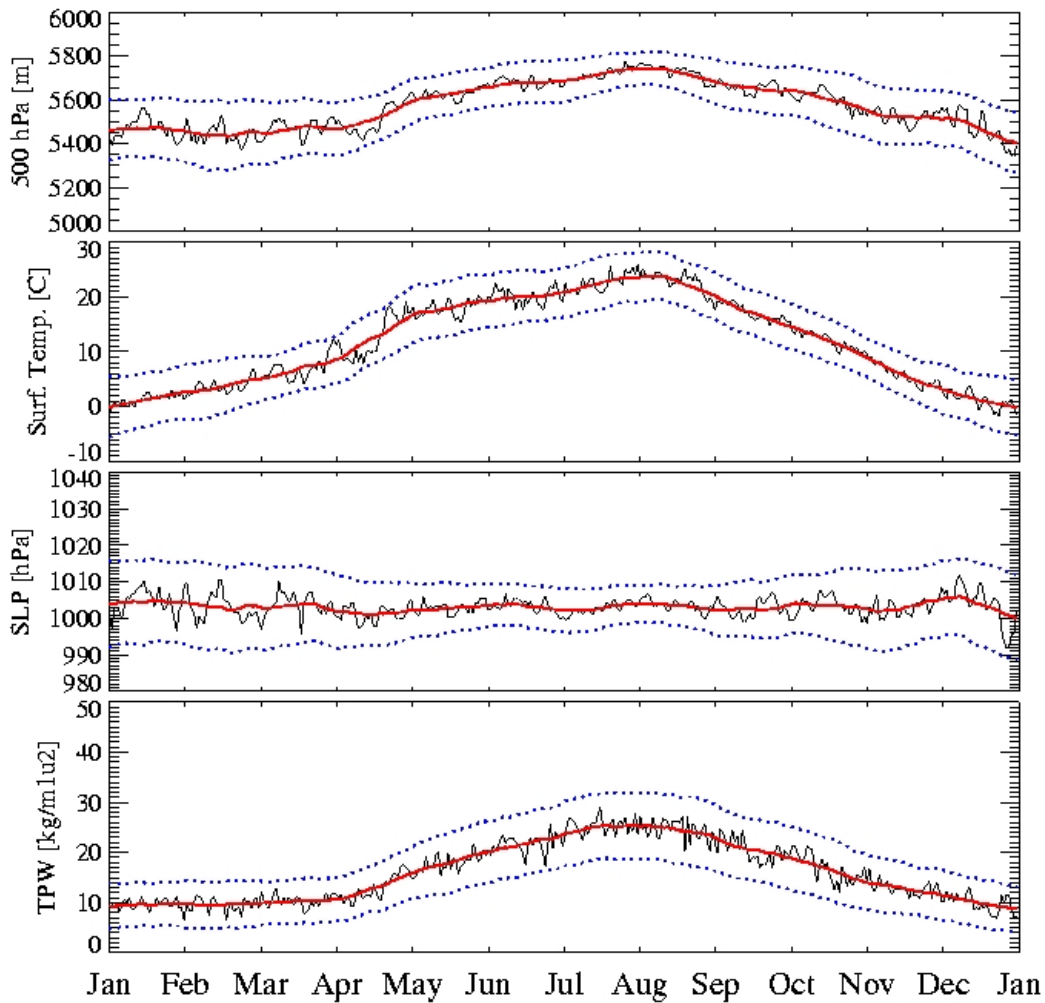


Figure 6.5: Annual cycles derived from the 10-years time series from Lindenberg in figure 6.4, from top to bottom: the height of the 500 hPa level, the temperature at the surface, surface pressure and the total precipitable water derived from the humidity profile. The red line denotes the running mean. The blue dotted lines give the standard deviation of the quantity.

On a seasonal basis the distributions of the surface pressure for Lindenberg shows a tendency towards high pressure in cases of clear skies. However the number of clear-sky observations at noon are limited (figure 6.7). The distinction in clear and cloudy ascents is achieved by the observed cloud cover in the synoptical data. For cloud cover below 5 octas the ascent is set to clear and above 5 octas the minimum dewpoint depression below 500 hPa has to be below 0.5 K for a cloud effected ascent. A more detailed description is given in chapter 6.2.

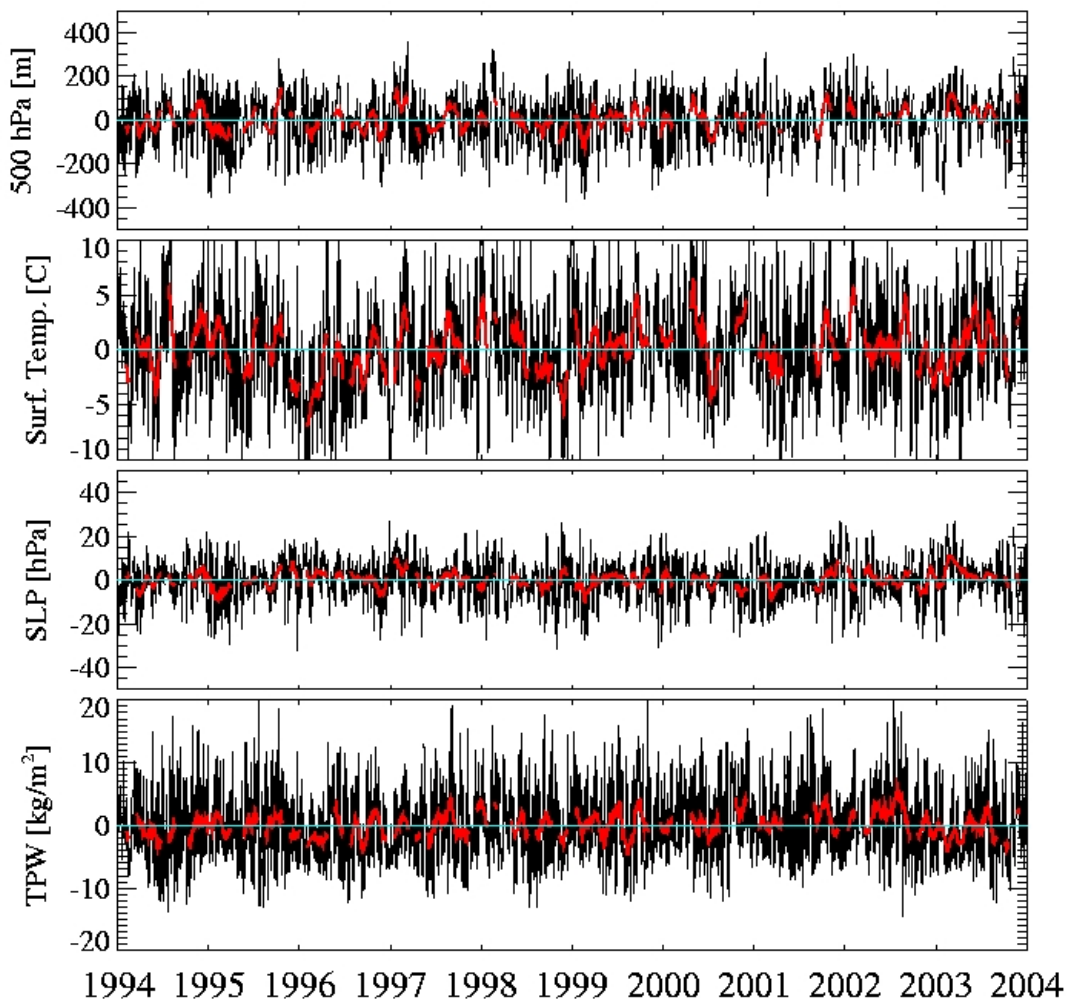
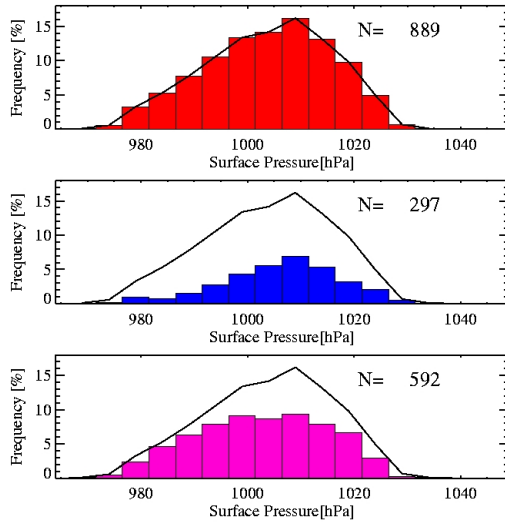


Figure 6.6: The anomalies of the time series shown in figure 6.4. The various panels top to bottom show: the height of the 500 hPa level, the temperature at the surface, surface pressure and the total precipitable water derived from the humidity profile. The red line denotes the 30-days running mean.

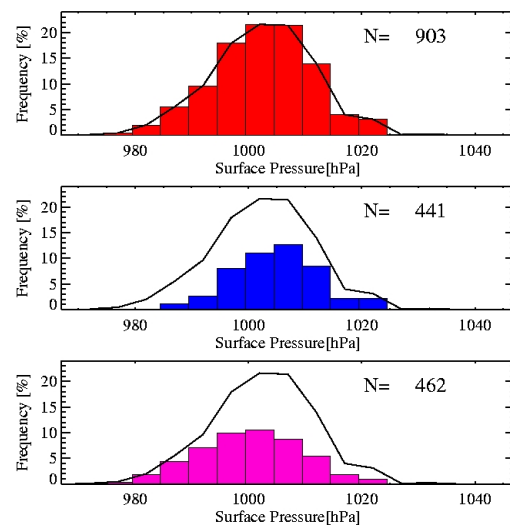
In summer the 2 m temperature shows a tendency of clear-sky days to higher temperature whereas for other seasons no preference is obvious. In winter for the station Schleswig (not shown) colder temperatures are connected to clear-sky cases. In spring and autumn, no preferred situations can be detected (figures 6.8).

The 2 m relative humidity shows no preferred value in clear-sky situations. Neverthe-

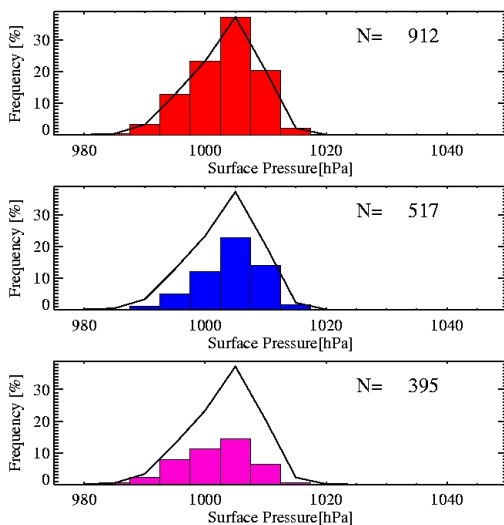
A: Winter



B: Spring



C: Summer



D: Autumn

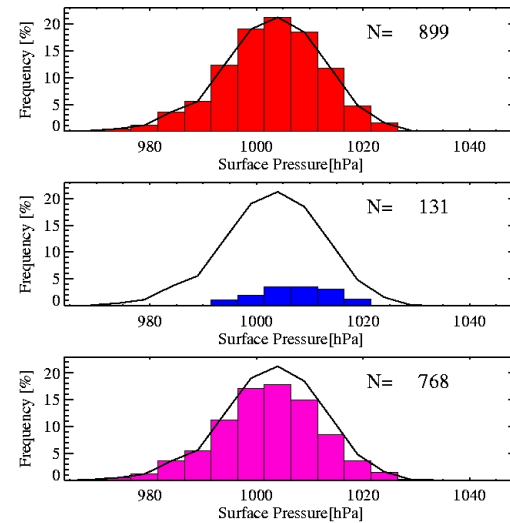


Figure 6.7: Distribution of the surface pressure for winter (A), spring (B), summer (C), and autumn (D) derived from noon radiosonde ascents at Lindenberg. Upper panel shows all cases, middle panel cloud free cases and the lowest cloudy-sky cases. The solid line gives the distribution over all cases.

less, the observed humidities are at the lower end of the distribution. The shape of the distribution is changing throughout the year. In spring the distribution is broad with a slight maximum for relative humidities smaller than 60 %. In summer the maximum of the distribution is shifted towards larger relative humidities, in winter to values just below 100 % (figure 6.9).

The shape of the TPW distribution follows the temperature, which is to be expected due

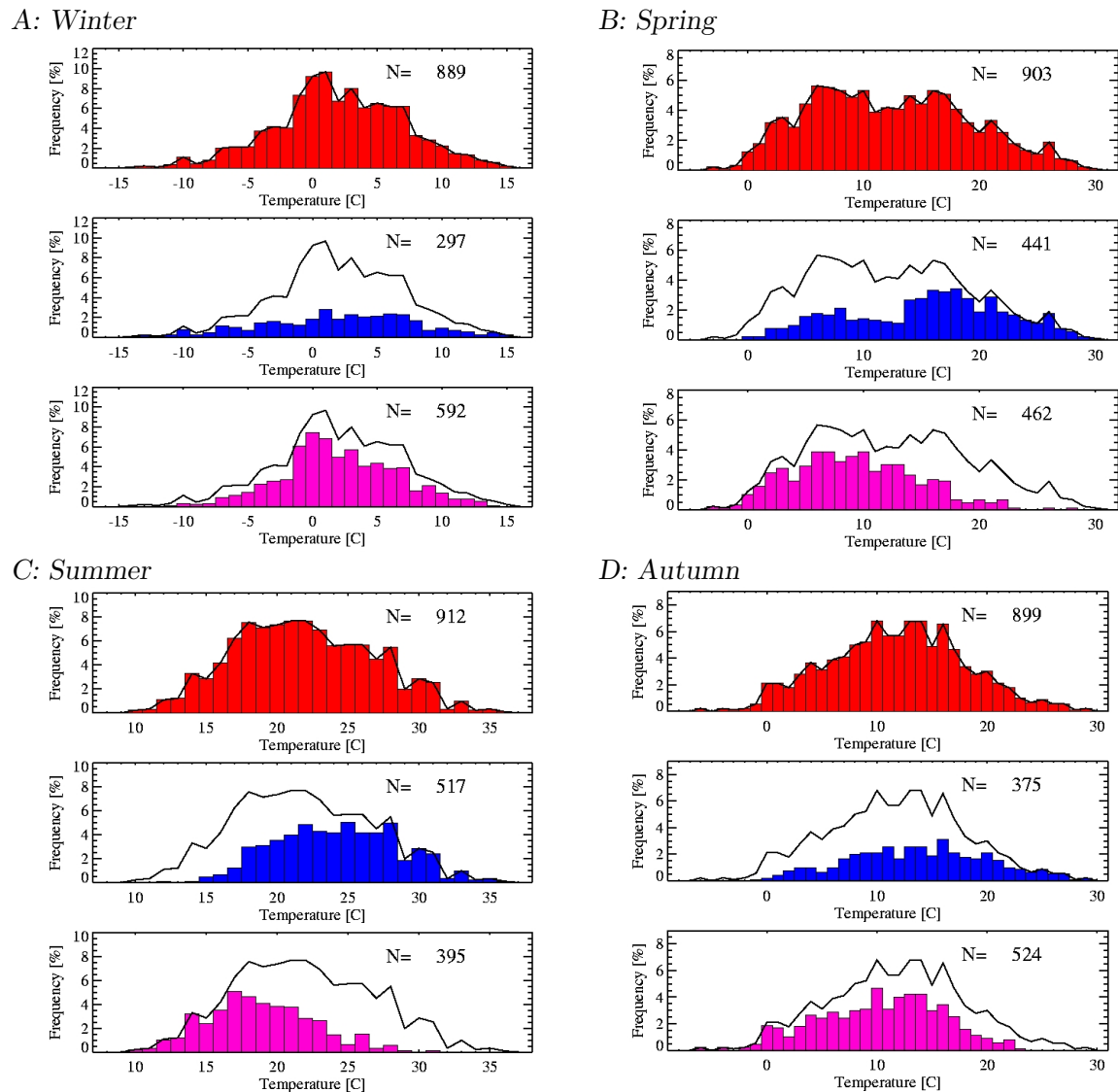
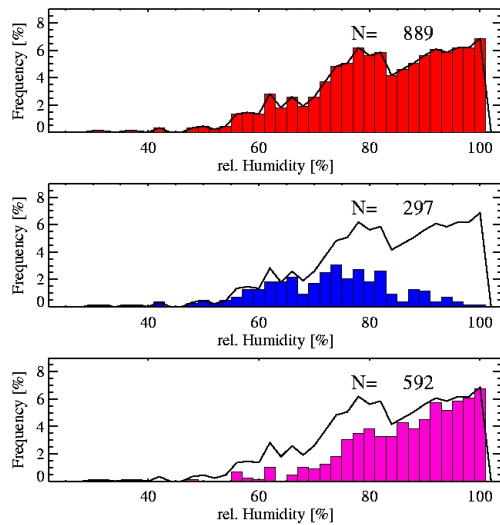


Figure 6.8: Distribution of the 2-m temperature for winter (A), spring (B), summer (C), and autumn (D)) derived from noon radiosonde ascents at Lindenberg. Upper panel shows all cases, middle panel cloud free cases and lowest the cloudy-sky cases. The solid line gives the distribution over all cases.

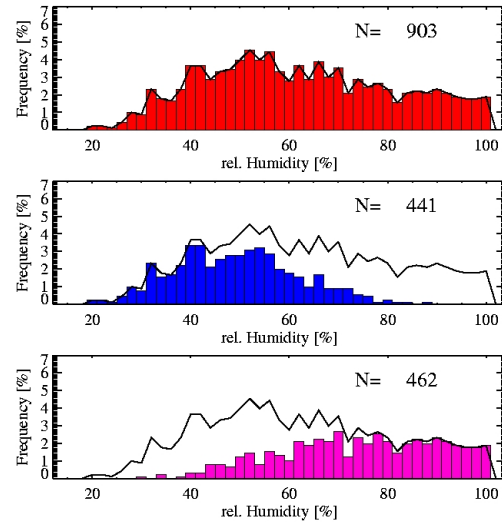
to the ability of air to contain different amounts of water vapour depending on temperature (figures 6.10). Table 6.6 and table 6.7 are summarising the main parameters describing the seasonal distributions.

It follows that the frequency distributions of the meteorological parameters, sea level pressure, relative humidity, temperature and TPW, mainly vary with season with the median

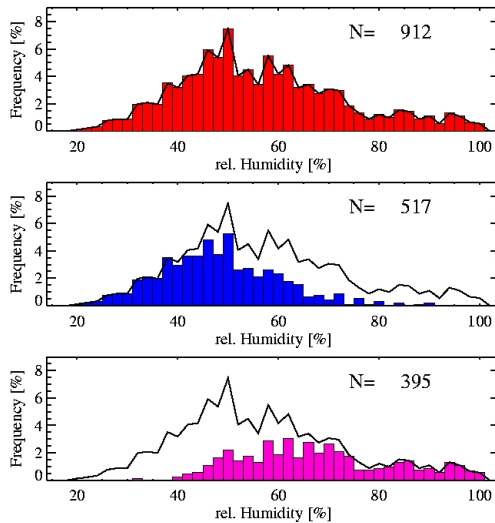
A: Winter



B: Spring



C: Summer



D: Autumn

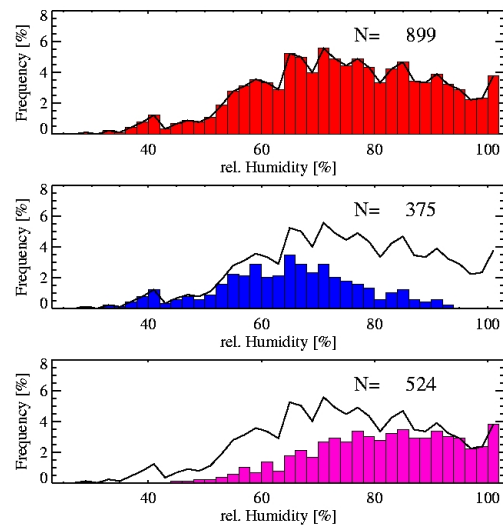


Figure 6.9: Distribution of the relative humidity for winter (A), spring (B), summer (C), and autumn (D) derived from noon radiosonde ascents at Lindenberg. Upper panel shows all cases, middle panel cloud free cases and the lowest cloudy-sky cases. The solid line gives the distribution over all cases.

of the distribution depending on the existence of clouds. This encourages us to investigate the excess water vapour in cloudy scenes on climatological scales.

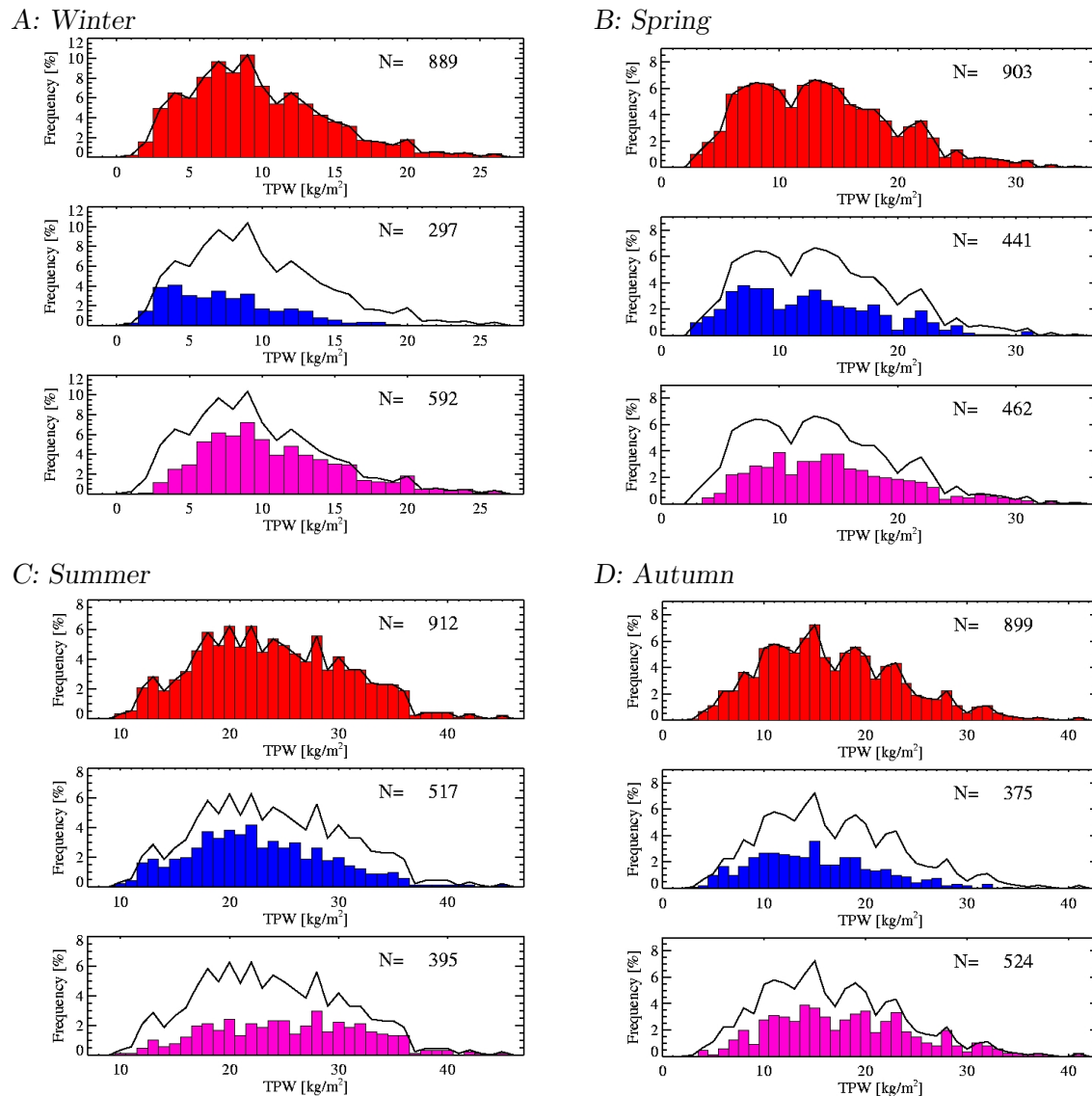


Figure 6.10: Distribution of the total precipitable water for winter (A), spring (B), summer (C), and autumn (D) derived from noon radiosonde ascents at Lindenberg. Upper panel shows all cases, middle panel cloud free cases and the lowest cloudy-sky cases. The solid line gives the distribution over all cases.

Season	Case	N	Median	Mean	Variance	Skewness	Kurtosis
TPW							
winter	total	889	8.918	9.667	22.025	0.749	0.354
	clear	297	6.871	7.386	14.592	0.687	-0.091
	cloud	592	9.802	10.812	21.856	0.749	0.230
spring	total	903	12.828	13.588	36.963	0.595	-0.080
	clear	441	11.847	12.584	35.516	0.567	-0.352
	cloud	462	13.931	14.547	36.536	0.651	0.079
summer	total	912	23.379	23.824	44.969	0.286	-0.441
	clear	517	21.888	22.627	39.881	0.391	-0.164
	cloud	395	25.066	25.390	47.409	0.102	-0.643
autumn	total	899	15.793	16.749	46.018	0.546	-0.013
	clear	375	14.507	15.007	37.036	0.494	-0.198
	cloud	524	17.414	17.995	48.797	0.500	-0.118
Temperature							
winter	total	889	1.800	1.969	24.648	-0.138	-0.015
	clear	297	2.400	1.873	34.753	-0.270	-0.375
	cloud	592	1.700	2.017	19.622	0.053	-0.092
spring	total	903	11.800	12.233	46.979	0.226	-0.716
	clear	441	16.300	15.420	45.814	-0.218	-0.757
	cloud	462	8.950	9.192	29.209	0.336	-0.223
summer	total	912	21.600	21.833	23.729	0.189	-0.498
	clear	517	24.100	24.180	18.336	0.072	-0.529
	cloud	395	18.500	18.761	14.162	0.313	-0.106
autumn	total	899	11.900	11.708	38.357	0.005	-0.284
	clear	375	13.900	13.771	41.258	-0.023	-0.537
	cloud	524	10.600	10.231	31.118	-0.239	-0.450
Surface pressure							
winter	total	889	1004.800	1003.857	140.877	-0.245	-0.591
	clear	297	1007.100	1006.255	116.239	-0.435	0.005
	cloud	592	1002.900	1002.654	149.114	-0.125	-0.767
spring	total	903	1003.200	1002.514	79.370	-0.126	-0.018
	clear	441	1005.300	1004.985	62.218	0.049	0.340
	cloud	462	1000.300	1000.156	84.504	-0.053	-0.379
summer	total	912	1003.900	1003.200	31.363	-0.479	0.050
	clear	517	1005.100	1004.381	26.035	-0.541	0.495
	cloud	395	1002.300	1001.655	34.196	-0.306	-0.339
autumn	total	899	1003.400	1002.954	86.150	-0.273	0.073
	clear	375	1005.000	1004.708	74.872	-0.390	0.084
	cloud	524	1001.700	1001.700	90.597	-0.157	0.107

Table 6.6: The statistical parameters of the TPW, temperature and surface pressure distribution for all-sky, cloudy and clear atmospheres.

Season	Case	N	Median	Mean	Variance	Skewness	Kurtosis
relative Humidity							
winter	total	889	83.488	82.300	165.363	-0.707	0.242
	clear	297	73.399	72.339	142.679	-0.462	0.542
	cloud	592	89.482	87.297	102.128	-0.859	0.414
spring	total	903	60.328	62.112	365.837	0.199	-0.877
	clear	441	48.784	49.165	155.820	0.245	-0.346
	cloud	462	75.253	74.471	253.654	-0.288	-0.770
summer	total	912	54.437	56.718	268.941	0.540	-0.116
	clear	517	47.638	48.263	140.845	0.499	0.472
	cloud	395	66.198	67.784	220.826	0.364	-0.684
autumn	total	899	74.412	74.474	228.537	-0.245	-0.498
	clear	375	64.969	64.574	160.995	-0.190	-0.235
	cloud	524	82.381	81.559	156.714	-0.380	-0.598
Dewpoint							
winter	total	889	4.000	4.450	6.987	0.879	0.461
	clear	297	3.900	4.174	5.636	1.030	1.108
	cloud	592	4.000	4.588	7.618	0.792	0.179
spring	total	903	4.000	4.176	4.796	0.953	1.065
	clear	441	3.600	3.744	3.392	0.906	1.464
	cloud	462	4.100	4.589	5.797	0.803	0.422
summer	total	912	3.500	3.715	3.846	0.924	1.400
	clear	517	3.100	3.363	2.774	0.812	0.435
	cloud	395	4.100	4.174	4.885	0.763	1.127
autumn	total	899	3.600	3.876	4.426	0.812	0.457
	clear	375	3.600	3.802	3.663	0.698	0.363
	cloud	524	3.600	3.929	4.974	0.835	0.347

Table 6.7: The statistical parameters of the relative humidity and dewpoint temperature distribution for all-sky, cloudy and clear atmospheres.

6.2 The excess water vapour

The focus in this study is to examine and quantify the difference in all-sky to clear-sky water vapour. The concept of the excess water vapour as ratio all-sky to clear-sky TPW is used. Further the absolute water vapour difference depending on the clear-sky TPW is derived. This section shows the excess water vapour for German station. Section concentrates on the distinction of cloud and clear cases from radiosonde. In section 6.2.2 the excess water vapour is retrieved. A sensitivity study was performed to proof the stability of the derived excess water vapour functions, see 6.2.3. The layered water vapour is examined in section 6.4.

6.2.1 Distinction of clear and cloudy cases from radiosoundings

When discussing the differences of all-sky to clear-sky total precipitable water the question arises, how reliable the identification of clear sky cases is. From ground-based observations the cloud cover is given in the synoptical data set. But for partly cloudy situations, the radiosonde does not necessarily pass a cloud. As an example, for 4 octas the sky is half cloud covered, the likelihood of the radiosonde to find a whole exceeds 50% because the observer may overestimate the cloud cover near the horizon due to his view on the cloud vertical extend. Additional to the cloud cover from synoptical observations a parameter from the ascent is chosen for the distinction of clear sky cases.

The basic criteria from cloud detection is taken from the synoptical data. If no cloud cover information is in the synoptical data set, then the minimum of the dewpoint difference profile below 500 hPa is compared to a threshold. A cloud is present when the dewpoint depression is below 0.5 K. The *no criteria* case in the following figures calculates the clear-sky TPW for the ascents where either the cloud cover value in the synoptical information is 0, or the dewpoint depression exceeds 0.5 K. The dewpoint depression is chosen that small because the number of cases is too low for a sufficient statistic.

The dewpoint depression threshold is chosen for various reasons. From the distribution of minimum dewpoint depression below the 500 hPa level of radiosonde ascent in overcast cases varies between 0.1 and 0.4 depending on the season (see figure 6.11 and 6.12). Including 7 octas in the overcast case the median lies between 0.1 and 0.5. For station Schleswig the median of the dewpoint depression distributions lies between 0.4 and 1.0. Furthermore the dependency of the monthly mean for clear-sky TPW on different dewpoint depression thresholds is shown in figure 6.13. Varying the dewpoint depression in the range of 0.3 to 0.6 does not effect the mean value significantly. Therefore, the threshold is set to 0.5. This choice ensures a sufficient number of monthly mean values for all stations.

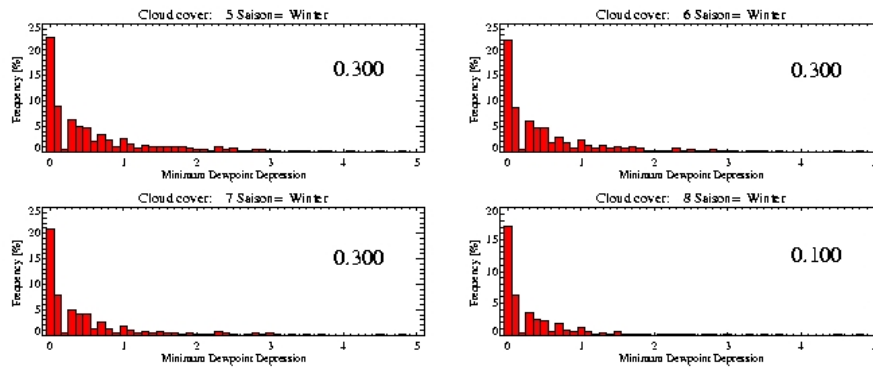
For broken cloudiness the radiosonde does not necessarily pass a cloud. Thus, the larger absolute humidities inside the clouds are missed. The monthly mean clear-sky TPW is

underestimated. Therefore a cloud cover of 5 octas is set as a threshold to define clear-sky ascents with an additional dewpoint depression threshold. For this study, the minimum value of the dewpoint depression up to 500 hPa is used as a identifier for cloud levels as described before. When the minimum is below 0.5 K it is assumed that a cloud has been passed by the radiosonde. Figure 6.13 shows the retrieved time series for the clear-sky TPW and the cloudy-sky TPW for varying dewpoint depression thresholds using a detection scheme for cases where the cloud cover exceed 5 octas (and 7 octas in figure 6.14). The monthly mean clear-sky TPW is larger in all cases compared to the no criteria case. Low clear-sky TPW values are corrected by larger TPW in cases with broken cloudiness. The same effect is observed for cloudy-sky cases. Here, the monthly means are larger in the two-threshold scheme compared to the no-criteria case. Cases of broken cloudiness, where the radiosonde does not pass a cloud are excluded from the mean value.

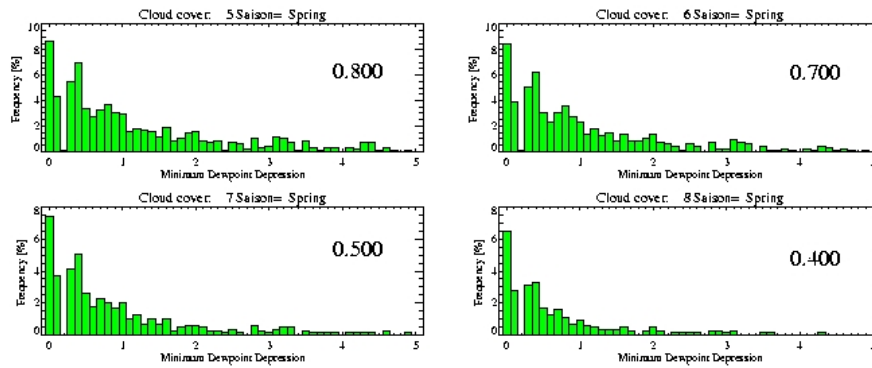
Figure 6.15 compares the mean values over different dewpoint depression thresholds for one starting cloud cover. The largest mean TPW values are derived for cloud cover thresholds of 7 and 8 octas. Here only extreme cases are detected as clouds. For cloud covers below 5 octas the number of month where no clear-sky or cloudy-sky TPW is derived is as high as for the *no criteria* case. From this point and from comparing the different TPW timeseries the cloud cover threshold is set to 5 octas. Furthermore, the threshold in dewpoint depression is set to 0.5 K.

Mean values of TPW are calculated when more than 3 ascents per month fulfill the criteria. For different stations the number of data points are the same. Differences mainly occur in the number of clear-sky days per monthly mean.

A: Winter



B: Spring



C: Summer

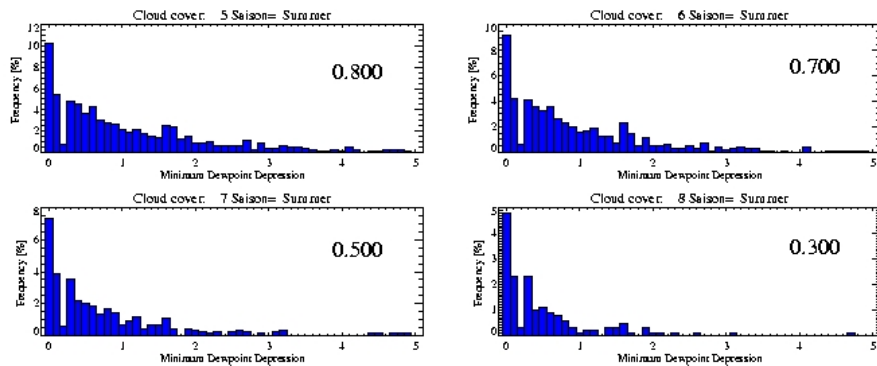


Figure 6.11: Distribution of the minimum dewpoint difference of radiosonde ascents for winter (A), spring (B), summer (C) derived from noon radiosonde ascents at Lindenberg. Separations are made by the observed cloud cover from the synoptical data set. Upper left (right) is for greater or equal 5 (6) octas, lower left for greater and equal 7 octas, and lower right for overcast cases. The numbers give the median of the distribution.

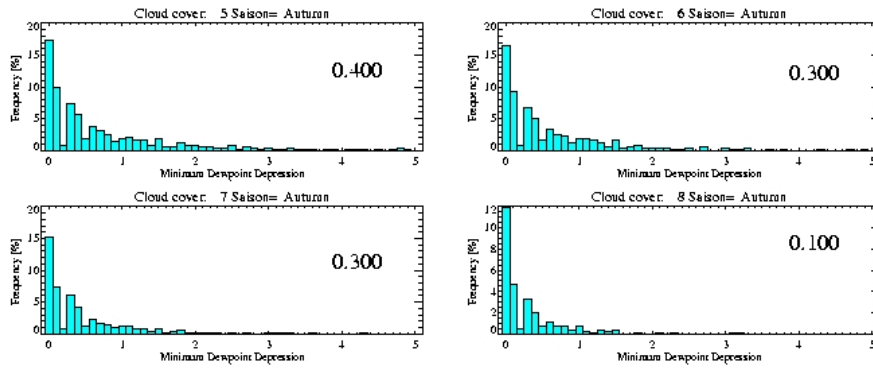
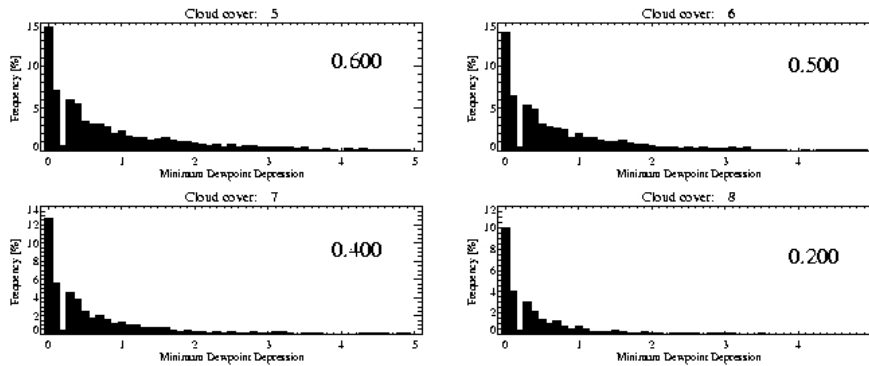
D: Autumn*E: All*

Figure 6.12: Distribution of the minimum dewpoint difference of radiosonde ascents for autumn (D), and for the whole data set derived from noon radiosonde ascents at Lindenberg. Separations are made by the observed cloud cover from the synoptical data set. Upper left (right) is for greater or equal 5 (6) octas, lower left for greater and equal 7 octas, and lower right for overcast cases. The numbers give the median of the distribution.

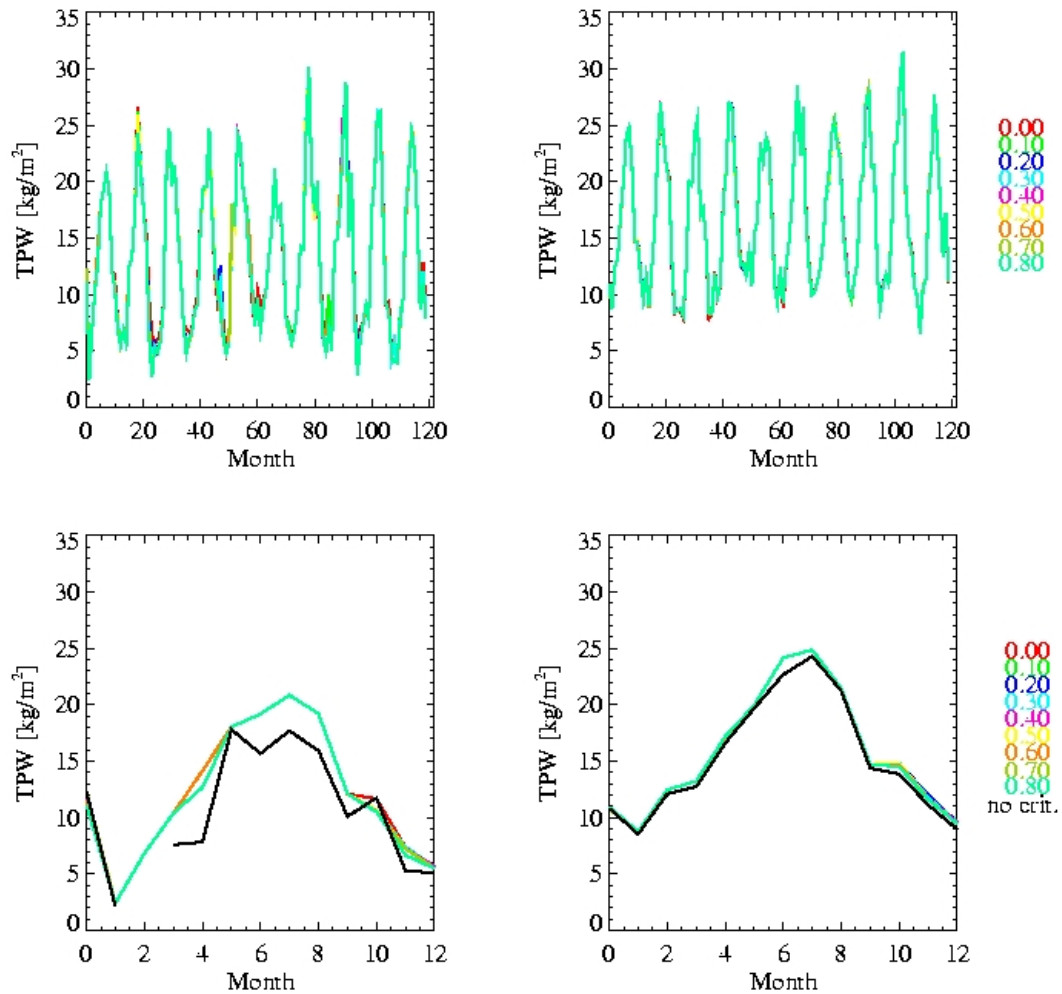


Figure 6.13: Monthly mean clear-sky (left) and cloudy-sky (right) TPW depending on the distinction criteria. Upper row for 10 years and lower panel for the first 13 months. Colours denote the dewpoint depression threshold. The dewpoint depression is used for cloud covers above 5 octas. No criteria denotes clear sky as zero octas and if no cloud flag is given (dummy value) then the minimum dewpoint depression below 500 hPa is higher than 0.5 K.

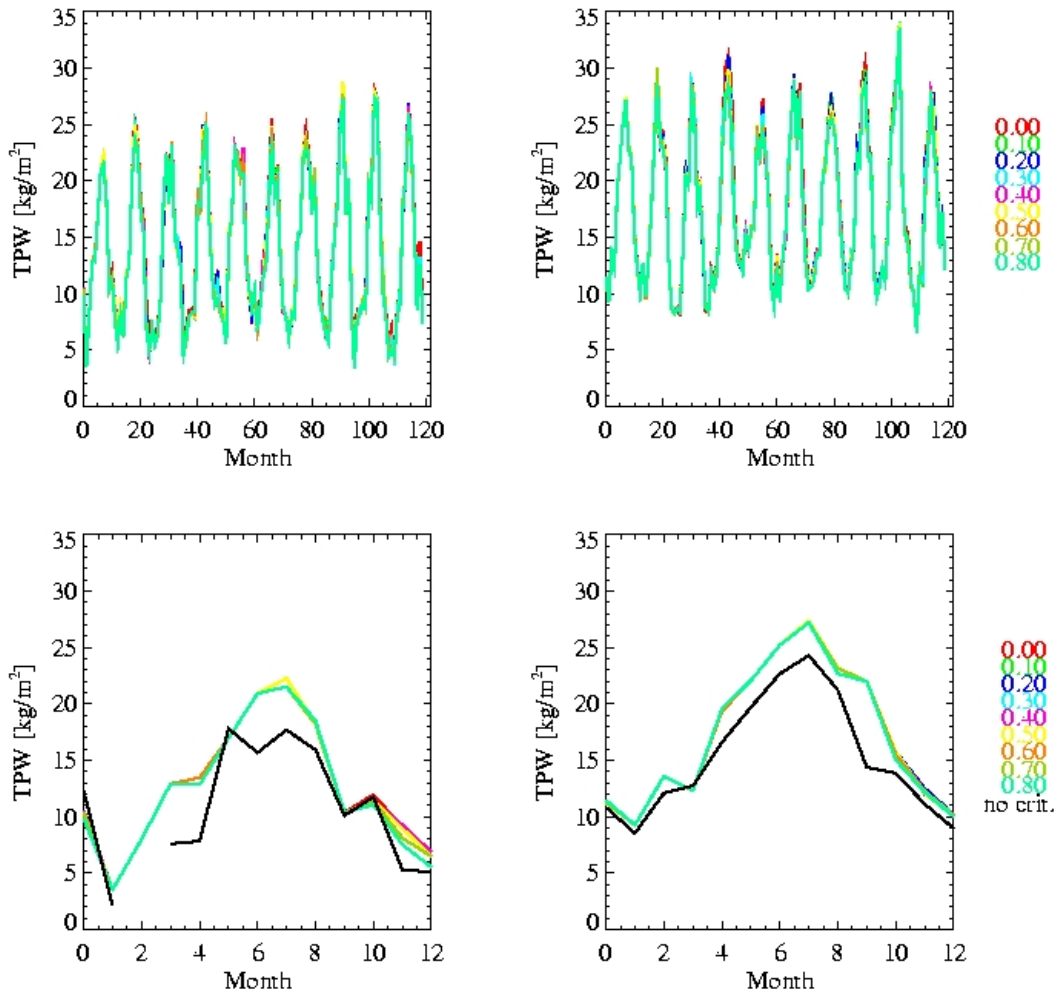


Figure 6.14: Monthly mean clear-sky (left) and cloudy-sky (right) TPW depending on the distinction criteria. Upper row for 10 years and lower panel for the first 13 months. Colours denote the dewpoint depression threshold. The dewpoint depression is used for cloud covers above 7 octas. No criteria denotes clear sky as zero octas and if no cloud flag is given (dummy value) then the minimum dewpoint depression below 500 hPa is higher than 0.5 K.

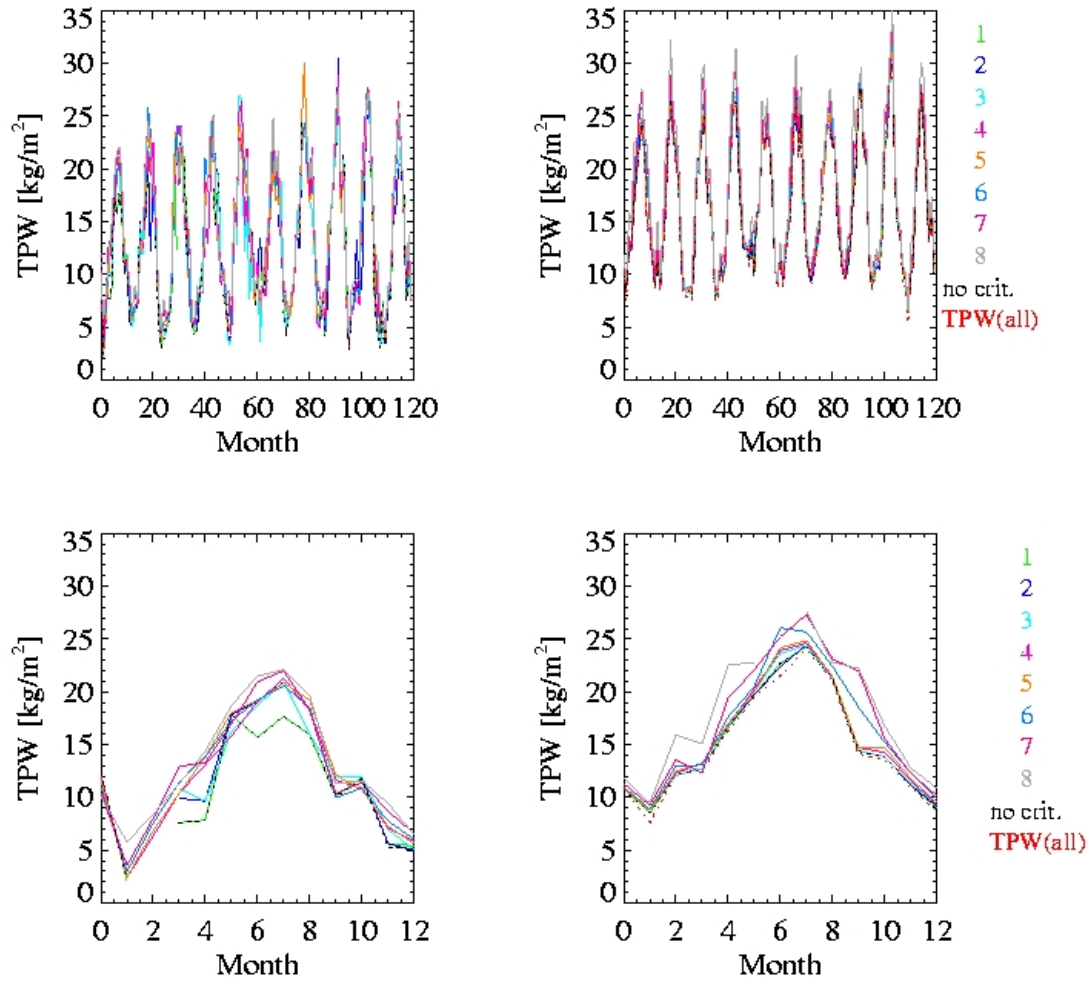


Figure 6.15: Monthly mean clear-sky (left) and cloudy-sky (right) TPW depending on the starting cloud cover for the dewpoint depression threshold. The monthly means represent the mean over the different dewpoint depression thresholds given in figure 6.13. Upper row for 10 years and lower panel for the first 13 months. Colours denote cloud cover as given by the observer used as a threshold for the dewpoint depression criteria. No criteria denotes clear sky as zero octas and if no cloud flag is given (dummy value) then the minimum dewpoint depression below 500 hPa is higher than 0.5 K. In red the all-sky TPW is given; this value is not affected by the thresholding.

6.2.2 All-sky vs clear-sky TPW

The TPW frequency distribution shown in the previous section are significantly different for clear and cloudy conditions. For monthly and seasonal means of clear-sky and all-sky cases the behaviour of TPW is examined. Figure 6.16 shows the ratio of clear-sky monthly mean TPW to cloudy-sky TPW and to all-sky TPW for station Lindenberg. Only a few

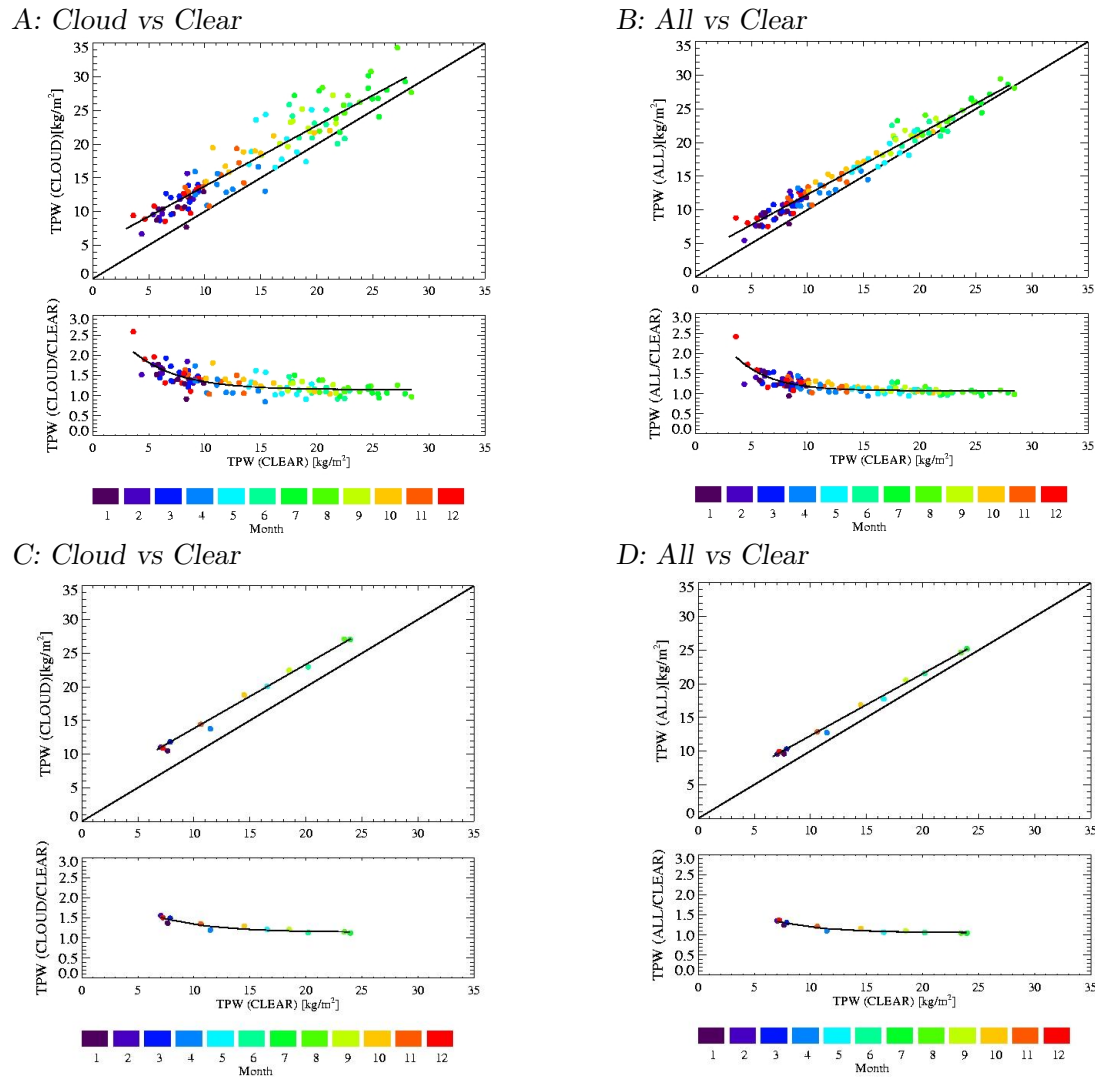


Figure 6.16: Monthly means for the 10 years of Lindenberg radiosonde measurements. A: The monthly mean TPW in clear-sky cases versus the cloudy-sky cases (upper panel) and versus the ratio (cloud/clear) (lower panel). B: The clear-sky TPW is shown in relation to the all-sky TPW. C: The yearly mean TPW for every month in clear-sky cases versus the cloudy-sky cases (upper panel) and versus the ratio (cloud/clear) (lower panel). D: The clear-sky TPW is shown in relation to the all-sky TPW. Colors denote the month.

months show a large TPW in clear-sky compared to cloudy or all-sky situations. Here, the clear-sky cases are related to warm air masses at high pressure conditions, whereas the cloudy-sky cases are related to cold air advection corresponding to frontal systems in low pressure systems. Colder air contains less water vapour. Therefore, the ratio of the all-sky TPW to the clear-sky TPW denoted as the excess water vapour is slightly below 1 for these cases. One example for a month with larger clear-sky TPW than all-sky TPW

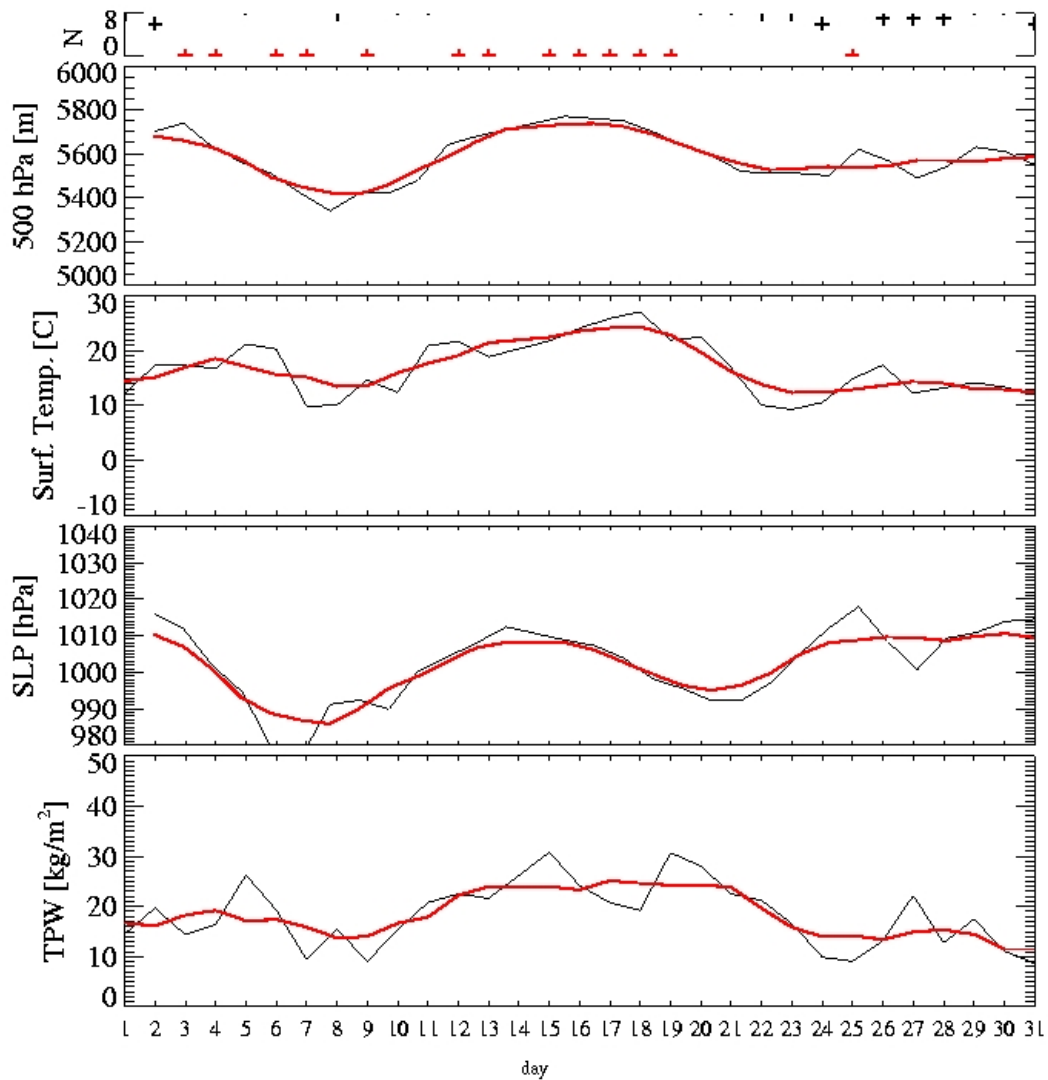
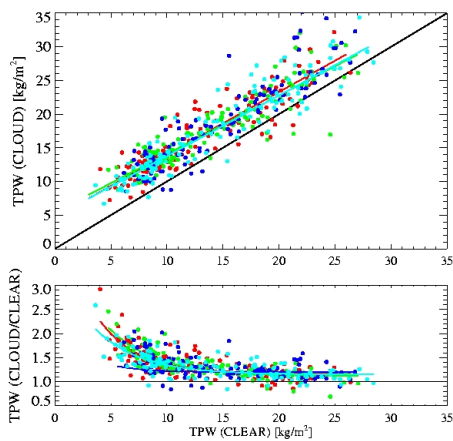


Figure 6.17: Time series of noon radiosonde ascents performed at DWD station Lindenberg in May 1997. The various panels top to bottom show: the cloud cover in octas (red accentuate the clear-sky), height of the 500 hPa level, temperature at the surface, surface pressure and total precipitable water derived from the humidity profile. The red line denotes the 5-day running mean.

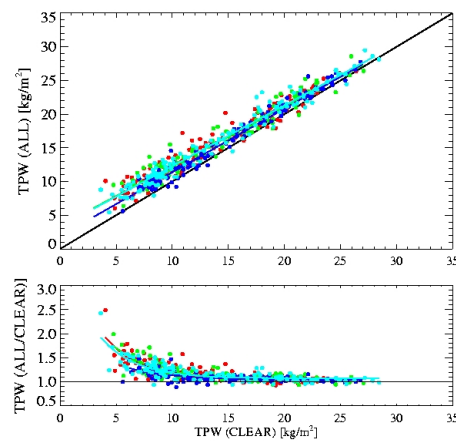
is May 1997 shown in figure 6.17.

During winter the clear- to cloudy-sky difference in TPW is larger than during summer. The difference between air masses related to frontal systems passing the station are stronger in winter compared to summer. However, for a derivation of a correction the number of clear-sky cases per month is too low.

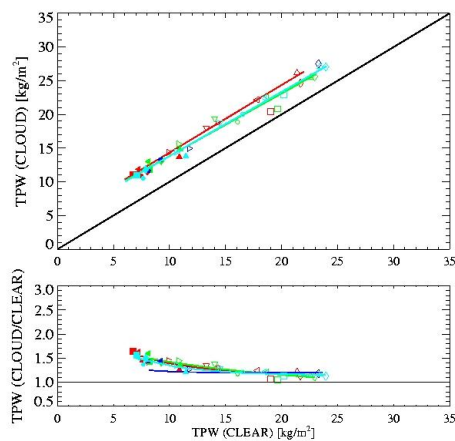
A: Cloud vs Clear



B: All vs Clear



C: Cloud vs Clear



D: All vs Clear

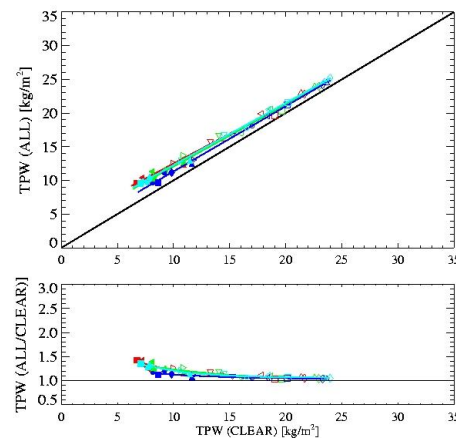


Figure 6.18: Monthly means for 10 years of radiosonde measurements for Schleswig (red), Essen (green), Stuttgart (blue), and Lindenberg (cyan). **A**: Monthly mean TPW in clear-sky cases versus cloudy-sky cases (upper panel) and versus the ratio (cloud/clear) (lower panel). **B**: Clear-sky TPW is shown in relation to all-sky TPW. **C**: Yearly mean TPW for every month in clear-sky cases versus cloudy-sky cases (upper panel) and versus the ratio (cloud/clear) (lower panel). **D**: Clear-sky TPW is shown in relation to all-sky TPW. Symbols in **C** and **D** represent the month.

Looking at yearly means for each month (figure 6.16, lower panel) the remaining 12 points give the annual cycle of the TPW. Large excess water vapour values which appear for small clear-sky TPWs are reduced.

The relation of clear TPW to cloudy- or all-sky TPW can be parameterised employing a linear fit in TPW clear, whereas the relation to the ratio all-to-clear is rather exponential and can be fitted as :

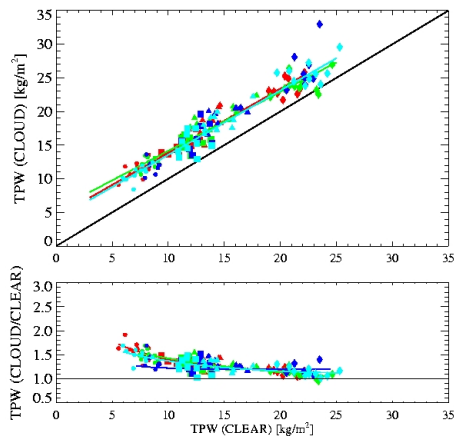
$$Y = a_0 a_1^x + a_2 . \quad (6.6)$$

The parameters a_0 to a_2 are given in table 6.8.

For different stations the regression functions look slightly different (figure 6.18). This is caused by different behaviours of the ratio in the low clear-sky TPW cases. Which in turn is mainly affected by the different number of clear-sky observations per month. For the regression parameters see table 6.8.

The relation of TPW (Cloud) or TPW (ALL) to TPW (Clear) shows good correspondence. For large clear-sky TPW all stations show an excess water vapour of 1.1, whereas differences occur for low clear-sky TPW. From a clear-sky TPW of 10 kg/m^2 up to larger TPW the ratio decreases from 1.3 to 1.1. This decrease does not depend on the averaging time. Yearly means for all months, seasonal means (see figure 6.19) and monthly means show the same behaviour. For lower clear-sky TPW the increase in excess water vapour is stronger, but the number of cases is limited and the spread of monthly means is broader. Except for Stuttgart all stations show an increase of excess water vapour for low clear-sky

A: Cloud vs Clear



B: All vs Clear

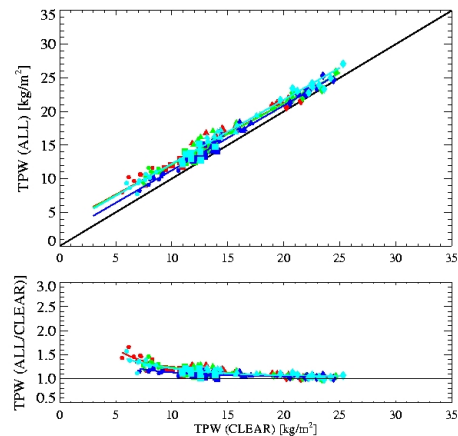


Figure 6.19: Seasonal means for 10 years of radiosonde measurements for Schleswig (red), Essen (green), Stuttgart (blue), and Lindenberg (cyan). **A:** Seasonal mean TPW in clear-sky cases versus cloudy-sky cases (upper panel) and versus the ratio (cloud/clear) (lower panel). **B:** Clear-sky TPW is shown in relation to all-sky TPW. Symbols represent the season; winter (circle), spring (square), summer (diamond), and autumn (triangle).

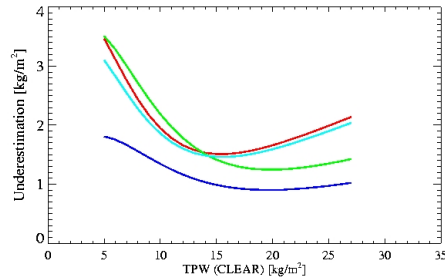


Figure 6.20: Underestimation retrieved for four German stations. In color: Schleswig (red), Essen (green), Stuttgart (blue), and Lindenberg (cyan)

TPW (from 10 to 5 kg/m²) up to 1.5. Stuttgart does not show TPWs less than 7 kg/m². Thus a parametrisation is not possible.

The derived regression function allows for a computation of the absolute underestimation in TPW for an observed clear-sky monthly mean. In Figure 6.20 the difference in all-to clear-sky TPW is shown versus the mean clear-sky TPW. For different stations the amount of water vapour for all-sky situations is about 2 kg/m² larger than for clear-sky case. For low mean clear-sky TPW the difference to all-sky cases is largest.

Case	N	Cor	RMS	Chi ²	A0	A 1	A 2
Lindenberg							
Year	12	0.96	0.03	0.012	1.4438	0.22813	1.057
Season	40	0.85	0.056	0.167	1.174	0.197	1.050
Month	120	0.79	0.09	1.696	2.741	0.323	1.08
Schleswig							
Year	12	0.93	0.039	0.026	2.034	0.262	1.064
Season	40	0.87	0.56	0.207	1.863	0.239	1.056
Month	120	0.78	0.099	2.12	3.318	0.337	1.079
Stuttgart							
Year	12	0.86	0.023	0.076	0.049	0.016	1.031
Season	40	0.75	0.037	0.068	0.662	0.189	1.034
Month	120	0.62	0.072	0.789	1.098	0.242	1.036
Essen							
Year	12	0.89	0.039	0.029	0.874	0.133	1.002
Season	40	0.83	0.05	0.15	0.828	0.123	0.991
Month	120	0.79	0.086	1.424	2.55	0.272	1.052
All Station							
Year	48	0.89	0.043	0.127	2.41	0.297	1.062
Season	160	0.81	0.058	0.771	1.604	0.24	1.052
Month	480	0.77	0.093	6.616	2.864	0.319	1.063

Table 6.8: Parameter describing the fitted function given in equation 6.6 for different stations and resulting of all available monthly means and the mean over all single months.

6.2.3 Sensitivity study

As we are dealing with mean values of classes, where the allocation is done via thresholds, the robustness of the retrieved parameterisation has to be investigated. The sensitivity of the regression on different parameters, like number of data points, number of ascents included in determining the mean value and the total data amount is investigated here. Figure 6.21 shows the variability of the regression resulting from randomly chosen data points. For Lindenberg data the number of cases is reduced to 25%, 50%, 75% and 90%. The different regressions look quite similar. Differences occur in the extreme end of the data range. Here the number of available points is low, and reducing the points affects the slope of the regression.

Figure 6.22 shows how the mean values of TPW are affected by reduced amounts of data. From the total noon ascents smaller samples are chosen for calculating the regression function. The resulting distribution of mean values and the regressions are shown. Obviously, the regression functions are stable. The introduced variability is small. Random samples containing 60% of Lindenberg data were also used to show the spread in the regression lines. The variability of the resulting functions is shown in figure 6.23. Differences in the slope of the linear regression clear- to all-sky TPW occur. For the relation of the excess water vapour the functions spread out for cases with low clear-sky TPW. Here the number of cases is small and the variability is high. Reducing the data amount results in different slopes for the regression.

The variability of the functional relation between the excess water vapour and the clear-sky TPW based on the cloud cover is shown in figure 6.24. The observed cloud cover for this cases is used as a threshold. The noise in the ratio is larger when including TPWs where small cloud covers are contained in the calculation of the clear-sky mean. But the

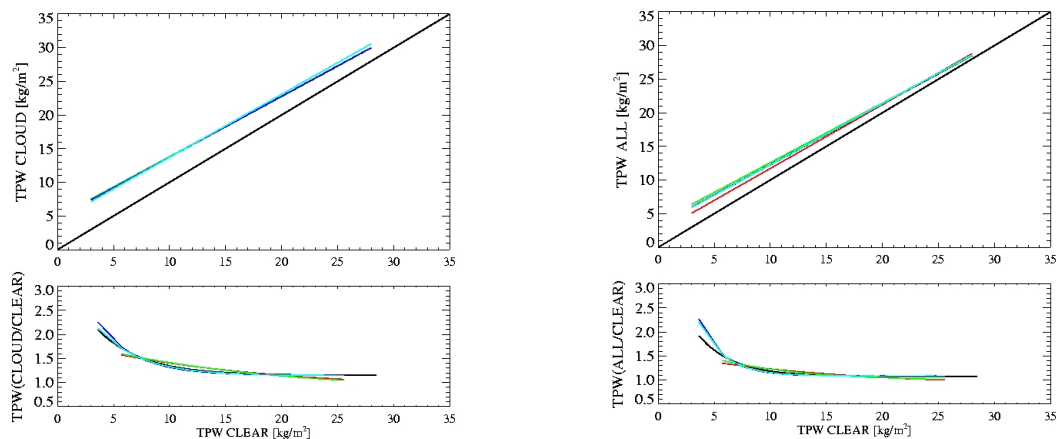


Figure 6.21: Variability of the functions introduced by different number of data points: 25% (red), 50% (green), 75% blue, 90% cyan and all data in black.

derived fitting functions are not influenced very much.

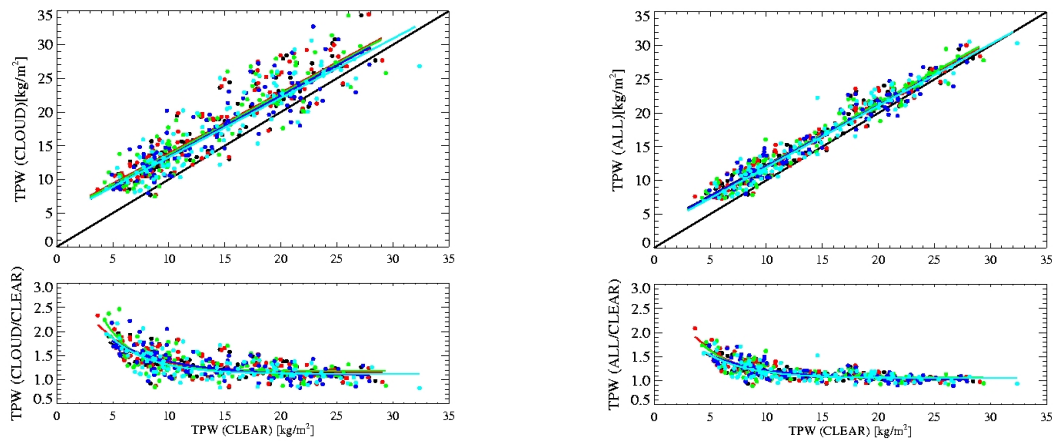


Figure 6.22: Dependency of clear-sky TPW to cloudy-sky TPW (left) or all-sky TPW (right) towards the amount of available data. All data used (black), 90% (red), 80% (green), 70% (blue), and 50% (cyan)

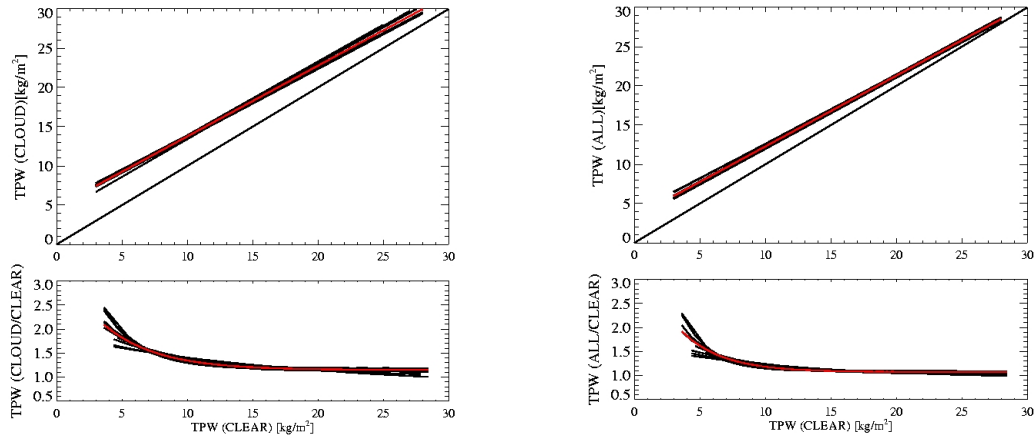


Figure 6.23: Randomly chosen 60% of daily data, in red the regression derived from all data is denoted.

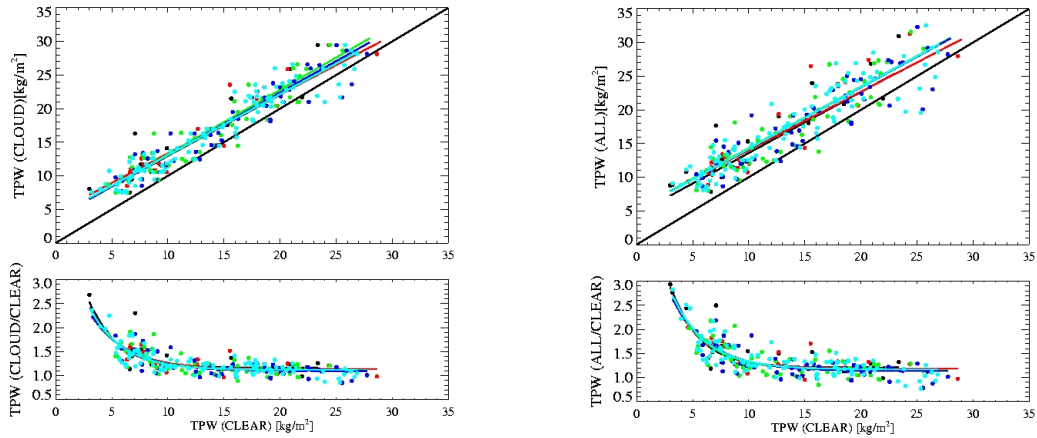


Figure 6.24: Dependency of clear-sky TPW to cloudy-sky TPW (left) or all-sky TPW (right) towards the definition of clear-sky. Given cloud cover from observer: cloud free (black), one octa (red), two octas (green), three octas (blue), and four octas (cyan)

Time	Pressure	Cor(Ratio, TPW(Clear))
All		-0.57
	High	-0.28
	Low	-0.55
Spring	Rest	-0.43
	High	-0.19
	Low	-0.62
Summer	Rest	-0.35
	High	-0.39
	Low	-0.55
Autumn	Rest	-0.58
	High	-0.4
	Low	-0.55
Winter	Rest	-0.34
	High	-0.44
	Low	-0.43
	Rest	-0.33

Table 6.9: Correlation coefficients for the relations given in figures 6.26 to 6.29.

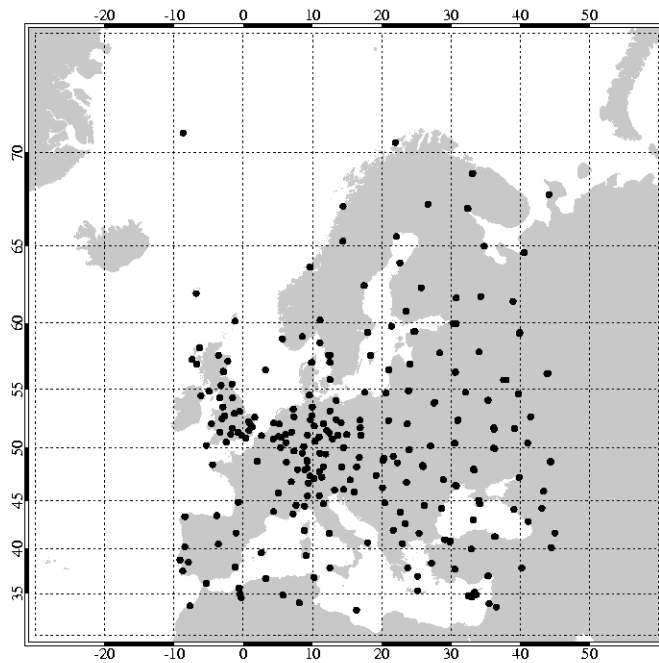


Figure 6.25: Geographical distribution of European stations. Atmospheric profiles are not continuously present for all stations in the years 1990 to 2000.

6.2.4 Excess water vapour for Europe

In chapter 6.2.2 TPW variability for a single station is investigated. The function describing the relation of the excess water vapour, expressed by the ratio of all to clear-sky TPW is analysed. The stability of the function is mainly driven by the number of cases included in the derivation of the regression. Regional variability does not influence the excess water vapour function much. The linear relationship of all-sky to clear-sky TPW shows a stronger dependency on the number of cases than on the different regions. In the following, investigation of excess water vapour is performed for several European stations shown in figure 6.25. These station data consist of radiosonde ascents. Unfortunately, no synoptical informations are included. Therefore, a threshold for the selection of cloudy cases is applied. The dewpoint depression is used to distinguish between clear- and cloudy-sky situations. As before it is assumed that the dewpoint depression falls below 0.5 K in cloud cases. The uncertainty of this assumption should not effect the validity of the results much. For the DWD data set over 80% of overcast radiosonde profiles show a dewpoint difference below 0.5 K. In section 6.2.1 the uncertainty in mean TPW introduced by thresholds for cloud detection is shown to be small. The influence of cloud distinction on excess water vapour is small as well, see figure 6.24. Here the amount of octas as threshold is varied.

For all station locations shown in figure 6.25 the monthly mean TPW relation is shown in figure 6.26. For large clear-sky TPW excess water vapour is low, whereas excess water vapour is high for small clear-sky TPWs. Here, the differences in air masses corresponding to clear- and cloudy-sky situations are larger as is the variability in excess water vapour. This variability is driven by regional and seasonal differences.

Largest differences in air masses most obviously occur in the vicinity of frontal systems. To investigate this in more detail, the data set is divided based on the pressure at the lowest level. Surface pressures below 1003 hPa are denoted as low pressure cases. Surface

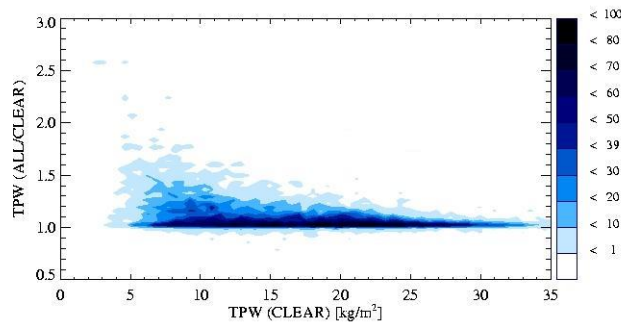


Figure 6.26: Relation of monthly mean TPW in all-sky depending on clear-sky TPW. Radiosonde profiles under investigation are European stations and four German stations. The upper panel shows the ratio (all to clear-sky TPW) versus clear-sky TPW. Colours denote the percentage of occurrence.

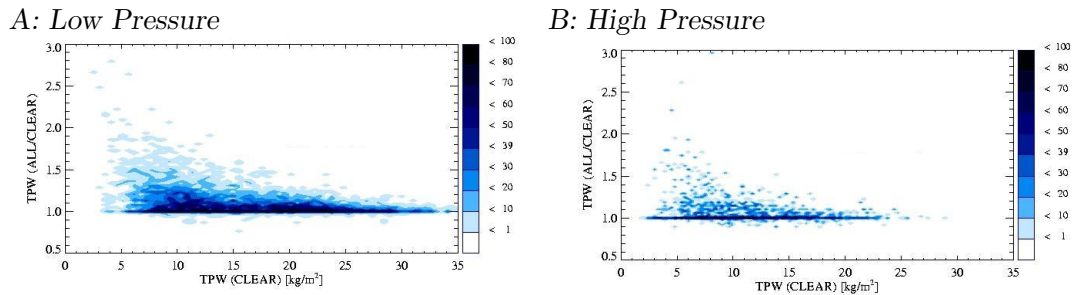


Figure 6.27: Same as figure 6.26 but the surface pressure is lower than 1003 hPa (left) and for surface pressures higher than 1023 hPa (right).

pressures above 1023 hPa are flagged as high pressure cases. Figure 6.27 shows a higher number of data points in the low case. A wider range of clear-sky TPW is observed. The dependency of excess water vapour on clear sky TPW is more prominent in the low pressure case.

Seasonal variability influences the variability in excess water vapour in cases with small clear-sky TPW. The observed mean clear-sky TPW is subject to annual variability. In summer (figure 6.29) larger values are reached than during the other seasons. The maximum excess water vapour is smaller during summer than in winter time (figure 6.28), which is related to the larger differences of the air masses related to frontal systems. The best regressions are derived for spring and autumn (figure 6.29). Correlations between

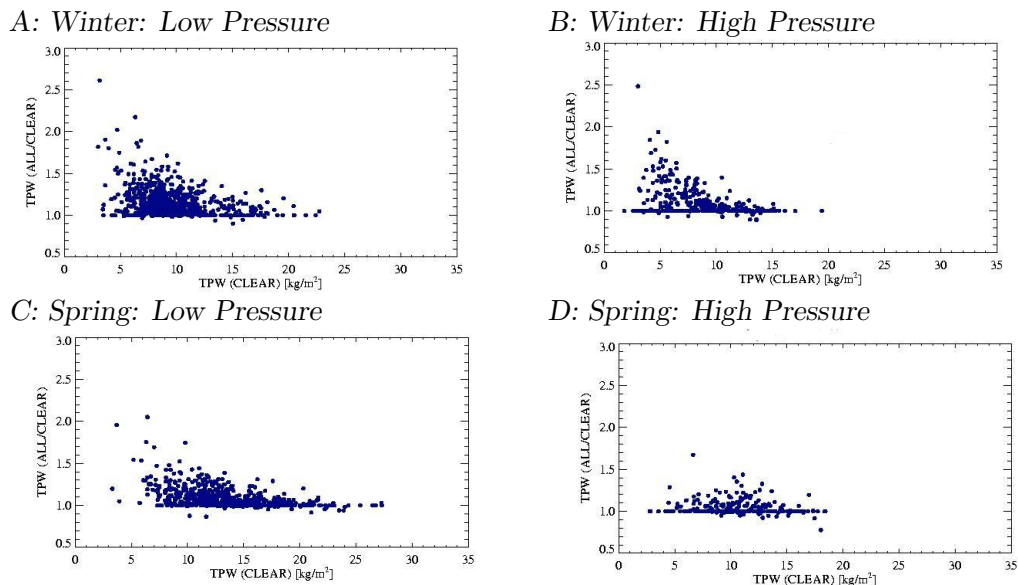


Figure 6.28: Same as figure 6.27 but for winter (A and B) and autumn (C and D).

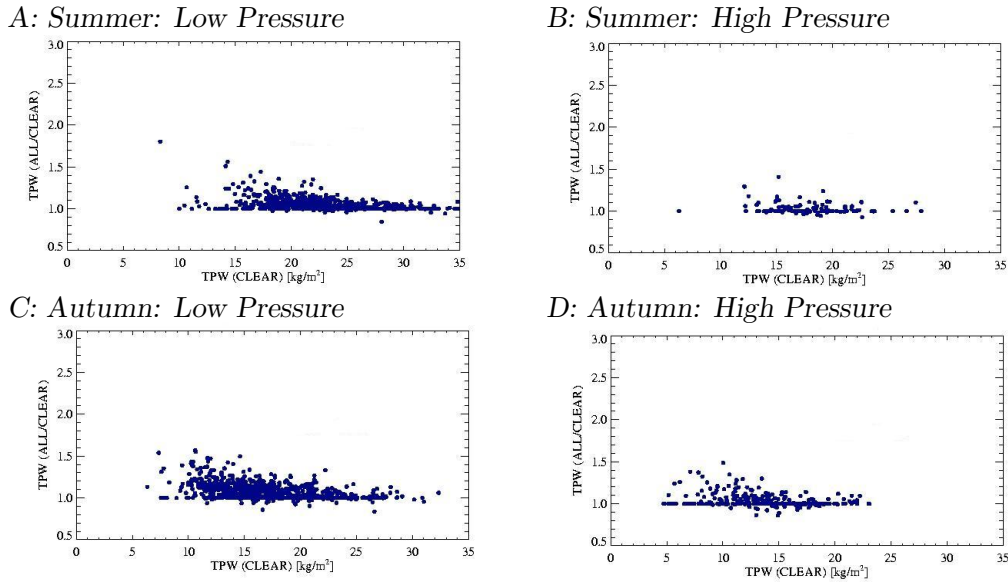


Figure 6.29: Same as figure 6.27 but for summer (A and B) and autumn (C and D).

clear-sky TPW and excess water vapour are summarised in table 6.9.

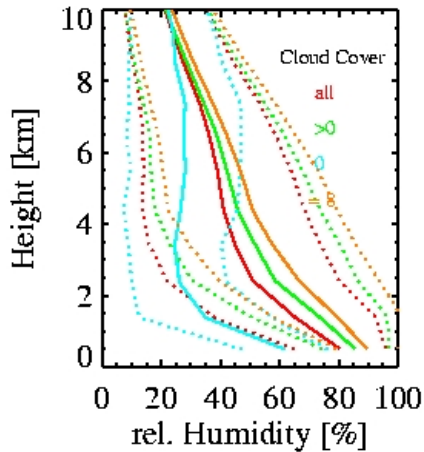
The excess water vapour is derived without cloud informations from coinciding synoptical observations. The distributions show more noise due to wrong detections in the thresholding scheme. On this larger region the dependency of the excess water vapour on surface pressure is shown to be small. For low pressure systems the correlation to the excess water vapour is larger than under high pressure conditions. Under low pressure conditions the difference in cloud to clear situations is dominated by the passing of frontal systems.

To conclude, the extension of the area from Germany to Europe for the radiosonde analysis leads to comparable results. The uncertainty increases because for the clear to cloud distinction only the dewpoint criteria is used. The relation of the ratio to the clear-sky TPW is more prominent in low pressure than for high pressure situations.

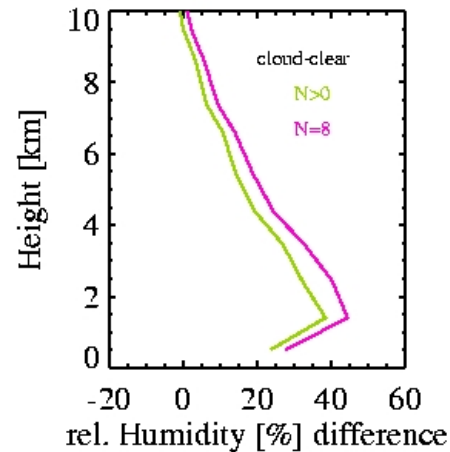
6.3 The vertical distribution of excess water vapour

Marsden and Valero (2004) show an increase in upper-tropospheric humidity in cloudy

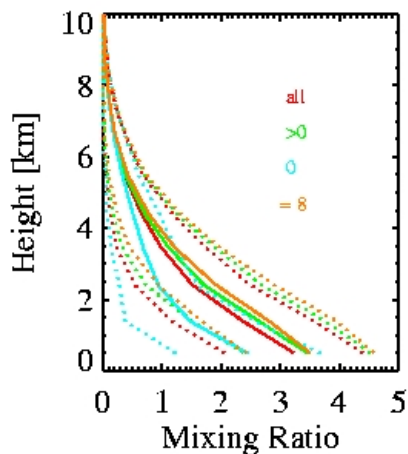
A: Relative Humidity



B: Relative Humidity



C: Mixing Ratio



D: Mixing Ratio

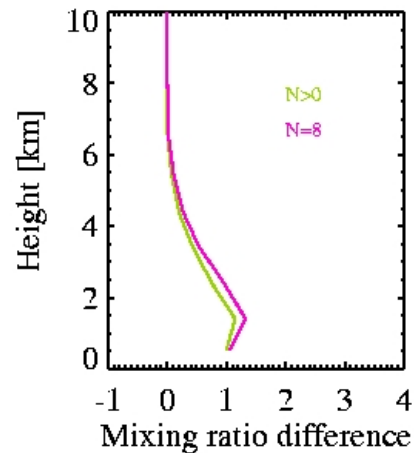
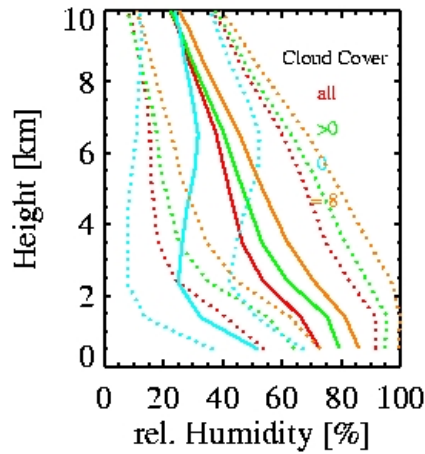


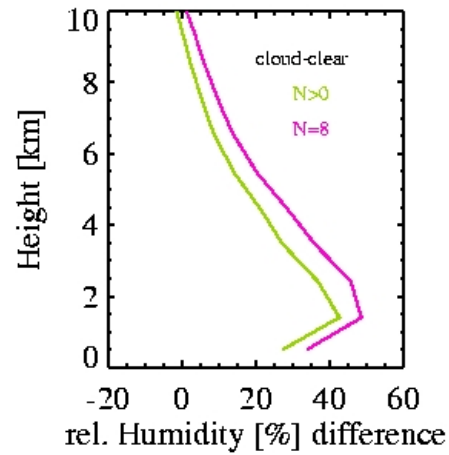
Figure 6.30: Mean vertical profiles for January. A: mean profile (solid line) and standard deviation (dashed lines) of relative humidity for clear-sky cases (cyan), cloudy (dark green), overcast cloud (orange), and all profiles (red). B: humidity difference profiles for mean cloudy to mean clear profile; all cloudy cases (green) and total cloud cover (magenta). C: mean profile (solid line) and standard deviation (dashed lines) of mixing ratio (in g/kg) for clear-sky cases (cyan), cloudy (dark green), total cloud cover (orange), and all profiles (red). D: mixing ratio difference profiles for mean cloudy to mean clear profile; all cloudy cases (green) and total cloud cover (magenta).

atmospheres compared to clear sky situations. For calculations of greenhouse radiative forcing the humidity profile is important. An increase in upper-tropospheric humidity has a higher impact on the radiative forcing than an increase in the lower atmosphere. There-

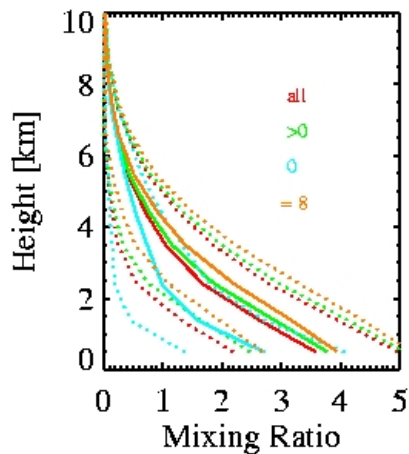
A: Relative Humidity



B: Relative Humidity



C: Mixing Ratio



D: Mixing Ratio

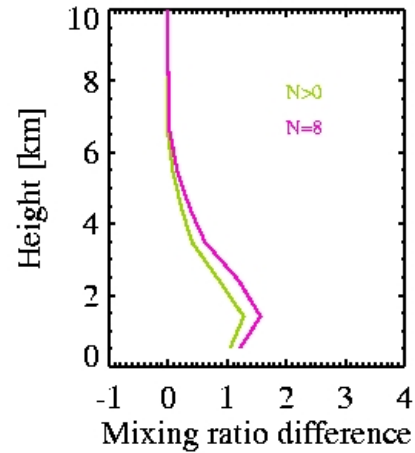
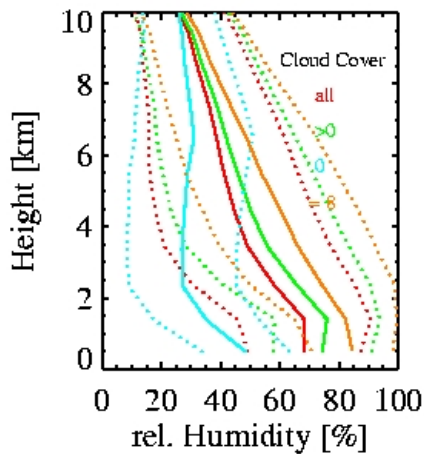


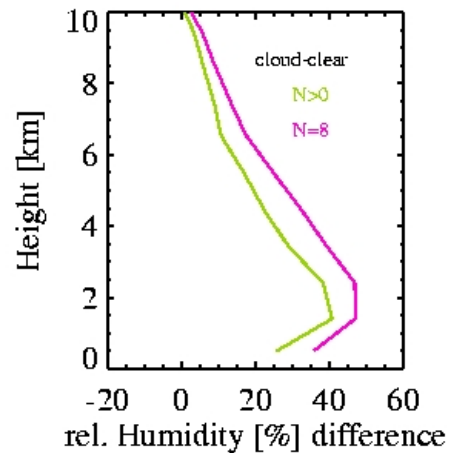
Figure 6.31: Mean vertical profiles for April. A: mean profile (solid line) and standard deviation (dashed lines) of relative humidity for clear-sky cases (cyan), cloudy (dark green), overcast cloud (orange), and all profiles (red). B: humidity difference profiles for mean cloudy to mean clear profile; all cloudy cases (green) and total cloud cover (magenta). C: mean profile (solid line) and standard deviation (dashed lines) of mixing ratio (in [g/kg]) for clear-sky cases (cyan), cloudy (dark green), total cloud cover (orange), and all profiles (red). D: mixing ratio difference profiles for mean cloudy to mean clear profile; all cloudy cases (green) and total cloud cover (magenta).

fore, differences in the humidity profiles between cloudy and clear skies are investigated here. Again only Lindenberg radiosoundings are used.

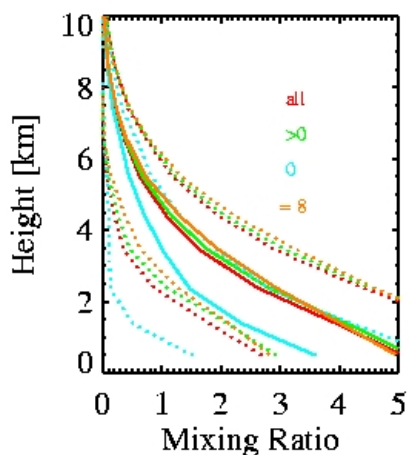
A: Relative Humidity



B: Relative Humidity



C: Mixing Ratio



D: Mixing Ratio

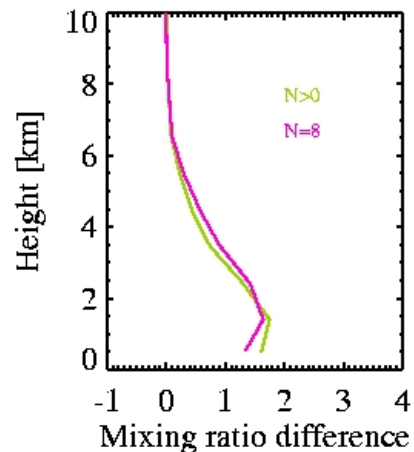
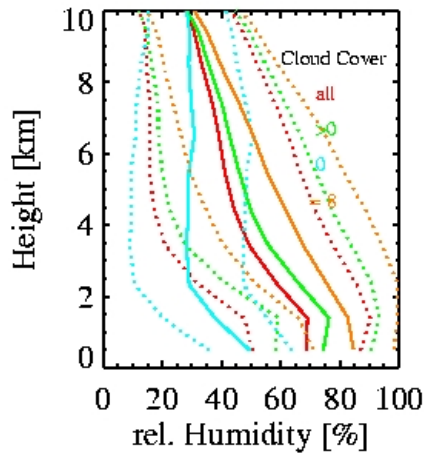


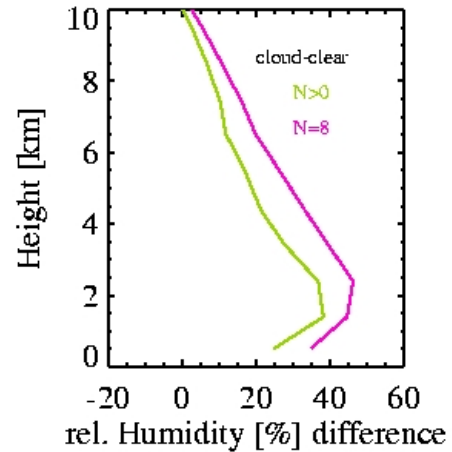
Figure 6.32: Mean vertical profiles for July. A: mean profile (solid line) and standard deviation (dashed lines) of relative humidity for clear-sky cases (cyan), cloudy (dark green), overcast cloud (orange), and all profiles (red). B: humidity difference profiles for mean cloudy to mean clear profile; all cloudy cases (green) and total cloud cover (magenta). C: mean profile (solid line) and standard deviation (dashed lines) of mixing ratio (in [g/kg]) for clear-sky cases (cyan), cloudy (dark green), total cloud cover (orange), and all profiles (red). D: mixing ratio difference profiles for mean cloudy to mean clear profile; all cloudy cases (green) and total cloud cover (magenta).

To answer the question whether there is a dominant height, where in cases of cloudiness the humidity is enlarged, monthly mean vertical relative humidity profiles are investigated. The humidity difference (mean cloudy to mean clear) is largest in 1.5 km height. This level is nearly constant throughout the year, but the vertical extend is larger in summer, whereas

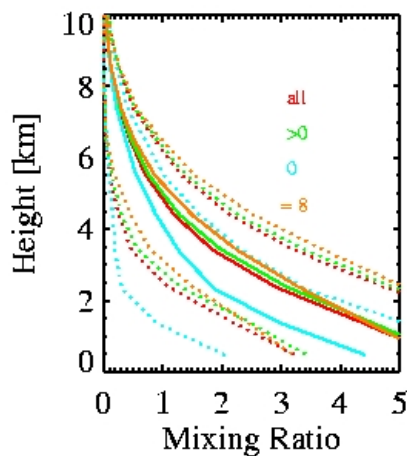
A: Relative Humidity



B: Relative Humidity



C: Mixing Ratio



D: Mixing Ratio

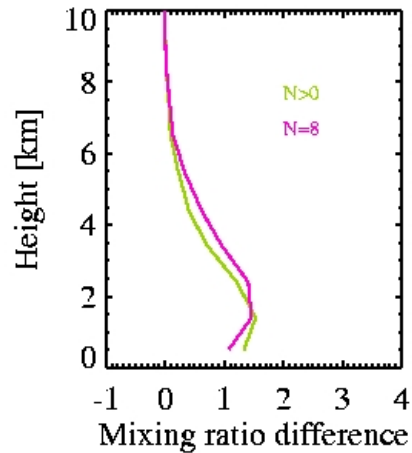


Figure 6.33: Mean vertical profiles for October. A: mean profile (solid line) and standard deviation (dashed lines) of relative humidity for clear-sky cases (cyan), cloudy (dark green), overcast cloud (orange), and all profiles (red). B: humidity difference profiles for mean cloudy to mean clear profile; all cloudy cases (green) and total cloud cover (magenta). C: mean profile (solid line) and standard deviation (dashed lines) of mixing ratio (in [g/kg]) for clear-sky cases (cyan), cloudy (dark green), total cloud cover (orange), and all profiles (red). D: mixing ratio difference profiles for mean cloudy to mean clear profile; all cloudy cases (green) and total cloud cover (magenta).

in winter and spring the maximum relative humidity has a small vertical extend. In the cloud layer the excess water vapour (cloud - clear relative humidity) is about 50 %. The cloudy-sky profile contains more humidity up to the tropopause. Below the cloud layer the excess water vapour is about 20 %, and in the upper troposphere additional 10 % relative humidity occurs, as is shown in figures 6.30 to 6.33.

The humidity increases with temperature. One can argue that the observed differences in excess water vapour profiles are related to temperature differences between clear and cloudy situations. Therefore the mixing ratio, which gives water vapour per dry air, is shown as well. An increase in mixing ratio over the whole profile is found for cloudy skies compared to clear sky observations. The maximum here is found in the cloud layer but up to 6 km height an increase in water vapour is found. In July and October the increase is in higher levels than in January and April.

Differences in the distributions of sea level pressure and the height of the 500 hPa level depending on cloudiness were shown in section 6.1.2. Figure 6.34 shows that the relation between surface pressure (500 hPa level height) and TPW is depending on cloudiness. For Lindenberg clear-sky cases show the maximum occurrences of low TPW under higher surface pressure situations coinciding with a higher 500 hPa level. Cloudy cases dominate under lower surface pressure situations and under lower 500 hPa level situations.

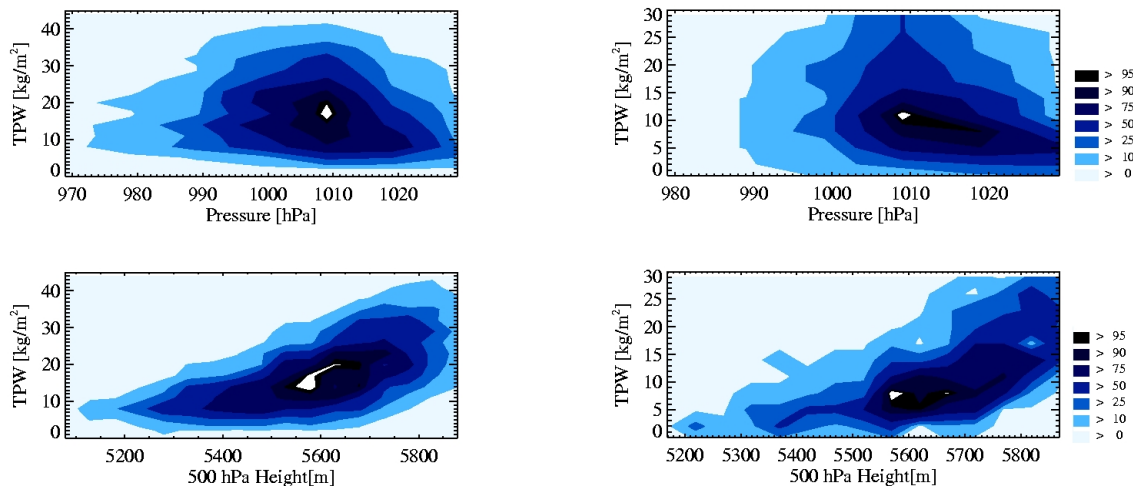


Figure 6.34: Upper row: Frequency distribution of surface pressure related to TPW for all radiosonde ascents at noon time. Lower row: Frequency distribution of 500 hPa level height related to TPW. Right for clear-sky and left for cloudy conditions. In colours the percentage of occurrence is given.

6.4 Layered excess water vapour

The relative humidity and mixing ratio is enlarged over the whole profile as shown in the previous section. The relation of excess water vapour to mean clear-sky TPW was shown for total column water vapour. But does this ratio vary with height? Figure 6.35(A) shows the relation of clear-sky to all-sky TPW for surface layer reaching up to 850 hPa. For large clear-sky TPW, all-sky cases do not differ in monthly mean TPW. In the height of cloud layers (Figure 6.36 (A and B) and 6.37 (A)) excess water vapour is largest. For the upper most layer from 300 hPa to 200 hPa (see figure 6.37 (B)), the measured TPW is low and the variability in the monthly all-sky means is large. For all layered excess water vapour the ratio is close to 1.1 for larger clear-sky TPW and increases towards lower clear-sky TPW values.

The excess water vapour as a function of clear-sky TPW is similar for the total TPW and for the layered TPW. Largest excess water vapour values are found in and below the cloud layers. Which is explained by the transport of humidity from the surface to higher level due to convection.

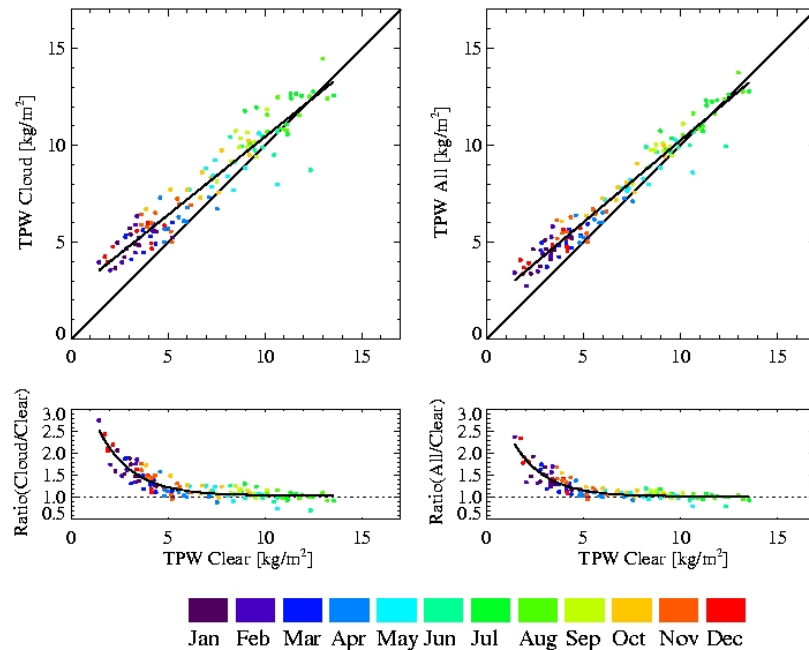
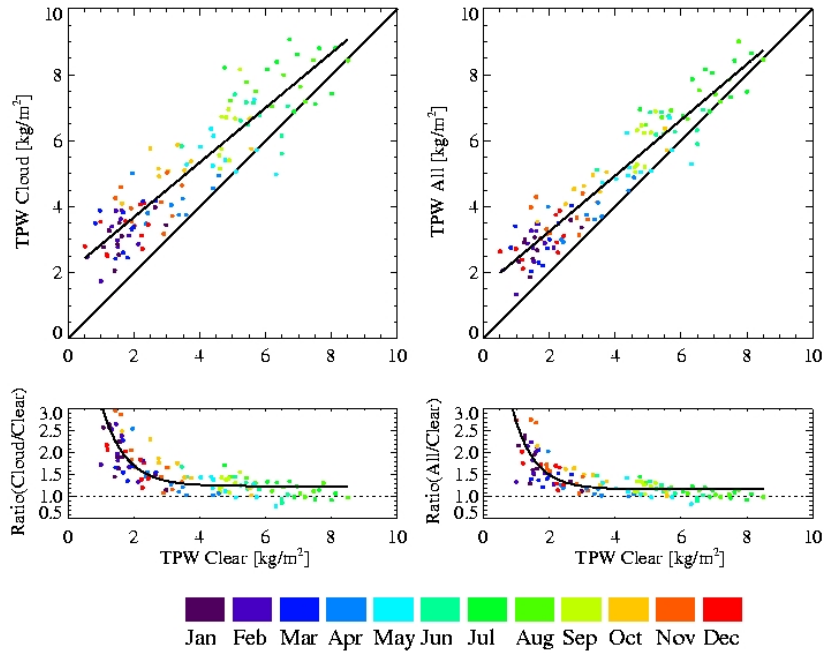


Figure 6.35: Monthly means for 10 years of Lindenberg radiosonde measurements for the layer 1000 hPa to 850 hPa. Monthly mean TPW in clear-sky cases versus cloudy-sky cases (upper panel) and versus the ratio (cloud/clear) (lower panel) (left). Clear-sky TPW is shown in relation to all-sky TPW (right). Colors denote the month.

A: 850 hPa to 700 hPa



B: 700 hPa to 500 hPa

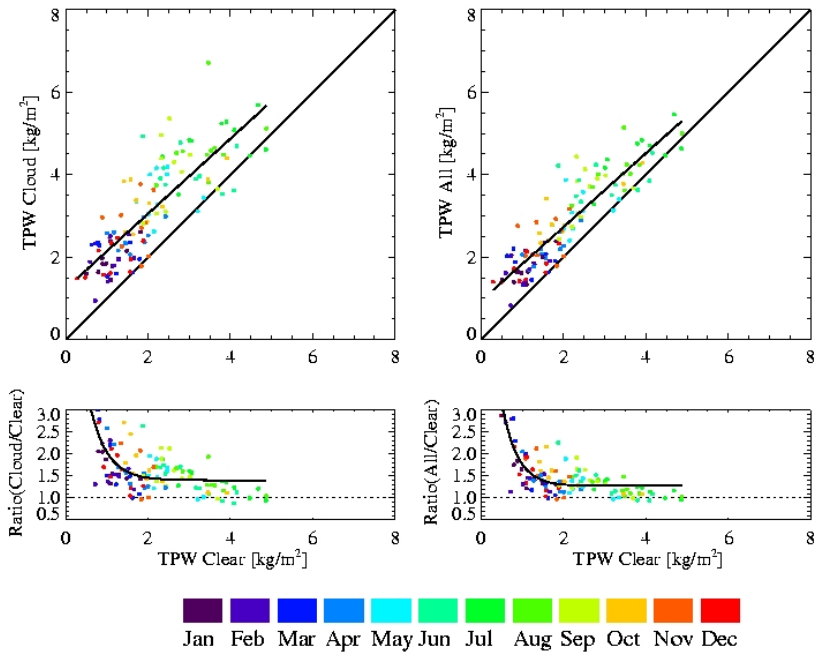
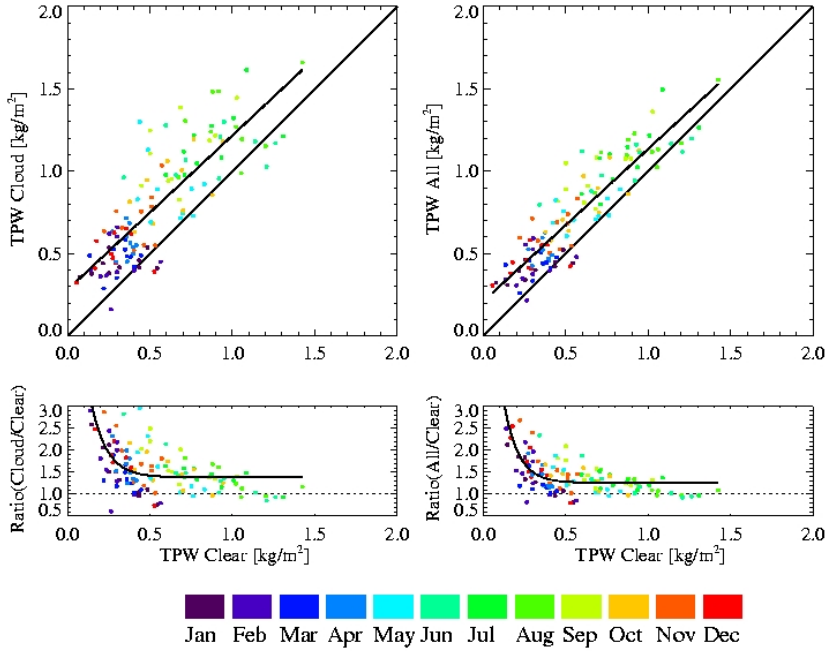


Figure 6.36: Monthly means for 10 years of Lindenberg radiosonde measurements for the layer 850 hPa to 700 hPa (A) and 700 hPa to 500 hPa (B). Monthly mean TPW in clear-sky cases versus cloudy-sky cases (upper panel) and versus the ratio (cloud/clear) (lower panel) (left). Clear-sky TPW is shown in relation to all-sky TPW (right). Colors denote the month.

A: 500 hPa to 300 hPa



B: 300 hPa to 200 hPa

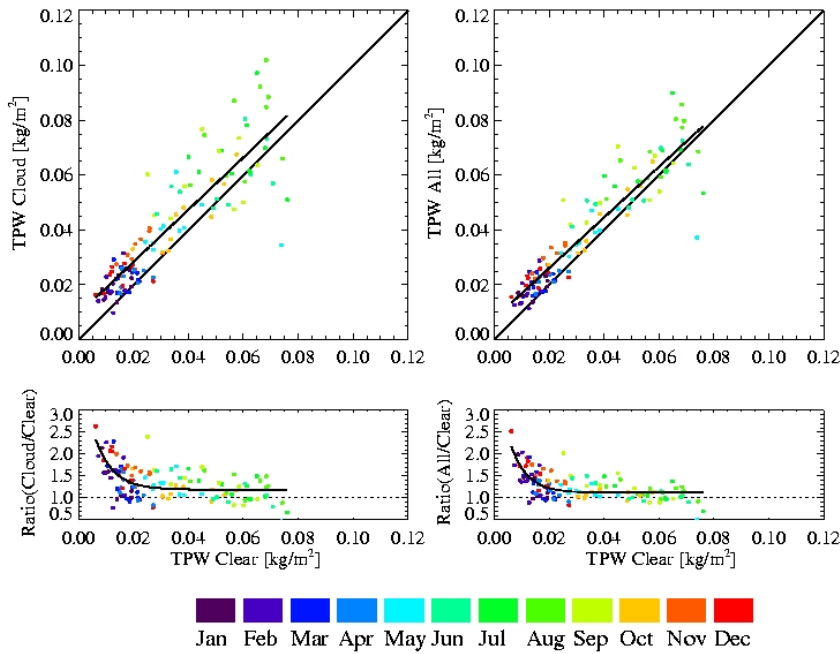


Figure 6.37: Monthly means for 10 years of Lindenberg radiosonde measurements for the layer 500 hPa to 300 hPa (A) and 300 hPa to 200 hPa (B). Monthly mean TPW in clear-sky cases versus cloudy-sky cases (upper panel) and versus the ratio (cloud/clear) (lower panel) (left). Clear-sky TPW is shown in relation to all-sky TPW (right). Colors denote the month.

6.5 Concluding remarks

The clear-sky TPW is significantly lower than TPW in cloudy atmospheres. The amount of water vapour added by the clouds is about 10% of the clear-sky TPW. The excess water vapour defined as the ratio of TPW in all-sky to the TPW in clear-sky situations is derived for German stations. The functional relation between the excess water vapour and the clear-sky TPW on a monthly mean basis can be described by an exponential function. The excess water vapour decreases with increasing clear-sky TPW. The underestimation in TPW by neglecting cloudy scenes is about 10%–20%. The relation is much more noisy due to missing cloud informations. Thus the same functional relation is found for the European area.

The cloud layers are identified in the mixing ratio and relative humidity profile. Looking at layered TPW the largest excess water vapour is found at the cloud levels. However, the functional relation of the excess water vapour depending on the clear-sky TPW is found to be the same for all layers.

6.6 NAO

The excess water vapour is depending on the season. Highest values are derived in cold atmospheres. Here the clear to cloud difference in water vapour is largest due to the different

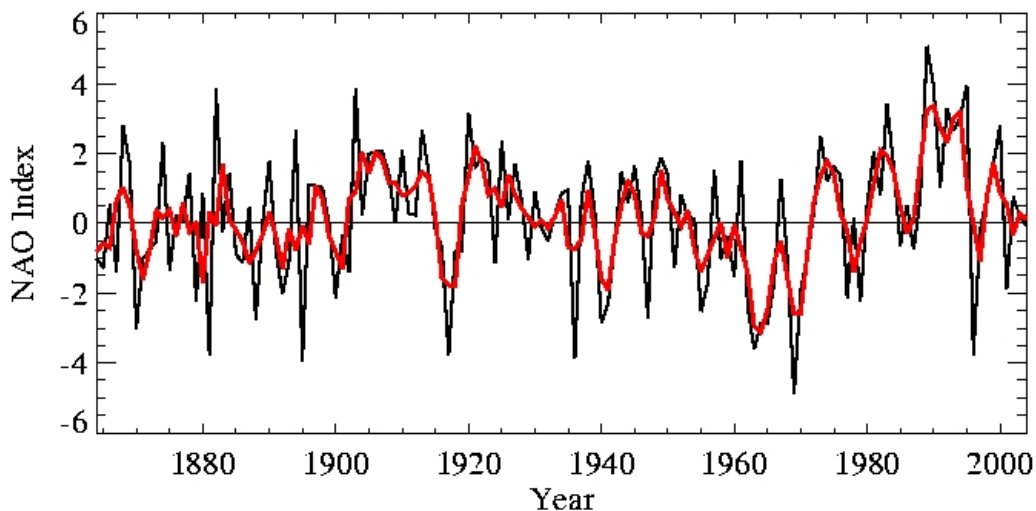


Figure 6.38: *The time series of the winter mean (December to March) NAO index after Hurrell is given in the upper panel. The red curve represents the 3-years running mean.*

origins of the air masses, which is directly coupled to the mean air temperature. In winter time the general weather situation in Europe can be described by the North Atlantic Oscillation NAO. In the following it is investigated whether the NAO is an estimator for the excess water vapour.

The NAO is the dominant mode of winter climate variability in the North Atlantic region

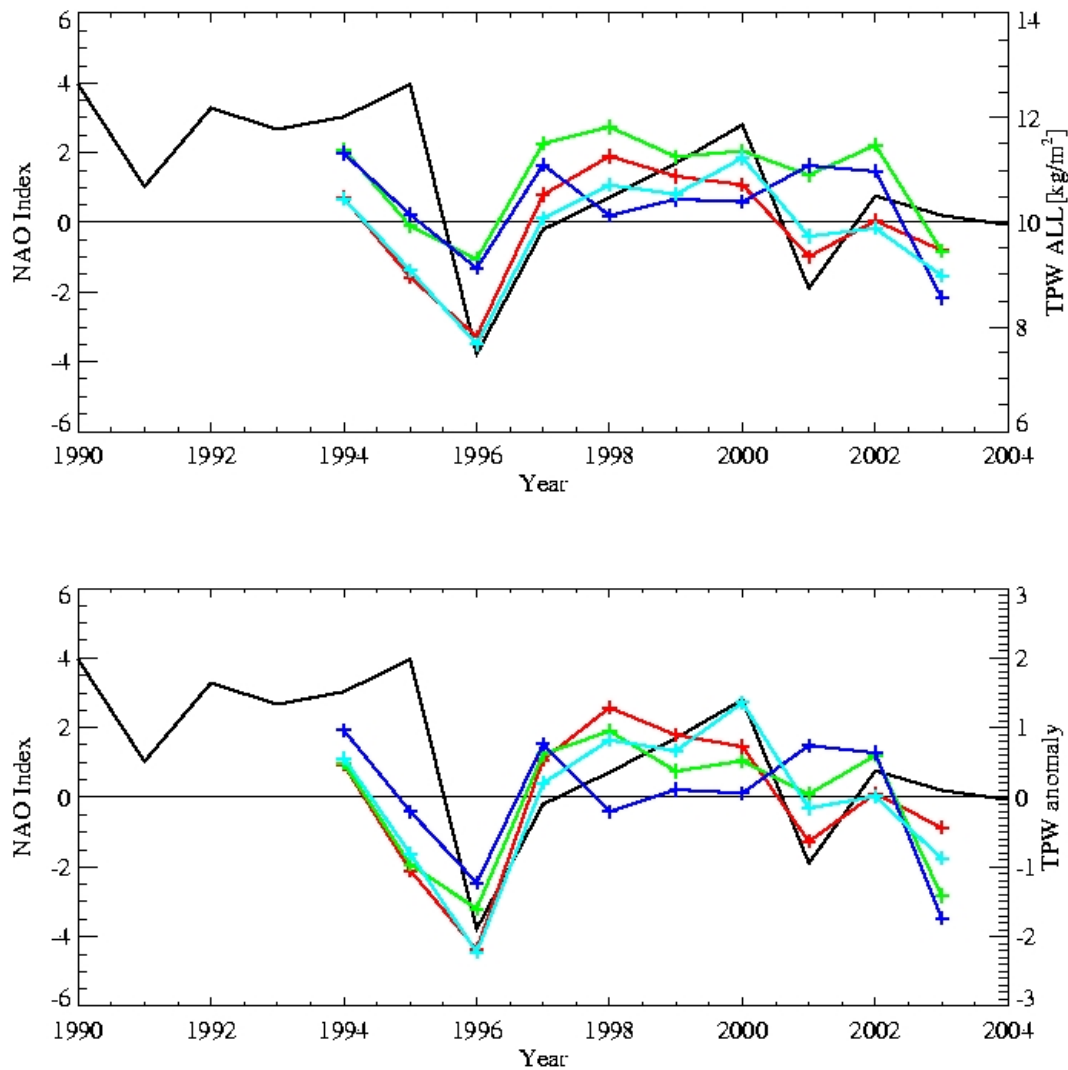


Figure 6.39: Comparison of the all-sky TPW time series and the NAO (top). The bottom panel shows the TPW anomaly and the NAO index. The coloured lines give the station TPW, Schleswig (red), Essen (green), Stuttgart (blue), and Lindenberg (cyan).

ranging from central North America to Europe and much into Northern Asia. The NAO is a large scale seesaw in atmospheric mass between the subtropical high and the polar low. The corresponding index varies from year to year, but also exhibits a tendency to remain in one phase for intervals lasting several years.

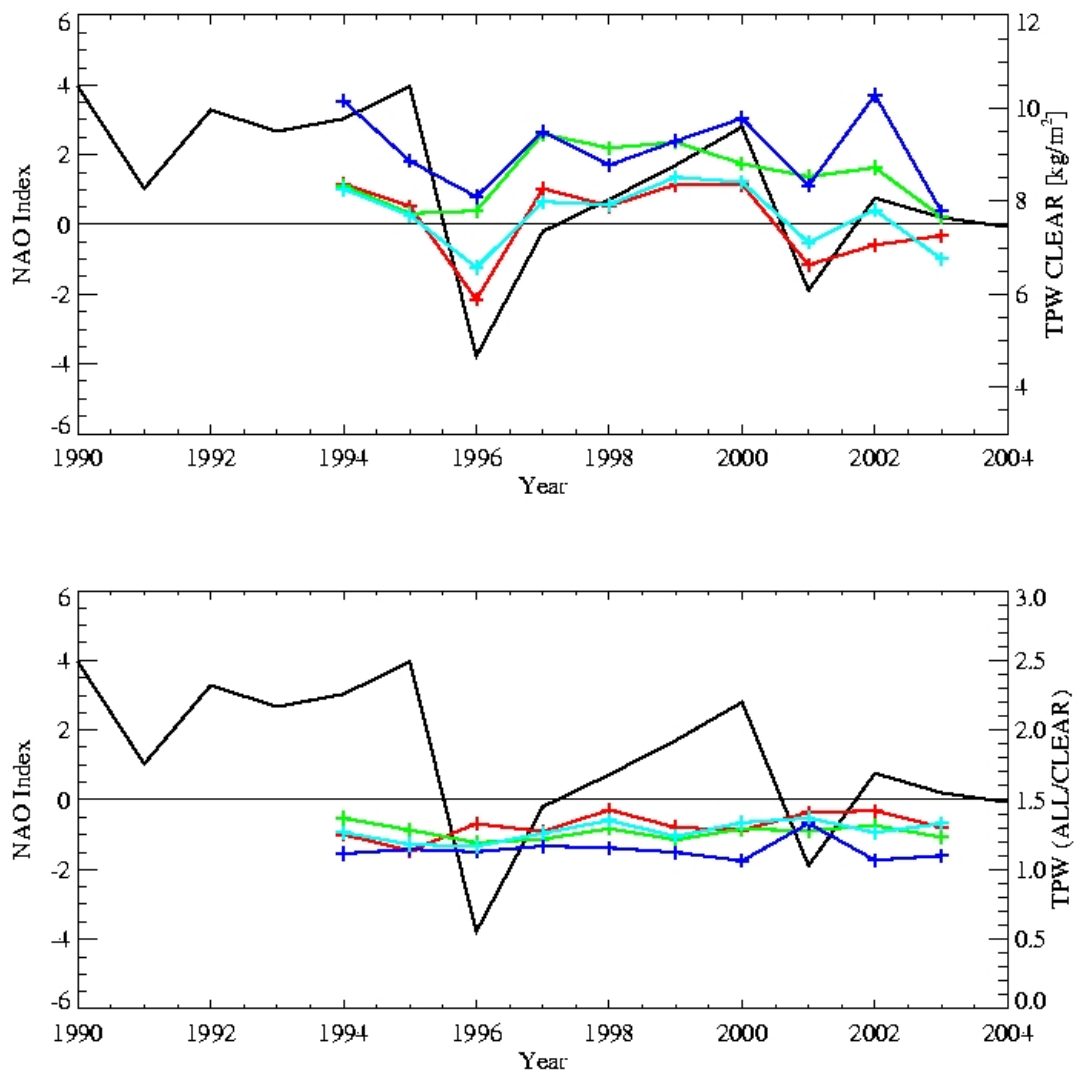


Figure 6.40: Comparison of the TPW time serie and the NAO. The coloured lines give the station TPW, Schleswig (red), Essen(green), Stuttgart (blue), and Lindenberg (cyan) . Upper panel TPW clear, lower panel excess water vapour.

Figure 6.38 shows the Winter (December to March) index of the NAO based on the difference of normalized sea level pressure (SLP) between Lisbon, Portugal and Stykkisholmur/Reykjavik, Iceland since 1864. The SLP anomalies at each station were normalized by dividing each seasonal mean pressure with the long-term mean (1864–1983) standard deviation in order to avoid the series being dominated by the larger variability of the northern station. Positive values of the index indicate stronger-than-average westerlies over the mid latitudes.

For the time periods investigated in this study, 1994 to 2003, the NAO index is shown in figure 6.39 together with the winter mean of the all-sky TPW for the German stations. The mean TPW roughly follows the NAO index. The large change in NAO from 1995 to 1996 from a positive index to negative values is visible in the TPW as a negative peak in the time series. For the stations Lindenberg and Schleswig the correlation of the NAO to the TPW is stronger than for the stations Essen and Stuttgart (table 6.10). The TPW anomaly follows the NAO index as well. For clear-sky TPW the stations show a lower relation to the NAO (figure 6.40). The excess water vapour, the ratio of TPW in all-sky and clear-sky atmospheres, is not influenced by the NAO. The excess water vapour varies from station to station in the range of 1.1 to 1.4. The variability in clear- and all-sky TPW is not affecting the ratio. Only ten winter mean values are compared to the NAO which leads to insignificant correlations, as can be seen in the range of the correlation uncertainty, which is given in the table as well.

We can conclude that neither cold and dry winter (negative NAO values) nor warm and wet winter (positive NAO index) have a significant influence on the excess water vapour under cloudy conditions compared to clear conditions. This supports our thesis, that small scale variability due to frontal systems dominate the excess water vapour signal.

		Lindenberg						
		TPW	Temp	SLP	TPW Clear	TPW Cloud	Ratio (All/Clear)	TPW anomaly
NAO	cor	0.59	0.69	-0.50	0.72	0.60	-0.01	0.54
	err	0.56	0.50	0.65	0.40	0.54	0.85	0.5
		Schleswig						
		TPW	Temp	SLP	TPW Clear	TPW Cloud	Ratio (All/Clear)	TPW anomaly
NAO	cor	0.51	0.62	-0.64	0.82	0.44	-0.56	0.39
	err	0.63	0.52	0.51	0.28	0.69	0.58	0.6
		Essen						
		TPW	Temp	SLP	TPW Clear	TPW Cloud	Ratio (All/Clear)	TPW anomaly
NAO	cor	0.35	0.63	-0.12	0.09	0.50	0.57	0.28
	err	0.76	0.52	0.85	0.85	0.65	0.57	0.66
		Stuttgart						
		TPW	Temp	SLP	TPW Clear	TPW Cloud	Ratio (All/Clear)	TPW anomaly
NAO	cor	0.30	0.65	0.23	0.56	0.01	-0.42	0.32
	err	0.78	0.50	0.81	0.58	0.85	0.70	0.64

Table 6.10: Correlation of the winter mean (December to March) NAO index after Hurrel and TPW, surface temperature, surface pressure, TPW clear, TPW cloud, ratio (ALL/CLEAR), and the TPW anomaly for the stations Schleswig, Lindenberg, Essen, and Stuttgart.

Chapter 7

Satellite-based retrieval of TPW in all-sky atmosphere

Polar orbiting satellites enable global observations of environmental properties. In this study the microwave emission from atmospheric water is measured with AMSU, the advanced microwave sounding unit, onboard the NOAA-16 polar orbiting satellite. The NOAA-16 satellite passes over Europe about noon (12 UTC) in ascending direction and descending orbit at night time (about 2 UTC). The microwave emission is independent of the solar radiation. The diurnal cycle of TPW is small. The ability of the atmosphere to contain water vapour is coupled to the atmospheric temperature which has a diurnal cycle. Therefore the relative humidity is affected by the time of day but not the absolute humidity. The exception are areas where a reservoir of water can compensate the drying of the air by temperature increase. The TPW is defined as the vertical integral of the absolute humidity. Changes in TPW are due to the annual temperature variations and passing of weather regimes like low pressure systems with their different air masses.

For this study the AMSU TPW and LWP algorithm described by Grody et al. (2001) has been applied. For the retrieval the emissions at 23.8 GHz and 31.4 GHz are used. Auxiliary data like sea surface temperature, air temperature and surface wind field are taken from the NCEP/NCAR reanalysis. For microwave retrieval a good knowledge of the emitting surface is important. Therefore most algorithms using this frequencies are operating over the oceans only. Sea ice as emitting surface is also critical in the water vapour and LWP retrieval. Pixels with a sea surface temperature lower than 2 K are not used in this study. Land surfaces in the vicinity of the field of view are increasing the measured radiance. To avoid overestimations of TPW and LWP grid boxes with land inside and boxes with land in the neighbouring boxes are excluded.

The mean LWP shown in this section denotes the mean LWP of non-precipitating clouds. A threshold of 0.5 kg/m^2 is used to eliminate precipitating clouds in the statistical analysis (see Crewell et al. (2002)). For field of views with a retrieved LWP of 0.0 kg/m^2 the pixel

is considered clear-sky. A mean over all pixels in a grid cell is denoted as clear-sky TPW. The spatial grid resolution used in this study is a $0.5^\circ \times 0.5^\circ$.

7.1 Global TPW distributions

Figure 7.1 shows the global distribution of all-sky TPW along its seasonal cycle. The tropical regions show largest values. The seasonal drift of the inner tropical convergence zone is clearly visible. Near the continents larger TPW values are connected to warm ocean boundary currents. Lower TPW values are related to the cold ocean currents. The subsidence regions of the Hadley circulation are related to dry atmosphere. These features are present in the clear-sky TPW as well (see figure 7.2). The absolute TPW is lower for clear-sky cases.

The monthly mean LWP shows some climatological structures, see figure 7.3. The dry subtropic areas are prominent. The ITCZ and the monsoon clouds are found in the mean fields. The mid-latitudes show larger LWP in areas where frontal systems are formed.

To analyse the water vapour in cloudy situations and the difference to the clear-sky case in section 6.2 the ratio of all-sky TPW to clear-sky TPW is defined as measure of the

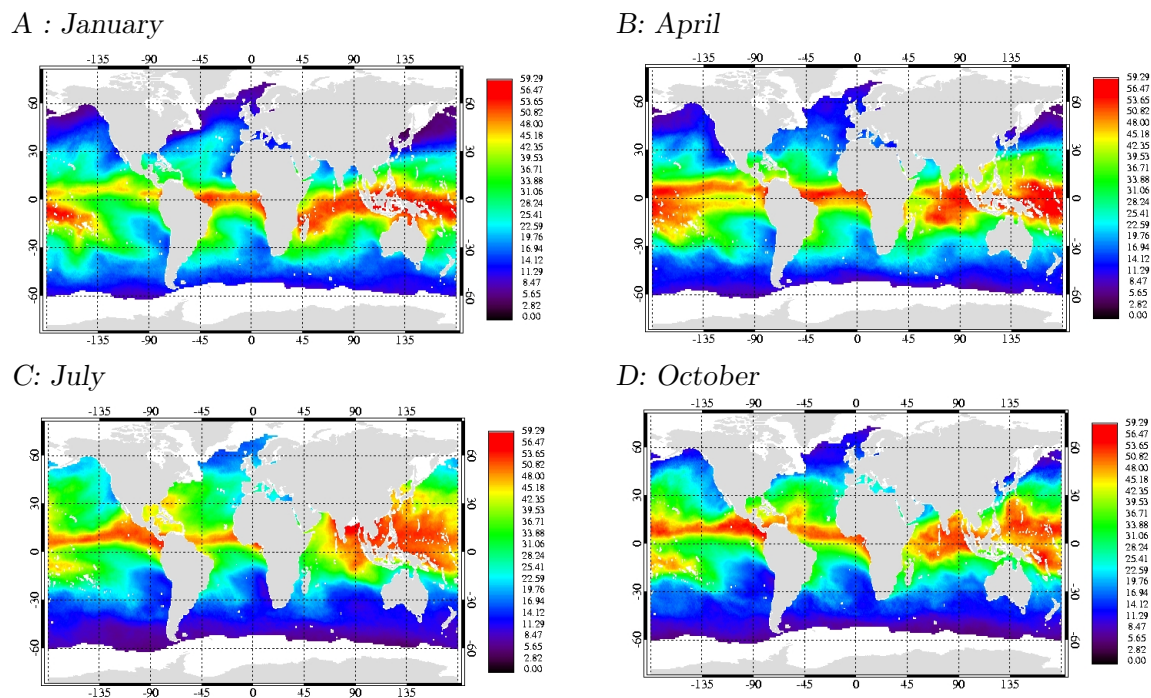
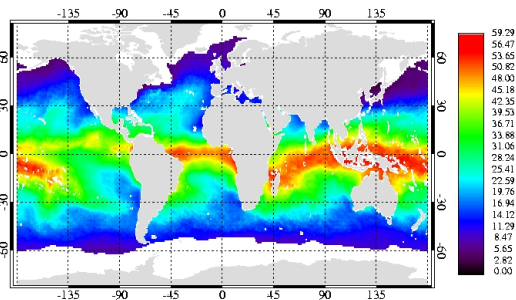


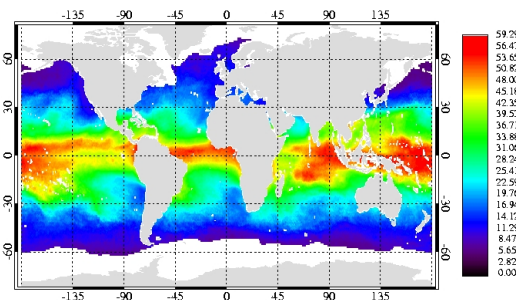
Figure 7.1: Monthly mean vertical integrated total precipitable water (TPW) in $[\text{kg/m}^2]$ derived from AMSU measurements for A January, B April, C July, and D October 2004.

so-called excess water vapour. In figure 7.4 the global distribution of excess water vapour is shown. In the subsidence regions the ratio is smaller than 1 which expresses larger TPW values in the clear-sky case. Here colder air related to changes in the sea surface temperature are related with a drier atmosphere due to changes in the capacity of the atmosphere to hold the water vapour. These colder sea surface temperatures are related to southward colder surface streams on the eastern part of the ocean basins. Mainly this air results from equatorwards winds. Nevertheless, the ratios are slightly smaller than 1, so the difference in TPW is small in these cases. Largest variability and largest ratios are found in the midlatitudes, where the storm tracks are visible in the excess water vapour fields. In January the cold and dry air of the American continent flow over the warm gulf stream and saturates. This is striking in a ratio below 0.85 (15% drier is the all-sky atmosphere compared to the clear-sky). The clear-sky cases are related to a gulf stream parallel flow with warmer but cloud free air. The same features are found in the all-sky minus clear-sky TPW fields in figure 7.5.

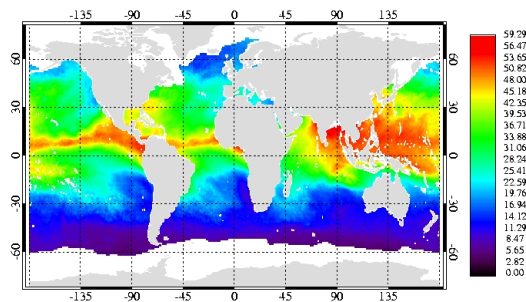
A : January



B: April



C: July



D: October

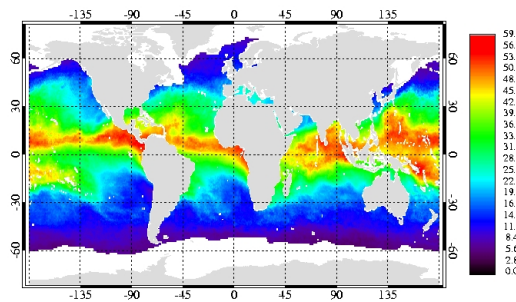
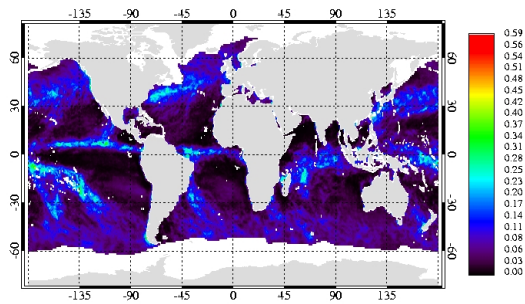
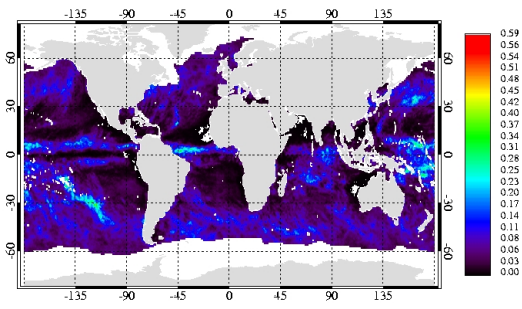


Figure 7.2: Monthly mean vertical integrated total precipitable water (TPW) in $[\text{kg}/\text{m}^2]$ for clear-sky situations derived from AMSU measurements for A January, B April, C July, and D October 2004.

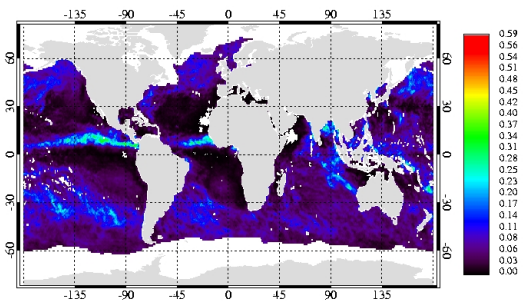
A : January



B: April



C: July



D: October

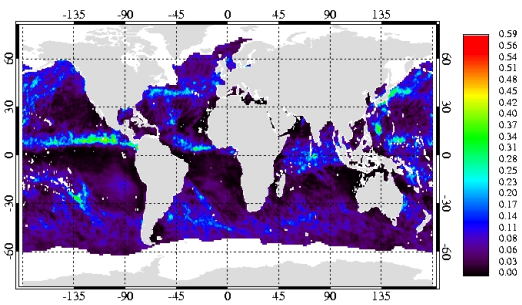
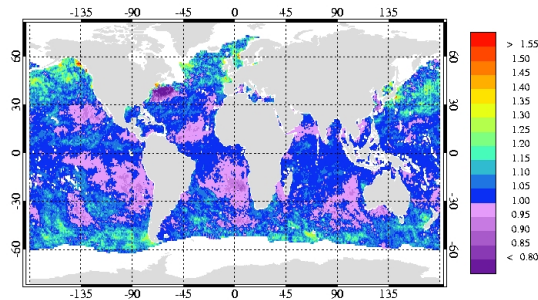
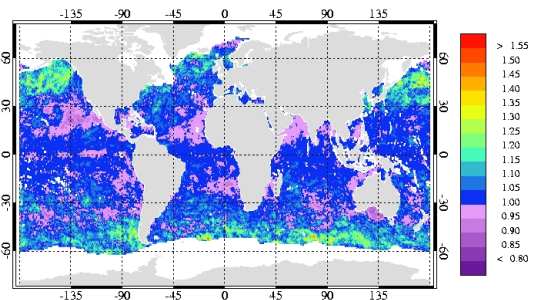


Figure 7.3: Monthly mean vertical integrated liquid water (LWP) in $[kg/m^2]$ for non-precipitating clouds derived from AMSU measurements for A January, B April, C July, and D October 2004.

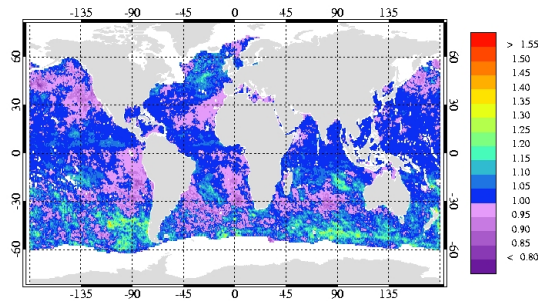
A : January



B: April



C: July



D: October

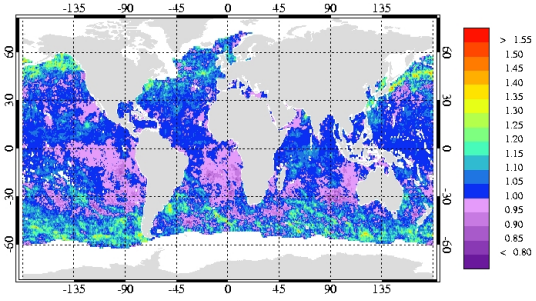
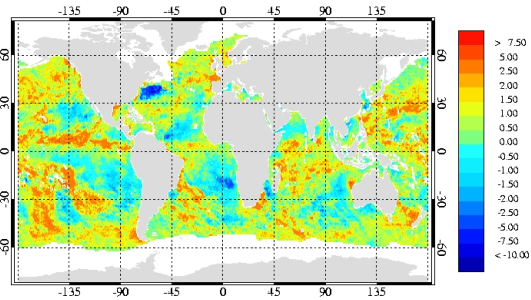
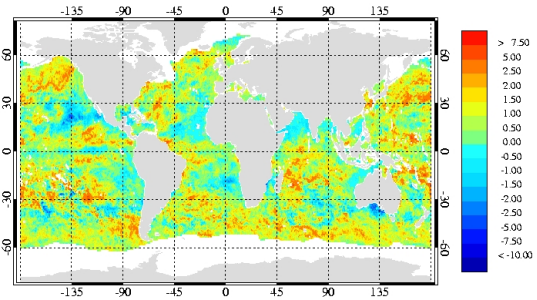


Figure 7.4: Monthly mean excess water vapour (all-sky TPW divided by clear-sky TPW) for non-precipitating clouds derived from AMSU measurements for A January, B April, C July, and D October 2004.

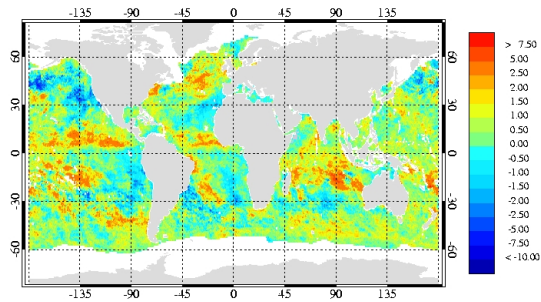
A : January



B: April



C: July



D: October

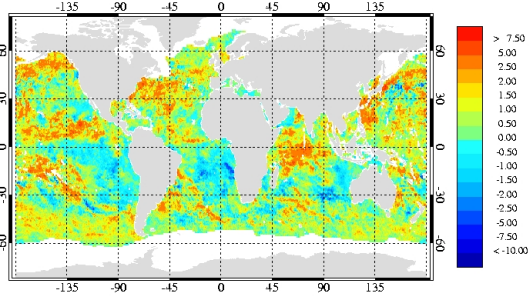
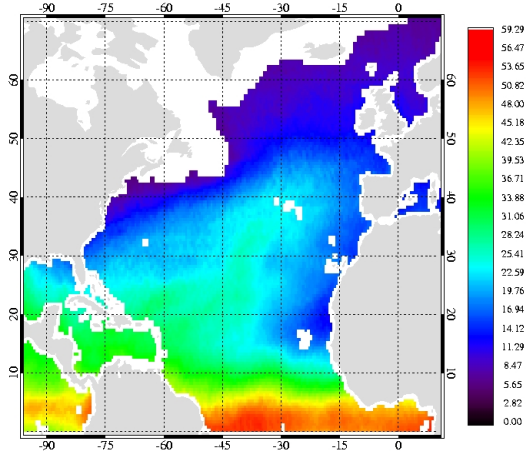


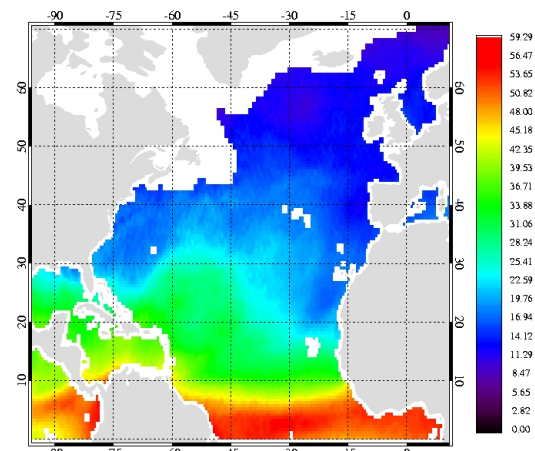
Figure 7.5: Monthly mean all-sky TPW minus clear-sky TPW In $[kg/m^2]$ for non-precipitating clouds derived from AMSU measurements for A January, B April, C July, and D October 2004.

7.2 Excess water vapour over the North Atlantic

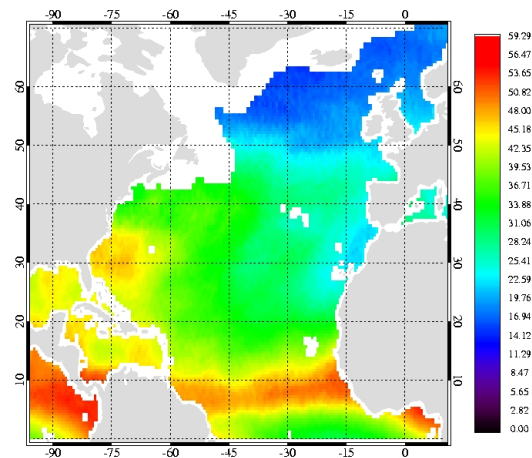
A : January



B: April



C: July



D: October

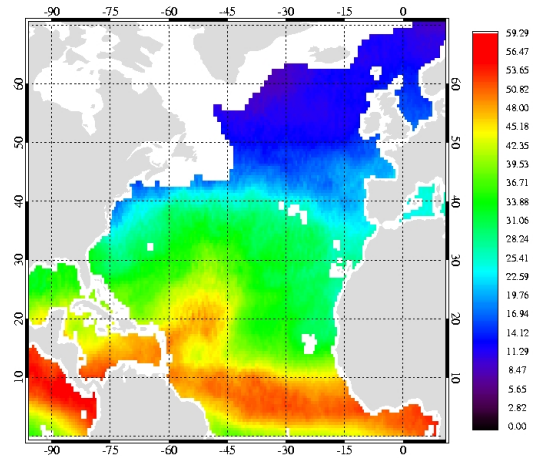


Figure 7.6: Monthly mean vertical integrated total precipitable water (TPW) in $[\text{kg}/\text{m}^2]$ derived from AMSU measurements for A January, B April, C July, and D October 2004.

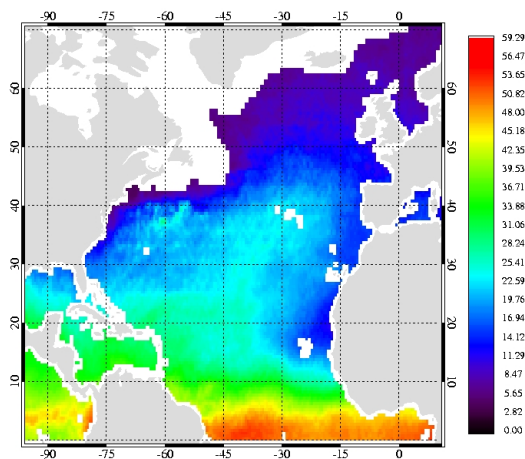
For a deeper description of the excess water vapour and its dependencies the North Atlantic is investigated. In the North Atlantic region we find largest variability on small regional scales compared to the other ocean areas. The other ocean basins are described in appendix E.

The all-sky TPW is shown in figure 7.6. The seasonal cycle of the TPW is clearly visible. The tropics with the ITCZ moves north during the northern hemispheric summer. Similar behaviour is shown in the clear-sky TPW in figure 7.7. The cloud liquid water fields (see figure 7.3) show largest values in the ITCZ and in the mid-latitudes, related to the frontal

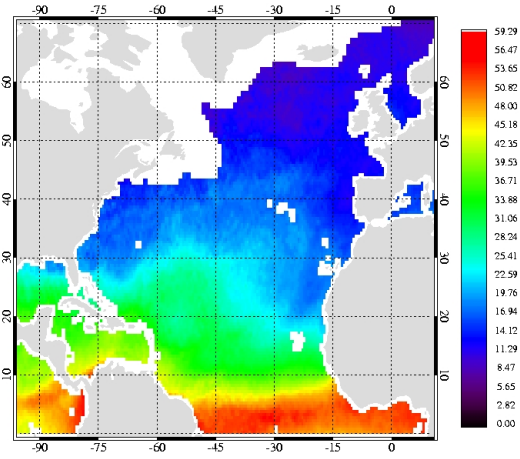
systems.

The excess water vapour is given in figure 7.8. In the mid latitudes the ratio of all-sky to clear-sky TPW is positive, and the largest values are found in the cyclogenetic regions (e.g. south east of Greenland). The variability in this region is high. Values below 1 characterises situations where cloudy atmospheres are drier than cloud free situations. The dominant cause for this is a change in air mass and thus an expression of the coupling of humidity and air temperature. The cloud free atmosphere is related to warm air, which can contain more water vapour than a colder saturated air mass. This situations are found in the subtropics. In absolute numbers of excess water vapour the values are close to 1. In

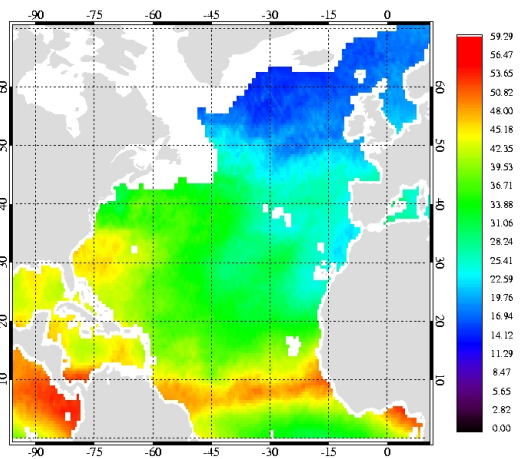
A : January



B: April



C: July



D: October

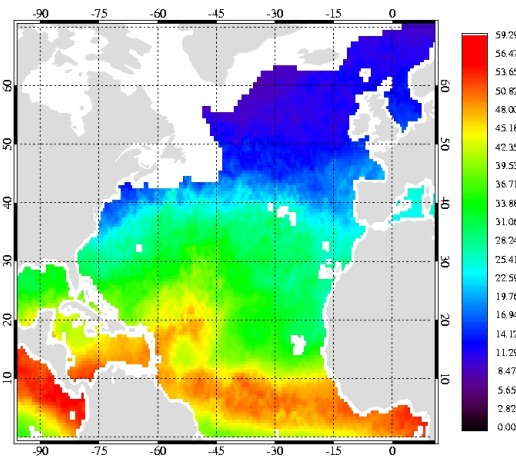
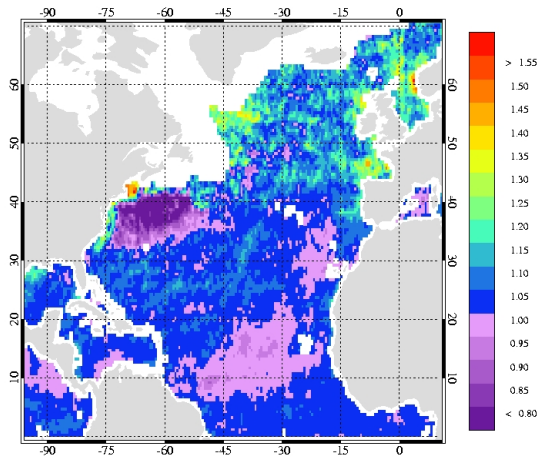


Figure 7.7: Monthly mean vertical integrated total precipitable water (TPW) in $[\text{kg}/\text{m}^2]$ for clear-sky situations derived from AMSU measurements for A January, B April, C July, and D October 2004.

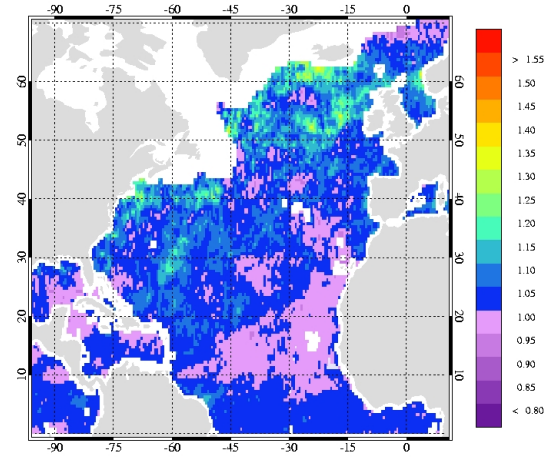
January a field with values below 0.9 is found close to New Foundland. Here two weather situations are present in winter time. A offshore cold dry air from the North American continent blows over the warm gulf stream and saturates at low absolute humidity levels. In contrast warm air flows along the gulf stream with larger absolute humidity values, but saturation does not occur. In summer the differences in air masses are smaller, therefore the ratios are closer to 1.

In figure 7.9 the relation of clear-sky to the all-sky TPW is given for one year and in figure 7.10 for four years. Due to technical problems for these figures the years 2001 and 2003-2005 have been used.

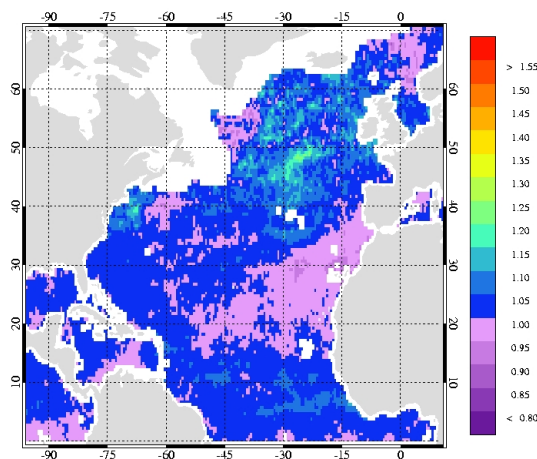
A : January



B: April



C: July



D: October

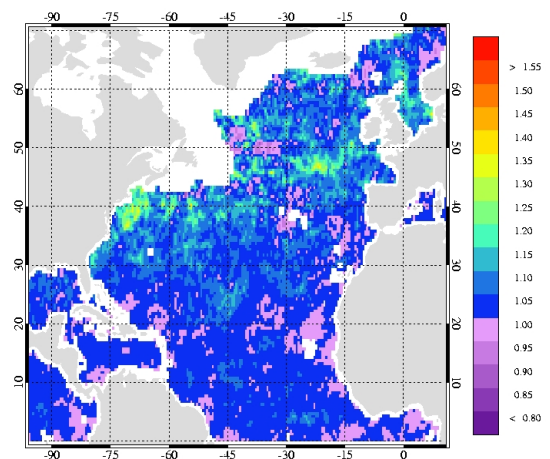
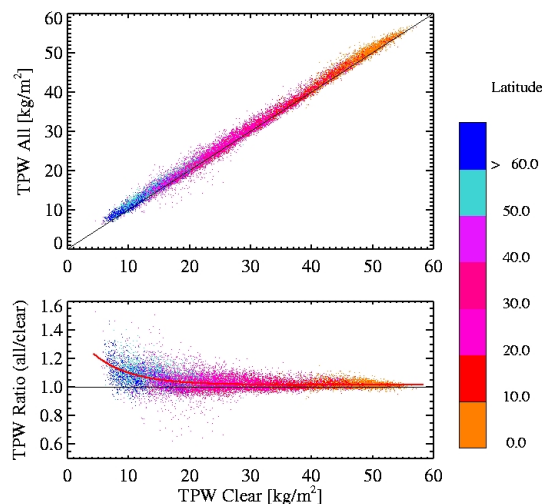


Figure 7.8: Monthly mean excess water vapour (all-sky TPW divided by the clear-sky TPW) for non-precipitating clouds derived from AMSU measurements for A January, B April, C July, and D October 2004.

The relation of clear-sky TPW to the all-sky TPW as shown in figure 7.9 and figure 7.10 shows a small positive bias. The temperature dependence of absolute humidity is clearly visible in the colour coding by latitude. The tropics are found in the large TPW area whereas the mid- to high-latitude mark the lower end. The ratio are stronger scattered for small clear-sky TPW. For larger clear-sky TPW the difference between cloud and cloud-free TPW is small, which might be explained by nearly saturated atmospheres. The frequency distribution of excess water vapour shows for most of the cases the ratio is above 1. Less then 10 % of the data points are smaller than one. The function describing the clear-sky TPW to the excess water vapour shows an exponential decrease to larger clear-sky TPW.

In figure 7.11 (A) the variation of the retrieved parameterisations of the excess water vapour according to the clear-sky TPW is shown for the year 2004 and in 7.12 (A) for the years 2001–2005 (except 2002). For low clear-sky TPW the ratio varies between 1.1 and 1.4 depending on the time of the year. Largest ratios and steepest increase of the fit function are found in summer and autumn. This is explained by the difference in air masses forced through a grid point by low pressure systems. Looking at the four-years mean the characteristics of the functions are similar to that for a single year. A power-law function (see equation 7.1) is used to express the results. In table 7.1 the coefficients for the proposed relation are given. The ratio can also be expressed in terms of kg/m^2 . The

A : Excess water vapour depending on Latitude



B: Excess water vapour frequency distribution

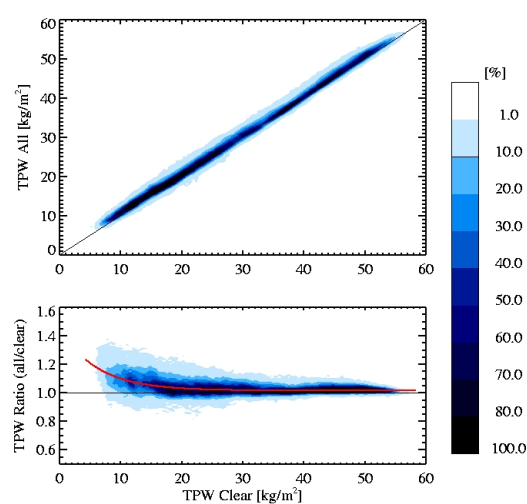


Figure 7.9: Relation of clear-sky TPW to the all-sky TPW (upper panel) and to the ratio of all-sky TPW and clear-sky TPW. The TPW is given in $[\text{kg}/\text{m}^2]$. Data are taken from the year 2004. A: Colours give the latitude range. B: Frequency distribution of the data points in figure A.

fit functions shown in the figures 7.11 (B) and 7.12 (B). For a monthly mean clear-sky TPW of 10 kg/m^2 the underestimation to an all-sky TPW is about 2 kg/m^2 for the summer month.

$$Y = a_0 a_1^X + a_2 \quad (7.1)$$

The zonal relation of the all to clear TPW ratio is shown in figure 7.13. Both the diagrams for one and for all years show an increase to high latitudes. In the mid-latitudes several excess water vapour values below 0.8 are observed mainly in winter time. On zonal average the excess water vapour is larger than 1. The maximum underestimation related to clear-sky TPW is about 20% corresponding to an excess water vapour of 1.2.

The frequency distributions of the monthly mean excess water vapour over the North Atlantic (see figure 7.14) and globally (see figure 7.15) show a peak close to 1. The frequency distribution for all years are given in figure 7.16. The mean and median are larger than 1 and are varying throughout the year with largest values in autumn. The mean and median are larger for the global distributions. The statistical parameters are given in table 7.2.

A : Excess water vapour depending on Latitude

B: Excess water vapour frequency distribution

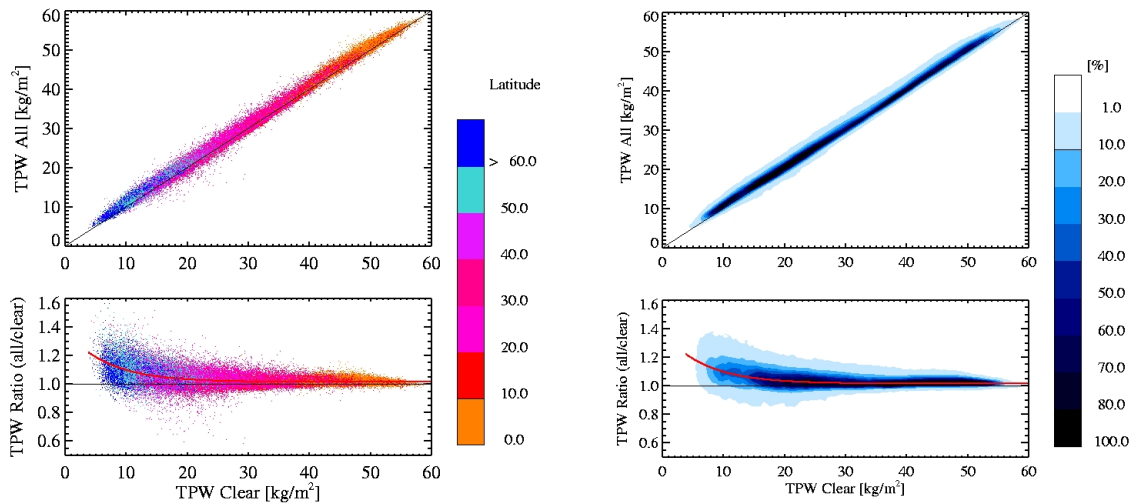


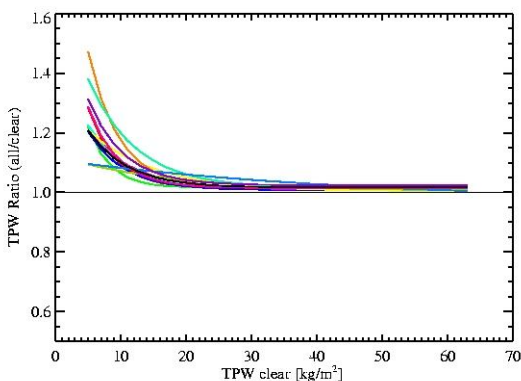
Figure 7.10: Relation of clear-sky TPW to the all-sky TPW (upper panel) and to the ratio of all-sky TPW and clear-sky TPW. The TPW is given in $[\text{kg/m}^2]$. Data are taken from February 2001 to October 2005 (except 2002). A: Colours give the latitude range. B: Frequency distribution of the data points in figure A.

The difference in all-sky to clear-sky TPW is largest in the mid- and high-latitudes. Due to the temperature humidity coupling the excess water vapour therefore is largest when the clear-sky TPW is related to cold dry atmospheres. Here the excess water vapour is about 20%, in absolute numbers about 1–2 kg/m². The excess water vapour decreases with increasing clear-sky TPW values but still 1% underestimation occurs for the tropics. The frequency distribution for global excess water vapour gives a mean underestimation in TPW of 2.6%.

7.3 Concluding remarks

The AMSU retrieval of TPW for non-precipitating clouds over four years of data are used to derive monthly mean excess water vapour. For the ocean areas a power-law function describes the relation of the excess water vapour on the clear-sky TPW. Largest all-to-clear TPW ratios are observed in the mid- to high-latitudes. Here the underestimation due to neglecting clouds in TPW climatologies is about 20% (1-2 kg/m²). The functional behaviour is established for monthly and seasonal means for individual years. This behaviour does not change significantly when multiyear averages are used. Thus, we conclude that it is feasible to perform an all-sky correction of TPW based on clear-sky measurements.

A: Excess water vapour



B: underestimation

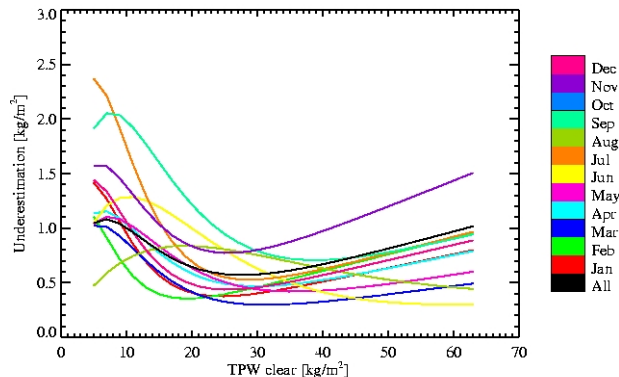
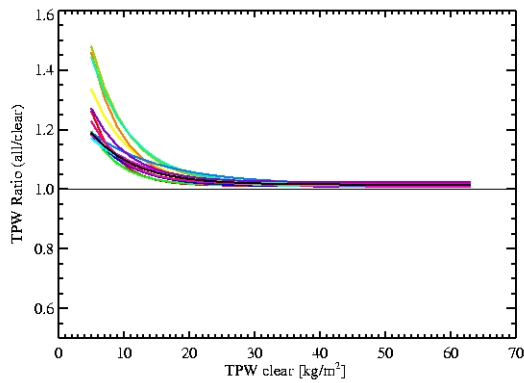


Figure 7.11: A Excess water vapour depending on the clear-sky TPW for the year 2004. B Clear-sky water vapour bias as derived from the excess water vapour. Colours denote the month. The underestimation is given in relation to the clear-sky water vapour path used in a climatology.

A: Excess water vapour



B: underestimation

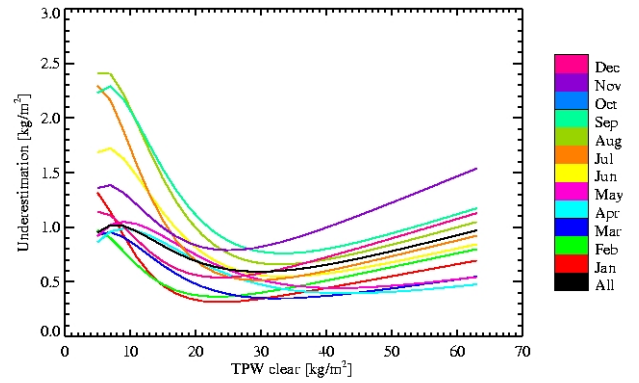
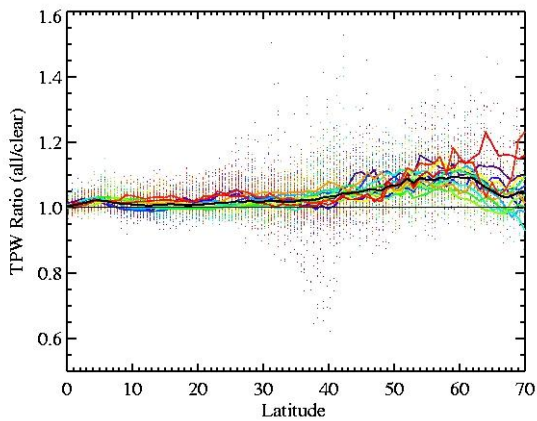


Figure 7.12: A Excess water vapour depending on the clear-sky TPW for the years 2001–2005 (except 2002). B Clear-sky water vapour bias as derived from the excess water vapour. Colours denote the month. The underestimation is given in relation to the clear-sky water vapour path used in a climatology.

A: 2004



C: 2001–2005

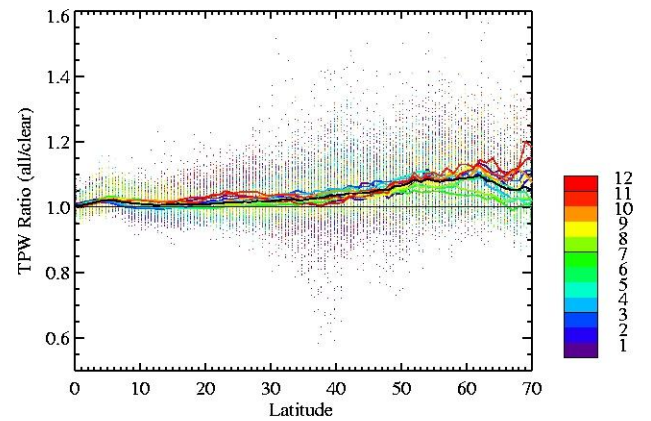


Figure 7.13: Zonal distribution of the ratio (all-sky TPW by clear-sky TPW). Colours denote the month. A: only 2004 data, and B: data are taken from February 2001 to October 2005 (except 2002).

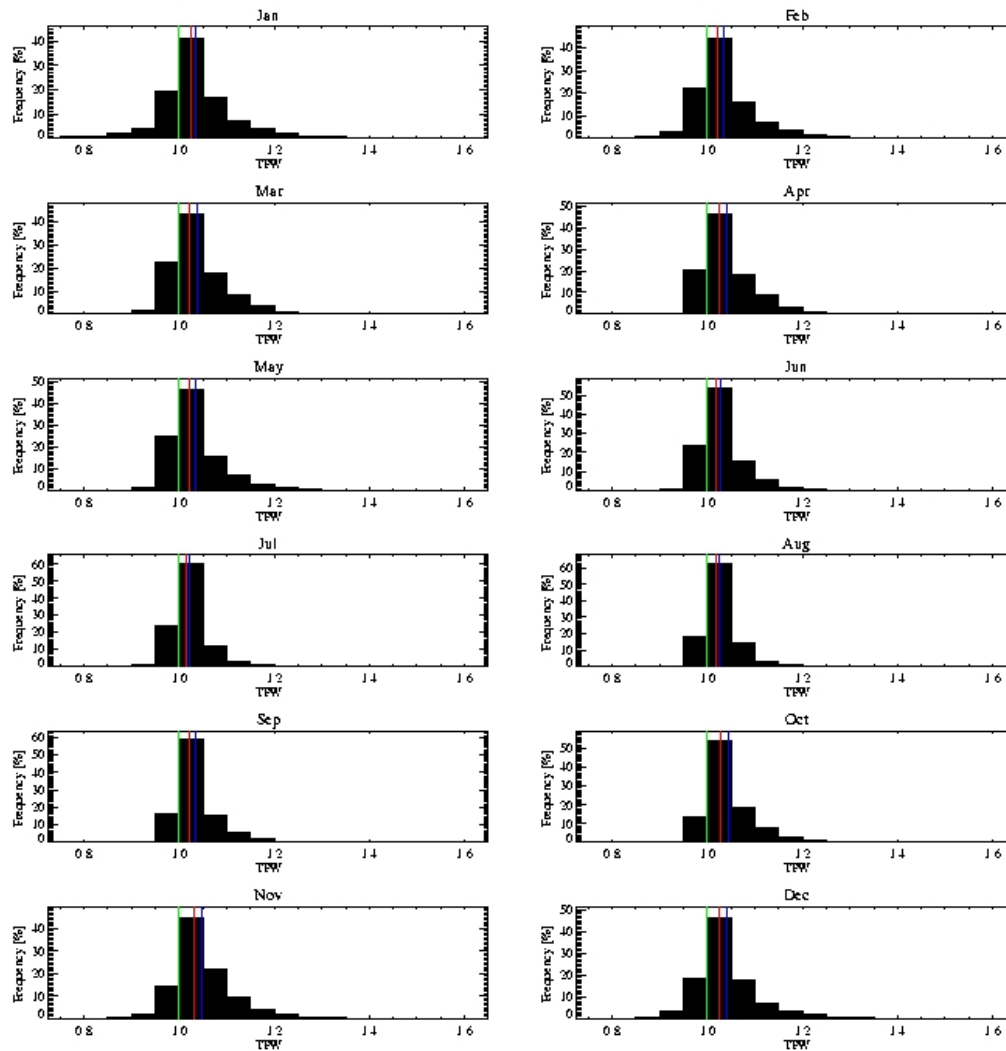


Figure 7.14: Frequency distribution of the excess water vapour of each month for the North Atlantic for the years 2001-2005 (except 2002). The green line gives the excess water vapour of 1. In red the median and in blue the mean value of the distribution is marked.

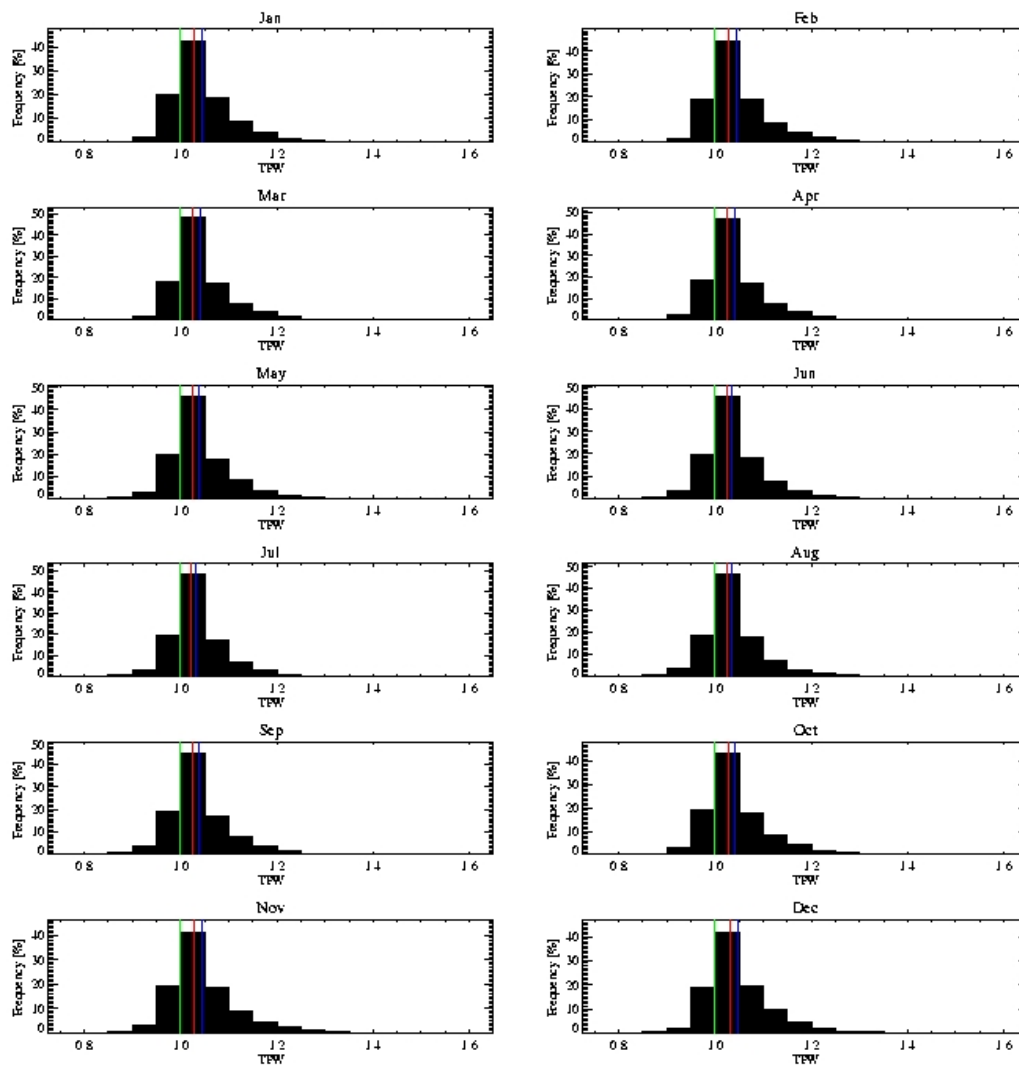
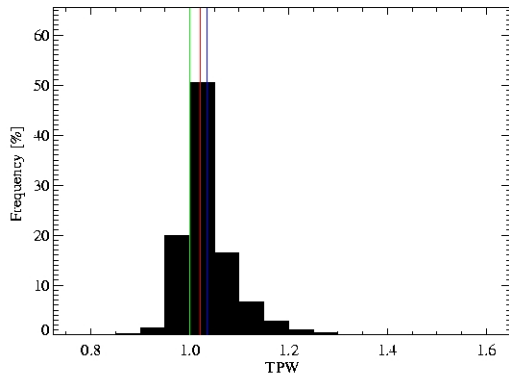


Figure 7.15: Global frequency distribution of the excess water vapour of each month for the years 2001-2005 (except 2002). The green line gives the excess water vapour of 1. In red the median and in blue the mean value of the distribution is marked.

A: North Atlantic



B: Global

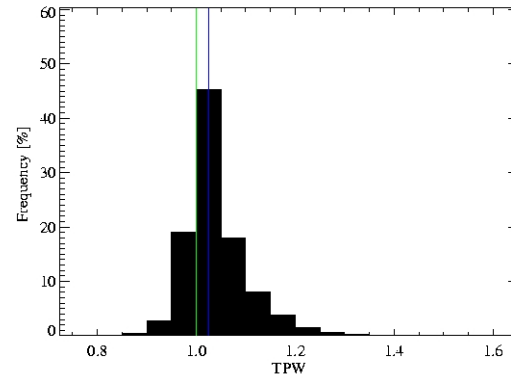


Figure 7.16: Frequency distribution of the excess water vapour for the North Atlantic (A) and global (B) for the years 2001-2005 (except 2002). The green line gives the excess water vapour of 1. In red the median and in blue the mean value of the distribution is marked.

Month	A_0	A_1	A_2
North Atlantic			
Jan	0.896	0.776	1.011
Feb	0.564	0.798	1.013
Mar	0.399	0.850	1.009
Apr	0.298	0.888	1.007
May	0.318	0.887	1.008
Jun	0.737	0.848	1.013
Jul	1.249	0.813	1.015
Aug	1.121	0.838	1.017
Sep	0.965	0.849	1.019
Oct	0.277	0.912	1.015
Nov	0.599	0.838	1.024
Dec	0.578	0.817	1.018
All	0.366	0.863	1.015

Table 7.1: The parameters of the function expressing the ratio vs clear-sky TPW using all years.

Year	N	N (1)	mean	median	Standart Dev.
North Atlantic					
Year	686087	1017	1.035	1.022	0.0575
Jan	59658	313	1.036	1.024	0.0831
Feb	59660	127	1.036	1.021	0.0678
Mar	59659	61	1.039	1.023	0.0599
Apr	59660	78	1.040	1.024	0.0548
May	59660	205	1.034	1.020	0.0551
Jun	59660	44	1.029	1.018	0.0442
Jul	59660	12	1.021	1.014	0.0345
Aug	59660	34	1.026	1.018	0.0358
Sep	59660	4	1.036	1.023	0.0478
Oct	59660	12	1.044	1.029	0.0549
Nov	44745	72	1.047	1.033	0.0663
Dec	44745	55	1.040	1.025	0.0669
Global					
Year	9435516	6371	1.026	1.026	0.0626
Jan	820477	1611	1.044	1.028	0.0686
Feb	820480	317	1.044	1.029	0.0628
Mar	820479	148	1.041	1.026	0.0604
Apr	820480	196	1.041	1.026	0.0617
May	820480	467	1.039	1.026	0.0596
Jun	820480	381	1.036	1.024	0.0599
Jul	820480	1063	1.032	1.022	0.0552
Aug	820480	1349	1.036	1.024	0.0612
Sep	820480	163	1.038	1.024	0.0648
Oct	820480	189	1.041	1.027	0.0646
Nov	615360	295	1.045	1.029	0.0697
Dec	615360	192	1.047	1.031	0.0659

Table 7.2: Statistical parameters discribing the frequency distributions of the excess water vapour.

Chapter 8

Final summary and conclusions

Investigating the variability of atmospheric water is an important task. This study summarises the various attempts to measure atmospheric water with ground-based and satellite-based techniques. In chapter 3 the methods under investigation are described. As part of this thesis the influence of clouds on the water vapour retrieval is investigated. Chapter 4 introduces a neural network technique for microwave retrieval of LWP and TPW from AMSU measurements. The large radiometer field of view of the AMSU instrument leads to the question whether sub-pixel inhomogeneity in clouds affect the LWP retrieval, as the measured brightness temperatures represent the integral over the projected field of view. Therefore, in chapter 5 the AMSU-NN retrieval was compared to retrieval using instrument with a higher resolution. The AVHRR instrument was used to retrieve the sub-pixel information. The comparison of AVHRR LWP retrieval with the AMSU-NN retrieval show that AVHRR-LWP is larger than the AMSU retrieved LWP. This result is explainable with both used algorithms and their limitations. The use of visible frequencies for the retrieval of cloud optical properties is based on the assumption, that the scattered signal from top of the cloud is directly related to the entire cloud. Ice layers on top of the cloud have a high albedo leading to a possible overestimation of the vertical integrated condensed water. On the other hand, ice particles scatter microwave emission and the emission of the ice water itself is lower than the emission of liquid water. An underestimation of LWP will result in cases of ice particles on top of the cloud.

The relation of the TPW and LWP retrieved with AMSU does not depend on the sub-pixel inhomogeneity. Here only cloud cover was investigated. In future work, further cloud properties like cloud type, surface temperature variability should be used to define the sub-pixel inhomogeneity. Comparing the neural network based algorithm with the results from the operational AMSU algorithm at NOAA-NESDIS show reasonable agreements. Differences can be explained by differences in available data used for the retrievals. The conclusion here is that the NN based retrieval does not provide a significant improvement compared to the simplified physically based retrievals. Therefore, the operational AMSU algorithm is used further on in this study.

This study focuses on the characterisation of water vapour in cloudy scenes. The relation of the water vapour in clear and all-sky situations is investigated using radiosonde humidity profiles and satellite based TPW. Previous work show a lower TPW in clear cases compared to cloudy cases. For example within the EU-Project CLIWA-NET three intensive field campaigns were performed to measure cloud properties and to validate satellite LWP algorithms with ground based radiometers. As a result of the first campaign, CNN1, during August and September 2000, Crewell et al. (2002) estimate as a climatological relationship that the TPW in clear sky is 80% of the TPW in cloudy atmospheres.

From radiosonde humidity profiles with colocated cloud observations it is proven that the vertically integrated absolute humidity is increasing with cloud cover. Compared to clear-sky TPW there is about 10–20% more water in cloudy atmospheres.

The examination of Lindenberg TPW (see chapter 6) in both clear- and all-sky situations shows a strong coupling of the monthly mean clear- to the all-sky values. The ratio of all- to clear-sky TPW, denoted as excess water vapour, is large in cases of small mean TPW, which occurs during winter time only. For low cloud cover the excess water vapour is not effected. Furthermore, small uncertainties in the definition of clear-sky situations are not effecting the determined excess water vapour. These results were based on cloud detection by the synoptical observations. However, for broken cloudiness the radiosonde not necessarily passes a cloud during the ascent. Therefore a threshold in the minimum dewpoint difference in the profile is used as an additional cloud detection criteria. With this the different stations have the same data amount and a sufficient number of cases for the calculation of monthly mean TPW. For clear-sky TPWs larger than 10 kg/m^2 the excess water vapour is nearly constant between 1.1 to 1.3. Towards lower clear-sky TPW the increase differs from station to station. Maximum excess water vapour values of 1.5 are found for clear-sky TPW of 5 kg/m^2 . These clear-sky TPW situations are rare and the regression is based on few data only.

For the European region a parameterisation for the dependency of clear- to all-sky TPW has been derived. The relation depends on season and surface pressure. In high pressure situations the relation of excess water vapour is not pronounced.

The results have also been discussed in terms of statistical sampling errors. Mean TPW values are sensitive to the number of cases included. The significance of these results is strongly depending on the number of input data. Specific weather situations may bias the mean, especially for clear-sky TPW.

A number of studies performed at the IFM-GEOMAR have demonstrated that the advection of water vapour from the Atlantic Ocean towards Europe is basically driven by the NAO pattern (Ruprecht et al. (2002) and Ruprecht and Kahl (2003)). It was shown in this study that the NAO index correlates well with the clear-sky and cloudy-sky TPW derived from radiosonde but the excess water vapour is not depending on the NAO index.

The monthly mean excess water vapour over the oceans is examined with AMSU measurements (chapter 7). For non-precipitating clouds a functional relation of the excess water vapour depending on the clear-sky TPW similar to the surface based analysis is found.

For the different oceans only small variations occur. The excess water vapour is about 1% in the tropics and increases polewards. The influence of clouds on the TPW is largest in the mid- to high latitudes. Here the underestimation due to neglecting clouds in TPW climatologies is about 20% (1-2 kg/m²), i.e. the ratio is 1.2. The functional behaviour is established for monthly and seasonal means for individual years. This behaviour does not change significantly when multiyear averages are used. Thus, we conclude that it is feasible to perform a climatological all-sky correction of TPW based on clear-sky measurements. The excess water vapour retrieved from AQUA measurements show values of the same magnitude on global scale as our study. With a ratio of 1.5 the median of the excess water vapour distribution is slightly larger, then the one derived here (private communications with Chris O'Dell, University Wisconsin, Madison).

Comparing the ratio in clear- to cloudy TPW over land using radiosonde and synoptical data to the AMSU retrieved ratio, the difference is small. Both retrieval techniques show mean ratios of 1.2 to 1.3. The latitudinal dependency found in the European data set is shown in the AMSU fields as well.

The present study is limited to non-precipitating clouds with LWP lower than 0.5 kg/m². Thus, taking all clouds into account may lead to different relations between clear- and cloudy-sky TPW. This is indicated by small difference between satellite and radiosonde excess water vapour. In this study the focus is on the difference in vertical integrated water vapour in clear and cloudy situations. The difference in the TPW is quantified. Since the Greenhouse efficiency of water vapour is depending on its vertical distribution, a more detailed study on the differences in vertical distributed water vapour in clear and cloudy atmospheres should be subject to future work.

Appendix A

Abbreviations and Acronyms

AERI	Atmospheric Emitted Radiance Interferometer
AMSU	Advanced Microwave Sounding Unit
ARM	Atmospheric Radiation Measurement Program
AQUA	NASA scientific satellite, EOS-PM1
ATOVS	Advanced TIROS Operational Sounder
ATSR	Along Track Scanning Radiometer
AVHRR	Advanced Very High Resolution Radiometer
BALTEX	Baltic Sea Experiment
BBC	BALTEX BRIDGE campaign
BKN	Broken Cloudiness
CAMP	CEOP Asia-Australia monsoon project
CART	Clouds and Radiation Testbed
CATCH	Coupling Tropical Atmosphere and Hydrologic Cycle
CEOP	Coordinated Enhanced Observational Periods
CEPEX	Central Equatorial Pacific Experiment
CHAMP	Challenging Minisatellite Payload
CLIWA NET	BALTEX Cloud Liquid Water Network
CLR	Clear Sky
CLW	Cloud Liquid Water
CM-SAF	Cloud Monitoring Satellite Application Facility
CNN	CLIWA-NET NETWORK
CRYSTAL	Cirrus Regional Study of Tropical Anvils and Cirrus Layers
DIAL	Differential Absorption Lidar
DMSP	Defense Meteorological Satellite Program
DOE	Department of Energy
DWD	Deutscher Wetterdienst
ECMWF	European Centre of Medium Range Weather Forecasts
ENVISAT	Environmental Satellite
EOS	Earth Observation System
ERS	European Remote Sensing Satellite

EWV	Excess Water Vapour
FACE	Florida Area Cirrus Experiment
FGGE	First GARP Global Experiment
FOV	Field of View
GAPP	GEWEX Americas Prediction Project
GARP	Global Atmospheric Research Program
GENLN2	General line-by-line atmospheric transmittance and radiance model
GEWEX	Global Energy and Water Cycle Experiment
GHz	Giga Hertz
GKSS	Gesellschaft für Kernforschung in Schiffbau und Schifffahrt
GOES	Geostationary Operational Environmental Satellite
GOME	Global Ozone Monitoring Experiment
GPS	Global Positioning System
GVAP	Global water Vapor Project
HIRS	High-resolution Infrared Radiation Sounder
HITRAN	High Resolution Transmission Molecular Absorption Database
IASI	Infrared Atmospheric Sounding Interferometer
IHOP	International H ₂ O Project
IPCC	International Panel on Climate Change
IR	Infrared
ITCZ	Inner Tropical Convergence Zone
IWP	Ice Water Path
JPL	Jet Propulsion Laboratory
KNMI	Koninklijk Nederlands Meteorologisch Instituut
LBA	The Large Scale Biosphere-Atmosphere Experiment
LIDAR	Light Detection and Ranging
LWP	Liquid Water Path
MAGS	Mackenzie GEWEX Study
MARSS	Microwave Airborne Radiometer Scanning System
MASTEX	Mediterranean Aircraft and Ship Transmission Experiment
MERIS	Medium Resolution Imaging Spectrometer
METEOSAT	Meteorological Satellite
MHS	Microwave Humidity Sounder
MODIS	Moderate Resolution Imaging Spectroradiometer
MOL	Meteorological Observatory Lindenberg
MOTH	Measurements of Tropospheric Humidity
MSG	Meteosat Second Generation
MSU	Microwave Sounding Unit
MW	Microwave
MWMOD	Microwave Model
MWR	Microwave Radiometer
NASA	National Aeronautics and Space Agency, USA
NAO	North Atlantic Oscillation
NCAR	National Center for Atmospheric Research, USA
NCEP	National Centers for Environmental Prediction, USA

NESDIS	National Environmental Satellite, Data and Information Services
NIR	Near Infrared
NN	Neural Network
NOAA	National Oceanic and Atmospheric Administration, USA
NVAP	NASA Water Vapor Project
OACS	Optical Absorption Coefficient Spectroscopy
OLR	Outgoing Longwave Radiation
OVC	Overcast
POES	Polar-Orbiting Operational Environmental Satellites
RMS	Root Mean Square
SAA	Satellite Active Archive
SAF	Satellite Application Facility
SAMEX	Storm and Mesoscale Ensemble Experiment
SCAMS	Scanning Microwave Spectrometer
SCIAMACHY	Scanning Imaging Absorption Spectrometer for Atmospheric Cartography
SCT	Scattered
SEVIRI	Spinning Enhanced Visible and Infrared Imager
SGP	Southern Great Plains
SHEBA	Surface Heat Budget of the Arctic Ocean Project
SIRTA	Le Site Instrumental de Recherche par Télédétection Atmosphérique
SMHI	Sveriges Meteorologiska och Hydrologiska Institut
SMMR	Scanning Multichannel Microwave Radiation
SSM/I	Special Sensor Microwave/Imager
SSM/T-2	Special Sensor Microwave/Temperature
SST	Sea Surface Temperature
TERRA	NASA scientific satellite, EOS-AM1
TIROS	Television Infra-Red Observation Satellite
TMI	TRMM Microwave Imager
TOVS	TIROS Operational Vertical Sounder
TPW	Total Precipitable Water
TRMM	Tropical Rainfall Measurement Mission
TSB	temporal Sampling Bias
UTH	Upper Tropospheric Humidity
UV	Ultra Violet
VAPIC	Water Vapour Profiling Inter-Comparison campaign
VLBI	Very Long Baseline Interferometry
WMO	World Meteorological Organisation
WVP	Water Vapour Path
WVR	Water Vapour Radiometer

Appendix B

Cloud Cover

For noon overpasses the cloud cover of a grid box is retrieved. For this purpose the AVHRR channels are used as described in chapter 3.2.4. The spatial mean LWP and TPW are correlated depending on the cloud cover of the grid cell. In figure B.1 the relation for a $4.0^\circ \times 4.0^\circ$ grid is shown. There are no dependencies found of the cloud cover to the correlation of the mean LWP to the TPW. Similar results are shown in figure B.2 for a $1.0^\circ \times 1.0^\circ$ grid.

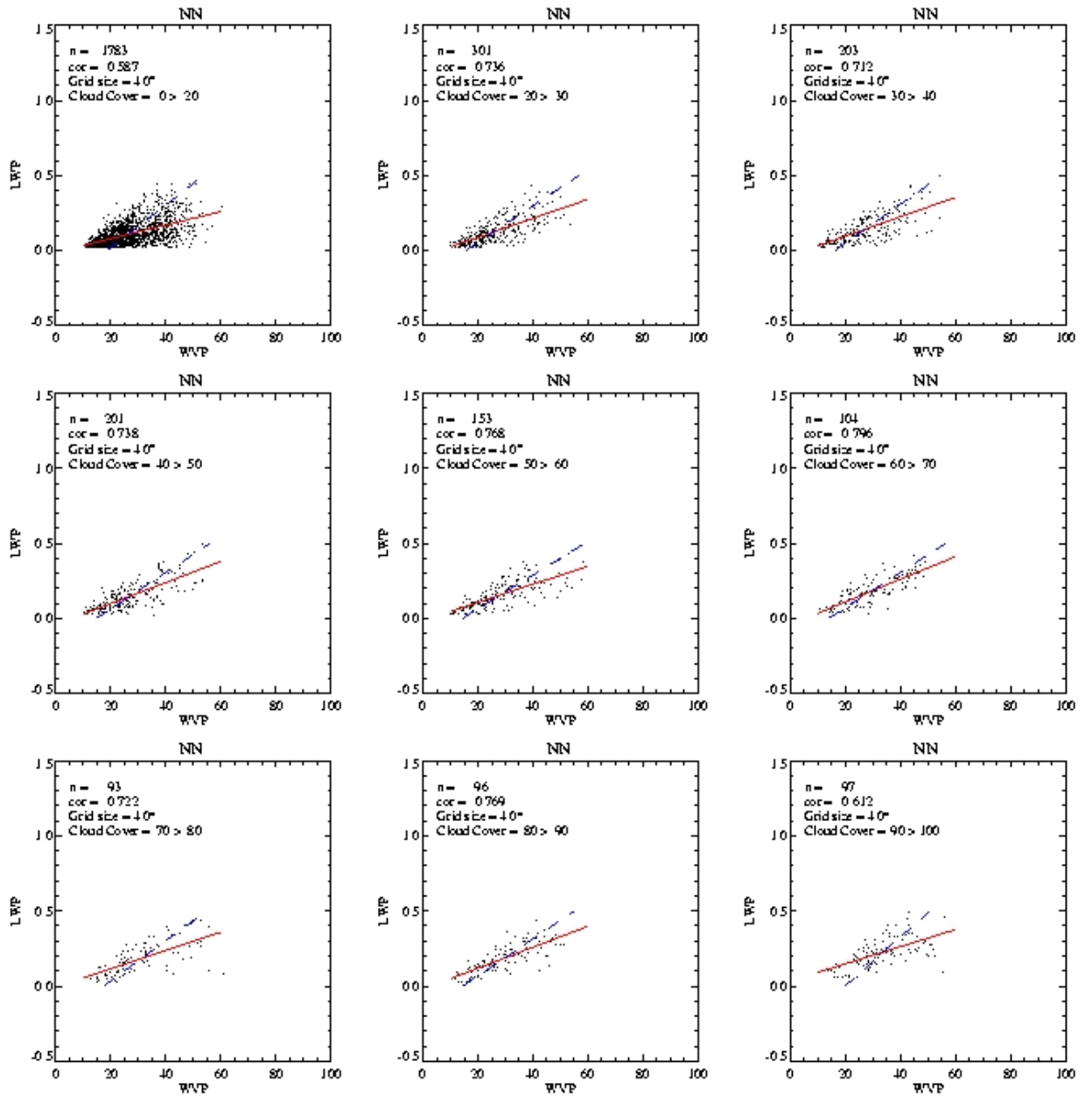


Figure B.1: Influence of cloud cover on the relation LWP to TPW . LWP is given in kg/m^2 and the TPW in kg/m^2 . The retrieved values are sampled on a $4.0^\circ \times 4.0^\circ$ grid.

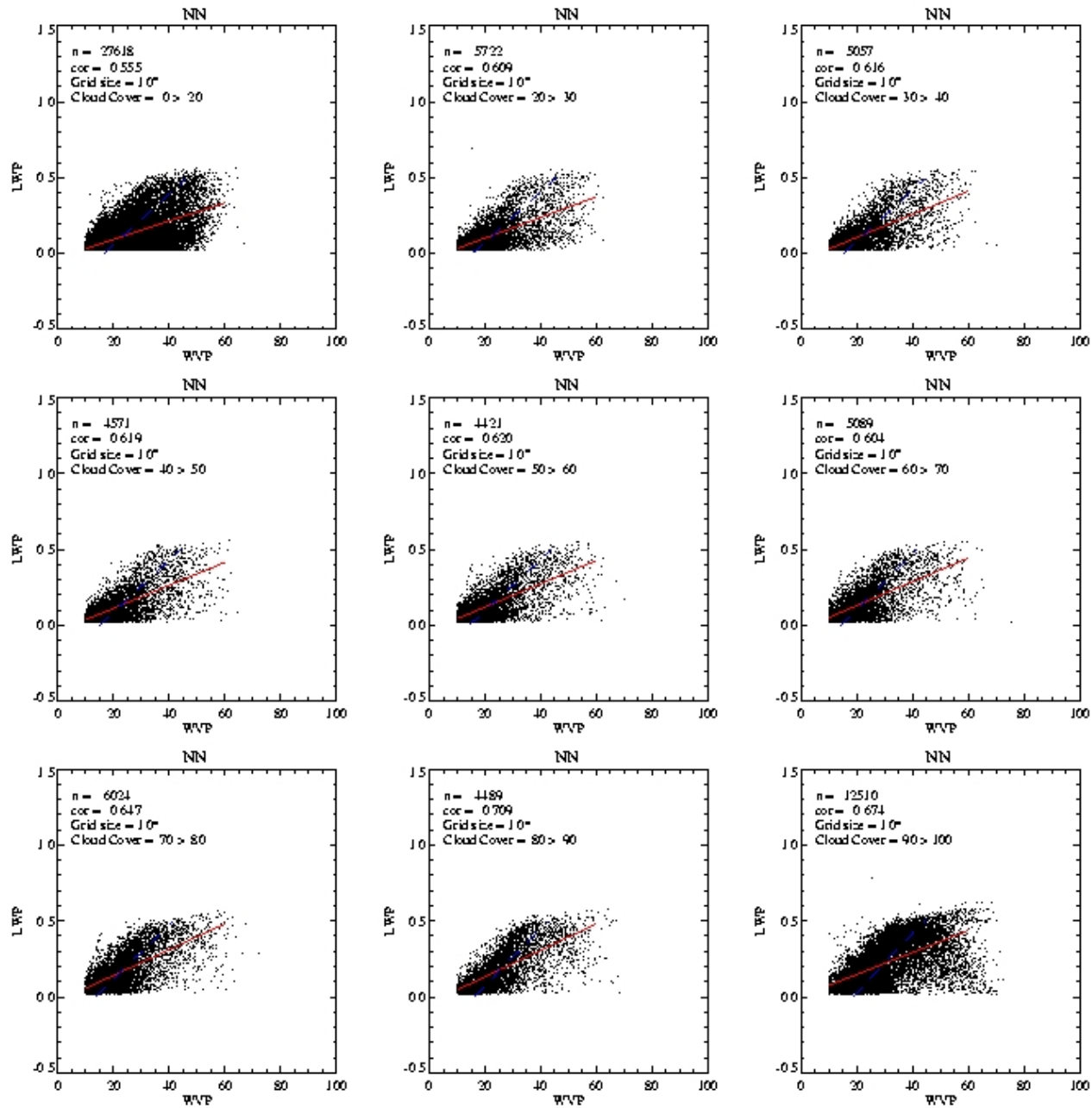


Figure B.2: Influence of cloud cover on the relation LWP to TPW. LWP is given in kg/m² and the TPW in kg/m². The retrieved values are sampled on a 1.0° × 1.0° grid.

Appendix C

Frequency distributions

The distribution of the TPW and LWP on a 1.0° grid is shown in figure C1. For the TPW a bimodal structure is found for the global ocean. A separate regard of the ocean basins and by the northern and southern part show, that the peak at high water vapour path is not strongly present. A cause can be found in the movement of the inner tropical convergence zone over the year.

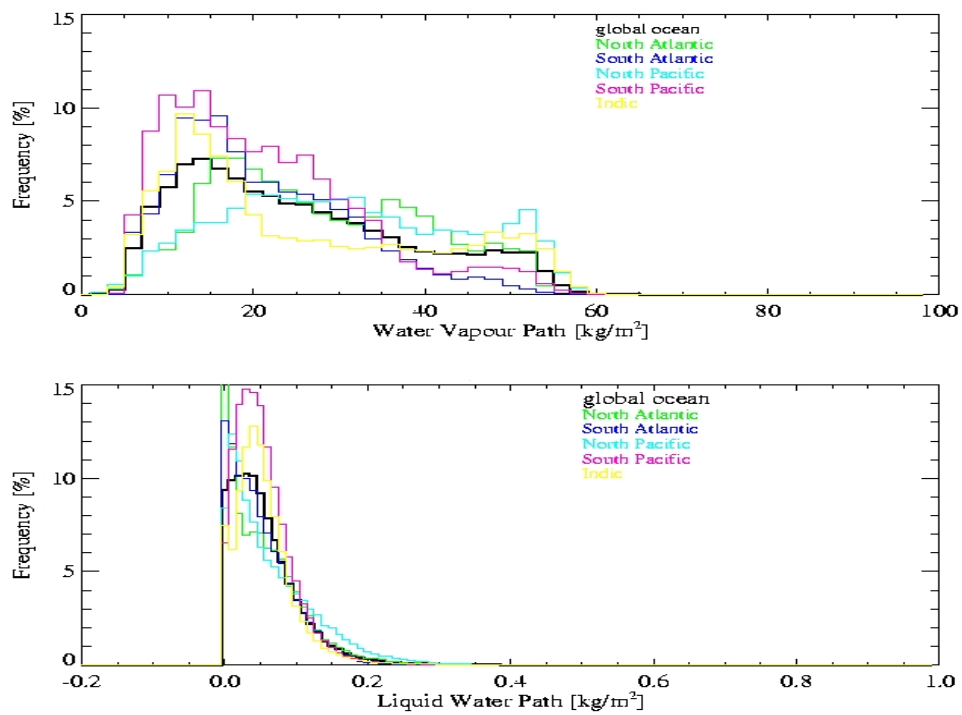


Figure C.1: TPW(upper) and LWP(lower) frequency distributions relative to the covered amount of pixels on a 1.0° grid. Monthly means are shown. (February to December 2001).

Appendix D

Cloud — clear statistics from radiosonde measurements

	DJF		MAM		JJA		SON		Year	
	TPW	N	TPW	N	TPW	N	TPW	N	TPW	N
Lindenberg										
CLR	4.95	67	9.04	45	18.09	24	12.94	42	9.64	178
SCT	6.89	104	12.26	180	22.78	212	14.32	157	15.31	653
BKN	9.15	308	13.20	413	23.24	520	16.60	422	16.45	1663
OVC	11.58	373	15.94	261	28.06	156	19.17	262	17.00	1052
ALL	9.61	852	13.60	899	23.82	912	16.79	883	16.06	3546
Schleswig										
CLR	4.45	19	10.56	32	24.67	8	13.63	10	10.96	69
SCT	6.03	139	10.11	192	20.22	222	12.63	169	13.02	722
BKN	8.93	356	12.24	454	21.47	561	15.41	477	15.22	1848
OVC	13.03	305	16.31	211	26.31	119	20.31	226	17.58	861
ALL	9.86	819	12.69	889	21.82	910	16.11	882	15.26	3500
Essen										
CLR	4.67	45	8.15	32	22.40	23	11.74	21	10.19	121
SCT	7.27	130	11.08	180	21.34	252	13.48	159	14.51	721
BKN	10.04	312	12.90	426	22.28	420	16.63	368	15.79	1526
OVC	13.62	290	17.87	201	27.92	123	19.80	243	18.42	857
ALL	10.60	777	13.52	839	22.84	818	16.84	791	15.99	3225
Stuttgart										
CLR	5.25	28	8.07	13	17.64	6	10.87	15	8.40	62
SCT	7.70	101	11.50	141	21.88	227	13.53	122	15.26	591
BKN	10.05	276	13.71	274	23.65	280	16.21	292	15.94	1122
OVC	11.61	253	16.36	182	26.85	98	18.92	201	16.82	734
ALL	10.09	658	13.87	610	23.45	611	16.43	630	15.85	2509

Table D.1: Seasonal and annual mean TPW in kg/m^2 in the cloud classes (CLR = clear, SCT = scattered (1-4 octas), BKN = broken (5-7 octas), OVC = overcast) and without regards to cloudiness (ALL) for the four German stations. N gives the number of observations comprising the mean.

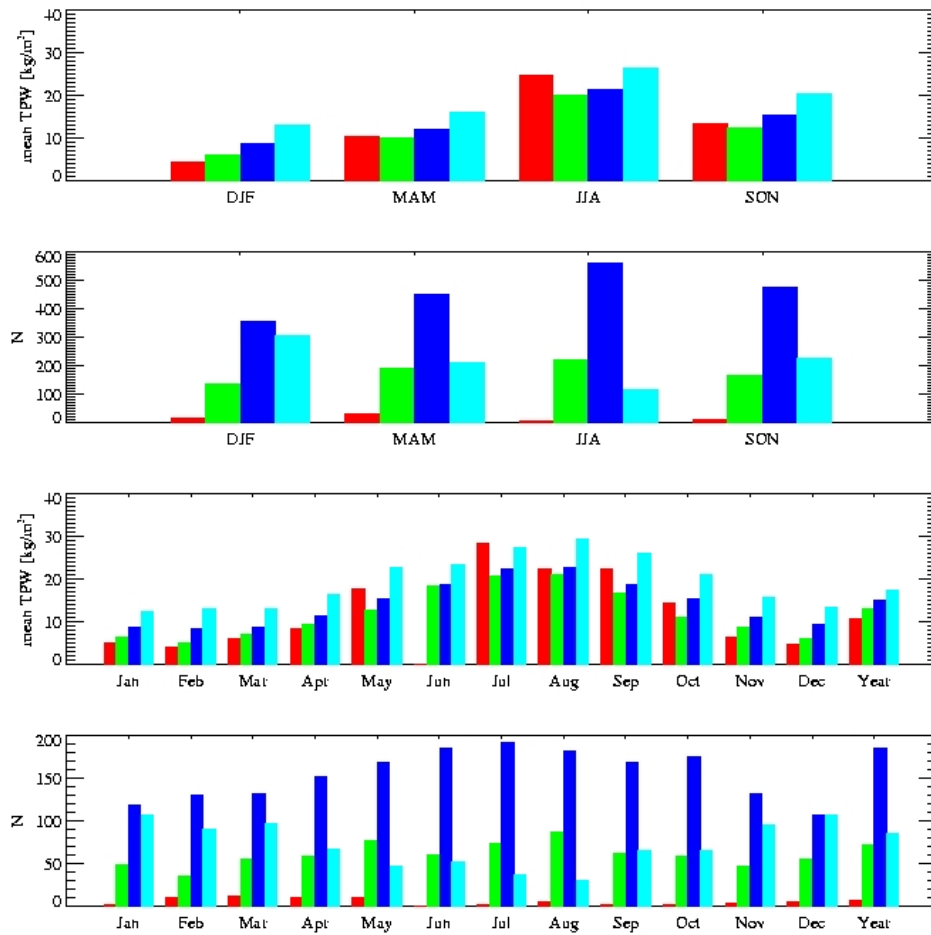


Figure D.1: 10 years of data from Schleswig sorted by the observed cloud cover: clear-sky in red, scattered cloudiness (1-4 octas) in green, broken cloudiness (5-7 octas) in blue, and overcast in cyan. From Top to bottom: Seasonal mean TPW in the cloud classes, number of cases per cloud class per season, monthly mean TPW per cloud classes and the number of cases per class. The last block in the monthly dispartment gives yearly mean (for the number of cases is given by the ordinate number times 10).

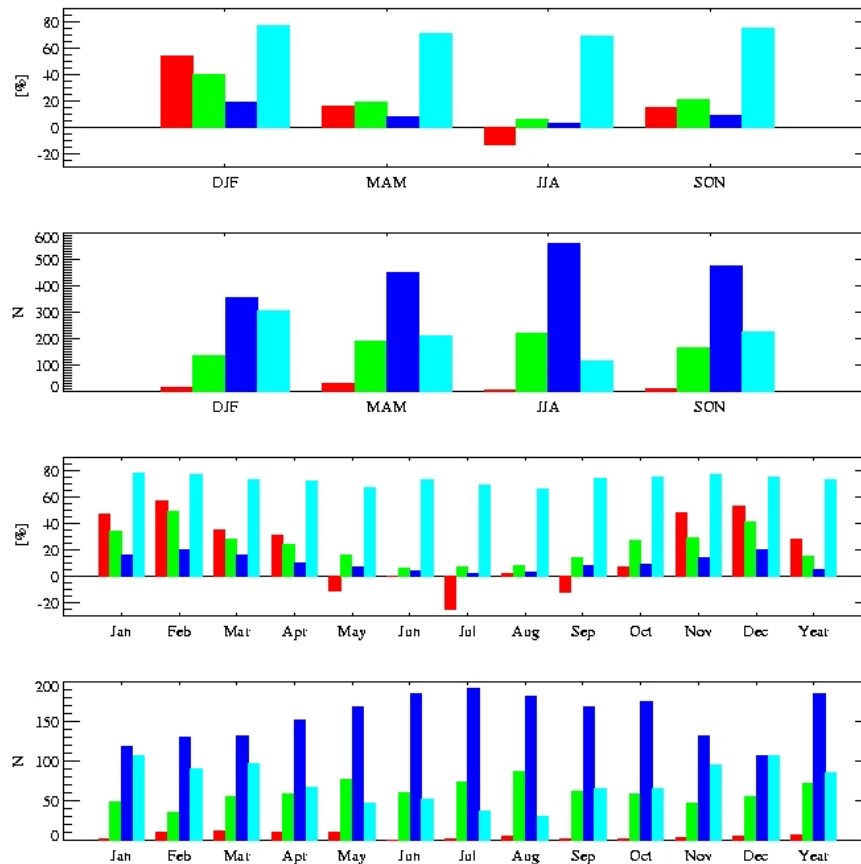


Figure D.2: The bias estimators and the probability according to Gaffen and Elliot (1993): the b_0 in red, b_4 in green, b_7 in blue, and the probability in cyan. From Top to bottom: Seasonal bias estimators, number of cases per cloud class (see figure D.1) per season, monthly bias estimators and the number of cases per class. The last block in the monthly dispartment gives yearly mean (for the number of cases is given by the ordinate number times 10).

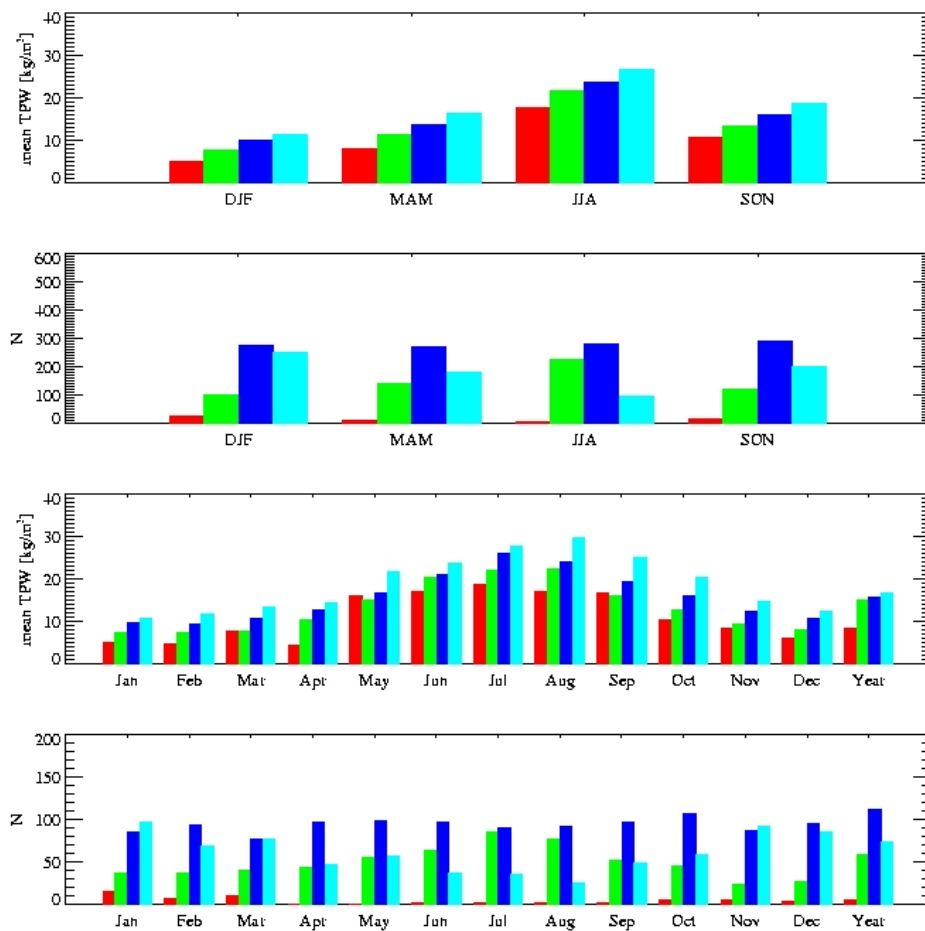


Figure D.3: 10 years of data from Stuttgart sorted by the observed cloud cover: clear-sky in red, scattered cloudiness (1-4 octas) in green, broken cloudiness (5-7 octas) in blue, and overcast in cyan. From Top to bottom: Seasonal mean TPW in the cloud classes, number of cases per cloud class per season, monthly mean TPW per cloud classes and the number of cases per class. The last block in the monthly dispartment gives yearly mean (for the number of cases is given by the ordinate number times 10).

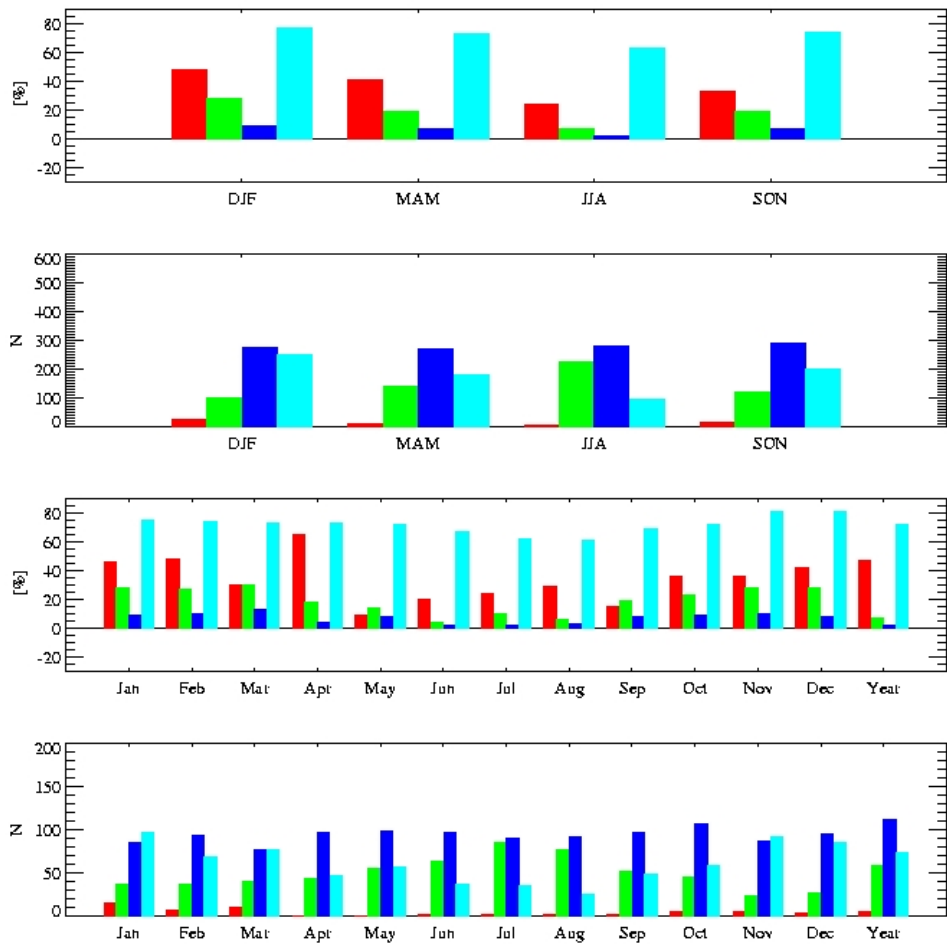


Figure D.4: The bias estimators and the probability according to Gaffen and Elliot (1993): the b_0 in red, b_4 in green, b_7 in blue, and the probability in cyan. From Top to bottom: Seasonal bias estimators, number of cases per cloud class (see figure D.3) per season, monthly bias estimators and the number of cases per class. The last block in the monthly dispartment gives yearly mean (for the number of cases is given by the ordinate number times 10).

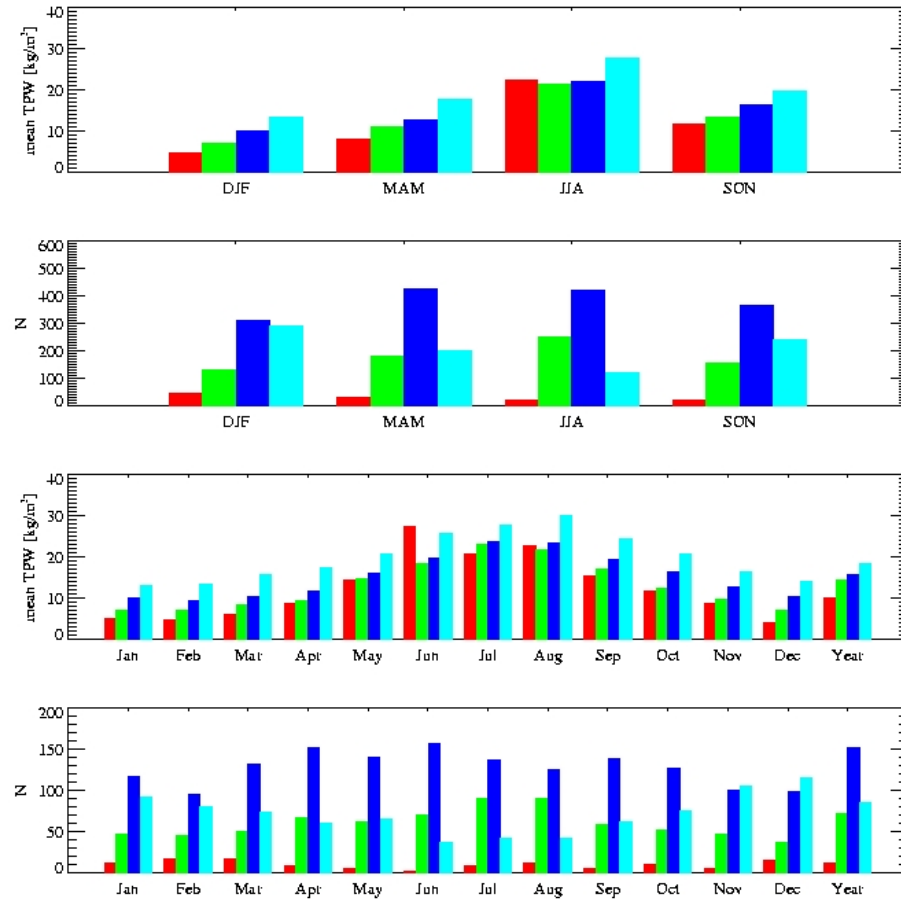


Figure D.5: 10 years of data from Essen sorted by the observed cloud cover: clear-sky in red, scattered cloudiness (1-4 octas) in green, broken cloudiness (5-7 octas) in blue, and overcast in cyan. From Top to bottom: Seasonal mean TPW in the cloud classes, number of cases per cloud class per season, monthly mean TPW per cloud classes and the number of cases per class. The last block in the monthly dispartment gives yearly mean (for the number of cases is given by the ordinate number times 10).

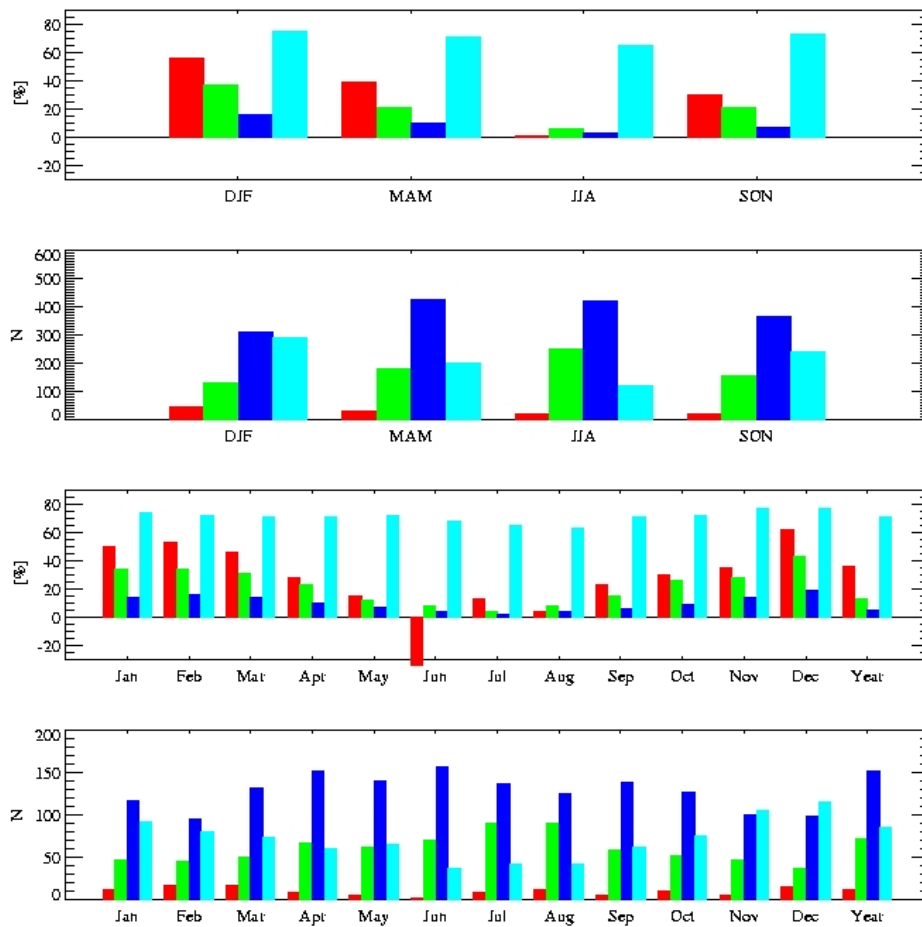


Figure D.6: The bias estimators and the probability according to Gaffen and Elliot (1993): the b_0 in red, b_4 in green, b_7 in blue, and the probability in cyan. From Top to bottom: Seasonal bias estimators, number of cases per cloud class (see figure D.5) per season, monthly bias estimators and the number of cases per class. The last block in the monthly dispartment gives yearly mean (for the number of cases is given by the ordinate number times 10).

	DJF	MAM	JJA	SON		DJF	MAM	JJA	SON
Lindenberg					Schleswig				
CLR/OVC	0.43	0.57	0.64	0.67	CLR/OVC	0.34	0.65	0.94*	0.67
SCT/OVC	0.60	0.77	0.81	0.75	SCT/OVC	0.46	0.62	0.77	0.62
BKN/OVC	0.79	0.83	0.83	0.87	BKN/OVC	0.68	0.75	0.82	0.76
B0	0.48	0.33	0.24	0.23	B0	0.55	0.17	-0.13*	0.15
B4	0.36	0.15	0.06	0.16	B4	0.41	0.20	0.07	0.21
B7	0.16	0.07	0.04	0.06	B7	0.19	0.09	0.03	0.09
P	0.76	0.71	0.68	0.73	P	0.77	0.71	0.70	0.76
Essen					Stuttgart				
CLR/OVC	0.34	0.46	0.80	0.59	CLR/OVC	0.45	0.49	0.66*	0.57
SCT/OVC	0.53	0.62	0.76	0.68	SCT/OVC	0.66	0.70	0.81	0.72
BKN/OVC	0.74	0.72	0.80	0.84	BKN/OVC	0.87	0.84	0.88	0.86
B0	0.56	0.40	0.02	0.30	B0	0.48	0.42	0.25*	0.34
B4	0.38	0.21	0.06	0.21	B4	0.29	0.19	0.07	0.19
B7	0.17	0.10	0.04	0.08	B7	0.09	0.08	0.03	0.07
P	0.75	0.72	0.66	0.74	P	0.77	0.73	0.64	0.74

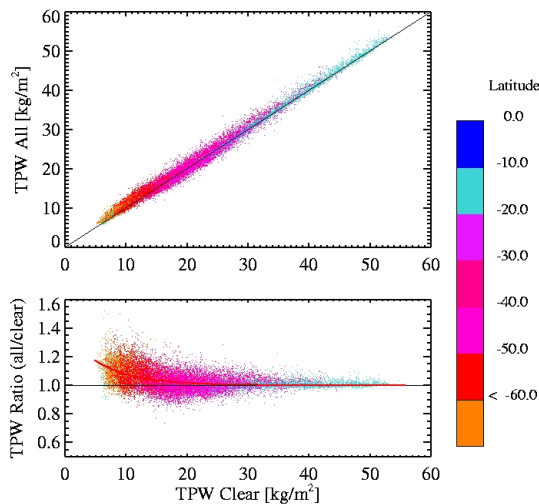
Table D.2: Seasonal ratios of the mean TPW in a cloud class (CLR = clear, SCT = scattered (1-4 octas), BKN = broken (5-7 octas)) towards the overcast mean TPW (OVC) for each station. The bias indices (dimensionless), and the probability of a sounding passing through a cloud as defined in the equations 6.2 to 6.5 are given. A dash is given when no clear-sky observations are done, ratios and indices based on less than 10 observations are marked (*).

Appendix E

Spatial TPW as measured from Satellite

E.1 South Atlantic

A : Excess water vapour depending on Latitude



B: Excess water vapour frequency distribution

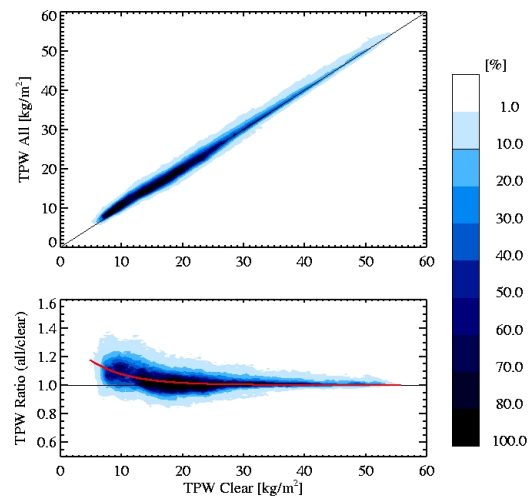
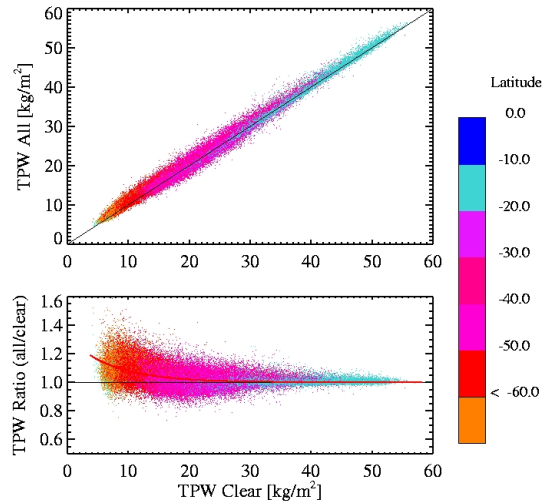


Figure E.1: *South Atlantic: Relation of clear-sky TPW to the all-sky TPW (upper panel) and to the ratio of all-sky TPW and clear-sky TPW. The TPW is given in $[\text{kg}/\text{m}^2]$. Data are taken from the year 2004. A: Colours give the latitude range. B: Frequency distribution of the data points in figure A.*

A : Excess water vapour depending on Latitude



B: Excess water vapour frequency distribution

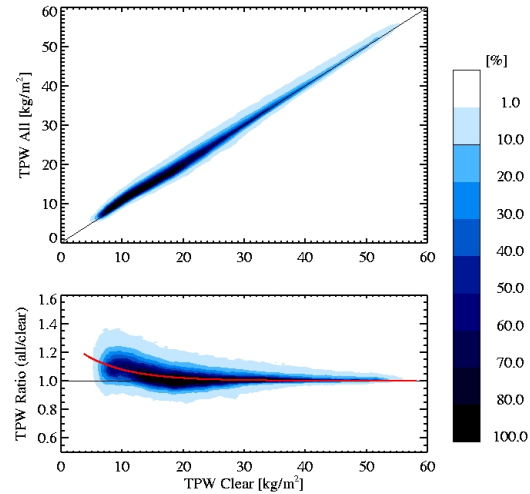
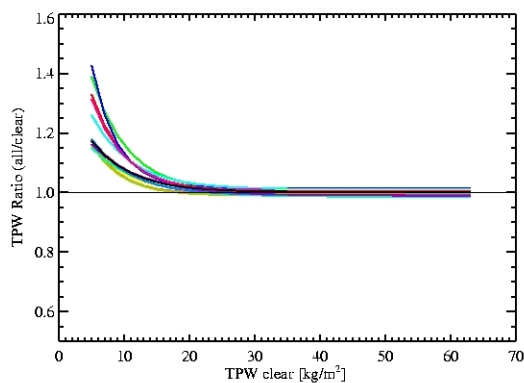


Figure E.2: South Atlantic: Relation of clear-sky TPW to the all-sky TPW (upper panel) and to the ratio of all-sky TPW and clear-sky TPW. The TPW is given in $[\text{kg}/\text{m}^2]$. Data are taken from February 2001 to October 2005 (except 2002). A: Colours give the latitude range. B: Frequency distribution of the data points in figure A.

A: Excess water vapour



B: underestimation

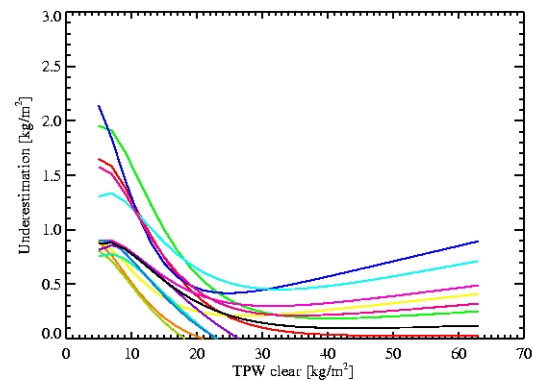
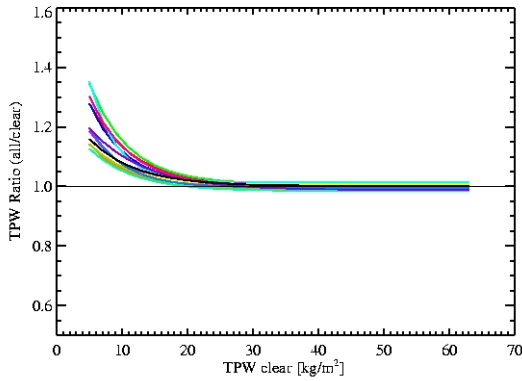


Figure E.3: South Atlantic: A Excess water vapour depending on the clear-sky TPW for the year 2004. B Clear-sky water vapour bias as derived from the excess water vapour. Colours denote the month. The underestimation is given in relation to the clear-sky water vapour path used in a climatology.

A: Excess water vapour



B: underestimation

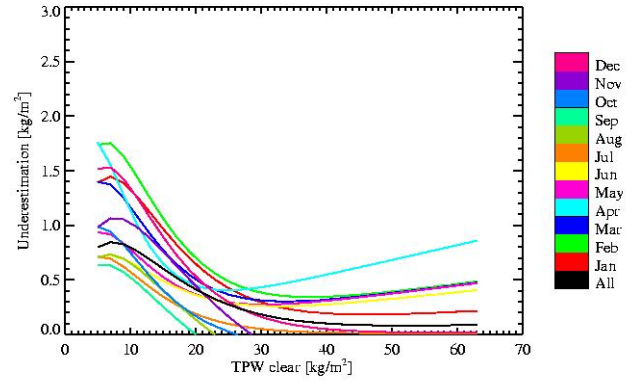
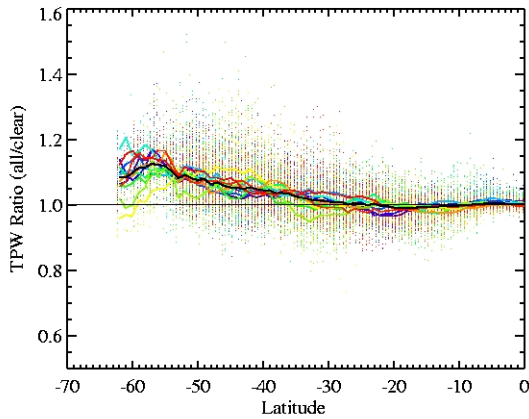


Figure E.4: South Atlantic: A Excess water vapour depending on the clear-sky TPW for the years 2001–2005 (except 2002). B Clear-sky water vapour bias as derived from the excess water vapour. Colours denote the month. The underestimation is given in relation to the clear-sky water vapour path used in a climatology.

A: 2004



C: 2001–2005

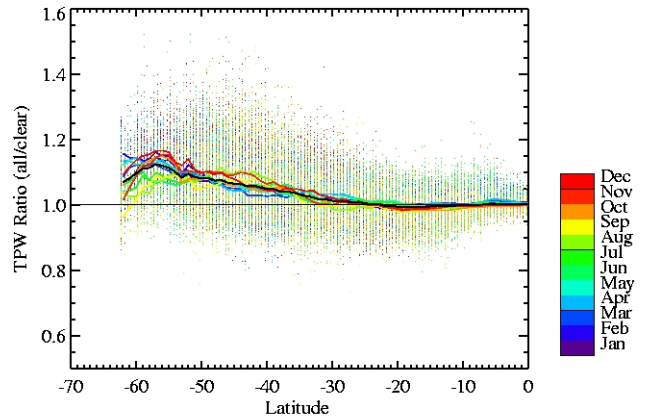


Figure E.5: South Atlantic: Zonal distribution of the ratio (all-sky TPW by clear-sky TPW). Colours denote the month. A: only 2004 data, and B: data are taken from February 2001 to October 2005 (except 2002).

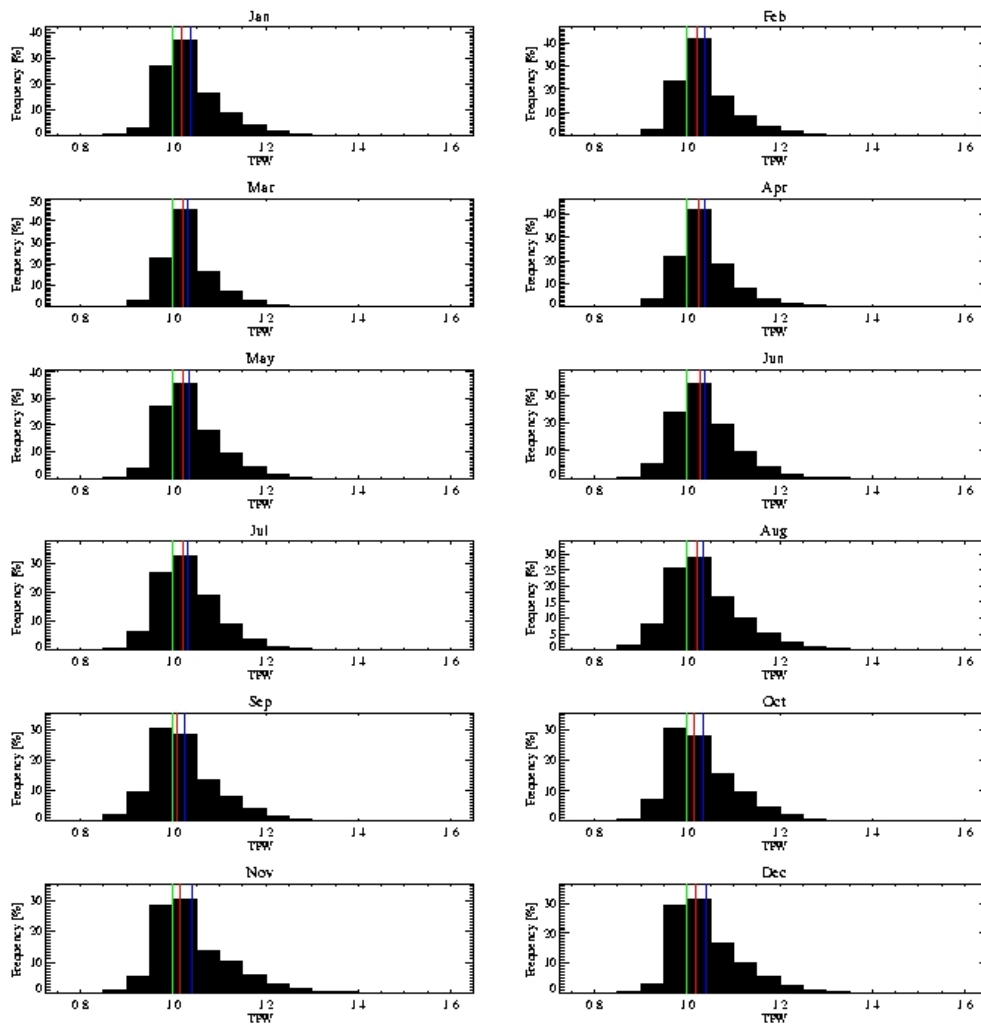
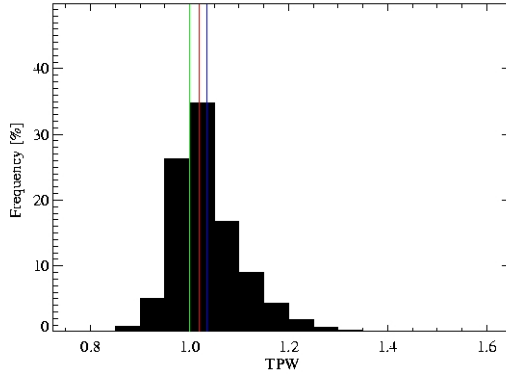


Figure E.6: Frequency distribution of the excess water vapour of each month for the South Atlantic for the years 2001-2005 (except 2002). The green line gives the excess water vapour of 1. In red the median and in blue the mean value of the distribution is marked.

A: South Atlantic



B: Global

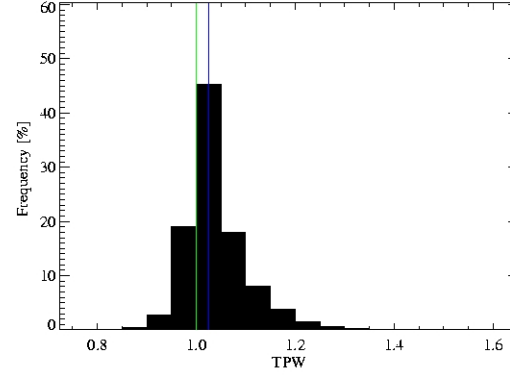


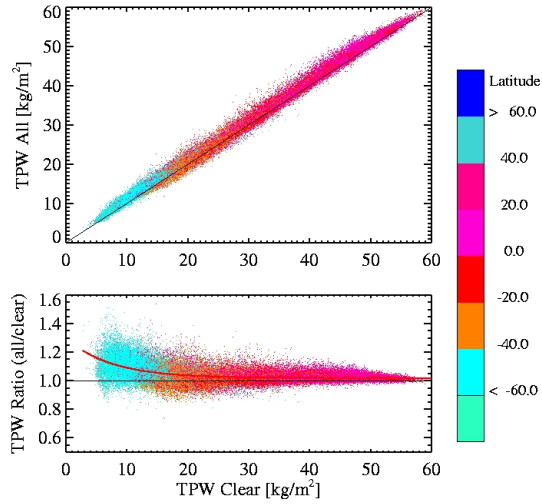
Figure E.7: Frequency distribution of the excess water vapour for the South Atlantic (A) and global (B) for the years 2001-2005 (except 2002). The green line gives the excess water vapour of 1. In red the median and in blue the mean value of the distribution is marked.

Month	A_0	A_1	A_2
South Atlantic			
Jan	0.582	0.869	1.003
Feb	0.787	0.861	1.008
Mar	0.676	0.845	1.007
Apr	1.146	0.833	1.014
May	0.458	0.784	1.008
Jun	0.306	0.829	1.006
Jul	0.354	0.849	1.000
Aug	0.303	0.833	0.986
Sep	0.298	0.875	0.985
Oct	0.514	0.863	0.996
Nov	0.380	0.829	0.987
Dec	0.684	0.887	1.002
All	0.319	0.850	1.001

Table E.1: South Atlantic: The parameters of the function expressing the ratio vs clear-sky TPW using all years.

E.2 Pacific

A : Excess water vapour depending on Latitude



B: Excess water vapour frequency distribution

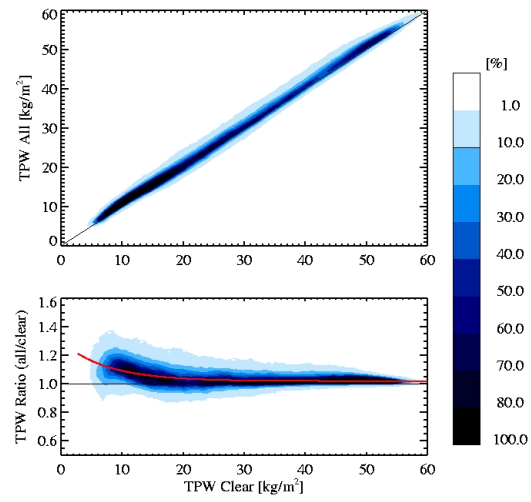
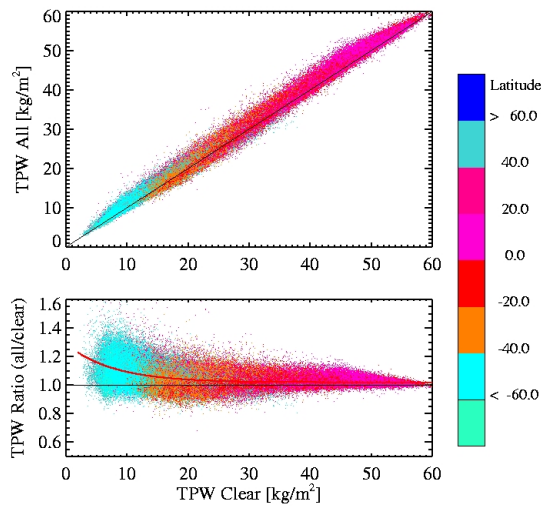


Figure E.8: Pacific: Relation of clear-sky TPW to the all-sky TPW (upper panel) and to the ratio of all-sky TPW and clear-sky TPW. The TPW is given in [kg/m²]. Data are taken from the year 2004. A: Colours give the latitude range. B: Frequency distribution of the data points in figure A.

A : Excess water vapour depending on Latitude



B: Excess water vapour frequency distribution

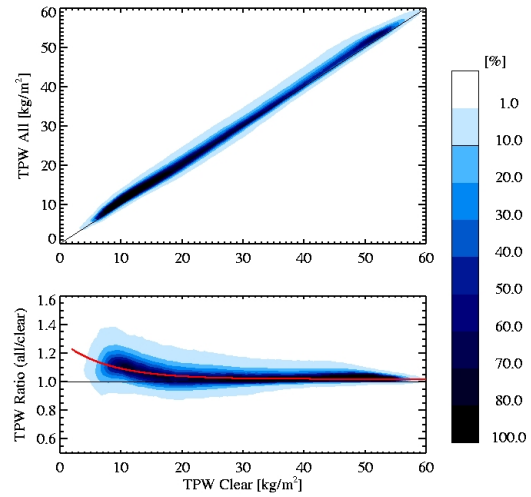
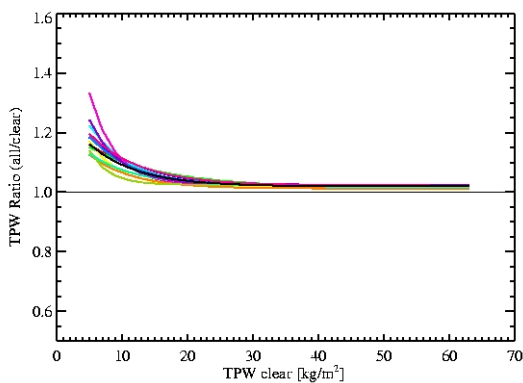


Figure E.9: Pacific: Relation of clear-sky TPW to the all-sky TPW (upper panel) and to the ratio of all-sky TPW and clear-sky TPW. The TPW is given in $[kg/m^2]$. Data are taken from February 2001 to October 2005 (except 2002). A: Colours give the latitude range. B: Frequency distribution of the data points in figure A.

A: Excess water vapour



B: underestimation

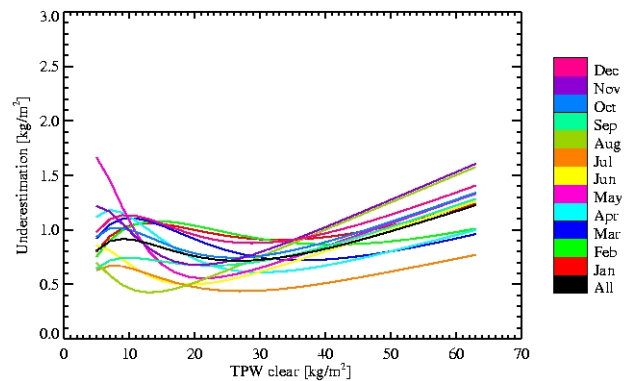
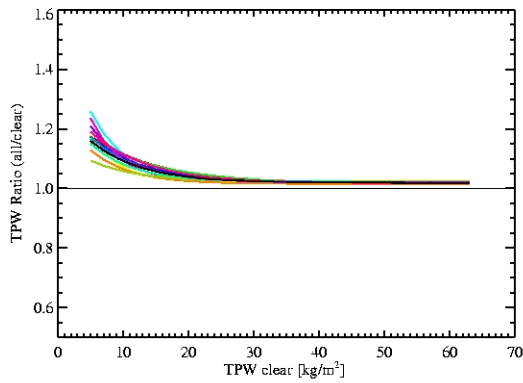


Figure E.10: Pacific: A Excess water vapour depending on the clear-sky TPW for the year 2004. B Clear-sky water vapour bias as derived from the excess water vapour. Colours denote the month. The underestimation is given in relation to the clear-sky water vapour path used in a climatology.

A: Excess water vapour



B: underestimation

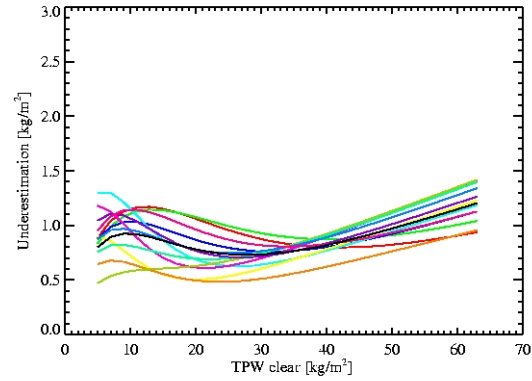
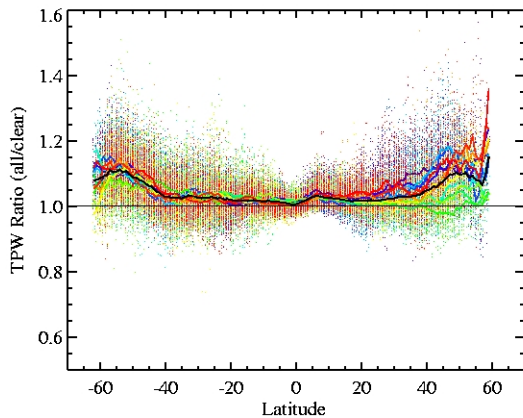
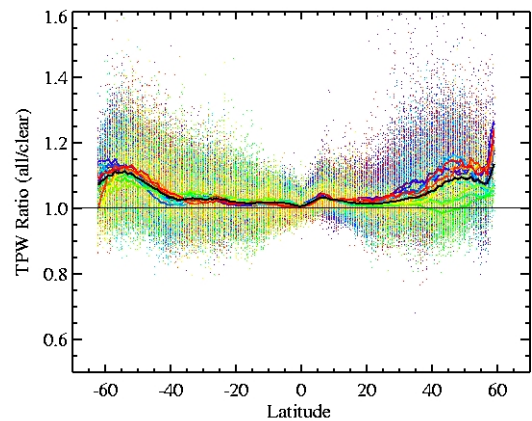


Figure E.11: Pacific: A Excess water vapour depending on the clear-sky TPW for the years 2001–2005 (except 2002). B Clear-sky water vapour bias as derived from the excess water vapour. Colours denote the month. The underestimation is given in relation to the clear-sky water vapour path used in a climatology.

A: 2004



C: 2001–2005



Month

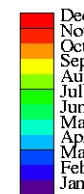


Figure E.12: Pacific: Zonal distribution of the ratio (all-sky TPW by clear-sky TPW). Colours denote the month. A: only 2004 data, and B: data are taken from February 2001 to October 2005 (except 2002).

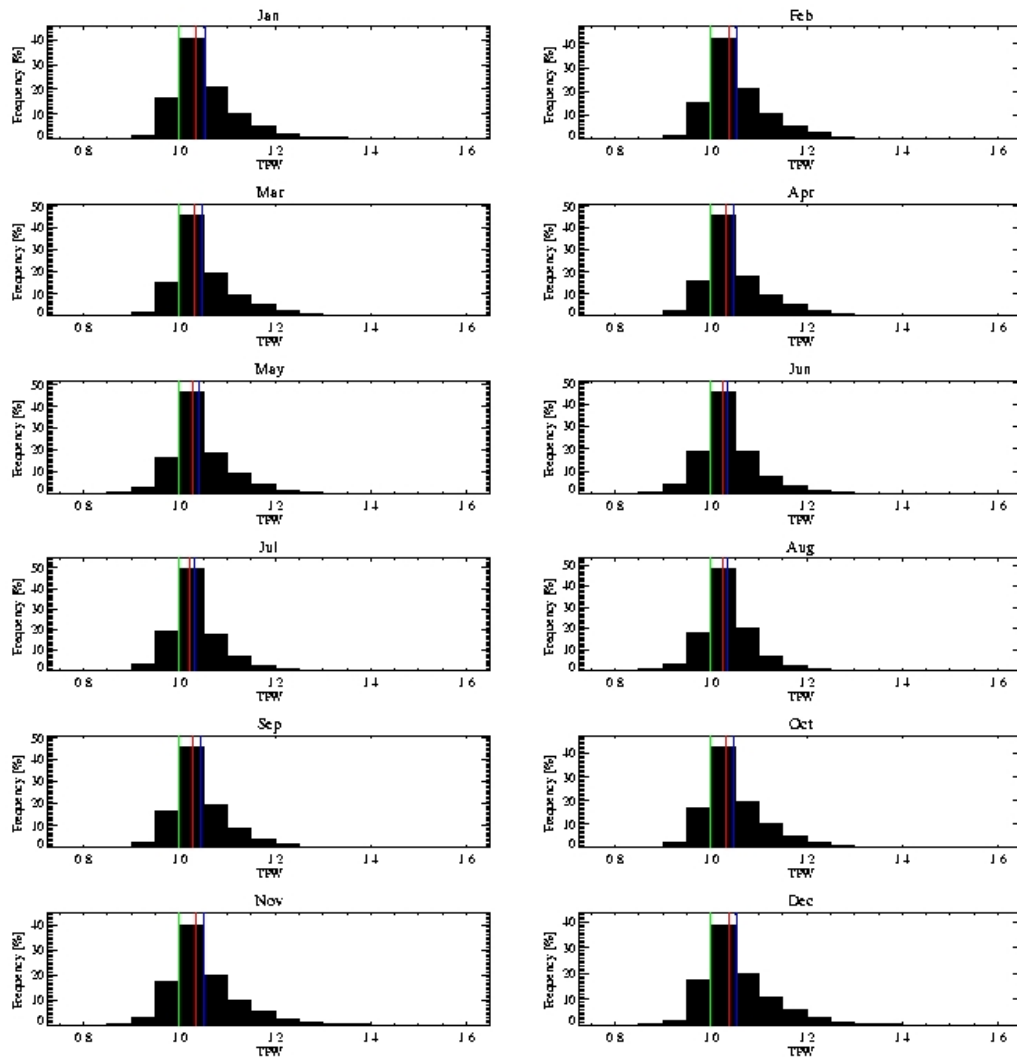
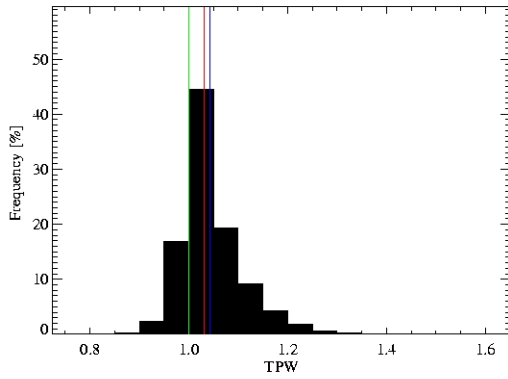


Figure E.13: Frequency distribution of the excess water vapour of each month for the Pacific for the years 2001-2005 (except 2002). The green line gives the excess water vapour of 1. In red the median and in blue the mean value of the distribution is marked.

A: Pacific



B: Global

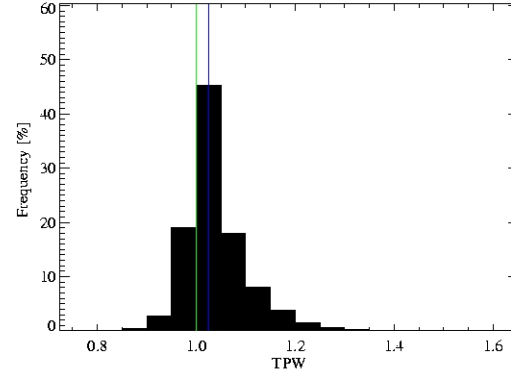


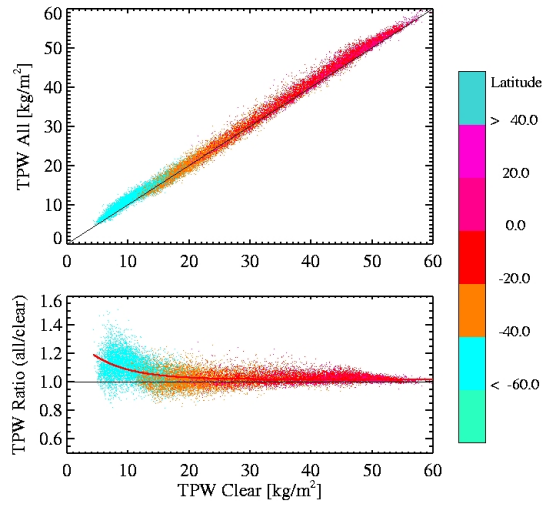
Figure E.14: Frequency distribution of the excess water vapour for the Pacific (A) and global (B) for the years 2001-2005 (except 2002). The green line gives the excess water vapour of 1. In red the median and in blue the mean value of the distribution is marked.

Month	A_0	A_1	A_2
North Atlantic			
Jan	0.262	0.909	1.014
Feb	0.239	0.912	1.016
Mar	0.287	0.886	1.018
Apr	0.599	0.833	1.019
May	0.631	0.805	1.022
Jun	0.492	0.800	1.019
Jul	0.260	0.848	1.015
Aug	0.143	0.870	1.022
Sep	0.280	0.857	1.022
Oct	0.316	0.866	1.021
Nov	0.411	0.856	1.020
Dec	0.309	0.891	1.018
All	0.270	0.878	1.019

Table E.2: Pacific: The parameters of the function expressing the ratio vs clear-sky TPW using all years.

E.3 Indic

A : Excess water vapour depending on Latitude



B: Excess water vapour frequency distribution

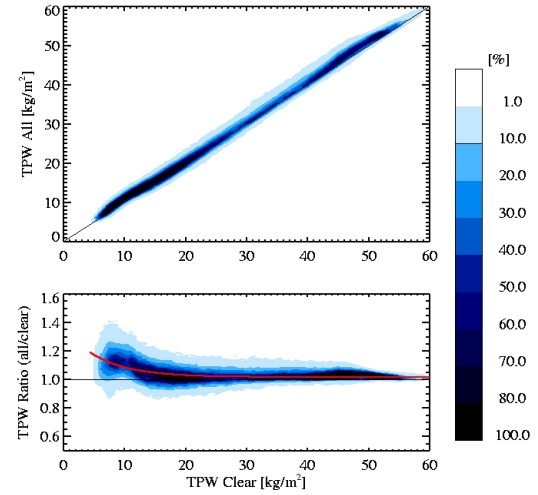
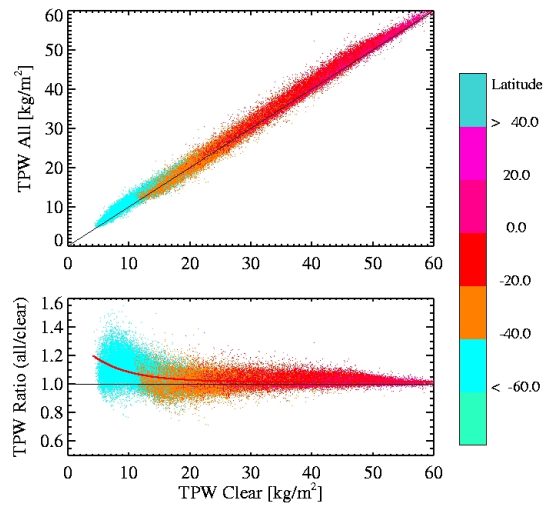


Figure E.15: Indic: Relation of clear-sky TPW to the all-sky TPW (upper panel) and to the ratio of all-sky TPW and clear-sky TPW. The TPW is given in $[\text{kg/m}^2]$. Data are taken from the year 2004. A: Colours give the latitude range. B: Frequency distribution of the data points in figure A.

A : Excess water vapour depending on Latitude



B: Excess water vapour frequency distribution

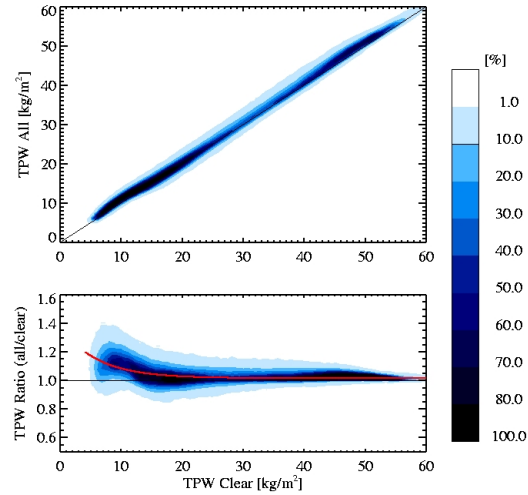
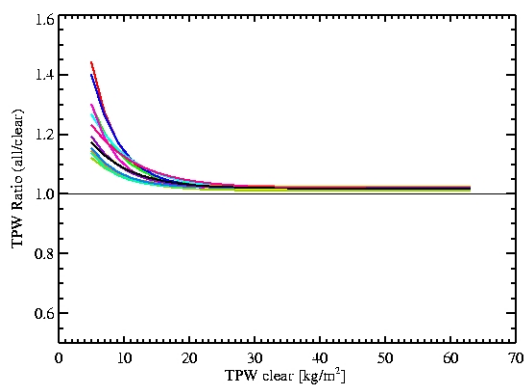


Figure E.16: Indic: Relation of clear-sky TPW to the all-sky TPW (upper panel) and to the ratio of all-sky TPW and clear-sky TPW. The TPW is given in $[\text{kg}/\text{m}^2]$. Data are taken from February 2001 to October 2005 (except 2002). A: Colours give the latitude range. B: Frequency distribution of the data points in figure A.

A: Excess water vapour



B: underestimation

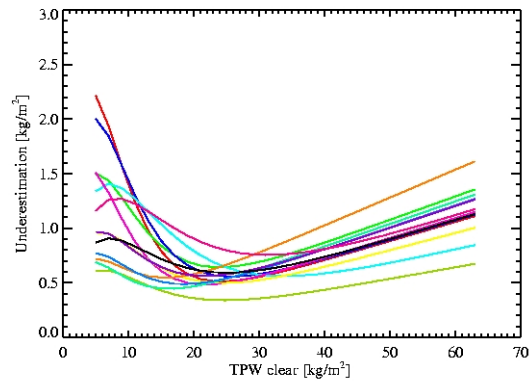
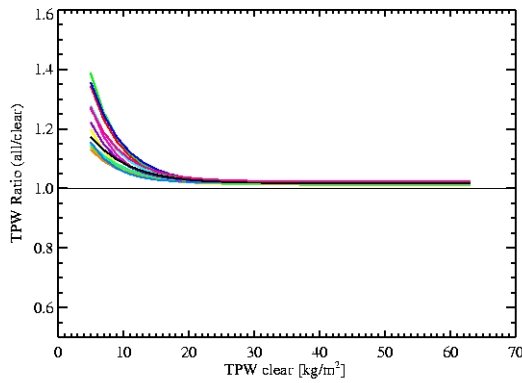


Figure E.17: Indic: A Excess water vapour depending on the clear-sky TPW for the year 2004. B Clear-sky water vapour bias as derived from the excess water vapour. Colours denote the month. The underestimation is given in relation to the clear-sky water vapour path used in a climatology.

A: Excess water vapour



B: underestimation

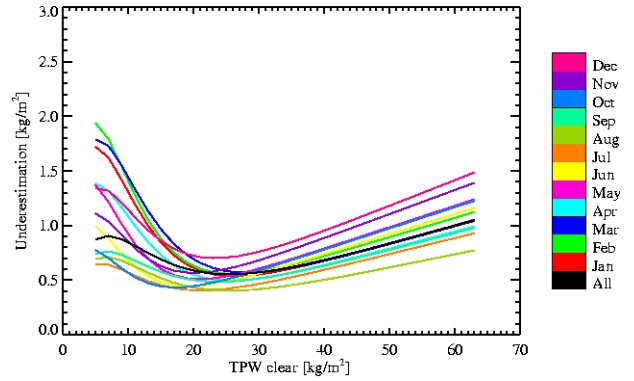
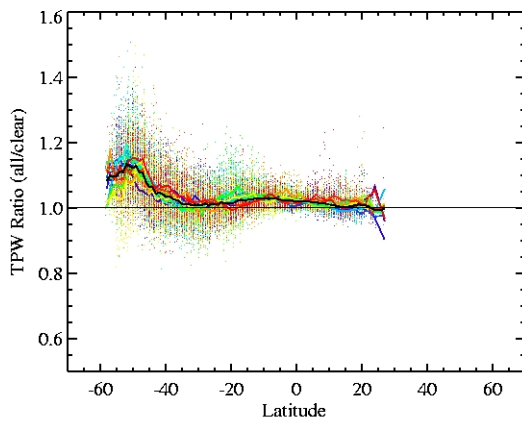


Figure E.18: *Indic*: A Excess water vapour depending on the clear-sky TPW for the years 2001–2005 (except 2002). B Clear-sky water vapour bias as derived from the excess water vapour. Colours denote the month. The underestimation is given in relation to the clear-sky water vapour path used in a climatology.

A: 2004



C: 2001–2005

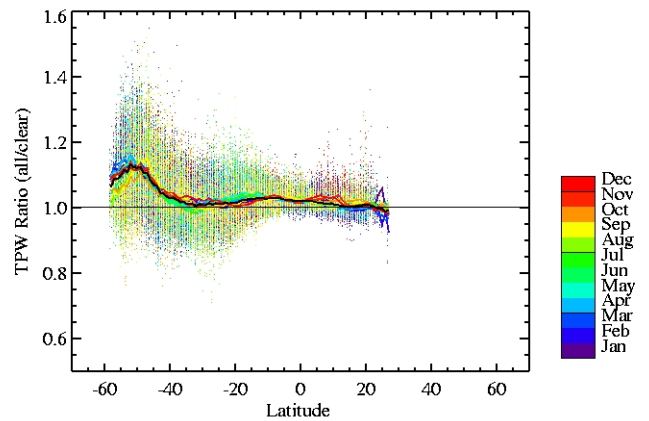


Figure E.19: *Indic*: Zonal distribution of the ratio (all-sky TPW by clear-sky TPW). Colours denote the month. A: only 2004 data, and B: data are taken from February 2001 to October 2005 (except 2002).

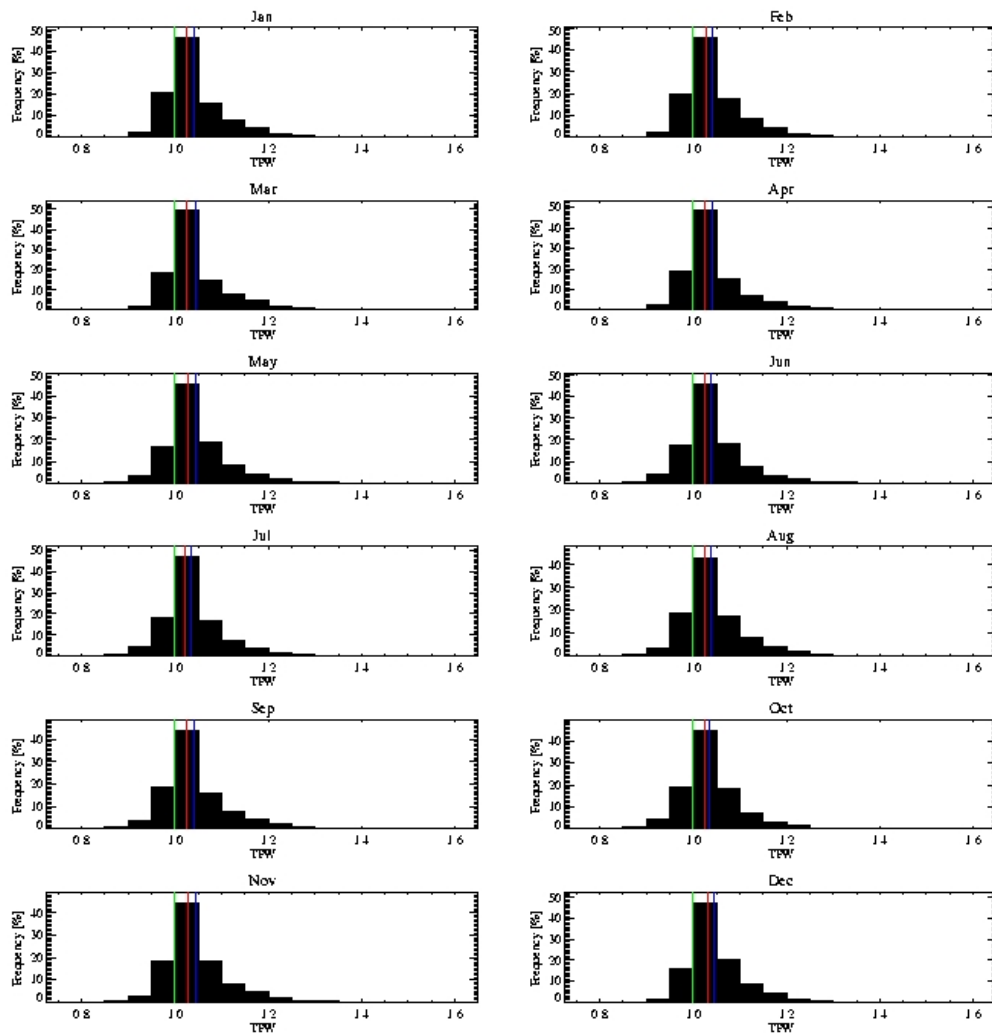
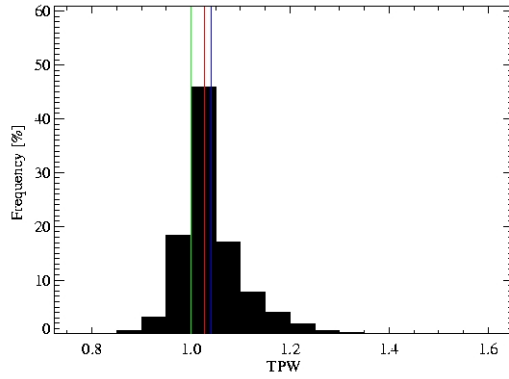


Figure E.20: Frequency distribution of the excess water vapour of each month for the Indic for the years 2001-2005 (except 2002). The green line gives the excess water vapour of 1. In red the median and in blue the mean value of the distribution is marked.

A: Indic



B: Global

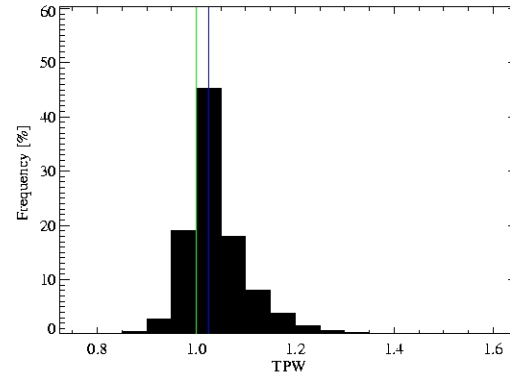


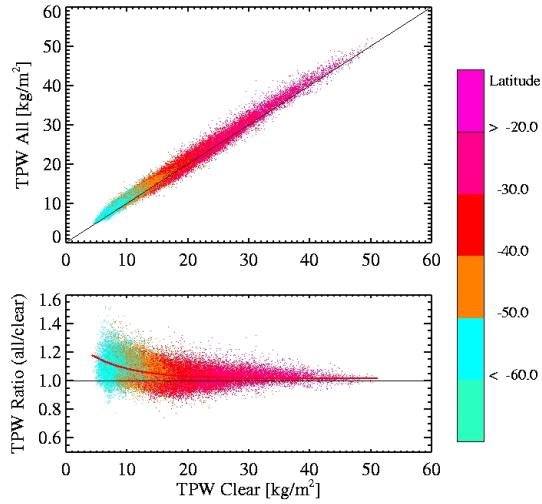
Figure E.21: Frequency distribution of the excess water vapour for the Indic (A) and global (B) for the years 2001-2005 (except 2002). The green line gives the excess water vapour of 1. In red the median and in blue the mean value of the distribution is marked.

Month	A_0	A_1	A_2
North Atlantic			
Jan	0.942	0.810	1.017
Feb	1.112	0.802	1.018
Mar	0.909	0.822	1.017
Apr	0.736	0.813	1.016
May	0.897	0.778	1.020
Jun	0.656	0.773	1.018
Jul	0.313	0.818	1.015
Aug	0.301	0.841	1.012
Sep	0.320	0.839	1.016
Oct	0.499	0.771	1.019
Nov	0.636	0.794	1.022
Dec	0.658	0.820	1.024
All	0.365	0.845	1.017

Table E.3: Indic: The parameters of the function expressing the ratio vs clear-sky TPW using all years.

E.4 Antarctic circumpolar ocean

A : Excess water vapour depending on Latitude



B: Excess water vapour frequency distribution

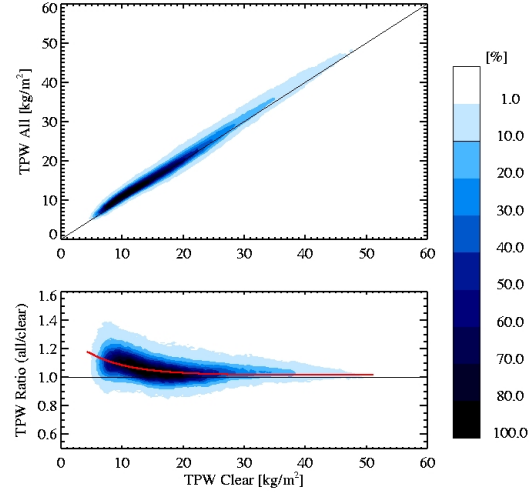
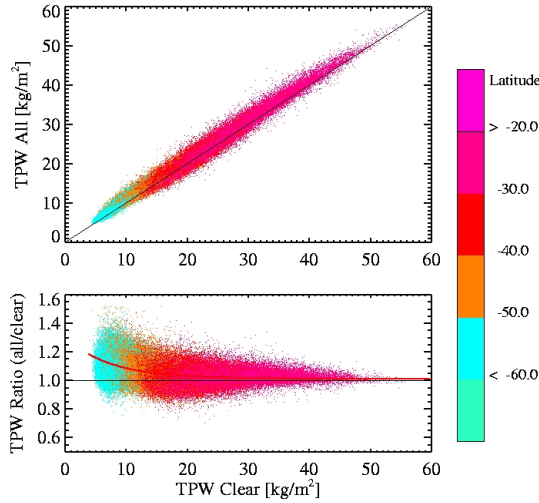


Figure E.22: Antarctic circumpolar ocean: Relation of clear-sky TPW to the all-sky TPW (upper panel) and to the ratio of all-sky TPW and clear-sky TPW. The TPW is given in [kg/m²]. Data are taken from the year 2004. A: Colours give the latitude range. B: Frequency distribution of the data points in figure A.

A : Excess water vapour depending on Latitude



B: Excess water vapour frequency distribution

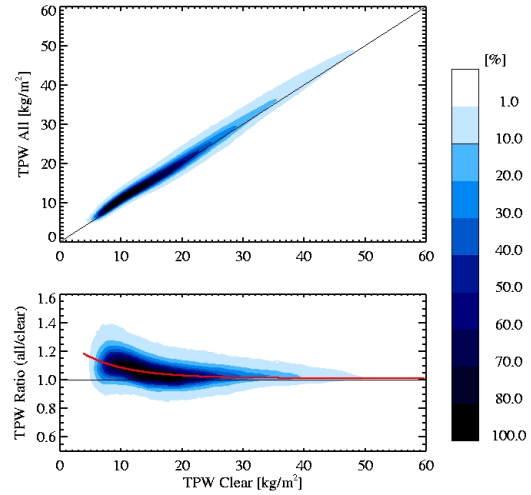
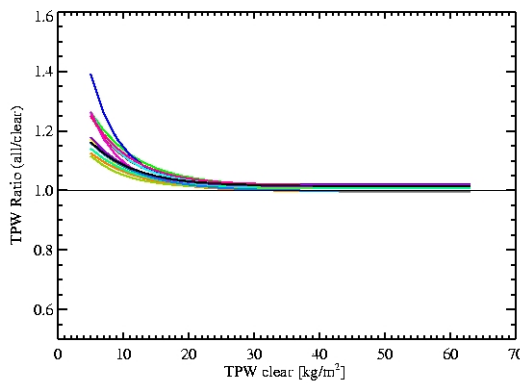


Figure E.23: Antarctic circumpolar ocean: Relation of clear-sky TPW to the all-sky TPW (upper panel) and to the ratio of all-sky TPW and clear-sky TPW. The TPW is given in [kg/m²]. Data are taken from February 2001 to October 2005 (except 2002). A: Colours give the latitude range. B: Frequency distribution of the data points in figure A.

A: Excess water vapour



B: underestimation

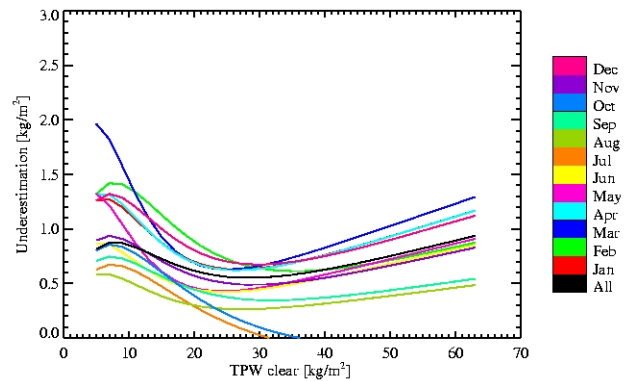
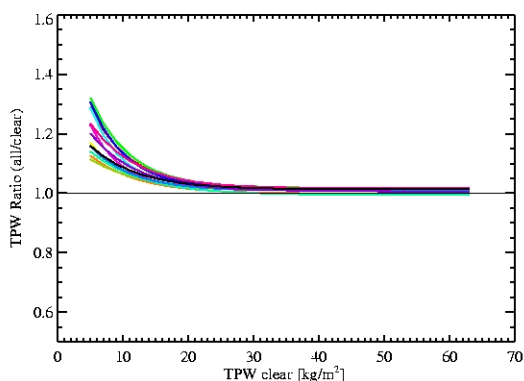


Figure E.24: Antarctic circumpolar ocean: A Excess water vapour depending on the clear-sky TPW for the year 2004. B Clear-sky water vapour bias as derived from the excess water vapour. Colours denote the month. The underestimation is given in relation to the clear-sky water vapour path used in a climatology.

A: Excess water vapour



B: underestimation

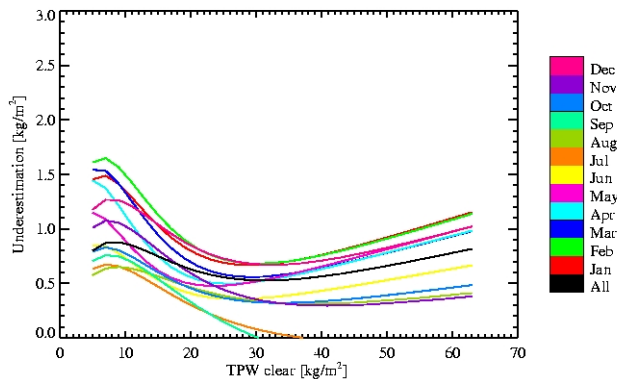
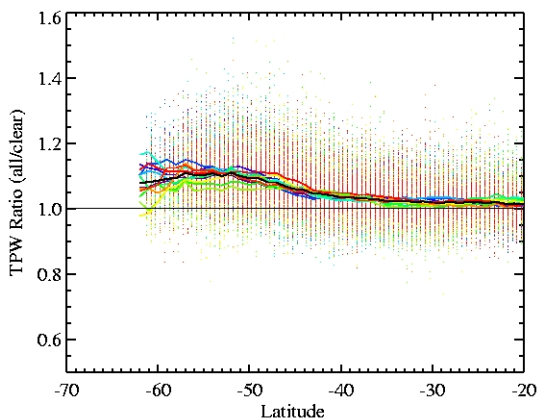


Figure E.25: Antarctic circumpolar ocean: A Excess water vapour depending on the clear-sky TPW for the years 2001–2005 (except 2002). B Clear-sky water vapour bias as derived from the excess water vapour. Colours denote the month. The underestimation is given in relation to the clear-sky water vapour path used in a climatology.

A: 2004



C: 2001–2005

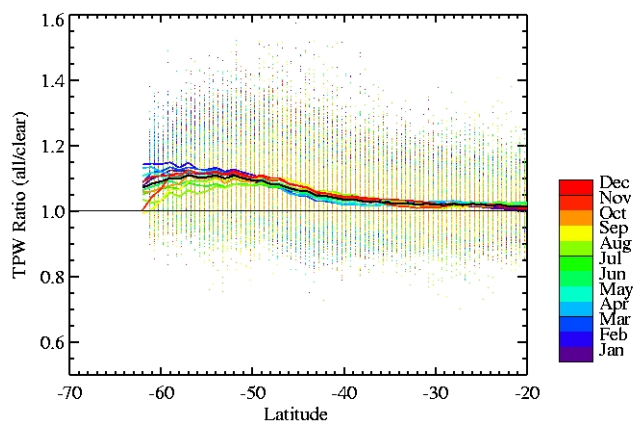


Figure E.26: Antarctic circumpolar ocean: Zonal distribution of the ratio (all-sky TPW by clear-sky TPW). Colours denote the month. A: only 2004 data, and B: data are taken from February 2001 to October 2005 (except 2002).

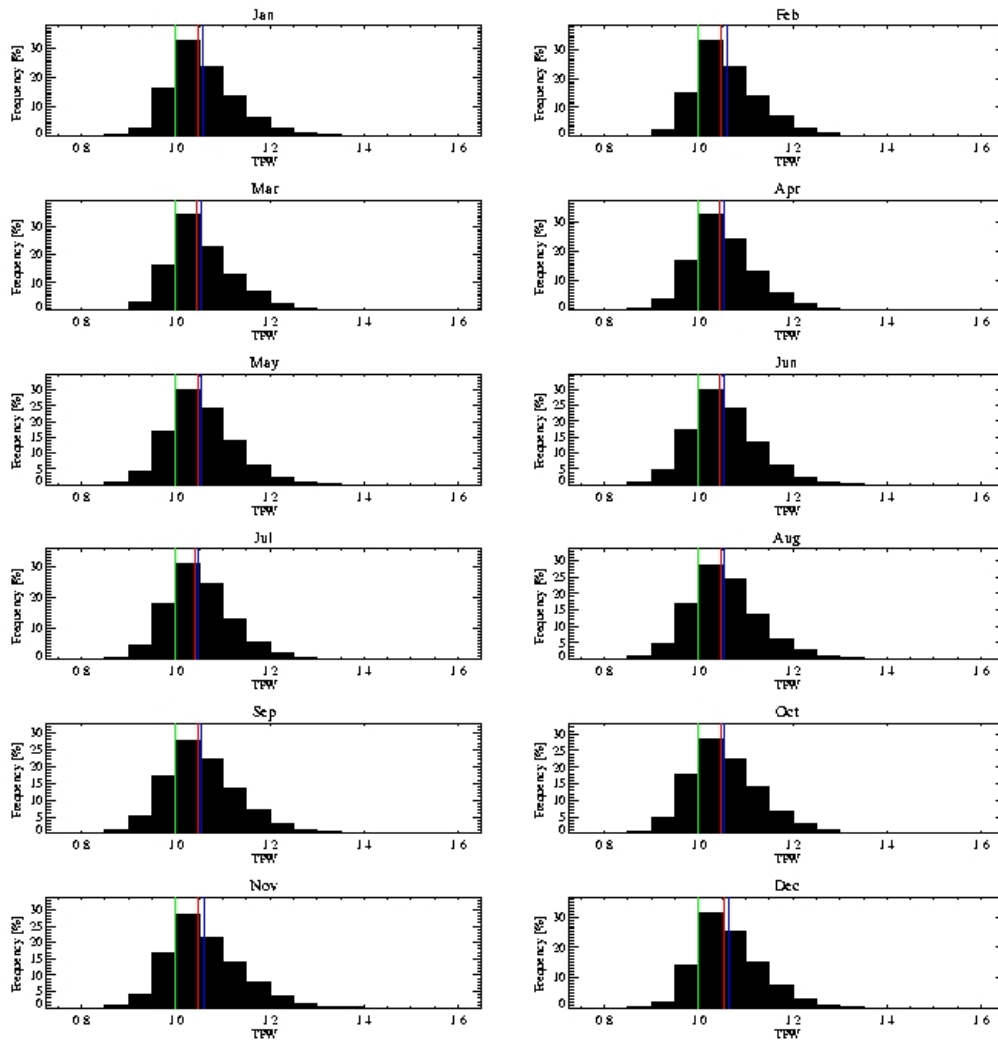
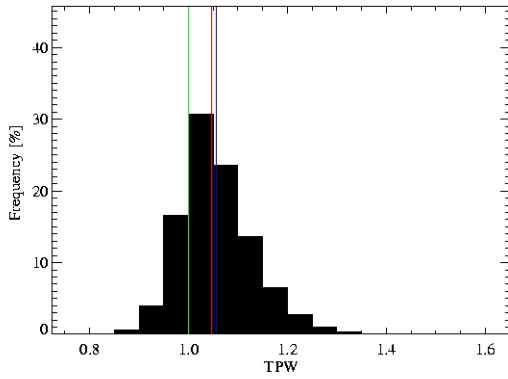


Figure E.27: Frequency distribution of the excess water vapour of each month for the Antarctic circumpolar ocean for the years 2001-2005 (except 2002). The green line gives the excess water vapour of 1. In red the median and in blue the mean value of the distribution is marked.

A: Antarctic circumpolar ocean



B: Global

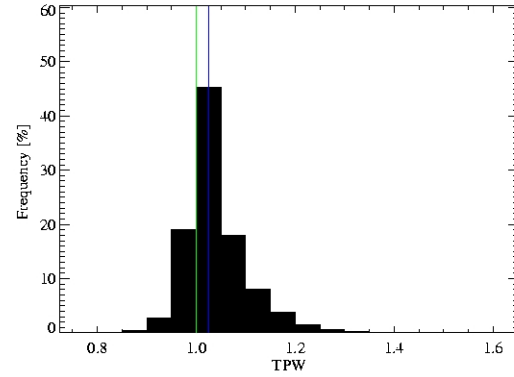


Figure E.28: Frequency distribution of the excess water vapour for the Antarctic circumpolar ocean(A) and global (B) for the years 2001-2005 (except 2002). The green line gives the excess water vapour of 1. In red the median and in blue the mean value of the distribution is marked.

Month	A_0	A_1	A_2
North Atlantic			
Jan	0.633	0.845	1.018
Feb	0.700	0.846	1.018
Mar	0.727	0.834	1.016
Apr	0.772	0.813	1.016
May	0.625	0.807	1.016
Jun	0.404	0.830	1.011
Jul	0.253	0.873	0.998
Aug	0.202	0.883	1.006
Sep	0.274	0.883	0.994
Oct	0.325	0.858	1.008
Nov	0.396	0.869	1.006
Dec	0.444	0.868	1.016
All	0.293	0.871	1.013

Table E.4: Antarctic circumpolar ocean: The parameters of the function expressing the ratio vs clear-sky TPW using all years.

Bibliography

- Albert, P., R. Bennartz, and J. Fischer, 2001: Remote sensing of atmospheric water vapor from backscattered sunlight in cloudy atmospheres. *Journal of Atmospheric and Oceanic Technology*, **18**(6), 865 – 874.
- Arabey, E., 1975: Radiosonde data as means for revealing cloud layers. *Meteor. Gidrol.*, **6**, 32–37.
- Atkinson, P. and A. Tatnell, 1997: Neural networks in remote sensing. *Int. J. Remote Sensing*, **18**(4), 699–709.
- Barton, I., 2004: Global water vapor analyses over the ocean using along track scanning radiometer infrared data. *Journal of Geophysical Research*, **109**(D2).
- Bates, J. and D. Jackson, 2001: Trends in upper-tropospheric humidity. *Geophysical Research Letters*, **28**(9), 1695–1698.
- Bennartz, R. and J. Fischer, 2001b: Retrieval of columnar water vapor over land from back-scattered solar radiation using the medium resolution imaging spectrometer (MERIS). *Remote Sensing of Environment*, **78**(3), 570 – 589.
- Bevis, M., S. Businger, and S. Chriswell, 1994: Gps meteorology: Mapping zenith wet delays onto precipitable water. *Journal of Applied Meteorology*, **33**, 379–386.
- Bokoye, A., A. Royer, N. Neill, P. Cliche, L. McArthur, P. Teillet, G. Fedosejevs, and J. Theriault, 2003: Multisensor analysis of integrated atmospheric water vapor over canada and alaska. *Journal of Geophysical Research*, **108**(D15).
- Bühler, S. and N. Couroux, 2003: The impact of temperature errors on perceived humidity supersaturation. *Geophysical Research Letters*, **30**(14).
- Bühler, S. and V. John, 2005: A simple method to relate microwave radiances to upper tropospheric humidity. *Journal of Geophysical Research*, **110**(D02110).
- Bühler, S., M. Kuvatov, V. John, U. Leiterer, and H. Dier, 2004e: Comparison of microwave satellite humidity data and radiosonde profiles: A case study. *Journal of Geophysical Research*, **109**(D13).

- Bühler, S., A. von Engeln, E. Brocard, V. John, T. Kuhn, and P. Erikson, 2004: The impact of humidity and temperature variations on clear-sky outgoing longwave radiation. *Journal of Geophysical Research*, **109**(D13103).
- Chaboureaud, J., A. Chedin, and N. Scott, 1998: Remote sensing of the vertical distribution of atmospheric water vapor from tovs observations: Method and validation. *Journal of Geophysical Research*, **103**(D8), 8743 – 8752.
- Chernykh, I. and R. Eskridge, 1996: Determination of cloud amount and level from radiosonde soundings. *Journal of Applied Meteorology*, **35**, 1362 – 1369.
- Crewell, S., M. Drusch, v. Meijgaard, and v. Lammeren, 2002: Cloud observations and modeling within the european baltex cloud liquid water network. *Boreal Environment Research*, **7**, 235–245.
- Crewell, S. and U. Löhnert, 2003: Accuracy of cloud liquid water path from ground-based microwave radiometry - 2. sensor accuracy and synergy. *Radio Science*, **38**(3).
- Cruz Pol, S., C. Ruf, and S. Keihm, 1998: Improved 20 - to 32 - ghz atmospheric absorption model. *Radio Science*, **33**, 1319 – 1333.
- Dlhopsky, R., 1998: *APOLLO Cloud detection and Cloud Property Retrieval as implemented at KNMI*. KNMI.
- Elachi, C., 1987: *Introduction to the Physics and Techniques of Remote Sensing*. Wiley Series in Remote Sensing.
- Elgered, G. and P. Jarlemark, 1998: Ground-based microwave radiometry and long-term observations of atmospheric water vapor. *Radio Science*, **33**(3), 707 – 717.
- Engelen, R. and G. Stephens, 1999: Characterization of water-vapor retrievals from TOVS/HIRS and SSM/T-2 measurements. *Quarterly Journal of the Royal Meteorological Society*, **125**(553), 331–351.
- English, S., 1999: Estimation of temperature and humidity profile information from microwave radiances over different surface types. *Journal of Applied Meteorology*, **38**, 1526–1541.
- Feijt, A. and H. Jonker, 1999: Comparison of scaling parameters from spatial and temporal distributions of cloud properties. *KNMI Preprints*, **20**.
- Ferrare, R., S. Melfi, D. Whiteman, K. Evans, F. Schmidlin, and D. Starr, 1995: A comparison of water vapor measurements made by raman lidar and radiosondes. *Journal of Atmospheric and Oceanic Technology*, **12**, 1177 – 1195.
- Gaffen, D. and W. Elliot, 1993: Column water vapour content in clear and cloudy skies. *Journal of Climate*, **6**, 2278–2286.
- Gao, B. and Y. Kaufman, 2003: Water vapor retrievals using moderate resolution imaging spectroradiometer (MODIS) near-infrared channels. *Journal of Geophysical Research*, **108**(D13).

- Greenwald, T., S. Christopher, and L. Chou, 1997: Cloud liquid water path comparisons from passive microwave and solar reflectance satellite measurements: Assessment of sub-field-of-view cloud effects in microwave retrievals. *Journal of Geophysical Research*, **102**(D16), 19,585–19,596.
- Grody, N., J. Zhao, R. Ferraro, F. Weng, and R. Boers, 2001: Determination of precipitable water and cloud liquid water over oceans from the NOAA-15 advanced microwave sounding unit. *Journal of Geophysical Research*, **106**(D3), 2943–2953.
- Güldner, J. and D. Spänkuch, 1999: results of year-round remotely sensed integrated water vapor by ground-based microwave radiometry. *Journal of Applied Meteorology*, **38**, 981 – 988.
- Han, Q., W. Rossow, and A. Lacis, 1994: Near-global survey of effective droplet radii in liquid water clouds using isccp data. *Journal of Climate*, **7**, 465–497.
- Hargens, U., 1992: Remote sensing of cloud liquid water during ice'89. In: *Proceedings of the Specialist Meeting on Microwave Radiometry and Remote Sensing Applications*. IEEE Trans. Microwave Theory and Tech. Soc.
- Hauschildt, H. and A. Macke, 2004: Precipitable water in cloudy atmospheres from combined solar, thermal and microwave measurements. literature study on existing tpw measurements in cloudy area. Technical report, CMSAF, DWD. Available at www.cmsaf.dwd.de.
- IPCC Working Group I, 2001: *Climate Change 2001: The Scientific Basis. Contributions of Working Group I to the third Assessment Report of the intergovernmental Panel on Climate Change*. Cambridge University Press, Cambridge, United Kingdom and New York, NY, USA.
- Kalnay, E. and Coauthors, 1996: The NCEP/NCAR 40-years reanalysis project. *Bulletin American Meteorological Society*, **77**, 437 – 471.
- Karstens, U., C. Simmer, and E. Ruprecht, 1994: Remote sensing of cloud liquid water. *Meteorol. Atmos. Phys.*, **54**, 157–171.
- Kästner, M. and K. Kriebel, 2000: Alpine cloud climatology using long-term noaa-avhrr satellite data. *DLR Report*, **140**.
- Kidder, S. and T. Vonder Haar, 1995: *Satellite Meteorology*. Academic Press.
- König-Langlo, G. and B. Marx, 1997: *The Meteorological Information System at the Alfred Wegener Institute*. Kluwer Academic Publisher. Printed in USA Norwell.
- Krasnopolsky, V., L. Breaker, and W. Gemmill, 1995: A neural network as a nonlinear transfer function model for retrieving surface wind speeds from the special sensor microwave imager. *Journal of Geophysical Research*, **100**(C6), 11,033–11,045.

- Lang, R., J. Williams, W. van der Zande, and A. Maurellis, 2003: Application of the spectral structure parameterization technique: retrieval of total water vapor columns from GOME. *Atmos. Chem. Phys.*, **3**, 145–160.
- Lanzante, J. and G. Gahrs, 2000: The "clear-sky bias" of TOVS upper-tropospheric humidity. *Journal of Climate*, **13**, 4034–4041.
- Li, Z., J. Muller, and P. Cross, 2003: Comparison of precipitable water vapor derived from radiosonde, GPS, and moderate-resolution imaging spectroradiometer measurements. *Journal of Geophysical Research*, **108**(D20).
- Liebe, H., 1989: MPM – an atmospheric millimeter-wave propagation model. *Int. J. Infrared Millimeter Waves*, **10**, 631 – 650.
- Liebe, H., G. Hufford, and M. Cotton, 1993: Propagation modelling of moist air and suspended water/ice particles at frequencies below 100 GHz. *Paper presented at AGARD 52nd Special Meeting of the Panel on Electromagnetic Wave Propagation, Adv. Group for Aerosp. Res. and Dev., Palma de Mallorca, Spain, 17 - 21 May, 1993.*
- Löhnert, U. and S. Crewell, 2003: Accuracy of cloud liquid water path from ground-based microwave radiometry - 1. dependency on cloud model statistics. *Radio Science*, **38**(3).
- Löhnert, U., S. Crewell, and C. Simmer, 2004: An integrated approach toward retrieving physically consistent profiles of temperature, humidity, and cloud liquid water. *Journal of Applied Meteorology*, **43**, 1295 – 1307.
- Lovelace, C. and F. Wagner, 1995: Minim — a variable metric minimization subroutine. tech. rep. *Institut für Theoretische Physik an der Christian-Albrechts-Universität Kiel.*
- Marsden, D. and F. Valero, 2004: Observation of water vapor greenhouse absorption over the gulf of Mexico using aircraft and satellite data. *Journal of Atmospheric Science*, **61**, 745 – 753.
- Maurellis, A., R. Lang, W. van der Sande, I. Aben, and W. Ubachs, 2000: Precipitable water column retrieval from GOME data. *Geophysical Research Letters*, **27**(6), 903–906.
- Miller, E., J. Wang, and H. Cole, 1999: Correction for dry bias in Vaisala radiosonde RH data. In: *Ninth ARM Science Team Meeting Proceedings, San Antonio, Texas, March 22-26, 1999*, p. 9.
- Mo, T., 1999: Amsu-a antenna pattern corrections. *IEEE Transactions of Geoscience and Remote Sensing*, **37**(1), 103–112.
- Nakajima, T. and M. King, 1990: Determination of optical thickness and effective particle radius of clouds from reflected solar radiation measurements. part I: Theory. *Journal of Atmospheric Science*, **47**(15), 1878–1893.
- Naud, C., J. Muller, and E. Clothiaux, 2003: Comparison between active sensor and radiosonde cloud boundaries over the ARM southern great plains site. *Journal of Geophysical Research*, **108**(D4).

- Niell, A., A. Coster, F. Solheim, V. Mendes, P. Toor, R. Langley, and C. Upham, 2001: Comparison of measurements of atmospheric wet delay by radiosonde, water vapor radiometer, GPS, and VLBI. *Journal of Atmospheric and Oceanic Technology*, **18**(6), 830 – 850.
- NOAA-KLM Users Guide, ., 1998: *NOAA-KLM Users Guide*, <http://www2.ncdc.noaa.gov/docs/klm/index.htm>. NOAA.
- Peixoto, J. and A. Oort, 1992: *Physics of Climate*. American Institute of Physics, New York.
- Peter, R., 1994: The retrieval of tropospheric water vapor and cloud liquid with an iterative non-linear algorithm. In: *Microwave Specialist Meeting 1994 in Rome*.
- Pruppacher, H. and J. Klett, 1997: *Microphysics of Clouds and Precipitation*. Reidel Publishing Company.
- Revercomb, H., D. Turner, D. Tobin, R. Knuteson, W. Feltz, J. Barnard, J. Bösenberg, S. Clough, D. Cook, R. Ferrare, J. Goldsmith, S. Gutman, R. Halthore, B. Lesht, J. Liljegren, H. Linne, J. Michalsky, V. Morris, W. Porch, S. Richardson, B. Schmid, M. Splitt, T. Van Hove, E. Westwater, and D. Whiteman, 2003: The ARM program's water vapor intensive observation periods. *Bulletin American Meteorological Society*, **84**(2), 217 – 237.
- Rojas, R., 1993: *Theorie der neuronalen Netze*. Springer Verlag, Berlin.
- Rosenkranz, P., 1998: Water vapor microwave continuum absorption: A comparison of measurements and models. *Radio Science*, **33**, 919 – 928. (Correction, *Radio Science*, **34**, 1025, 1999).
- Ruprecht, E., 1996: Atmospheric water vapor and cloud water: an overview. *Adv. Space Res.*, **18**(7).
- Ruprecht, E. and T. Kahl, 2003: Investigation of the atmospheric water budget of the baltex area using ncep/ncar reanalysis data. *Tellus*, **55a**, 426–437.
- Ruprecht, E., S. Schröder, and S. Ubl, 2002: On the relation of the NAO and water vapor transport towards europe. *Meteorologische Zeitschrift*, **11**, 701–702.
- Saunders, R., 1986: An automated scheme for the removal of cloud contermination from avhrr radiances over western europe. *International Journal of Remote Sensing*, **7**(7), 867–886.
- Saunders, R. and K. Kriebel, 1988: An improved method for detecting clear sky and cloudy radiances from avhrr data. *International Journal of Remote Sensing*, **9**(1), 123–150.
- Schlüssel, P. and M. Goldberg, 2002: Retrieval of atmospheric temperature and water vapour from IASI measurements in partly cloudy situations. *Adv. Space Res.*, **29**(11), 1703–1706.

- Schmidt, T., J. Wickert, C. Marquardt, G. Beyerle, C. Reigber, R. Galas, and R. König, 2004: GPS radio occultation with CHAMP: an innovative remote sensing method of the atmosphere. *Advances in Space Research*, **33**, 1036–1040.
- Simmer, C., 1994: *Satellitenfernerkundung hydrologischer Parameter der Atmosphäre mit Mikrowellen*. Verlag Dr. Kovač, Hamburg.
- Soden, B. and J. Lanzante, 1996: An assessment of satellite and radiosonde climatologies of upper-tropospheric water vapor. *Journal of Climate*, **9**, 1235–1250.
- Soden, B., D. Turner, B. Lesht, and L. Miloshevich, 2004: An analysis of satellite, radiosonde, and lidar observations of upper tropospheric water vapor from the atmospheric radiation measurement program. *Geophysical Research Letters*, **109**(D4).
- Stephens, G., 1984: The parametrization of radiation for numerical weather prediction and climate models. *Monthly Weather Review*, **112**, 826–866.
- Stephens, G. and S. Tjemkes, 1993: Water vapor and its role in the earth's greenhouse. *Aust. J. Phys.*, **46**.
- Tjemkes, S. and M. Visser, 1994: Horizontal variability of water vapor and cloud liquid water as derived from space borne observations. In: *Microwave Specialist Meeting 1994 in Rome*.
- Trenberth, K., J. Christy, and J. Olson, 1987: Global atmospheric mass, surface pressure, and water vapor variations. *Journal of Geophysical Research*, **92**(D12), 14,815–14,826.
- Turner, D., W. Feltz, and R. Ferrare, 2000: Continuous water vapor profiles from observational ground-based active and passive remote sensors. *Bulletin American Meteorological Society*, **81**(6), 1301 – 1317.
- Turner, D., B. Lesht, S. Clough, J. Liljegren, H. Revercomb, and D. Tobin, 2003: Dry bias and variability in vaisala rs80-h radiosondes: The ARM experience. *Journal of Atmospheric and Oceanic Technology*, **20**, 117–132.
- Ulaby, F., R. Moore, and A. Fung, 1981: *Microwave Remote Sensing, Active and Passive*. Artech House INC., Norwood, MA.
- Verdes, C., S. Bühler, A. von Engelen, T. Kuhn, K. Künzi, P. Erikson, and B. Sinnhuber, 2002: Pointing and temperature retrieval from millimeter-submillimeter limb soundings. *Journal of Geophysical Research*, **107**(D16).
- von Bremen, L., E. Ruprecht, and A. Macke, 2002: Errors in liquid water path retrieval arising from cloud inhomogeneities: The beamfilling effect. *Meteorologische Zeitschrift*, **11**(1), 13–19.
- Wagner, F., 1996: Manual for netfit, version 1.1, tech. rep. *Institut für Theoretische Physik an der Christian-Albrechts-Universität Kiel*.

- Wahl, S., A. Macke, and J. Schulz, 2003: Precipitable water in cloudy areas. *VS-Plan 7.7*, p. 26.
- Wang, J. and W. Rossow, 1995: Determination of cloud vertical structure from upper-air observations. *Journal of Applied Meteorology*, **34**, 2243 – 2258.
- Wang, J., W. Rossow, T. Uttal, and M. Rozendaal, 1999: Variability of cloud vertical structure during astex observed from a combination of rawinsonde, radar, ceilometer, and satellite. *Monthly Weather Review*, **127**, 2484 – 2502.
- Weinstock, E., E. Hintsala, A. Dessler, and J. Anderson, 1995: Measurements of water vapor in the tropical lower stratosphere during the CEPEX campaign: Results and interpretation. *Geophysical Research Letters*, **22**(23), 3231 – 3234.
- Westwater, E., 1997: Remote sensing of tropospheric temperature and water vapor by integrated observing systems. *Bulletin American Meteorological Society*, **78**(9), 1991 – 2006.
- Whiteman, D., K. Evans, B. Demoz, D. Starr, E. Eloranta, D. Tobin, W. Feltz, G. Jedlovec, S. Gutman, G. Schwemmer, M. Cadirola, S. Melfi, and F. Schmidlin, 2001: Raman lidar measurements of water vapor and cirrus clouds during the passage of hurricane bonnie. *Journal of Geophysical Research*, **106**(D6), 5211–5225.
- Whiteman, D. and R. Ferrare, 1992: Raman lidar system for the measurement of water vapor and aerosols in the earth's atmosphere. *Appl. Opt.*, **31**, 3068–3082.
- Wulfmeyer, V. and J. Bösenberg, 1998: Ground-based differential absorption lidar for water vapor profiling: Assessment of accuracy, resolution, and meteorological applications. *Appl. Opt.*, **37**, 3825–3844.

Acknowledgement

I would like to thank all people who accompanied me during the last years. There are some persons I like to highlight.

I thank

... Prof. Dr. Andreas Macke, for his continuous support in the Ph.D. program. He was always there to listen and to give advice.

....Dr. Karl Bumke for great discussions, his nerves to read the thesis in advance and for the good ideas how to proceed.

....the members of the working group 'clouds and radiation' for the constructive discussions.

....the colleagues placed in the 'Alte Botanik' for coffee, discussions, help with technical problems and lots of fun.

....the colleagues of the department of Meteorology at the Institute.

....the computer and data center of the Institute for their support.

....the 'Stammtisch' for the nice thursdays.

This work was funded by the European Project "Cloud Liquid Water - Network" CLIWA-NET (EU contract No. EVK2CT-1999-00007) and the Deutscher Wetterdienst Climate Monitoring - Satellite Application Facilities study 'Precipitable Water in Cloudy Area'.

I would like to thank all participants of these projects, especially Dr. Jörg Schulz for the discussions, data, and many ideas.

6. Oktober 1972	geboren in Hamburg deutsche Staatsangehörigkeit
August 1978–Juli 1982 August 1982–Juli 1984 August 1984–Juli 1991	Grundschule I, Neu Wulmstorf, Niedersachsen Orientierungsstufe, Neu Wulmstorf, Niedersachsen Gymnasium Neu Wulmstorf, Neu Wulmstorf Niedersachsen Abschluss: Allgemeine Hochschulreife
August 1991–Juli 1994	Deutsches Elektronen Synchrotron DESY Hamburg Ausbildung zur technische Zeichnerin, Fachrichtung Maschinenbau
August 1994–Oktober 1994	Weiterbeschäftigung in der Arbeitsgruppe H1.
November 1994–November 2000	Studium der Meteorologie an der Christian–Albrechts–Universität zu Kiel Abschluss: Diplom im Fach Meteorologie
November 2000–April 2003	Institut für Meereskunde, Kiel wissenschaftliche Mitarbeiterin im Projekt CLIWA–NET
Mai 2003–Dezember 2003	KNMI, de Bilt, Niederlande wissenschaftliche Mitarbeiterin in der Arbeitsgruppe Fernerkundung
Januar 2004–Dezember 2005	IFM–GEOMAR, Kiel wissenschaftliche Mitarbeiterin im Projekt CM–SAF Während der Zeit am IFM–GEOMAR, Kiel, Gelegenheit zur Promotion mit dem Thema: Fernkundung von atmosphärischen Wasser mit Mikrowellen Sensoren
Seit Januar 2006	ECOMA GmbH, Honigsee Projektingenieur, Bestimmung von Geruchsemissionen und –immissionen genehmigungspflichtiger Anlagen

Erklärung

Hiermit bestätige ich, dass ich die vorliegende Dissertation selbstständig verfasst und keine anderen als die angegebenen Quellen und Hilfsmittel verwendet habe.

Ich versichere, dass diese Arbeit noch nicht zur Erlangung eines Doktorgrades an anderer Stelle vorgelegen hat.

Ich erkläre, dass die vorliegende Arbeit gemäß der Grundsätze zur Sicherung guter wissenschaftlicher Praxis der Deutschen Forschungsgemeinschaft erstellt wurde.

Kiel, Dezember 2006

(Heike Hauschildt)